Evaluation of microstructure and mechanical properties of 0.5Cr-0.5Mo-0.25V steam piping after long-term service in creep conditions

Sibusiso Siphesihle Mngoma

School of Chemical and Metallurgical Engineering University of the Witwatersrand, Johannesburg

A dissertation submitted to the Faculty of Engineering and the Built Environment in fulfilment of the requirements for the degree of *Master of Science* in Metallurgy and Materials Engineering

October 2025

Declaration

I Sibusiso Siphesihle Mngoma
(Student number: 1867059) am a student registered for MSc
in the year 2025. I hereby declare the following

- I am aware that plagiarism (the use of someone else's work without their permission and/or without acknowledging the original source) is wrong.
- I confirm that the work submitted for assessment for the above course is my own unaided work except where I have explicitly indicated otherwise.
- I have followed the required conventions in referencing the thoughts and ideas of others.
- I understand that the University of the Witwatersrand may take disciplinary action against me if there is a belief that this is not my own unaided work or that I have failed to acknowledge the source of the ideas or words in my writing.

Student Signature: 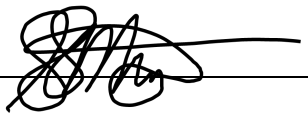 Date: 2025/10/03

Abstract

This work is part of the ongoing research by the South African power utility aimed at addressing the issues related to creep damage and safe extension of service life to meet the country's increasing electricity demand. Creep damage in low-alloy steels remains a major concern for the safe and reliable operation of high-temperature components in power plants. This study evaluates the microstructural evolution and mechanical property degradation of ½Cr–½Mo–¼V (14MoV6-3) steam piping that was in service for more than 270,000 hours. Optical microscopy, scanning electron microscopy, and X-ray diffraction were used to characterize microstructural evolution of the new and service-exposed materials, while Thermo-Calc software was employed to predict equilibrium carbides. Mechanical performance was assessed through hardness, tensile tests at room temperature and high temperatures (500°C –560°C), impact testing at -30°C to 200°C, and creep testing using standard and Gleeble® machine. The results revealed significant microstructural changes in the service-exposed material, with the disappearance of ferrite–pearlite/bainite structures and the presence of ferrite and carbides, predominantly $M_{23}C_6$ and M_6C along grain boundaries. Mechanical properties largely remained within the lower acceptance bounds but showed pronounced deterioration at elevated temperatures. Replica analysis confirmed creep damage to be most severe in the heat-affected zone, consistent with Type-IV failure. Cross-weld creep testing aligned with the lower limit of the European Creep Collaborative Committee (ECCC) master curve. The deviations from ECCC curve were attributed to prior long-term exposure. Overall, the findings highlight that prolonged creep service significantly reduces creep strength, underscoring the need for additional testing to establish reliable strength reduction factors for life extension assessments.

Keywords: 14MoV6-3 steel, creep damage, life assessment, microstructural evolution, mechanical properties

Dedication

This work is dedicated to my aunt Sibongile Mtshali who passed away in 2020. May her soul rest in eternal peace.

Acknowledgements

I would like to acknowledge the following people and institutions for their contribution in making this work a success:

- Eskom for the provision of financial support and affording me an opportunity to develop my competency under their Eskom Power Plant Engineering Institute (EPPEI) study programme.
- My supervisor, Professor N. Maledi and my former supervisor Professor L. Chown for their supervision, advice, support and valuable contribution throughout this work.
- My industrial mentors, Dr T. Pete and M. Bezuidenhout (may his soul RIP) for their guidance, mentoring and encouragement throughout my time of study.
- My colleagues T. Thage, M. Mabaso, J. Calitz, W. Mtambo, B. Potgieter, T. Molokwane, M. Raseroka, N. Mbatha, T. Ngoasheng and the rest of ERIC staff for their work, support and technical assistance on replica lifting, mechanical testing and microscopy analysis.
- Professor A. Ziegler and the staff at the Microscopy and Microanalysis Unit (MMU), Wits University, for their assistance on the XRD analysis work, providing training on the use of the diffractometer and associated software packages.
- J. Obiko and M. Bodunrin for their great assistance with the simulation and testing on the Gleeble® machine.
- D. Klenam, M. Mavundla and K. Nape for their valuable assistance with the thermodynamics modelling on the Thermo-Calc software.
- Dr J. Westraadt and the staff at Centre for High Resolution TEM, Nelson Mandela University for their assistance on the SEM EBSD and TKD work.
- K Bolokang, M. Pepeteni, J. Makuleka, S. Motshudi and the rest of the staff at Matla Power Station Boiler Engineering and Outage departments for their assistance in acquiring pipe material for this work.
- N. Mpasha, P. Sikhwari, H. Gumede, S. Moqabolane, P. Dinham and many other staff and fellow students at the School of Chemical & Metallurgical Engineering, Wits University, for lab assistance and words of encouragement.
- My dear friend N. Zungu and his former employers at LB Pipes for assistance with the plasma cutting of research pipe material to manageable parts.
- M. Rikhotso, W. Janse van Rensburg and all my colleagues at Matimba Power Station Engineering department and station wide for their continued support.

Let me further convey my gratitude to my mother, my sister and all my sibling, extended family and relatives, my friends and teammates whom I enjoy soccer with, fellow members of the Martians motorbike club and everyone who has supported me throughout this journey.

Finally, I am thanking my wife and my daughter, Nomcebo and Nandi Mngoma, for being my source of strength and bringing me great joy in life – even when faced with adversity!

Table of Contents

List of Figures

List of Tables

List of Abbreviations and Symbols

Abbreviation/Symbol	Description
ACR	Accelerated Creep Rupture
APU	Asymmetric Pattern Unit
ASTM	American Society for Testing and Materials
ATS	Applied Testing Systems
AWS	American Welding Society
A-USC	advanced ultra-supercritical
BC	Band Contrast
BCC	Body-Centred Cubic
BSE	Backscattered Electron
CALPHAD	Calculations of Phase Diagrams
CCT	Continuous Cooling Transformation
CE	Carbon Equivalency
CEF	Compound Energy Formalism
CGHAZ	Coarse-Grained Heat Affected Zone
CHRTEM	Centre for High Resolution Transmission Electron Microscopy
CS	Reheat Crack Susceptibility
CUI	Character User Interface
DBTT	Ductile to Brittle Transition Temperature
DIN	Deutsches Institut für Normung (*in English, the German Institute for Standardization*)
DPN	Diamond Pyramid Number
EBSD	Electron Backscatter Diffraction
ECCC	European Creep Collaborative Committee
EDS or EDX	Energy-Dispersive X-Ray Spectroscopy
ERIC	Eskom Research & Innovation Centre
FATT	Fracture Appearance Transition Temperature
FCC	Face-Centred Cubic
FGHAZ	Fine Grained Heat Affected Zone
FIB	Focused Ion Beam

Abbreviation/Symbol	Description
FOM	Figure Of Merit
FWHM	Full Width at Half Maximum
GTAW	Gas Tungsten Arc Welding
GUI	Graphic User Interface
GWh	Gigawatt Hours
HAZ	Heat Affected Zone
HRTEM	High Resolution Transmission Electron Microscopy
ICDD	International Centre for Diffraction Data
ICHAZ	Intercritical Heat Affected Zone
IPF	Inverse Pole Figures
LECO	Laboratory Equipment Corporation
LF	Life Fraction
LFR	Life Fraction Rule
MMA	Manual Metal Arc
NDE	Non-Destructive Examination
NDT	Non-Destructive Testing
OEM	Origin Equipment Manufacturer
OES	Optical Emission Spectroscopy
OM	Optical Microscopy
PAGB	Prior Austenite Grain Boundary
PDF	Powder Diffraction Files
PM	Parent Metal
PSF	Percentage of Shear Fracture
PWHT	Post Weld Heat Treatment
RA	Reduction in Area
RLE	Remaining Life Estimations
SE	Secondary Electrons
SEM	Scanning Electron Microscopy
SFR	Strains Fraction Rule
SGTE	Scientific Group Thermodata Europe
SMAW	Shielded Metal Arc Welding
SPCT	Small Punch Creep Test
Std. Dev.	Standard Deviation

Abbreviation/Symbol	Description
STEM	Scanning Transmission Electron Microscopy
T/T_m	Homologous Temperatures
TCC	Thermo-Calc Classic
TCFE	Thermo-Calc Database for Steel and FE-Alloys
TCW	Thermo-Calc Windows
TEM	Transmission Electron Microscopy
TIG	Tungsten Inert Gas
TKD	Transmission Kikuchi Diffraction
T_m	Melting Temperature
TOFD	Time of Flight Diffraction
T_p	Peak Temperature
TTP	Time-Temperature Parameter
UT	Ultrasonic Testing
UTS	Ultimate Tensile Strength
VHN	Vickers Hardness Number
WJ	Weld Joint
WM	Weld Metal
WPS	Welding Procedure Specifications
WSF	Weld Strength Factor
WSRF or SRF	Weld Strength Reduction Factor
XRD	X-Ray Diffraction
YS	Yield Strength
YTR	Yield to Tensile Strength Ratio

Chapter 1: Introduction

1.1 Background

Power generation plant components operating under high temperature and stress (within the creep range) are typically designed for a service life of at least 100,000 hours, corresponding to an expected operational lifespan of approximately 25 years (Maharaj et al., 2009; Janovec et al., 2012). In South Africa, most power-generation plants operate well beyond their design life, a trend also observed in many coal-fired power plants worldwide that operate within the creep regime (Abe et al., 2008; Rasiawan, 2017;). The combined average age of coal-fired power plants in South Africa is approximately 37 years. The power plant age and operating hours from inception until 2017 are presented in Figures 1.1 and 1.2 (van Zyl, 2019).

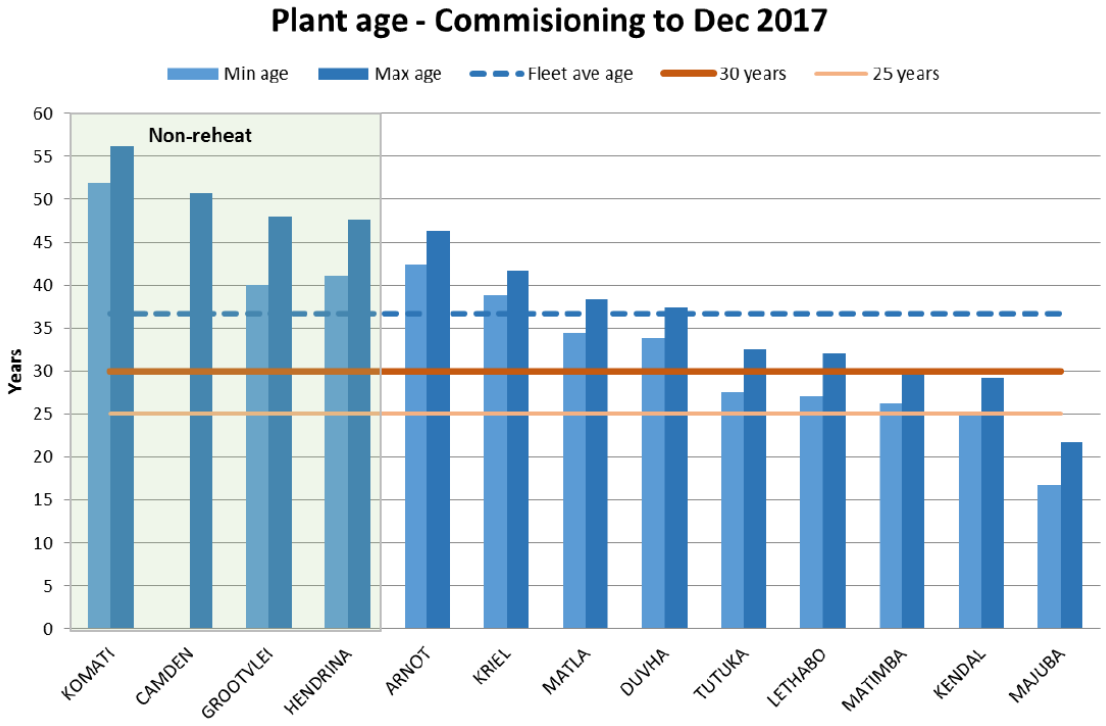

Figure 1.1 Plant age in years since commissioning until December 2017 (van Zyl , 2019)

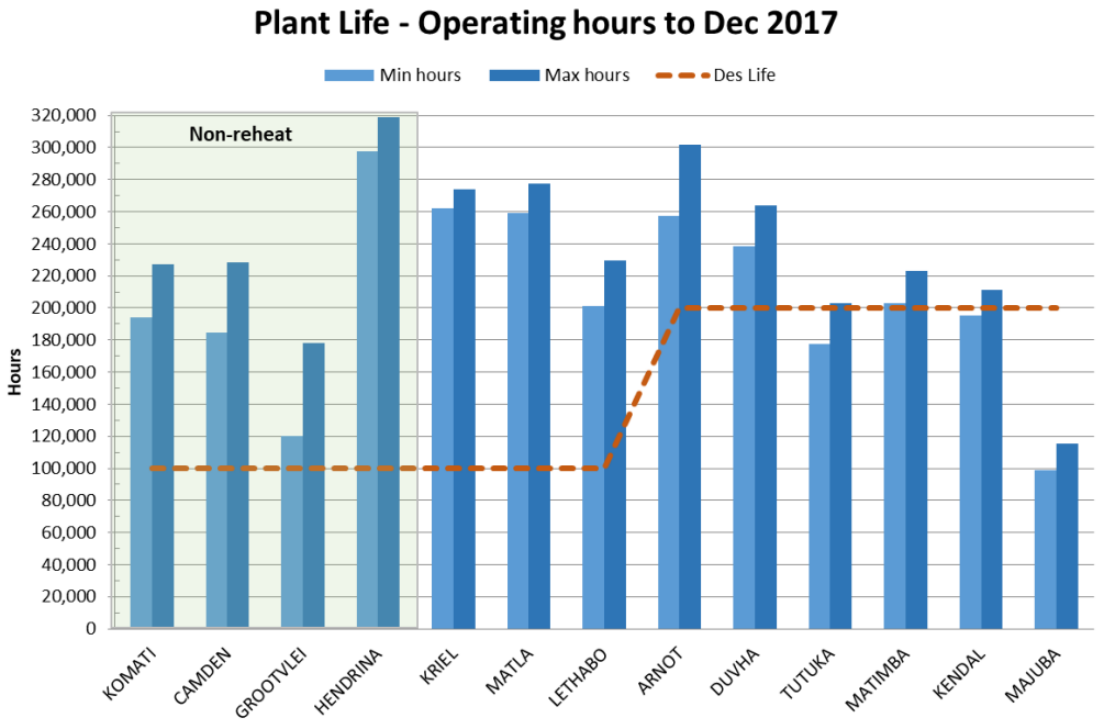

Figure 1.2 Plant age in estimated operating hours at 31 December 2017 (van Zyl, 2019)

Currently, replacement and new construction materials of pipes intended to operate under the creep regime must have a minimum design life of 200,000 hours and a component life of 50 years (Abe et al., 2008; van Zyl., 2013). However, the actual component life strongly depends on the manufacturing, construction, operation, and maintenance processes, as well as variations in operating conditions, changes in material properties, and time dependent degradation mechanisms that influence the performance and integrity of high-pressure piping systems.

To mitigate the risk of component failure and achieve the desired service life, extensive life and asset management programs are used to evaluate and estimate the extent of creep damage on power plants. These programs include using non-destructive testing (NDT) techniques and systematically incorporating periodic inspections as the components ages. The most used inspection-based procedures include replication and NDT, which effectively monitor component degradation and support timely interventions (Maharaj et al., 2009).

A full system replacement of the creep-exhausted material is the most economical approach. However, it is largely impractical owing to the combined effects of aging infrastructure, financial constraints, limited energy capacity, and reduced maintenance opportunities. In many instances, only weld repairs or partial replacements of creep-exhausted components

can be performed to enable safe operation and maintenance. Fusion welding a new material to a creep-aged component poses a risk due to the reduced remaining life of the aged material.

Components that are frequently subjected to welding in power generation plants include pipes, tubes, and headers (Hyde and Sun, 1998). These components typically operate in the creep range for long periods and are normally constructed from creep resistant alloy steels such as ½Cr-½Mo-¼V. The ½Cr-½Mo-¼V is a creep-resistant low alloy steel commonly known as 14MoV6-3 (British Standard Institution, 1990). The alloy is made to DIN standards and used in the manufacturing of many high-pressure components installed in older coal-fired power generation plants in South Africa.

The life of 14MoV6-3 components is limited by creep damage mechanism. The creep damage does not occur uniformly throughout the welded component, and it is most severe in the weld joint, while the surrounding base metal experiences less damage (Loots, 2003; Molokwane, 2013). This is attributed to the microstructural gradient in the heat affected zone (HAZ) resulting from the varying thermal cycles introduced during welding in fabrication and construction. As such, creep damage in 14MoV6-3 steam pipes subjected to plant stresses in the range of 40–60 MPa and high temperatures of 540–600°C tends to be restricted to butt, terminal, and attachment welds (Maharaj et al., 2009).

Over the past decades, extensive research has been conducted to understand the creep behaviour of welded structures, particularly those fabricated from ferritic steels. These studies were driven by the widespread failures of steam piping systems observed during the 1990s (Abe et al., 2008). This prompted studies into creep characterisation, testing methods, life prediction, repairs, material improvements, and welding procedures.

Notably, the weldability of materials decreases with creep ageing, eventually reaching a point where welding on aged material is no longer feasible. Consequently, assessing both the current condition of the in-service material and the initial behaviour of the replacement material is essential when undertaking weld repairs or partial replacements. This understanding is critical for optimising component life management strategies (Sroka et al., 2017; Janovec et al., 2012). Therefore, the effect of welding on creep-aged material, with particular focus on the resulting microstructural changes and mechanical properties, must be investigated and quantified.

1.2 Problem Statement

The power generation industry worldwide is facing growing challenges associated with aging coal-fired power station fleets amidst unfavourable energy demands and stringent environmental laws (Craddock et al., 2016). In South Africa, these challenges have led to the implementation of fleet renewal strategies that focus on extending plant life (Majola, 2016). However, renewal strategies also have several drawbacks, particularly when the conditions of installed components are not fully understood or cannot be conclusively determined. An extensive study of components used in service allows for a thorough assessment of microstructural evolution, determination of degradation levels, and estimation of the remaining service life. These assessments support the refinement of maintenance and monitoring strategies. This study can be used to complement conventional component creep exhaustion estimates, provide quantitative data for improving life management strategies, and set weldability limits and welding parameters for creep-exposed materials (Maharaj et al., 2009).

1.3 Justification of the Research

The DIN 14MoV6-3 alloy is a creep-resistant steel used on some boiler components of older power generation plants in South Africa. Most boiler components and systems operate at high temperatures and pressures and are exposed to creep. The failure of these components or systems could be catastrophic, resulting in serious injuries or fatalities and extensive plant damage with long unplanned outages.

South African power plants have adopted a risk-based life management strategy, where the creep life is monitored by periodic inspection of components and remaining life estimations (RLE). The inspection frequency depends on the rate of material degradation. The life management strategy is governed by the weldability and continued safe operation. Conservative limits are normally set in relation to creep damage accumulation. This necessitates the continual improvement and modification of life assessment strategies so that realistic weldability and operation limits can be set for the safe operation of components.

1.4 Research Questions

i. What is the effect of operating 14MoV6-3 steam piping material well beyond the design life of 100,000 hours at high temperature and low stress conditions?

ii. When is the full exhaustion of the creep life reached for 14MoV6-3 steam piping material?
iii. What is the effect of welding on the deformation behaviour and mechanical properties of creep aged 14MoV6-3 material?

1.5 Research Hypothesis

The long-term service operation of 14MoV6-3 steam pipes at high temperature and low stress leads to changes in the microstructure of the materials, resulting in mechanical properties degradation.

1.6 Aim and Objectives

1.6.1 Research Aim

This study aims to assess the remaining creep life and to characterise microstructure and mechanical properties of creep-aged 14MoV6-3 steel.

1.6.2 Research Objectives

The objectives of this research are as follows:

1. To determine the extent of life consumed in the base metal and welding ligaments of creep aged 14MoV6-3 pipe samples through conventional creep exhaustion estimates, mechanical testing, and microstructural evaluation.
2. To evaluate the effect of long-term high-temperature service on the properties of 14MoV6-3 material
3. To study the correlation between the microstructural changes and degradation of material properties due to long-term service exposure
4. To estimate the equilibrium phases and their composition in 14MoV6-3 samples.
5. To conduct HAZ simulations on creep aged samples

1.7 Outline of Thesis

The first chapter of the dissertation provides the background and challenges faced by creep-exhausted materials that have led to the need for this study. The research problem and the justification of the research are stated. The research aim and objectives are also presented in this chapter.

Chapter 2 reviews previous work, discussing the history and application of Cr-Mo-V low alloy steels in coal-fired power plants, material properties and microstructure of 14MoV6-3, including the role and effect of alloying elements. The chapter also addressed the welding and life assessment of service-exposed 14MoV6-3 steam piping.

Chapter 3 discusses the experimental procedures that were used to address the research objectives including, sampling, material preparation, mechanical testing, physical simulation and material characterisation. The specifications and onset conditions of the research material are also presented.

Chapter 4 presents the study results. The results are discussed in detail and contrast with the literature and industry norms. This includes the analysis and interpretation of the results obtained from microstructural examinations, mechanical property assessment, remaining life estimations, physical simulations, and thermodynamics modelling.

Chapter 5 presents conclusions and recommendations for future work.

Chapter 2: Literature Review

In this chapter, a systematic review of the historical development, metallurgical characteristics, and service performance of 14MoV6-3 steel is presented. The review explores creep mechanisms, microstructural evolution, weldment behaviour, and life assessment methodologies that are applied in coal-fired power plants across the world. The chapter also identifies gaps in the research of service-exposed 14MoV6-3.

2.1 Application of Cr-Mo-V Low Alloy Steels in Coal Fired Power Plants

Older coal-fired power plants worldwide use creep-resistant low-alloy steels, known as Cr-Mo-V steels, for components such as headers and steam pipelines that operate at elevated temperatures and high pressure. These steels are heat treated to produce the required creep properties and are crucial for the power generation industry due to their physical properties, thermal conductivity, thermal expansion coefficient, and high creep strength. However, many components manufactured from Cr-Mo-V ferritic alloy steels have experienced structural changes and degradation, leading to potential failure due to creep cavitation and long-term cracking of welds (Eskom, 1985; Cole, 2000; Igwemezie, et al., 2016).

The failure is mainly due to a decrease in yield strength and hardness of welds and parent metal over time in service. To assess the safe service life of these components, it is necessary to accurately predict or estimate the extent of creep damage and creep rupture life (Mohyla & Koukal, 2000; Spindler, et al., 2010; Dobrzanski, et al, 2011; Hodzic & Hajro, 2012;). The service life of a component consists of two distinct parts: the original design life, typically 100,000 hours, and the safe economic life, which is not influenced by design codes but usually represents a significant fraction of the overall service life (Cane & Aplin, 1994; Sun, 1996).

2.2 History of 14MoV6-3 Creep Resistant Low Alloy Steel in Coal Fired Power Plants

Molybdenum–vanadium (MoV) steel with higher creep strength was developed in Europe in the 1950s for application in gas turbines (Zrilic & Aleksic, 2003; Abe et al., 2008). Following extensive long-term creep testing, this alloy was later qualified for use in boilers due to superior creep strength and was designated as 14MoV6-3 (Abe et al., 2008; Rantala et al., 2009).

The development of 14MoV6-3 was driven by the demand for stronger and more durable materials capable of operating under high temperatures and pressures in coal-fired power plants. Historically, steels such as 14MoV6-3 formed the foundation of subcritical and early supercritical power plant technology, preceding the adoption of more advanced 9–12% Cr martensitic steels developed for ultra-supercritical conditions (Abe, et al, 2008; Shibli, 2014; Ennis, 2014;).

With a typical composition of 0.14%C–0.5%Mo–0.3%V, it was initially applied in gas turbines and later qualified through long-term creep testing for use in boilers and steam piping systems (Zrilic & Aleksic, 2003; Abe et al., 2008; Rantala et al., 2009). Its high creep rupture strength made it the material of choice for pipes carrying live and superheated steam.
The ability of 14MoV6-3 to provide reliable long-term service under such demanding conditions made it central to the advancement of subcritical and early supercritical coal-fired power plants.

The use of 14MoV6-3 in new plants began to decline from the late 1970s into the early 1980s. One reason was the emergence of poor ductility issues, which limited its long-term reliability (Rantala et al., 2009). Additionally, the development of advanced creep-resistant steels with higher chromium content, such as P91 (X10CrMoVNb9-1) and X20 (12Cr-1Mo-¼V) exhibited improved mechanical strength and creep resistance at higher operating conditions.

The 9 - 12% Cr martensitic steels became the preferred materials for modern ultra-supercritical power plants. Nevertheless, their higher alloying element content significantly increased production costs compared to low alloy steels (Burke, 2009). Despite its eventual replacement in new installations, 14MoV6-3 played a critical historical role in extending the safe operating envelope of coal-fired power plants. It bridged the transition from

conventional carbon steels, which were limited to ~450 °C, to more advanced alloys capable of withstanding higher thermal and mechanical demands, thereby enabling major improvements in efficiency and plant performance (Abe, et al., 2008; Rantala, et. al., 2009).

In recent decades, the continued development of creep-resistant steels has been strongly influenced by the global need to reduce emissions of harmful flue gases from coal-fired power plants. The major pollutants—carbon oxides (COX), nitrogen oxides (NOX), and sulphur oxides (SOX)—pose significant environmental and health concerns, driving stricter regulations and the adoption of advanced materials (Zeman, 2003; Abe, et. al., 2008;Maharaj, et al, 2009; Rantala, et al., 2009; Shibli, 2014; Heuser & Jochum, 2017;). As illustrated in Figure 2.1, improvements in plant materials have been closely tied to the evolution of efficiency and the reduction of CO_2 emissions (Di Gianfrancesco, 2017).

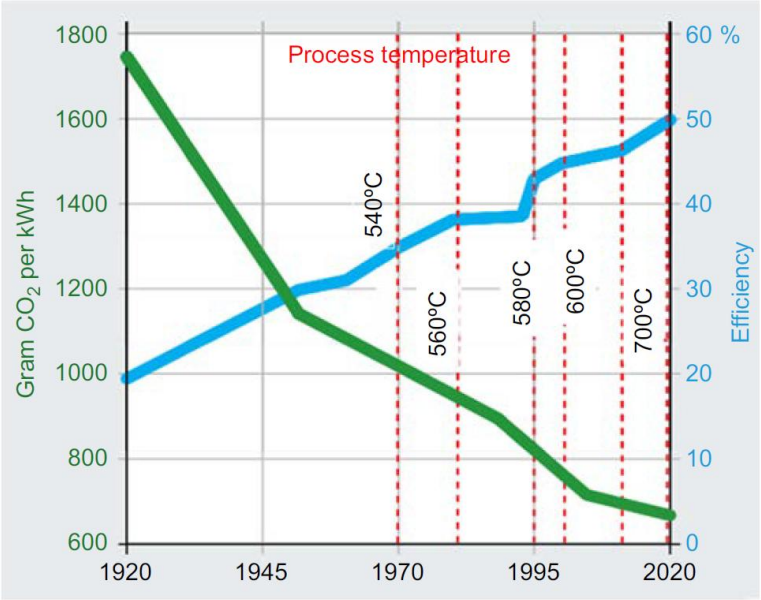

Figure 2.1 Evolution of efficiency and CO_2 emission in coal-fired power plants (Di Gianfrancesco, 2017)

Achieving higher thermal efficiencies requires coal-fired power plants to operate at elevated temperatures and pressures, which in turn significantly reduces specific fuel consumption and, consequently, pollutant emissions. For example, advanced ultra-supercritical (A-USC) technologies target efficiencies above 45%, a step-change compared to older subcritical plants with efficiencies of ~35%. However, operating under these more demanding conditions necessitates the use of higher-grade materials capable of withstanding extreme thermal and mechanical stresses over long service life (Rantala et al., 2009).

Conventional low-alloy steels such as 14MoV6-3, while effective up to ~565 °C, could not support the higher operating conditions required for modern ultra-supercritical plants. This limitation spurred the development of advanced 9 – 12% Cr martensitic steels, nickel-based alloys, and other next-generation materials, designed to provide superior creep resistance, oxidation resistance, and structural stability at elevated service conditions. Thus, the trajectory of material innovation in power plants reflects the dual imperative of efficiency and environmental sustainability by enabling higher operating conditions. Advanced steels directly support both increased power generation efficiency and the reduction of harmful flue gas emissions (Ennis, 2014; Di Gianfrancesco, 2017).

2.3 Material Properties and Characteristics of 14MoV6-3 Steel Pipes

The 14MoV6-3 steel has been extensively applied in the power generation industry worldwide, with several variations recognized under different international standards. Table 2.1 summarises the equivalent grades as specified in standards such as EN10216-2/DIN17715, BS 3640-660/UNI 5462, PN 84024, GOST 20072, and CSN 415128, which reflect its wide acceptance across Europe and beyond (Janovec et al., 2012).

Table 2.1 Equivalent materials of 14MoV6-3 according to some international standards (Janovec, et al., 2012)

Standard	EN10216-2/DIN17715		BS 3640-660/UNI 5462	PN 84024	GOST 20072	CSN 415128
Country	Great Britain	Germany	United Kingdom/Italy	Poland	Germany	Czech
Grade	1.7715 **EN steel no.**	14MoV6-3 **EN name**	12CrMoV6 2	13HMF	12Ch1MF	Grade 15128

The chemical composition of 14MoV6-3 is defined in BS EN 10216-2 (British Standards Institution, 2007) with typical values presented in Table 2.2. This low-alloy ferritic steel contains controlled amounts of carbon (0.10–0.15 wt.%), molybdenum (0.50–0.70 wt.%), vanadium (0.22–0.28 wt.%), and chromium (0.30–0.60 wt.%), along with small quantities of silicon, manganese, and trace elements (Holdsworth, 2004; Steel Data, 2019).

The combination of Mo, V, and Cr provides the steel with enhanced creep resistance, oxidation resistance, and mechanical stability at elevated temperatures. The designation "14MoV6-3" reflects the nominal concentrations of alloying elements. It is also referred to as ½Cr-½Mo-¼V or 0.5CrMoV steel, emphasizing its alloying composition

Table 2.2 Typical chemical composition (wt.%) of 14MoV6-3 steel (British Standards Institution, 2007)

C	Si	Mn	P	S	Cr	Mo	Ni	Al	Cu	V
0.10 to 0.15	0.15 to 0.35	0.40 to 0.70	0.025 (max)	0.020 (max)	0.30 to 0.60	0.50 to 0.70	≤0.30	≤0.040 (total)	≤0.30	0.22 to 0.28

The 14MoV6-3 alloy exhibit excellent strength and toughness at room temperature, with minimum proof strength of 320 MPa (for wall thickness $16 < T \leq 40$ mm), tensile strength in the range of 460–610 MPa, elongation values of 20% in the longitudinal direction and 18% in the transverse direction. The impact resistance is also notable, with minimum absorbed energy values of 40 J and 27 J in the longitudinal and transverse direction, respectively. Mechanical properties are summarised in Table 2.3. Acceptable hardness values ranges from 140 to 192 HV_{10}, ensuring adequate resistance to wear and deformation (British Standards Institution, 2007; Hodzic & Hajro, 2011; Junek & Janovec, 2015).

Table 2.3 Mechanical properties of 14MoV6-3 at room temperature (British Standards Institution, 2007)

Tensile properties				**Impact properties**	
Upper yield strength or proof strength R_{eH} or $Rp_{0.2}$ for Wall Thickness T min [MPa]	Tensile strength [MPa]	Elongation A min. [%]		Minimum average absorbed energy [J]	
$16 < T \leq 40$		Longitudinal	Transverse	Longitudinal	Transverse
320	460 - 610	20	18	40	27

The high-temperature creep properties of 14MoV6-3 are among its most important characteristics in power plant applications. Table 2.4 presents the creep rupture strength at

540°C, showing values of 162 MPa at 10,000 hours, decreasing to 102 MPa at 100,000 hours, and stabilizing at around 82 MPa for up to 250,000 hours of service.

Table 2.4 Creep rupture strength of 14MoV6-3 steel at 540°C (British Standards Institution, 2007)

Rupture time [hours]	Creep rupture strength [MPa]
10,000	162
100,000	102
200,000	88
250,000	82

Figure 2.2 shows the variation of minimum proof strength at elevated temperatures. This data confirm that 14MoV6-3 provides reliable long-term performance in components such as superheaters, reheaters, headers, and steam lines operating under high thermal and pressure stresses.

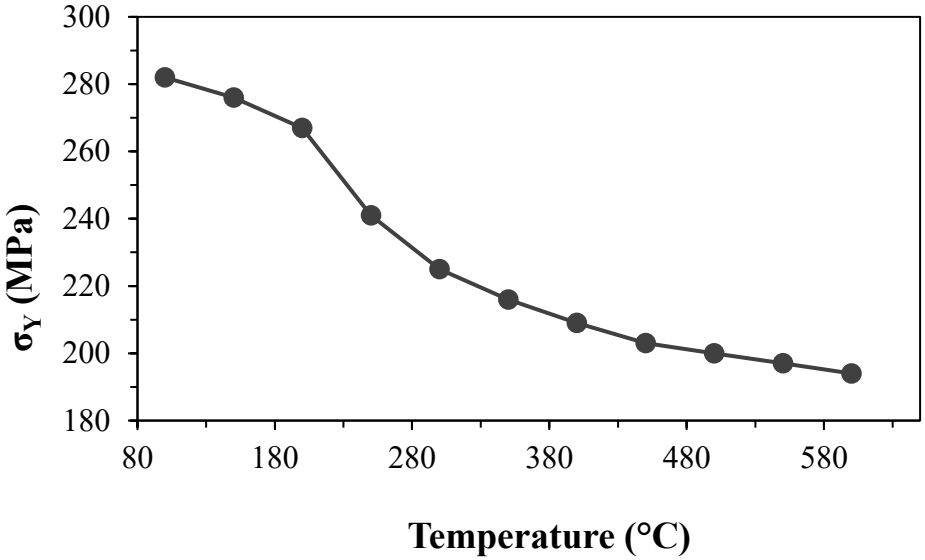

Figure 2.2 Minimum proof strength of 14MoV6-3 at elevated temperature (British Standards Institution, 2007)

In summary, the specification of 14MoV6-3 steel demonstrates why it became a widely adopted material in the mid-20th century for critical high-temperature components in coal-fired power plants.

2.4 The Role and Effect of Individual Elements on 14MoV6-3 Steel Composition

Power plant steels are produced by adding alloying elements to iron (Fe). Typical elements include carbon (C), chromium (Cr), nickel (Ni), manganese (Mn), sulphur (S), tungsten (W), titanium (Ti), vanadium (V), molybdenum (Mo), aluminium (Al), etc. The material is further heat treated to obtain the desired microstructure and mechanical properties (Totten, 2007; EPRI, 2008).

It is well established that minor changes in the quantity of alloying elements can have great effect on material properties (Abe, et. al., 2008; Burke, 2009). Furthermore, the effect of these small differences can influence the creep strength and service life of the material. Figure 2.3 shows the effect of different alloying elements on the eutectoid transformation temperature and the effective carbon content (ASM International, 2012). Therefore, it is worthwhile to understand the effect of each alloying element on the mechanical performance and the formation of precipitates, which influence creep properties.

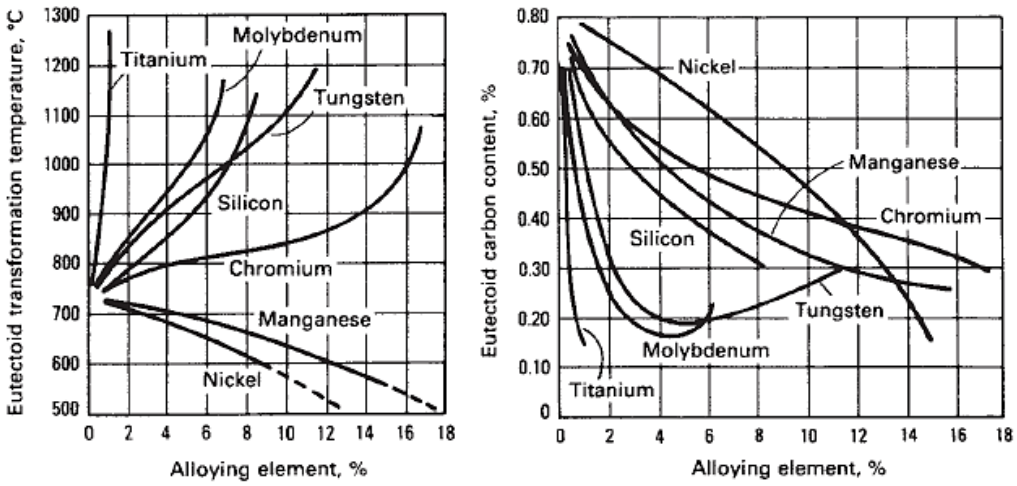

Figure 2.3 Effect of alloying elements on the eutectoid temperature and effective carbon content (ASM International, 2012)

Carbon

Carbon (C) is a crucial austenite stabilizing element in steels, responsible for carbide formation and secondary hardening. It increases tensile strength, hardness, and hardenability, and promotes precipitation of M23C6 and MX. However, increasing carbon content leads to

decreased toughness, ductility, and weldability. The transition temperature of material fracture behaviour increases with carbon content, and weldability decreases due to increased hardenability. High levels of carbon can reduce material properties, making steel susceptible to failure after welding or heat treatment. A 0.15 wt.% C level is optimum for 12% Cr steels (Cole, 2000; Totten, 2007; EPRI, 2008; Burke, 2009; Akhtar, 2017).

Chromium

Chromium (Cr) is a carbide former in creep resistant steels, stabilizing ferrite and improving oxidation, scaling, strength, and corrosion resistance at high temperatures. It reacts with carbon to form precipitation-hardening carbides like $Cr_{23}C_6$, Cr_7C_3, and Cr_3C_2, which dissolve iron. Alloyed cementite forms at low Cr/C ratios, while other chromium carbides appear as the ratio increases. Chromium is also added in low alloy steels to improve hardenability, achieving the hardenability required for bainitic steel. Even at low contents, Cr allows bainite formation at normal air cooling rates without expensive mediums (Loots, 2003; Totten, 2007; Burke, 2009; Vyrostkova, et al., 2011; Ibrahim, 2011; Dowling, 2012; Zielinski, et al., 2013; Shibli, 2014; Ennis, 2014;Sroka M. , et al., 2017; Akhtar, 2017).

Molybdenum

Molybdenum (Mo) is a crucial carbide former and ferrite stabilizing element in alloy steels. It increases high temperature tensile strength and creep resistance in alloys exposed to harsh environments. Molybdenum also delays the effect of trace elements like phosphorus on temper embrittlement. It forms stable carbides like Mo_2C, Fe_4Mo_2C, and $Fe_{21}Mo_2C_6$ and contributes to solution hardening and Mo_2C precipitation in ferrite. 14MoV6-3 steel has higher 100,000 hrs creep rupture strength than low alloy steels. Molybdenum improves machinability in chromium-containing steels, stabilizing M_6C and $M_{23}C_6$ carbides. However, without chromium, molybdenum may lead to graphitisation (Loots, 2003; Holdsworth, 2004; Brett, 2004; Totten, 2007; Abe, et al., 2008; EPRI, 2008; Burke, 2009; Vyrostkova, et al., 2011; Shibli, 2014; Bhadeshia, 2015).

Vanadium

Vanadium (V) acts as ferrite stabiliser and strong carbide former (Totten, 2007; EPRI, 2008; Burke, 2009;). Vanadium is usually present as stable VC carbides or carbonitrides that improve the elevated strength of the material, provide resistance to tempering and hydrogen attack, and prevent grain growth during heat treatment. Vanadium further improves creep strength due to the V_4C_3 precipitates which are very stable in ferritic microstructure and

stabilises the M_2X and MX phases (Loots, 2003; Holdsworth, 2004; Brett, 2004; Abe, et al., 2008; Shibli, 2014;). The diffusion of carbon into vanadium carbides may also enhance its strengthening effect by contributing to the solid solution strengthening. Vanadium also resists softening at high temperature, but the steel must be correctly heat treated to make sure that the VC carbide is taken into solid solution. Addition of small amounts of vanadium tend to increase hardenability but larger amounts are likely to reduce hardenability due to the extensive carbide formation. In addition, excessive strengthening may result in reheat cracking during welding (Brett, 2004).

Manganese

Manganese (Mn) is an austenite stabiliser and carbide former. Manganese is usually found to negatively affect the creep strength of low alloy steels as it promotes the retention of austenite that is rich in carbon and nitrogen, which subsequently hinders secondary hardening (Totten, 2007; EPRI, 2008; Shibli, 2014). Manganese tends to promote temper embrittlement and increase the segregation of trace elements to the grain boundaries. Manganese reacts with sulphur (S) to form manganese-sulphide (MnS). Although MnS tends to enhance reheat-cracking susceptibility in low alloy steels, the formation of MnS reduces susceptibility to hot shortness that is caused by the free sulphur (EPRI, 2008; Shibli, 2014).

Sulphur

Sulphur (S) is a ferrite stabiliser and its addition in low alloy steel may lead to solidification cracking due to the strong tendency of segregating at the grain boundaries and forming low-melting-point (~990°C) compounds of iron sulphides (FeS) (Bailey, 1994; Kou, 2003; Totten; 2007; EPRI, 2008;). Furthermore, sulphur can cause the formation of sulphides (MnS) that provide preferential nucleation sites (grain boundaries) for cavity formation. This is because of the low interfacial adhesion between MnS and the ferrite matrix, which also contributes to the reduction of strength (traverse), weldability and impact toughness. However, MnS is less detrimental than FeS due to its globular morphology and higher melting point (EPRI, 2008).

Silicon

Silicon (Si) is a ferrite stabiliser and a non-carbide forming element that is typically found in the matrix (Totten, 2007; EPRI, 2008). However, silicon has been found to influence the rate at which carbides precipitate. Also, silicon contributes to the formation of protective oxidation layers that reduces the amount of surface scale, which can form during high

temperature operation. A major drawback of silicon addition (>0.4 wt.%) is that it promotes the formation of undesirable *δ-ferrite* phase in the same way as chromium. The formation of *δ-ferrite* may lead to the reduction in tensile strength, creep rupture strength and toughness. Nevertheless, silicon increases strength without greatly affecting ductility when its contest is below 0.3 wt.%. Also, silicon produces greater hardenability of steels when combined with manganese or molybdenum (Totten, 2007)

Aluminium

Aluminium (Al) is a ferrite stabiliser and a non-carbide forming element that is commonly added to control grain size and deoxidise steel (Totten, 2007; EPRI, 2008; Bhadeshia, 2015). Aluminium is also used to improve scaling resistance or corrosion resistance of steels and alloys. However, the addition of aluminium is normally restricted to very small quantities since aluminium tends to promote graphitisation (Totten, 2007; EPRI, 2008).

Phosphorus

Phosphorus (P) is a ferrite stabiliser and a non-carbide forming element that dissolves in ferrite and increase the strength of steel (Totten, 2007; EPRI, 2008). However, it is typically considered to be a low purity element, as it forms a very brittle $(Fe)_3P$ phase in its solid state. The presence of phosphorus in substantial amounts may lead to temper embrittlement of alloying steel since it tends to segregate at grain boundaries. Also, the ductility and impact toughness of steel decreases with the increase of phosphorus content. As such, the content of phosphorus is usually limited to levels below 0.04 wt.% (Totten, 2007; EPRI, 2008).

Niobium

Niobium (Nb) is a ferrite stabiliser and a very strong carbide/nitride. The addition of niobium contributes to grain refinement, which leads to a shift in fracture transition temperature to lower values and increases the yield strength of the material at high temperature (Totten, 2007; EPRI, 2008).

Titanium

Titanium (Ti) is a very strong carbide and nitride former that has the same alloying effects as niobium and vanadium (Totten, 2007; EPRI, 2008). However, titanium carbides and nitrides are more stable compared to niobium and vanadium carbides and nitrides. Titanium nitrides improve creep rupture strength and provide finer grain size at elevated temperature (Totten, 2007; EPRI, 2008).

Nickel

Nickel (Ni) is an austenite stabilising element that does not form carbides. It improves hardenability, impact toughness and fatigue resistance in Cr and Mo containing steels (Totten, 2007; EPRI, 2008).

Cobalt

Cobalt (Co) is a non-carbide forming element that stabilises austenite. The addition of cobalt in steel promotes precipitation hardening, improves high temperature strength and prevents grain growth at elevated temperatures (Cole, 2000; Totten, 2007).

Copper

Copper (Cu) is an austenite stabiliser and a non-carbide forming element that is usually added to power plant steels purely for counteracting the undesired formation of *δ-ferrite* (Totten, 2007; EPRI, 2008). The addition of copper in low alloy steels improves tensile properties and atmospheric corrosion resistance. Copper also contributes to precipitation hardening when its composition is above 0.3 wt.%. However, copper has adverse effects on hot workability of steel and leads to poor surface quality. Copper may also decrease the creep ductility of steel (Cole, 2000; Totten, 2007; EPRI, 2008;).

Boron

Boron (B) is a ferrite stabilising element that is usually added to alloy steels in very small amounts to improve hardenability (Totten, 2007; EPRI, 2008). The addition of boron is generally considered to have beneficial effects on high temperature strength of alloys. However, increased levels of boron may have a negative effect on ductility and weldability. Also, the excess boron can react with nitrogen to form coarse boron nitride precipitates that may lead to finer nitrides (*e.g.* VN) being reduced in the alloy (Totten, 2007).

2.5 Microstructure of 14MoV6-3 Steels

The 14MoV6-3 is normally supplied in the normalised and tempered condition with a ferritic and bainitic/pearlitic microstructure (Suman and Pal, 2004; Holdsworth, 2004; Dobrzanski, et al., 2007; Rantala, et al., 2009; Vyrostkova, et al., 2011; Janovec, et al., 2012; Zielinski, et al., 2013;Shibli, 2014; Sroka, et al., 2017). A typical continuous cooling transformation (CCT) diagram of 14MoV6-3 steel is shown in Figure 2.4.

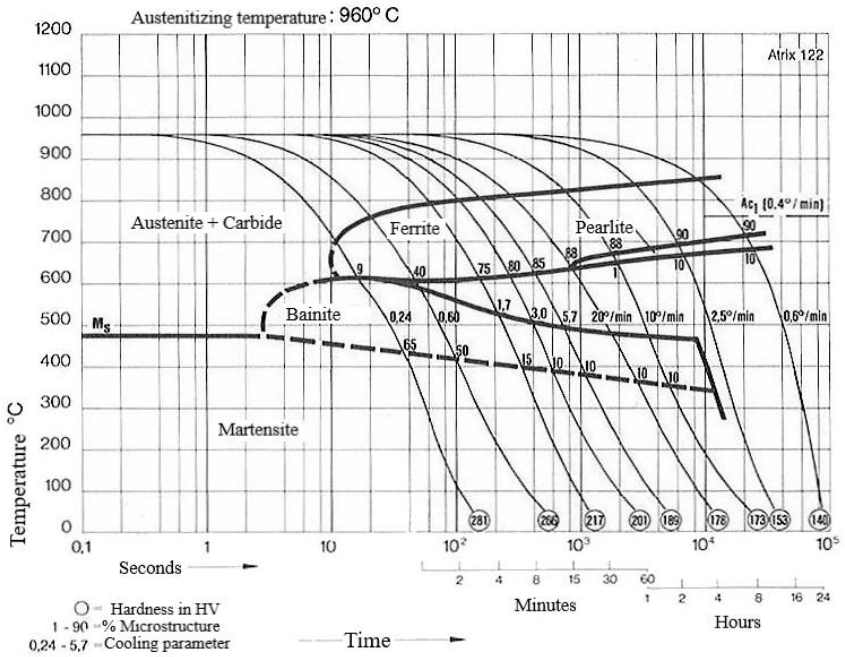

Figure 2.4 Typical continuous cooling transformation diagram of 14MoV6-3 steel (Steel Data, 2019)

The CCT diagram is a plot of various cooling curves that show the effect of cooling rates on the structure and changes in the hardness. For instance, a ferrite pearlitic structure may be achieved with slower cooling rates (*e.g.* air-cooling) and on the other hand, more rapid cooling rates (*e.g.* water quenching) may be used for the formation of bainite or even martensite. At the cooling rate of 10°C/min, the achieved structure consists of approximately 10% Bainite, 1% Pearlite and 88% Ferrite with a hardness of 173 HV. However, at cooling parameter of 0.24, the achieved structure has a hardness of 281 HV and consists of 9% ferrite, 65% bainite and martensite balance (Steel Data, 2019).

The initial microstructure (as-received condition) of 14MoV6-3 steel has the following mixture of phases that may be observed depending on the heat treatment and cooling rates:

1) Bainite – small spheroidal (non-lamellar aggregates) cementite precipitates
2) Ferrite – very fine precipitation of MC carbides inside ferrite grains
3) Pearlite (very small amount) – cementite lamellae in the pearlite colonies

The bainite transformation start (B_s) temperature can be calculated using Equation 2.1 (ASM International, 2012). This empirical formula considers the effect of alloying elements on B_s. The formula is valid for low carbon bainitic steels that have a carbon content of 0.15 – 0.29 wt.% and operating in creep conditions in power generation plants.

For 14MoV6-3, the B_s temperature may be expected to fall between 659°C and 731°C (British Standards Institution, 2007).

$$\boldsymbol{B_s = 844 - 597(\%C) - 63(\%Mn) - 16(\%Ni) - 78(\%Cr)} \quad \textbf{(2.1)}$$

The low alloy steel 14MoV6-3 has good long-term microstructural stability in service that is normally attributed to the MX-type precipitation strengthening, achieved through PWHT (Ennis, 2014).

The 14MoV6-3 steel experiences a decrease in hardness and strength due to coarsening of carbide precipitates, which leads to a reduction of the dislocation density. The resulting structure after long-term service is that of ferrite with fine carbide. The 14MoV6-3 steel is capable of operating at high temperatures of 480 – 580°C and pressures of 3 MPa to 18 MPa (Zrilic & Aleksic, 2003; Brett, 2004; Dwornicka & Pietraszek, 2010; Vyrostkova, et al., 2011).

The main active mechanism in ferritic creep resistant steels is precipitation strengthening (Abe, et al., 2008). The grain size is also particularly important as it is a crucial element for good mechanical properties such as creep rupture strength (Abe, et al., 2008; Rantala, et al., 2009; Vyrostkova, et al., 2011). Also, the susceptibility of the steel to reheat cracking and type IV cracking can be estimated making use of grain size.

2.6 Carbides and Phase Compositions in Cr-Mo-V Steels

There are two nucleation mechanisms that take place during the aging of low alloy steels (Dobrzanski, et al., 2011; Liu, et al., 2019). These mechanisms are termed in-situ transformation and separation nucleation. During in-situ transformation, new carbides form directly from the existing carbides and grow at the expense of the existing carbides. In separation nucleation, the existing carbides are dissolved into the matrix whilst the new carbides form and grow at the same time. The class of carbides that typically form in Cr-Mo-V low alloy steels and other ferritic steels are shown in Figure 2.5. The description of the carbides that are typically present in low alloy steels are summarised in Table 2.5 (Cole, 2000; Masuyama, 2001; Brett, et al., 2005).

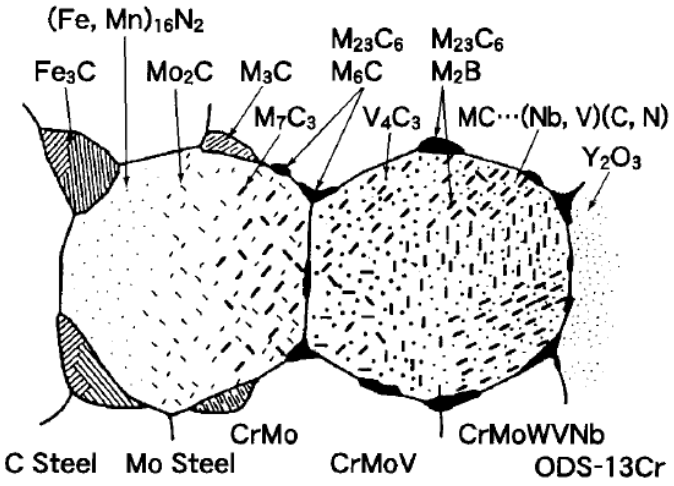

Figure 2.5 Typical microstructure and precipitates found in various ferritic steels (Masuyama, 2001)

Table 2.5 Typical carbides present in low alloy steels (Brett, et al., 2005; Cole, 2000; Burke, 2009; Shibli, 2014)

Carbide	Description
M_3C	Generally, cementite (Fe_3C) but typically includes other metallic elements, mainly Mn. The tendency of elements to partitioning between ferrite matrix and affinity to carbon carbide formation controls the content of other elements in cementite. M_3C has the same orthorhombic structure of cementite. The general formula $(Fe, Cr, Mn, Mo, etc.)_3C$ can be used to refer to M_3C carbides.
M_7C_3	This is a group of chromium rich carbides with a trigonal structure. M_7C_3 forms after M_2X or after cementite forming without any M_2X being observed. M_7C_3 may also include Mn, Mo and V metallic elements. Fe dissolves with smaller solubilities for Mn, V and Mo, respectively. The general formula of M_7C_3 can be written as $(Fe, Cr, Mn, Mo, V, etc.)_7C_3$.
$M_{23}C_6$	These are generally Mo and W rich carbides for steel containing Mo and W. However, they are Cr rich for other steels that do not contain Mo and W. In addition, the $M_{23}C_6$ carbides normally include Fe and Mn, and are commonly observed at the grain boundaries. Nonetheless, they do occasionally form within the grains as small carbides. $M_{23}C_6$ is the basic chemical formula for $Cr_{23}C_6$ since the other alloying elements are generally found to substitute partially for chromium.
M_6C	M_6C is a ternary carbide of Fe-Mo or Fe-W with an appreciable solubility for other elements. M_6C has a face-centred cubic (FCC) structure and usually contains Mo and Fe but it is not high in Cr. The M_6C carbides may lead to a reduction in creep strength.
MC	MC carbides are mostly formed by V, Nb and Ti. They have a cubic structure and may also exist as MX. In the V rich carbides, the V_4C_3 and VC concentration are generally linked to same group. However, the Mo and W rich carbides are normally considered separately since they have a hexagonal structure.
M_2C	M_2C is usually a Mo rich carbide with FCC structure. The precipitation of M_2C causes secondary hardening, which is of particular importance in low-alloyed steels where M_2C contributes significantly to the creep strength of the alloy. The general formula for M_2C carbides is $(Mo)_2C$.

Several carbides and precipitates can form in creep resistant alloy steels. These carbides and precipitates have a direct influence on the properties of the alloy. The composition and heat treatment are very important in determining the type of precipitates formed. Equilibrium diagrams can be used to estimate the structure that is likely to be encountered in practice since it is possible to construct a diagram that shows expected phases for a group of steels at a certain temperature. Figure 2.6 shows a carbide constitution diagram for a 0.2 wt.% carbon steel at 700°C, with varying chromium and vanadium content.

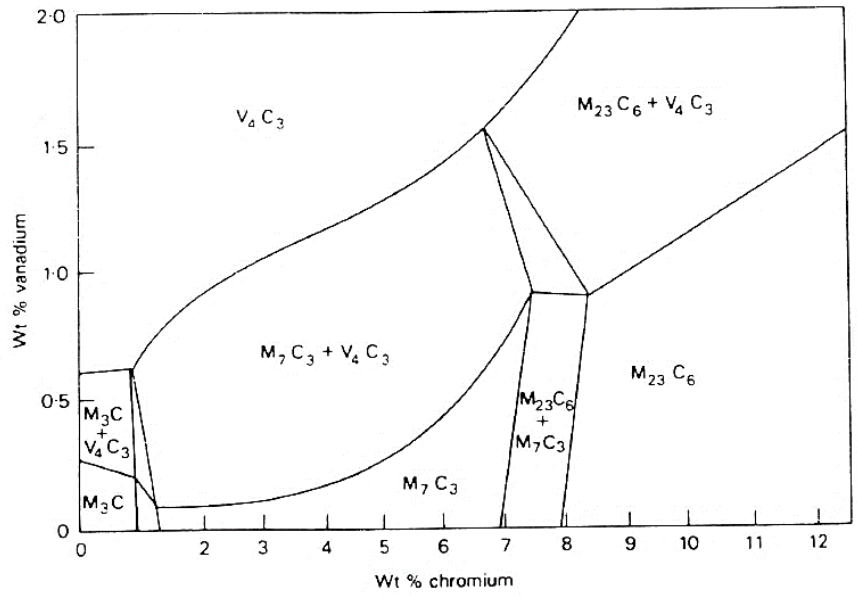

Figure 2.6 Carbide constitution at 700°C in a 0.20 wt.% C chromium vanadium steel (Cole, 2000)

Vyrostkova et al. (2011) examined the microstructure and mechanical properties of 14MoV6-3 from a steam pipe after 200,000 hours at 565°C. The material was found to be over-tempered, with exhausted plasticity, and recrystallized post-service microstructure and low dislocation density. The microstructure consisted of ferrite and carbide mixtures, with many voids at grain boundaries, typical of creep degradation. Large Fe-rich $M_{23}C_6$ carbide particles are found inside ferrite grains, while Mo_2C carbides are found along grain boundaries and inside the grains. Differences were observed in grain size, number of cracks, and void presence in the middle of the pipe wall compared to the inner side, with grain size at the middle being slightly larger.

2.7 Sequence of Carbide Precipitation in 14MoV6-3 Steels

Low alloy creep resistant steel pipes can experience microstructural changes due to long-term operation in creep conditions. These changes involve the decay of pearlite/bainite areas

and changes in the morphology and number of precipitated carbides (Zeman, 2003; Zielinski, et al., 2012). The deterioration of the microstructure can lead to excessive loss of component life. Thermodynamic calculations of 14MoV6-3 indicate the material should consist of body-centered cubic (BCC), MC, M_2C, and M_7C_3. However, Vyrostkova et al. (2011) found the M_7C_3 carbide in all service-exposed 14MoV6-3 material investigated, while Zielinski et al. (2012) found the presence of the M_7C_3 carbide in service-exposed 14MoV6-3 steel. The type and form of carbides in 14MoV6-3 material evolve as time in service increases. Figure 2.7 shows the estimated phase composition of the 14MoV6-3 system at 838K (Vyrostkova, et al., 2011).

$$M_3C+MC+M_2C \rightarrow M_3C+MC+M_{23}C_6+M_2C \rightarrow MC+M_{23}C_6+M_2C+M_6C$$

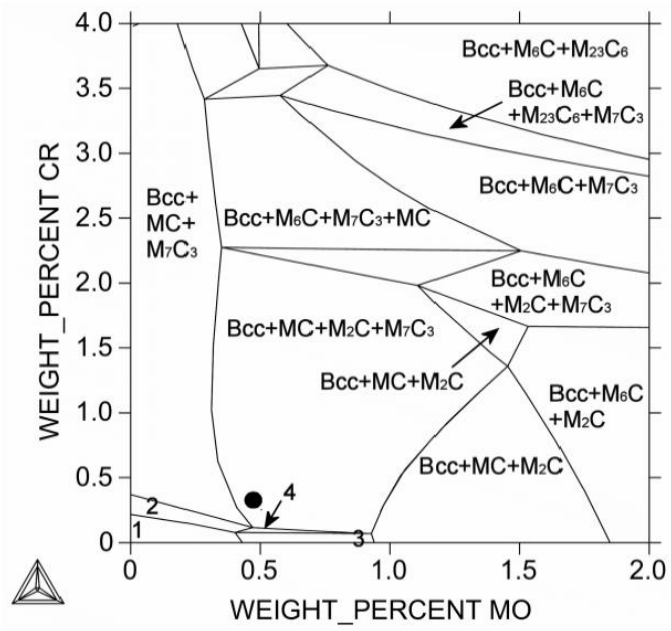

Figure 2.7 Estimated phase composition of the 14MoV6-3 system at 838K (Vyrostkova, et al., 2011)

2.8 Welding of 14MoV6-3 Steel

Fusion welding is the primary method for joining and repairing high-pressure components in power generating plants (Cerjak, 2008). 14MoV6-3 and other Cr-Mo-V steels are joined using matching consumables of 2.25Cr1Mo (10CrMo9-10), which provide good creep properties. Matching consumables specifically made for welding 14MoV6-3 are also available (Smith, et al., 2003; Brett, 2004; Rantala, et al., 2009; Bohler Welding, 2009; Shibli, 2014)

Low hydrogen consumables with lower carbon content are recommended for low alloy steels. Most arc welding processes are suitable for 14MoV6-3 steel welding. Welding Procedure Specifications (WPS) for steam piping made of 14MoV6-3 steel usually specify Gas Tungsten Arc Welding (GTAW) and the Shielded Metal Arc Welding (SMAW) (Du Toit, 2012; Shibli, 2014).

Carbon Equivalency (CE) is used to determine the hardenability of a steel and assess if preheat is required in welding that steel (Kou, 2003; Bailey, 1994). The chemical composition of basic core wire alloyed electrode and rod filler material for welding 14MoV6-3 base metal is typically required to comply with AWS A5.5M and A5.28M specifications, which are also required for welding coal-fired power plants in South Africa (Bohler Welding, 2009; Dlamini, 2013).

2.9 Preheat and Post Weld Heat Treatment of 14M0V6-3 Weldments

Preheat is often applied prior to welding of low alloy steels to eliminate the risk of hydrogen cracking, reduce the effect of residual stresses and reduce HAZ hardness. It is more difficult to weld steels with higher carbon content, especially at ambient temperature due to the HAZ cooling rates between 800°C – 500°C (Hinton & Wiswesser, 2008).

The steel weldability is represented by carbon content and alloy elements that are combined as the CE. The hardenability of alloy steels is derived from their carbon content together with the content of several other alloying elements. Other alloying elements give the same hardness as 1% carbon and their relative amounts are known, which makes it possible to estimate the hardenability of the material.

The CE of 14MoV6-3 steel is estimated at $0.41 \leq CE \leq 0.62$, based on the specified chemical composition and it is calculated using Equation 2.2 (Bailey, 1994; British Standards Institution, 2007; Hinton & Wiswesser, 2008). The preheating temperature that is recommended for 14MoV6-3 is 150°C – 200°C. Furthermore, interpass temperatures of up to 300°C are usually specified to control weldment properties in multipass welds.

$$CE = \%C + \frac{\%Mn}{6} + \frac{\%(Cr+Mo+V)}{5} + \frac{\%(Ni+Cu)}{15} \quad (2.2)$$

PWHT is applied to reduce residual stress levels and temper the weldment, making the joint tougher and less susceptible to cracking than in the as-welded condition. Temperatures of 650°C and above are normally used for PWHT of Cr-Mo-V steels depending on the required properties and intended application (Bailey, 1994).

An intermediate temperature is often used to get optimum creep resistance. Lower temperatures are applied to obtain highest strength, and the higher temperatures are used to achieve the maximum softening and stress relaxation.

In South African power plants, maximum heating and cooling rates are normally specified based on pipe thickness (Dlamini, 2013). The heating and cooling rates are limited to 220°C/h for pipework with thickness of ≤ 25 mm. Otherwise, the PWHT temperature and time is generally specified at 730±5°C for 2 hours when welding 14MoV6-3 steel. However, when welding is done on material that has exceeded its creep design life, PWHT parameters (especially the heating and cooling rates) are specified considering the material condition and the pipework configuration. This is done to limit any further degradation of the material properties (Dlamini, 2013; Molokwane, 2013).

2.10 Heat Affected Zone of 14MoV6-3 Steel

The properties of steel and its microstructure are altered during welding due to the high thermal cycle experienced by the PM (Abe, et al., 2008). The change in the microstructure of the steel results in a HAZ is made up of several sub-zones as depicted in Figure 2.8 (Blondeau, 2008). Furthermore, the mechanical properties of the HAZ sub-zones will most likely not be the same (Easterling, 1992).

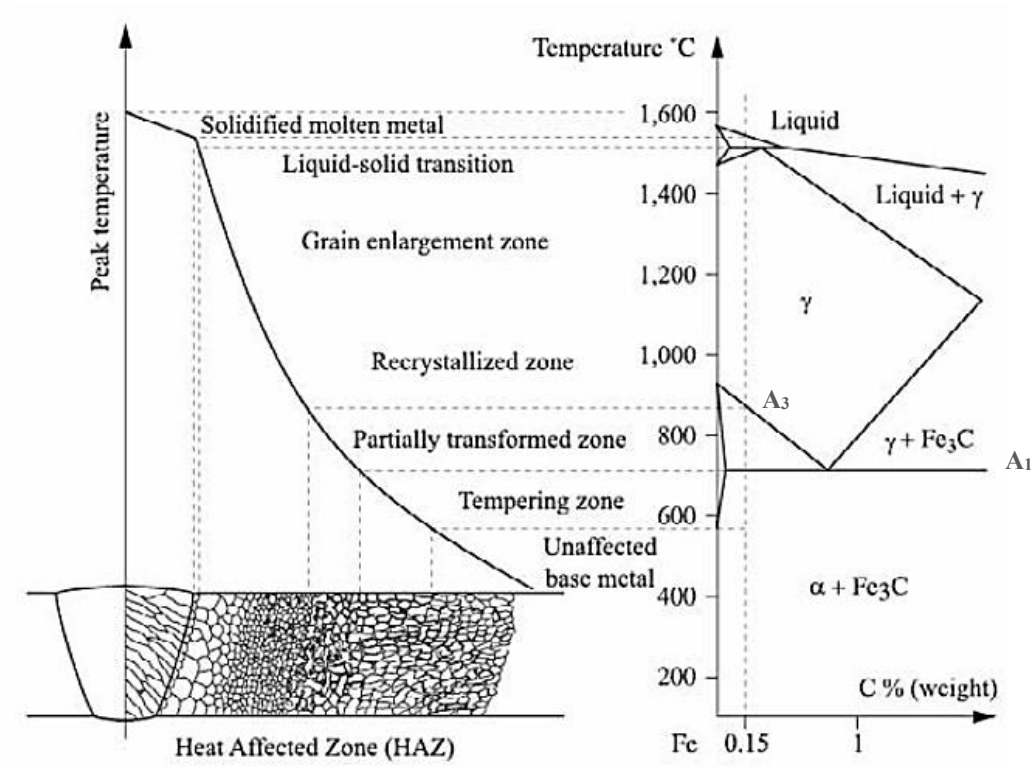

Figure 2.8 Various HAZ sub regions of a weldment corresponding to 0.15 wt.% C on the Fe-Fe_3C equilibrium diagram (Blondeau, 2008)

The final microstructure of the HAZ greatly depends on the peak temperature (T_p) reached at that sub-zone (Blondeau, 2008). The final microstructure also depends on the cooling time between 800°C and 500°C. The cooling time from 800°C to 500°C is constant and may be calculated using Equation 2.3 (Blondeau, 2008). It is denoted by the cooling parameter Δt_{8-5}.

$$\Delta t_{8-5} = \frac{q/v}{2\pi\lambda}\left[\frac{1}{500-T_0} - \frac{1}{800-T_0}\right] \quad \textbf{(2.3)}$$

Where

T_0 – preheat temperature (K)

q – arc energy (J)

v – travel speed of heat source (m/s).

λ – thermal conductivity (J m^{-1} $K^{-1}s^{-1}$ or W/m K),

The heat input per unit length of a weld run is expressed by the term *q/v*, which normally has the units of *kJ/m*. The thermal conductivity of 14MoV6-3 steel at the preheat temperature of 200°C is approximately 46.5 W/m K (Taler & Duda, 2006).

2.10.1 Unaffected Base Metal

The base metal that is heated below the A_1 transformation temperature (~727°C) does not undergo any transformation and retains a ferrite and pearlite microstructure (Blondeau, 2008). However, a possible reduction in creep strength was noted in welded 1% Cr-M-V steels, because of over-tempering (Abe, et al., 2008).

2.10.2 Tempering Zone

No phase transformation takes place in this subcritical zone as well. However, the material can be tempered at temperatures above 600°C. The tempering zone region lies between the unaffected base metal and the partially transformed zone (Blondeau, 2008).

2.10.3 Partially Transformed Zone

The partially transformed zone occurs at peak temperature between A_1 and A_3 transformation temperatures, leading to a partial phase transformation of ferrite (α) into austenite (γ). For the 0.15 wt.% C composition presented in Figure 2.8, the peak temperature is approximately 830°C. The partially transformed zone is also known as the *intercritical heat affected zone* (ICHAZ). The ICHAZ is characterised by small grain size and normally has the lowest hardness values measured across a weld joint and is prone to type IV cracking. The ICHAZ is the furthest HAZ region from the weld fusion line (Brett, 2004; Blondeau, 2008; Abe, et al., 2008;).

2.10.4 Recrystallized Zone

The recrystallized zone is observed at peak temperatures between A_3 transformation temperature and ~1100°C. These relatively low peak temperatures lead to small austenitic grains being produced due to improper transformation of austenite. The recrystallized zone is also known as the *fine-grained heat affected zone* (FGHAZ) and is weakest region of a weldment operating in creep conditions. The FGHAZ is also susceptible to type IV cracking. The FGHAZ and the ICHAZ typically have very similar microstructural features, which makes it difficult to clearly distinguish the two regions (Brett, 2004; Blondeau, 2008; Abe, et al., 2008;).

2.10.5 Grain Enlargement Zone

Austenitic grain enlargement takes place at peak temperatures well above the A_3 transformation temperature and up to about 1495°C. The grain enlargement region is also known as the *coarse-grained heat affected zone* (CGHAZ). The CGHAZ generally has the

highest hardness of the HAZ and typically low toughness values. The CGHAZ is generally susceptible to intergranular cracking known as *reheat cracking* (Brett, 2004; Blondeau, 2008).

2.10.6 Liquid-Solid Transition Zone

The liquid-solid transition zone corresponds to the weld fusion line and connects the base metal to the molten metal. It is partially in liquid state at which the solid ferritic phase (δ) exists together with a liquid phase. It is not easy to observe the liquid-solid transition zone micrographically as it is very small (Blondeau, 2008).

2.11 Welding Repair of Creep-aged Welds

Often when creep damage is detected on steam piping, repair or replacement needs to be planned, depending on estimated creep exhaustion level (Ozaki, et al., 2005). During this task, it is often necessary to weld new material to one that has been in service. This process introduces the likelihood of accelerated damage due to the differences in creep properties of service-exposed material and the new material and typically leads to cracking in the HAZ of the repair-welded joint. Sroka et al. (2017) defined repair-welded joints as welding of a material that has been in service to a material that has also been in service or joints made by welding virgin material to a material that has been in service. Examples of repair-welded joints include operations such as partial replacement of a piping system or local excavation on a certain area of a weldment to remove damage and filling the cavity with new weld metal.

2.11.1 Creep Deformation Behaviour of Low Alloy Cr-Mo-V Steel Welds

Creep is a time-dependant material ageing process whereby the material loses its strength and ductility (Ryner, 2004; Abe, et al., 2008). Creep is a form of gradual plastic deformation of material that happens continuously over time, under constant stress or load below yield stress and at high temperatures (Loots, 2003; Abe, et al., 2008; Maharaj, et al., 2009; Abbaschian, et al., 2009; Middleton, 2017). Creep conditions prevail at the temperature range of about 30 – 60% of absolute melting temperature (T_m) and higher than 0.4 T_m for low alloy steels. The accumulation of creep damage is dependent on the load, material, temperature and component dimensions and configuration (Loots, 2003; Ryner, 2004). Creep damage occurs in three distinct stages, categorised as the primary (transient) creep stage, secondary (steady-state) creep stage and the tertiary (acceleration) creep stages, as seen in Figure 2.9(a) (Dieter, 1961; Maharaj, et al., 2009; Abbaschian, et al., 2009; Dowling, 2012). Most of the

life of components operating in creep conditions is spent in the secondary creep stage, due to the balance of strain hardening and recovery (softening) processes (Abe, et al., 2008; Maharaj, et al., 2009; Sroka, et al., 2017). Varying the applied stress (at constant temperature) or applying different temperatures (at constant stress) produces similar curves with an increase in creep rate as shown in Figure 2.9(b). This can be seen by an increase in total elongation whilst time to rupture and extent of steady state creep decreases (Dieter, 1961; Abe, et al., 2008; Maharaj, et al., 2009).

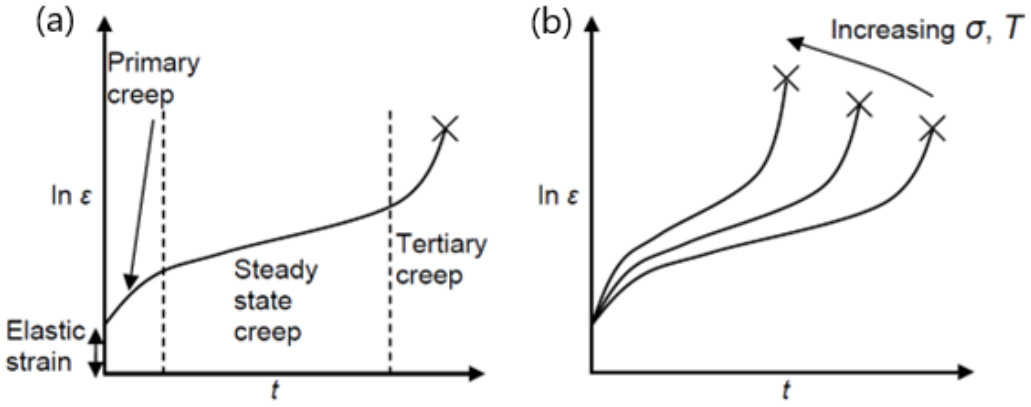

Figure 2.9 Creep strain vs time curves: (a) creep stages; (b) increasing temperature or stress (Maharaj, Dear, & Morris, 2009)

Creep failure could either be by excessive deformation (necking) or creep rupture caused by formation of voids and cracks during the tertiary creep stage (Suman & Pal, 2004; Zielinski Dowling, 2012;, et al., 2012; Hodzic & Hajro, 2012). Several physical mechanisms occur in creep deformation that are classified into two broad categories, named *diffusional flow* and *dislocation creep* (Abe, et al., 2008; Dowling, 2012; Knutsen & George, 2015). *Grain boundary sliding* is sometimes considered a distinct mechanism as well. The possible driving mechanisms for creep in metals are listed in Table 2.6.

Table 2.6 Creep deformation mechanisms in metals

Deformation mechanism	Description of driving mechanism
Diffusion creep	
– Bulk (volume) diffusion (Nabarro-Herring creep)	Creep rate decreases with increasing grain size.
– Grain boundary diffusion (Coble creep)	More sensitive to grain size growth than Nabarro-Herring creep.
Dislocation (power law) creep	Controlled by movement of dislocations and is a function of applied stress.
Grain boundary sliding	Sliding is accommodated by diffusion through the crystal lattice or along the grain boundaries.

Creep deformation mechanisms occur at different stages of creep, with one dominating depending on the conditions. Dislocation glide is the main deformation mechanism at stresses higher than yield stress, while a combination of dislocation creep and diffusion creep can occur at stresses below yield stress (Abe, et al., 2008; Tejedor, 2011). Dislocation creep can be accompanied by elastic deformation at low T/Tm and volume diffusion at high values of T/Tm. At lower stresses, grain boundary and volume diffusion creep dominate. Deformation mechanism maps shown in Figure 2.10 are used to summarise creep behaviour for materials at different temperatures and stress, helping in selecting suitable materials for high-temperature service (Abe, et al., 2008; Maharaj, et al., 2009; Tejedor, 2011).

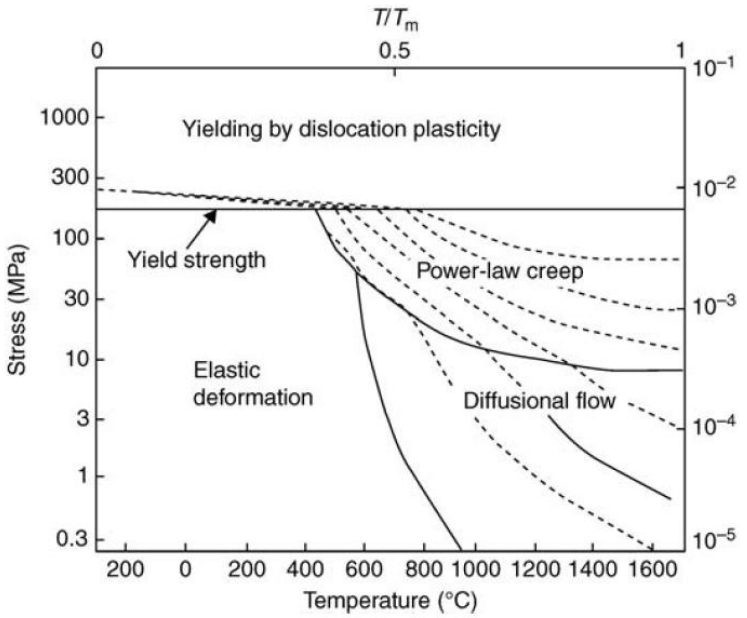

Figure 2.10 Typical deformation mechanism map indicating the temperature range in which each mechanism occurs (Tejedor, 2011)

2.11.2 Weld Joint Degradation

The weldability of a material decreases with creep ageing, but the weld metal is rarely the location of failure. This is more evident in creep resistant welded pipes, where the intercritically transformed zone (HAZ) is the location for maximum creep damage accumulation. The creep rupture strength of weldments diminishes by up to 50% as the testing temperature increases and the applied stress lowered (Ryner, 2004; Mayr, 2007; Maharaj, et al., 2009; Dobrzanski, et al., 2011; Janovec, et al., 2012; Shibli, 2014; Rasiawan, 2017;). Creep-exposed weldments in power generation systems are prone to reheat cracking, also known as type III cracking or stress relief cracking. Reheat cracking is linked to temper embrittlement and the presence of trace elements in steels. It generally occurs on coarse-

grained microstructures, where excessive grain growth occurs due to precipitates dissolved by the weld thermal cycle. Type III cracking is also thought to be related to creep rupture but to a lesser extent than type IV cracking. The effect of alloying elements on reheat crack susceptibility (CS) can be qualitatively measured using Equation 2.4 or it can be determined by mechanical testing. However, a poor correlation has been found between the parameters that quantify reheat cracking susceptibility and the actual reheat cracking of different alloys (Bailey, 1994; Kou, 2003; Loots, 2003; Ryner, 2004; Abe, et al., 2008; Maharaj, et al., 2009; Du Toit, 2012; The Welding Institute, 2014).

$$\boldsymbol{CS = \%Cr + 3.3 \times \%Mo + 8.1 \times \%V - 2} \qquad \textbf{(2.4)}$$

2.11.3 Creep-induced Cracking and Failure Location

The classification of creep-induced cracks that have been observed in heat resistant steels is shown in Figure 2.11 (Maharaj, et al., 2009). The cracks are categorised based on their position and orientation in and around the weldment (Li, et al., 2006; Mayr, 2007; Abe, et al., 2008; Maharaj, et al., 2009; EPRI, 2009; Shibli, 2014). This nomenclature system for the different types of cracking in creep resistant steels was developed by Schuller et al. (1974) and was initially used for girth welds in 14MoV6-3 piping made with 2.5Cr-1Mo filler metal that experienced solidification cracking of the weld metal (type I) (EPRI, 2007). The classification model that was developed by Schuller et al. (1974) was modified to include Type IIIa cracking (Brett, 2004; Abe, et al., 2008).

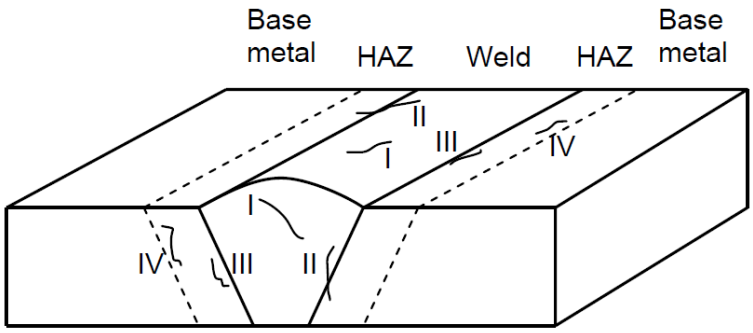

Figure 2.11 Types of creep induced cracking observed in welds and HAZ of heat-resistant steels (Maharaj, et al., 2009)

Type I, II, and III cracks in steel piping systems are caused by inadequate welding procedures and can be addressed through welding maintenance programs. Type I and II cracks grow either longitudinally or transversely, while Type II cracks continue to grow into the HAZ and sometimes into the parent material. Type III cracks initiate in the CGHAZ area next to the

fusion line and may grow into the PM. Type III cracking is enhanced by mechanisms that weaken or embrittle grain boundaries and appears macroscopically as intergranular cracks along prior austenite grain boundary (PAGB) with low rupture ductility. Elimination of type III cracks can be achieved by reducing residual stresses or applying multipass welding, which produces a fine grain microstructure. However, the additional heat input from layering welds onto the previously generated HAZ and weld metal results in a more complex microstructure (Loots, 2003; Brett, 2004; Ryner, 2004; Mayr, 2007; Abe, et al., 2008; The Welding Institute, 2014).

Type IV and IIIa cracks are medium and long-term service crack growth controlled by creep damage accumulation due to high temperatures and loading. Type IIIa cracks form in the FGHAZ region instead of the CGHAZ region of type III cracks. Type IV cracking failure mechanism is driven by creep cavitation, where creep voids form below the surface and grow by diffusion. Once type IV creep damage has been detected, the entire HAZ must be excavated (Smith, et al., 2003; Brett, 2004; Ryner, 2004; Mayr, 2007; Abe, et al., 2008; EPRI, 2009; Shibli, 2014;)

In creep resistant steel piping systems, the HAZ can be stressed in series and parallel, neglecting all other loading and only considering plain steam pressure (P) loading. Type IV cracks have been observed in both circumferential and longitudinal seam welds, with failure by a “leak before break” mechanism in circumferential welds but potentially catastrophic on seam welds under hoop stress. Eliminating the FGHAZ can avoid type IV mechanism creep damage (Mayr, 2007; Abe, et al., 2008).

2.12 Life Assessment of Steam Pipelines

Weldments are a life-limiting feature in steam pipelines, often due to defects. To ensure safe operation, in-service inspection programs are necessary to estimate the amount of life exhausted and determine their useful remaining or residual life. These processes are known as Remaining Life Estimations (RLE) programs. The degree of life exhaustion is defined as the ratio of service time to time to rupture (t_e/t_r). The end of useful component life is typically at the end of the secondary creep stage, approximately at 0.6 t_r. The residual component life (t_{re}) is given by the difference between time in service and time to rupture. The disposable residual life ($t_{re0.6}$) indicates the remaining time for safe continued operation under assumed creep test conditions (Dobrzanski, 2005; Mayr, 2007; Maharaj, et al., 2009; Janovec, et al.,

2012; Sroka, et al., 2014; Shibli, 2014; Sroka, et al., 2017; Dobrzanski, 2020). Figures 2.13 and 2.14 show life exhaustion estimation measurements.

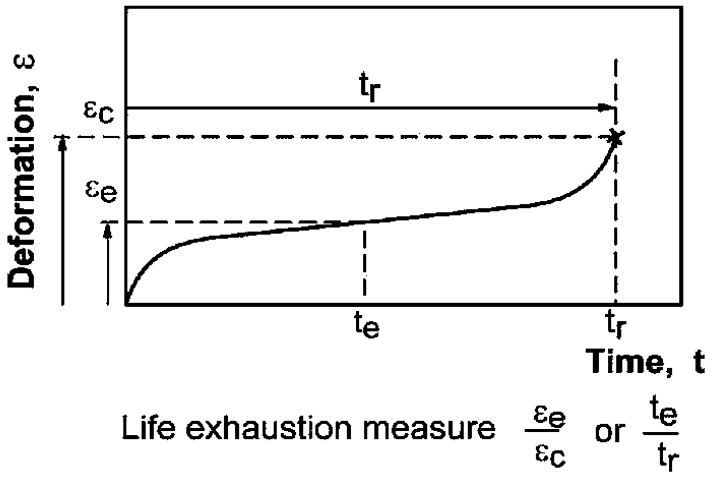

Figure 2.12 Measure of life exhaustion extent of components operating in creep conditions (Dobrzanski, 2005)

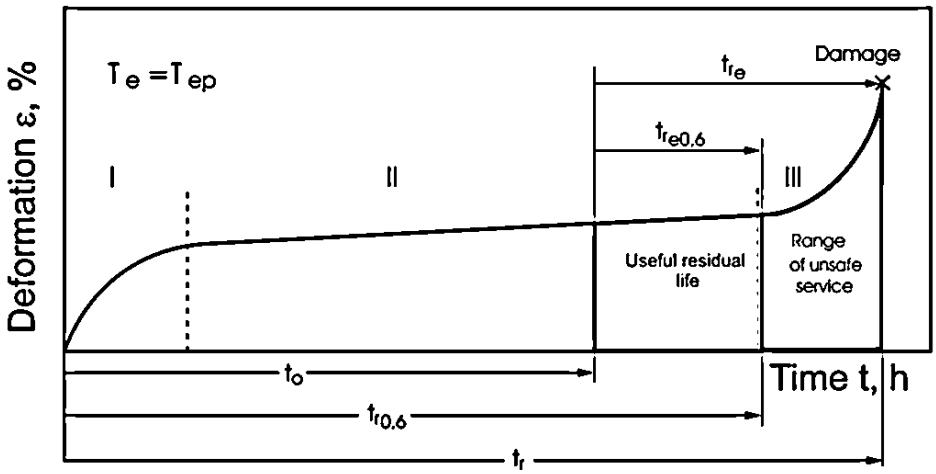

Figure 2.13 Remaining life and useful remaining life relation (Sroka, et al., 2017)

The RLE creep life management strategies are supplemented by welding maintenance to restore equipment to an acceptable condition once it contains defects (Sroka, et al., 2017). However, in components that have been in service for more than 150,000h, estimation of residual life by NDT is not sufficient. For these components, estimation of residual life needs to be determined by destructive tests that are done on representative test specimens made from material that has been taken from service. Remaining life predictions that are made specifically for new material with specified properties are not valid for materials that have

been in long-term service. (Zeman, 2003; Maharaj, et al., 2009; Rantala, et al., 2009; Shibli, 2014;). This is mainly due to lower creep properties of service-exposed samples compared to the creep properties of a newer material.

Investigation of mechanical properties of service-exposed creep resistant welds are usually done using creep and creep rupture tests, hardness measurement of all weldment areas, static tensile tests at ambient temperature and at elevated temperature, and impact tests on standard Charpy V-notched specimens (Kou, 2003; Milicka & Dobe, 2004; Zielinski, et al., 2013; Sroka, et al., 2014; Dorazila, et al., 2015; Craddock Dyson, et al., 2016). Most recently, the use of small sample testing techniques for the evaluation of tensile, fracture and creep characteristics of materials has gained popularity.

2.12.1 Creep Strength of Weld Joints

Determining the creep strength of weld joints, especially repair-welded joints, and providing a numerical value to the time for safe further operation of the welded components is of particular importance (Sroka, et al., 2017; Dobrzanski, 2020). Satisfactory residual life investigations on weldments have been achieved by supplementing metallographic replication with advanced *ultrasonic testing* (UT) inspection or more complex techniques that can detect creep voids and micro-cracks at early stages of creep *e.g. time-of-flight diffraction* (TOFD) (Mayr, 2007; Abe, et al., 2008; Maharaj, et al., 2009; Smit, 2015; Middleton, 2017).

Risk-based inspection strategies, qualitative damage classification schemes and models based on creep void density are used in the life assessments of welds susceptible to type IV cracking (Abe, et al., 2008; Mayr, 2007; Maharaj, et al., 2009; Smit, 2015; Middleton, 2017). A *weld strength factor* (WSF) or *weld strength reduction factor* (WSRF or SRF) must be considered during the remaining life estimates of service-exposed components as the creep rupture strength of weldments and that of parent materials can vary significantly (Abe, et al., 2008). The ECCC defines the WSF as the ratio of weld strength to that of parent material at a given duration and temperature (Auerkari, et al., 2011). The WSRF or SRF is defined as the reduction in strength of weldment relative to that of base metal at given duration and temperature. However, Tu et. al. (1996) suggested that the definition of the WSRF may be insufficient as it does not take multiaxial effect into account and only applies to weldments of relatively lower weld metal strength. The WSF and WSRF/SRF parameters can be assessed using Equations 2.5 and 2.6, respectively.

$$\boldsymbol{WSF(t,T) = \frac{R_{u(w)/t/T}}{R_{u/t/T}}} \quad \textbf{(2.5)}$$

$$\boldsymbol{SRF(t,T) = \frac{R_{u/t/T} - R_{u(w)/t/T}}{R_{u/t/T}}} \quad \textbf{(2.6)}$$

Where

$R_{u(w)/t/T}$ – creep rupture strength of cross-weld samples, at time t and temperature T

$R_{u/t/T}$ – creep rupture strength of base material samples, at time t and temperature T

There are three approaches that are typically used to define the WSRF, depending on the desired levels of accuracy. The three approaches that are used to quantify the WSRF are shown schematically in Figure 2.14 (Tu, et al., 1996). Firstly, the strength of a weld metal specimen can be compared to the strength of a parent material specimen. Alternatively, the strength of a cross-weld specimen can be compared to the strength of a parent material specimen. However, a more precise approach would be to compare the strength of an actual welded structure to that of a parent structure that is not welded. The approach of using cross-weld specimens is commonly used in assessing the WSRF of power plant steel components (Tu, et al., 1996; Auerkari, et al., 2011; Molokwane, 2013).

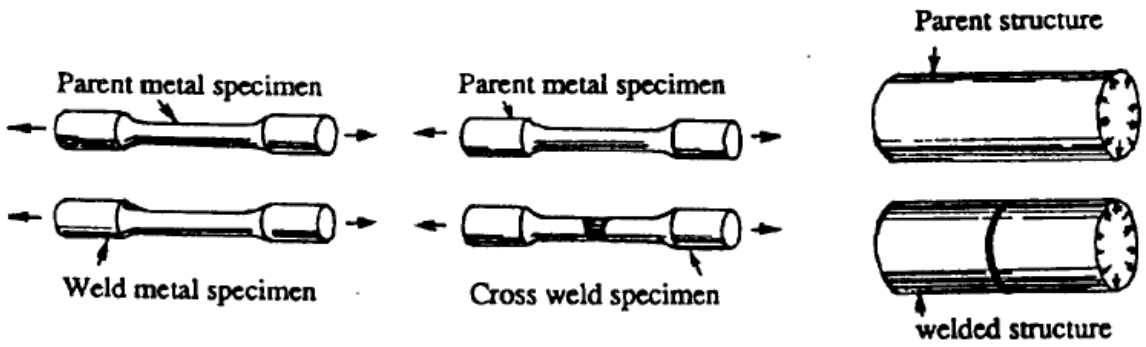

Figure 2.14 Three approaches to define the weldment strength reduction factors (Tu, et al., 1996)

2.12.2 Time-Temperature Parameters

Estimation of long-term creep behaviour has been found to be more successful when done using data obtained from relatively short tests, which were done at temperatures above the service temperature of interest. For instance, by doing several *accelerated creep rupture* (ACR) tests and then using the ACR results as input for *time-temperature parameter* (TTP)

to estimate the time to rupture of a component. TTP methods have been widely used in previous years to estimate the long-term life of power plant components (Abe, et al., 2008). In general, the Larson–Miller or Sherby–Dorn parameters are used in the RLE of power plant steels (Dowling, 2012; Middleton, 2017). However, it is now understood that TTP methods have a tendency of overestimating the long-term strength of materials, since they do not consider the effects of microstructural changes. To address the shortcoming of the TTP methods, some new analysis techniques that consider the creep deformation and creep rupture mechanism have been proposed. The Larson–Miller parameter (P_{LM}) can be calculated using Equation 2.7. The Larson–Miller parameter method assumes a linear relationship between *log* t_r and *1/T*, and that constant C is unchanged in the rupture data set of a material. It is common to take the value for the constant C to be 20, for many power plant steels (EPRI, 2007).

$$\boldsymbol{P_{LM} = (log\ t_r + C)T} \tag{2.7}$$

Where

P_{LM} – Larson–Miller parameter

t_r – time to rupture

C – Larson–Miller constant

T – temperature

The TTP calculations are usually combined with short-term creep test experimental data to construct the so-called master curves. The most commonly used master curves that are used for power plant steels are those developed by the ECCC (Spindler, 2017). The ECCC is an independent group of high temperature plant manufacturers, plant operators and alloy producers formed to coordinate creep data development activities throughout Europe. The ECCC master curves are generally used for sensitivity analysis, since they only rely on the service history and operating parameters of the component (Auerkari, et al., 2001).

2.12.3 Creep Damage Models

In field applications, creep damage is strongly influenced by local stresses and temperatures (Viswanathan, 1989; EPRI, 2007). The rate at which creep damage accumulates varies significantly due to the considerable variation that occurs in stress and temperature. Therefore, damage rules have been developed to calculate the amount of life expended as a function of specific stress and temperature conditions. The *Robinson life-fraction rule* (LFR)

and *strains-fraction rule* (SFR) are two of the most common damage rules. The LFR is based on the summation of time for a given time of service and estimated time of failure, as shown in Equation 2.8. The SFR is based on the summation of strain fractions as shown in Equation 2.9. Power plant components have been successfully analysed using the Robinson rule.

$$\boldsymbol{D = \sum \frac{t_i}{t_{ri}}} \tag{2.8}$$

Where;

t_i – the time spent under condition *i*.

t_{ri} – the time to rupture under condition *i*.

$$\boldsymbol{D = \sum \frac{\varepsilon_i}{\varepsilon_{ri}}} \tag{2.9}$$

Where

ε_i – the strain accumulated under condition *i*.

ε_{ri} – the strain to rupture under condition *i*.

The life assessment process used in South African power generation plants is summarised by Smit (2015) and applies the time fraction approach. The accuracy of LFR has been evaluated considerably and it has been noted that it tends to underestimate the remaining life of ductile materials and overestimate the life of brittle materials. Furthermore, the Robinson rule has a shortcoming in that it does not incorporate the gradual degradation of material with other constitutive properties, which can result in large errors when analysing statically indeterminate structures. The *reference stress* (σ_{ref}) method can be used to address or supplement the shortcomings of the Robinson rule and other damage models (Jelwan, et al., 2011).

2.12.4 Application of the Reference Stress Method

The reference stress method is a creep life prediction method that is widely used for analysis and design of engineering components operating under creep conditions (van Zyl F. , 1997; Jelwan, et al., 2011; Ali, 2014). Researchers have used the reference stress method to estimate the deformation, creep crack growth and remaining life of power plant components (Bezuidenhout, et al., 2010; Molokwane, 2013). The reference stress method assumes that

there exists a time invariant stress, which when it is combined with uniaxial creep rupture data results in the creep life of a component. The reference stress is a function of the effective stress and hydrostatic stress. However, in practice the reference stress is estimated using the effective stress only. The limit load (P_L) and yield stress of the component are normally used to calculate the reference stress as shown in Equation 2.10. The P_L is the plastic collapse load at the yield strength, when the material behaviour is taken to be elastic perfectly plastic (van Zyl F. , 1997).

$$\boldsymbol{\sigma_{ref} = \frac{P\sigma_y}{P_L}} \quad \textbf{(2.10)}$$

Where

P – applied load acting on the component

σ_y – material yield stress

P_L – limit load

In the steady state loading of an internally pressurised cylinder such as the thin wall pipe shown in Figure 2.15, the reference stress can be estimated using Equation 2.11 (Jelwan, et al., 2011). Equation 2.11 assumes that the yield surface and creep deformation are similar in shape, and the collapse mechanism is dominated by the hoop stress (*Tresca yield criterion*). Therefore, an arbitrary value of yield strength may be used to determine the limit load since the ration σ_y/P_L is only dependent on the geometry for a given pattern of loading (Ali, 2014).

$$\boldsymbol{\sigma_{ref} = \frac{P\sigma_y}{P_L} = \frac{P}{ln(R_o/R_i)}} \quad \textbf{(2.11)}$$

Where:

R_o – outer radius

R_i – inner radius

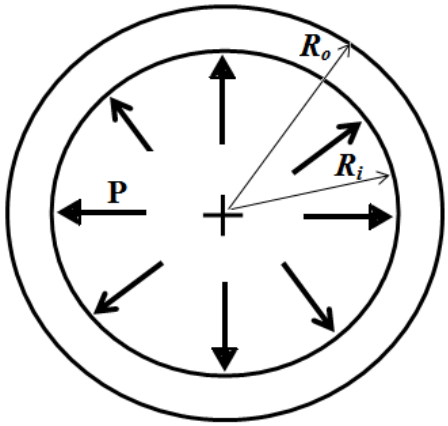

Figure 2.15 Schematic of a cylinder subjected to internal pressure

The reference stress of a welded pipe under hoop stress domination may be obtained using Equation 2.12, which is a modified version of Equation 2.11 (Jelwan, et al., 2011). A stress redistribution factor (κ) is introduced to make provision for the weldment in the pipeline. The stress redistribution factor varies due to creep deformation properties of each weldment area under the constraint of compatibility between the parent material and HAZ or the HAZ and weld metal. For 14MoV6-3 low alloy steel, the stress redistribution factor is taken as 1.0 for the parent material, 1.4 for the HAZ and 0.7 for the weld metal (Jelwan, et al., 2011).

$$\boldsymbol{\sigma_{ref}} = \frac{\boldsymbol{P\sigma_y}}{\boldsymbol{P_L}} = \boldsymbol{\kappa}\frac{\boldsymbol{P}}{\boldsymbol{ln(R_o/R_i)}} \tag{2.12}$$

Jelwan, et. al. (2011) suggested that Equation 2.10 could lead to non-conservative life predictions since it is derived based on the lower bound theorem and underestimates the true reference stress. Therefore, for tubes, they proposed the use of the reference stress formula that is defined by von Mises as shown in Equation 2.13. The constant K depends on the geometry of the tube area that is being thinned in service. It is common to assume a value of unity (1) for the constant K .

$$\boldsymbol{\sigma_{ref}} = \boldsymbol{K}\frac{\sqrt{\boldsymbol{3}}}{\boldsymbol{2}}\frac{\boldsymbol{P_e}}{\boldsymbol{ln}\left(\frac{\boldsymbol{d+H}}{\boldsymbol{d-H}}\right)} \tag{2.13}$$

Where

P_e – operating pressure of the component

d – tube mean diameter at any time (t)

H – tube thickness at any time (t)

K – constant, which is normally taken as unity

Sun (1996) presented a detailed derivation of Equation 2.13 using *L'Hopital's rule* and showed that the reference stress is independent of the radial position. Therefore, the reference stress may be expressed by Equation 2.14. In South Africa, Equation 2.14 is normally used to estimate the stress that matches the operating reference hoop stress of a specific pipe section when conducting constant load creep tests for power plant materials (Bezuidenhout, et al., 1997).

$$\boldsymbol{\sigma_{ref}} = \frac{\sqrt{3}}{2}\frac{\boldsymbol{P}}{\boldsymbol{ln(R_o/R_i)}} \tag{2.14}$$

Deformation in a thick-walled tube can also be related to the deformation of a single conventional creep test performed at a stress equal to the *tube reference stress*, if the reference stress of the tube is obtained (Ali, 2014). The deformation of the uniaxial creep test gives a close approximation to the actual deformation of a tube. Equation 2.15 gives an expression for the tube reference stress based on the tube geometry and the internal pressure.

$$\boldsymbol{\sigma_{ref}} = \frac{\boldsymbol{P_i}}{\boldsymbol{ln(D_o/D_i)}} \tag{2.15}$$

Where

P_i – applied internal pressure

D_o – outer diameter of the tube

D_i – inner diameter of the tube

According to Ali (2014) the strain rates and failure time of a thick-walled tube are close to those obtained from a uniaxial test performed at a stress equal to the mean diameter hoop stress (σ_{mdh}), which is given by Equation 2.16. Steel designers typically use the reference stress for the pressure tubes and pipes to be the same as the mean diameter hoop stress for these components. This is because the reference stress does not vary much from the mean diameter hoop stress for the same D_o/D_i ratio.

$$\boldsymbol{\sigma_{mdh}} = \frac{\boldsymbol{P_i}}{\boldsymbol{2}}\frac{\left(\frac{\boldsymbol{D_o}}{\boldsymbol{D_i}}+\boldsymbol{1}\right)}{\left(\frac{\boldsymbol{D_o}}{\boldsymbol{D_i}}-\boldsymbol{1}\right)} \tag{2.16}$$

The operating stress level can also be estimated using Equation 2.17 (Dobrzanski, 2020). This equation also requires the actual dimensions and operating parameters of the component being assessed, similar to the reference stress concept. It can also be used to determine the minimum wall thickness required for safe further service.

$$\sigma_e = \frac{P_e[D_o - g_{min} \cdot (2-z)]}{2 \cdot g_{min} \cdot z} \quad \textbf{(2.17)}$$

Where

g_{min} – actual minimum wall thickness of the component

z – weakening coefficient, which is approximately unity

σ_e – operating stress

2.13 Creep and Creep Rupture Testing

Creep tests and creep rupture tests are used to characterize the creep deformation and rupture behaviour of materials. Creep tests measure creep strain and time to rupture, while creep rupture tests focus on the gradual deformation of a specimen and the time for rupture. Creep tests are conducted at low stress to avoid tertiary creep stages, with total strain usually limited to less than 0.5%. The strain vs time curve of the material can be used to determine the minimum creep rate for component design or relate creep specimen behaviour with real components (Dieter, 1961; ASTM International, 2003; Dowling, 2012).

The stress rupture test is another method used to determine creep properties of materials, using higher loads than the creep test and always carried out to failure. It results in time to cause failure, elongation, and area reduction at fracture for a given nominal stress at constant temperature. The stress rupture test is usually concluded within 1,000 hours and can be plotted with the creep curve. Both tests are essential for understanding the behaviour of materials under various conditions (Dieter, 1961; Maile, 2003).

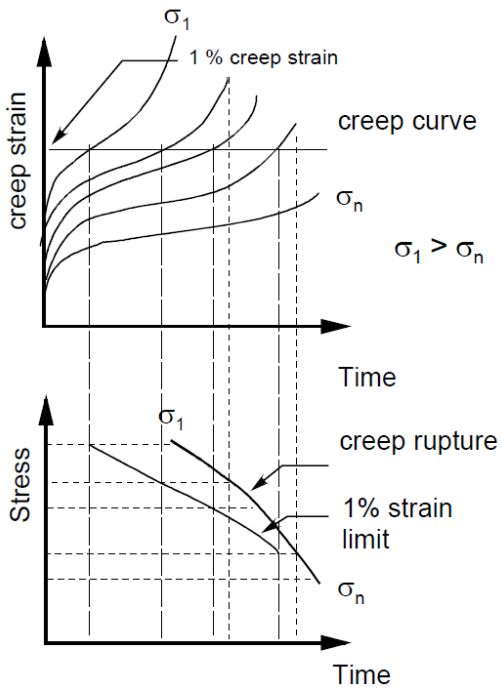

Figure 2.16 Creep test (strain *vs* time) curve in relation to stress rupture test (stress *vs* rupture time) (Maile, 2003)

The Abridged Creep Test is a variation of the creep test that accelerates the creep process by testing at varying temperatures at specific intervals, while maintaining constant stress. This results in a significant reduction in test duration by selecting testing temperatures above the suitable operating temperature and maintaining constant stress. The test results are plotted as a straight line, with the relationship between time to rupture and test temperature as shown in Figure 2.17, can be expressed by Equation 2.18. The remaining life is extrapolated towards a lower temperature, equivalent to the operating temperature (Zeman, 2003; Dobrzanski, et al., 2007; Sroka, et al., 2014; Dziuba-Kałuża, et al., 2014; Sroka, et al., 2017).

$$\boldsymbol{log t_r = f(T_b)} \tag{2.18}$$

Where

t_r – time to rupture

T_b – test temperature

σ_b – test stress (σ_b = constant)

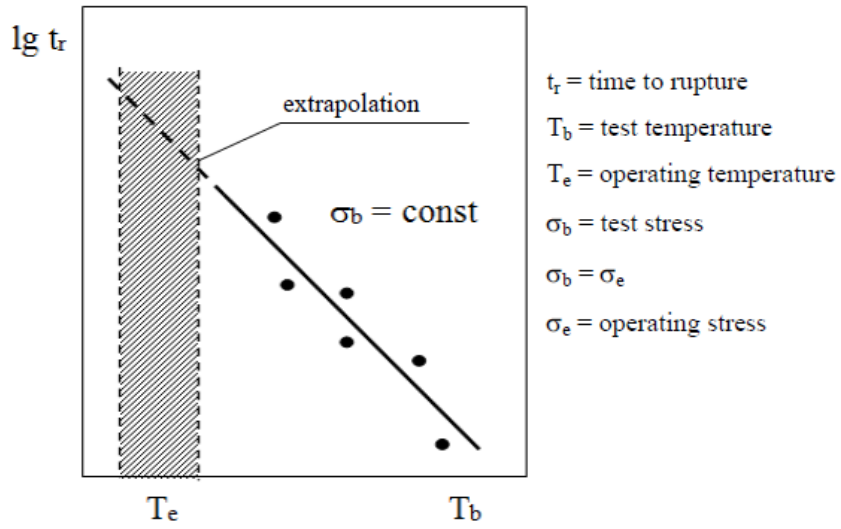

Figure 2.17 Schematic illustration of the abridged creep test method (Zielinski, et al., 2013)

A cylindrical, smooth cross-weld specimen is commonly used for creep testing of weldments for creep characterisation. The two most recognized standards for conducting creep tests are ASTM E139 (2003) and ISO 204 (2009). The results of a single creep test provide information on stress, temperature, steady-state creep rate, and time to rupture (Auerkari, et al., 2005; Dowling, 2012).

The safe time of continued service, or disposable remaining life, can be estimated for all examined weld regions. Different sampling techniques are used to determine creep characteristics of service-exposed welded joints. For sampling weldments from pipes taken out of creep service, cross-weld creep specimens consisting of different zones of a weld are used. These specimens are cut perpendicular to the weld symmetry axis or fusion line as shown in Figure 2.18 (Maile, 2003; Sroka, et al., 2017).

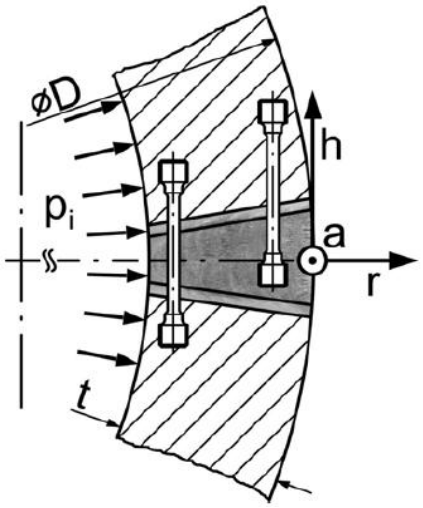

Figure 2.18 Cross-weld creep specimens containing all or some parts of the weldment (Maile, 2003)

In recent developments, small specimen creep testing has received a lot of interest (Craddock Dyson, et al., 2016). This is mainly due to the need to use small samples of simple geometry from in-service or material removed from service to produce creep rupture data. The small specimen creep testing is also useful in remaining life assessment of components operating in creep conditions. Examples of small specimen creep test include the conventional sub-size uniaxial creep test, the impression creep test, the small punch creep test (SPCT), the small ring test and the two bar test (Milicka & Dobe, 2004; Dorazila, et al., 2015; Craddock Dyson, et al., 2016).

2.14 Hardness Testing

Hardness is a measure of a material's resistance to a permanent shape change when a constant compressive force is applied. It is closely related to other mechanical properties of the material, such as strength, ductility, and fatigue resistance. Hardness testing is the most valuable and widely used mechanical test for evaluating the properties of metals and other materials (ASM International, 1999; Broitman, 2017).

Modern hardness testing machines are simple, fast, inexpensive, and relatively non-destructive. Early hardness testing was divided into macrohardness and microhardness, with macrohardness testing referring to testing with applied loads of more than 1 kg, and microhardness testing referring to testing with loads of 1 kg and below. The arrival of microelectronics and nanotechnology has led to the development of novel methods for measuring hardness at nanoscale size (Callister & Rethwisch, 2008). The main indentation hardness testing methods used at macroscale are Brinell, Meyer, Vickers, and Rockwell,

while Knoop and Vickers hardness testing methods are used for microhardness testing. A comprehensive scheme for expressing hardness on one scale to another has not been developed (Callister & Rethwisch, 2008; ASTM International, 2013).

The Vickers hardness test method was developed in the early 1920s as an alternative to the Brinell hardness testing method (Broitman, 2017). In the Vickers hardness testing method, the hardness is calculated from the size of an impression produced under load by a pyramid-shaped diamond indenter and is referred to as the *Vickers diamond hardness number* (VHN) or *diamond pyramid number* (DPN) and denoted by *HV*. Equation 2.19 is used to calculate the HV with the indenter load (L) and the actual surface area of the impression (A_c).

$$\boldsymbol{HV = \frac{L}{A_c} = \frac{2L}{d^2} sin \frac{136°}{2} = 1.8544 \frac{L}{d^2}} \qquad \textbf{(2.19)}$$

The indenter load L is measured in *kgf* and d (mm) is equal to the length of the diagonals measured from corner to corner on the residual impression in the specimen surface as shown in Figure 2.19 (Mathers, 2019).

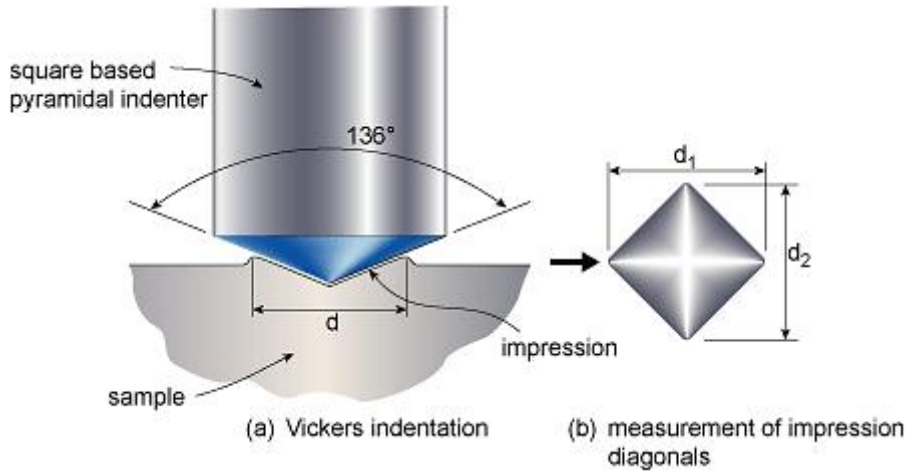

Figure 2.19 Vickers square-based pyramidal-shaped diamond indenter and the impression it makes (Mathers, 2019)

The range and designation of the different test forces (F) that are used for testing metals with the Vickers hardness test method are shown in Table 2.7 test method are shown in Table 2.7 (International Organisation for Standardization, 2018). The denotation of the Vickers hardness test and the test force make up the hardness symbol, which is used as the units of the Vickers hardness test results (Callister & Rethwisch, 2008).

Table 2.7 Range and designation of the test forces used in the Vickers hardness test (International Organisation for Standardization, 2018)

Test force range [N]	Hardness symbol	Designation
$F \geq 49.03$	≥HV 5	Vickers hardness test
$1.961 \leq F < 49.03$	HV 0.2 to <HV 5	Low-force Vickers hardness test
$0.009807 \leq F < 1.961$	HV 0.001 to <HV 0.2	Vickers microhardness test

The hardness of a material is roughly proportional to its tensile strength (Callister & Rethwisch, 2008). This is because both hardness and tensile strength are indicators of the material's resistance to plastic deformation. The empirical relation between hardness and tensile strength for most steels may be estimated using Equation 2.20 for the *ultimate tensile strength* (UTS) and Equation 2.21 for the proof strength, which is commonly taken at 0.2% offset of the *yield strength* (YS) (ASM International, 1999). The exponent n, known as the Meyer index, usually lies between $2 - 2.5$ for fully strain hardened materials and fully annealed materials, respectively (Broitman, 2017). Figure 2.20 shows the graphical representation of the relationship of the UTS and hardness of carbon and alloy steels (Dowling, 2012).

$$\boldsymbol{UTS = \frac{VHN}{3}[1 - (n - 2)]\left\{\frac{12.5(n-2)}{1-(n-2)}\right\}^{(n-2)}} \quad \textbf{(2.20)}$$

$$\boldsymbol{YS_{0.2} = \frac{VHN}{3}(0.1)^{(n-2)}} \quad \textbf{(2.21)}$$

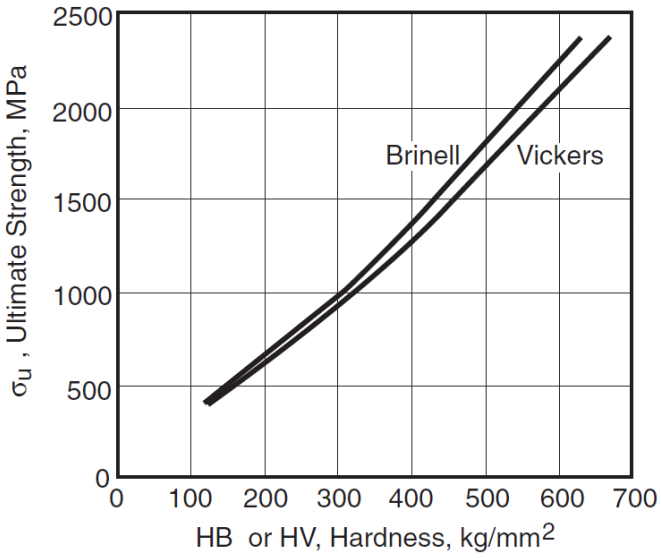

Figure 2.20 Approximation of the relationship between ultimate tensile strength and hardness of hardness of carbon and alloy steels (Dowling, 2012).

2.15 Uniaxial Tensile Testing at Room Temperature and Elevated Temperature

The uniaxial tension test is extensively used to obtain basic design information on the strength of materials and as an acceptance test for the specification of materials (Dieter, 1961). The test consists of slowly pulling a specimen material with an axial force, until it fractures (Dowling, 2012).

The dog-bone shaped test specimens with circular cross-section are normally used for the uniaxial tensile test, but rectangular specimens are also common (Callister & Rethwisch, 2008). A standard circular tensile specimen, with an original cross-section area (A_o) is shown in Figure 2.21 (Hibbeler, 2011). The dog-bone shaped specimen configuration was chosen to provide extra area for gripping and so that during testing, deformation is confined to the narrow centre region of the specimen. Furthermore, the configuration is to avoid having the specimen fracture at the ends, where it is being gripped. The specimen gripping ends vary with specimen geometry, but threaded or shouldered ends are typically used in circular specimens.

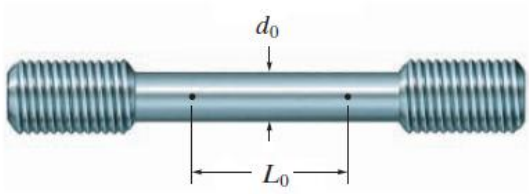

Figure 2.21 Schematic of a standard tensile specimen (Hibbeler, 2011)

The nominal or engineering stress (σ) is obtained by dividing the applied load (P) by the original cross-section area of the specimen. Two small punch marks are normally made along the uniform length of the specimen prior to testing (Davis, 2004; Hibbeler, 2011). The distance between the punch marks represents the *gauge-length* (L_o). Dividing the elongation of the specimens' gauge length (δ) by its original gauge length gives the nominal or engineering strain (ε). Both these parameters, the engineering stress and strain, are used to plot a curve called the stress-strain diagram (Davis, 2004; Hibbeler, 2011).

Most materials undergo *elastic and plastic deformation* when subjected to some loading (Davis, 2004). Elastic deformation is reversible and occurs at low stresses, where the material retains its original shape when the load is removed. Plastic deformation, on the other hand,

occurs at higher stresses and results in permanent deformation of the material. The *offset yield strength* is a convenient parameter that is used to describe the onset plasticity of materials. This yield strength is found by drawing a straight line, typically offset by 0.2%, parallel to the linear section at the beginning of stress-strain curve (Davis, 2004; Dowling, 2012).

During the tensile test, the specimen is mounted by its ends into the holding grips of the testing machine (Davis, 2004; Callister & Rethwisch, 2008). The holding grip ends of the testing machine are normally fitted with bearings to provide a pure tensile force and with no undesirable bending. A tensile testing machine, similar to the one shown in in Figure 2.22 (Hibbeler, 2011), is used to deform a tensile specimen at constant rate. At the same time, the machine continuously and simultaneously measures the instantaneous applied load and the resulting elongation until the specimen fails as seen in Figure 2.23 (Callister & Rethwisch, 2008).

Several mechanical properties of a material can be directly determined from a tensile test including the strength properties (tensile strength and yield strength) and ductility parameters (elongation and percentage reduction in area). Additionally, elastic deformation properties such as the modulus of elasticity and strain hardening features can also be determined (Davis, 2004; Callister & Rethwisch, 2008; Hibbeler, 2011).

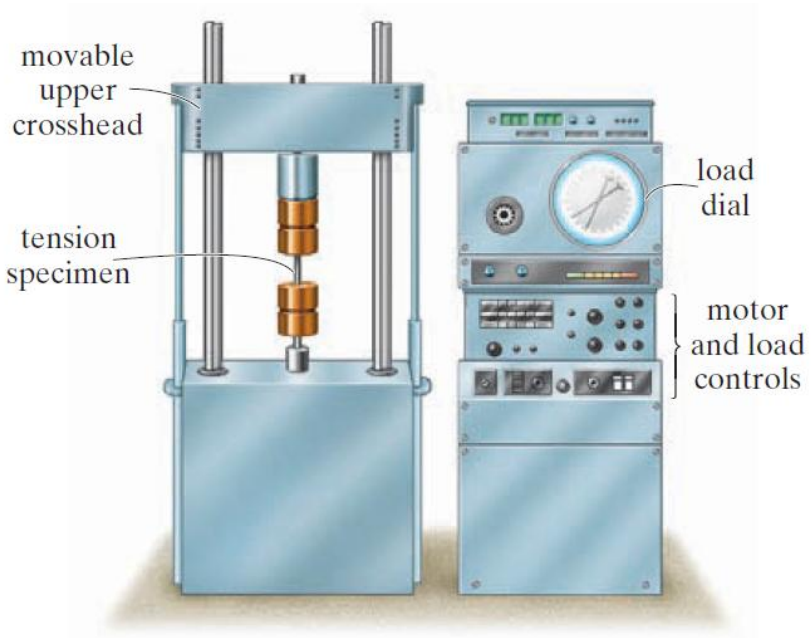

Figure 2.22 Schematic of a uniaxial tensile tension-testing machine (Hibbeler, 2011)

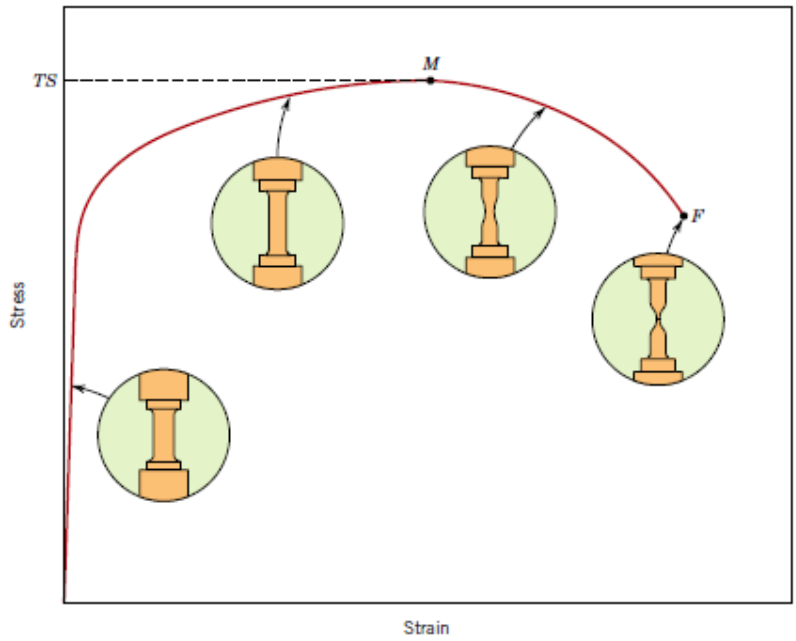

Figure 2.23 Specimen engineering stress–strain behaviour to fracture during tensile test (Callister & Rethwisch, 2008)

2.16 Impact Testing with Charpy V-notch Method

The toughness of a material can be described as an extent to which the material can absorb energy before it fractures (Callister & Rethwisch, 2008). The area under the stress-strain curve can be used to determine the toughness of materials. However, this approach is only suitable for static loading conditions (low rate of deformation) and does not represent the behaviour of material when subjected to a dynamic load (high rate of deformation). The impact test was introduced to estimate the behaviour of materials when they are subjected to *worst-case* conditions. Charpy and Izod tests are two methods that have been adopted as standard to quantify the impact energy of materials. V-notched or keyhole notched, square bar specimens are used in both Charpy and Izod tests. Only the Charpy V-notch test is discussed further in this report.

The Charpy V-notch (CVN) impact test is shown in Figure 2.24 (Callister & Rethwisch, 2008). The specimen is loaded horizontally in the vice and supported at the ends like a simple beam (Avner, 1974). To apply the load, the specimen is struck at the centre behind the V-notch with a heavy pendulum hammer that is released from a standard height. Absorbed energy is the product of the pendulum weight and the difference between the starting height

of the pendulum and the maximum height reached on the other side of the machine after specimen rupture.

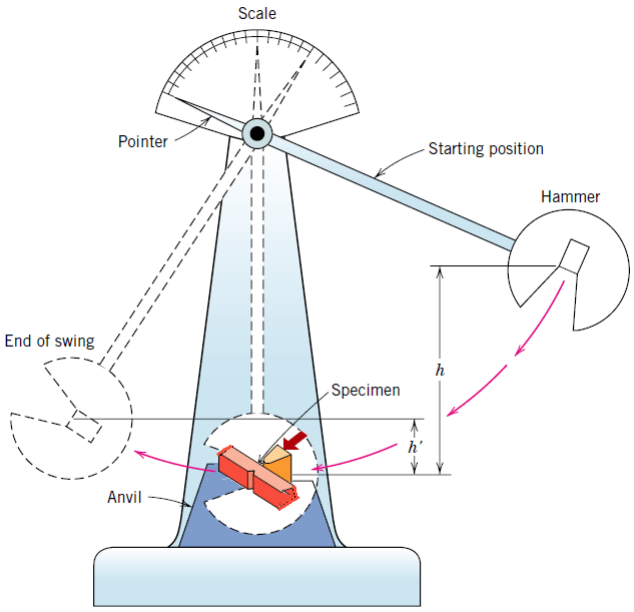

Figure 2.24 Set up for the Charpy V-notch impact test (Callister & Rethwisch, 2008)

Dimensions and notation of the standard 10×10×55 mm Charpy V-notch specimen are shown in Figure 2.25 (Server, 1978). The specimen orientation and notch orientation are designated relative to symmetry direction and the direction in which fracture propagates (Anderson, 2005; ASTM International, 2013). Letters L, R and C are used to denote the longitudinal, radial and circumferential directions, respectively, of specimens obtained from round bars of hollow cylinders. The letters for the specimen-axis designation and notch orientation are put together and separated by a hyphen to give the overall specimen orientation. For example, the L-R orientation corresponds to loading in the longitudinal direction and crack propagation in the radial direction. In specimens obtained from a plate, the longitudinal, transverse, and short transverse directions are denoted by the letters L, T and S, respectively, and in relation to the rolling direction or forging axis (Anderson, 2005; ASTM International, 2013).

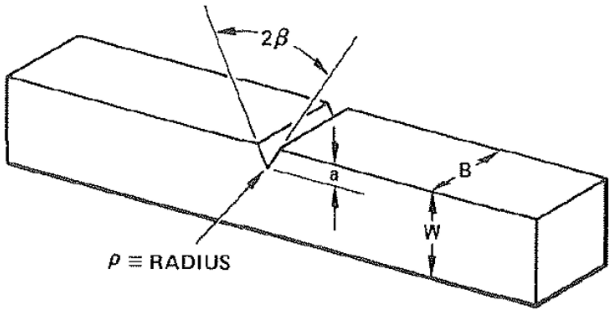

CHARPY V-NOTCH DIMENSIONS

B = 10 mm
W = 10 mm
a = 2 mm
W-a = 8 mm
2β = 45°
ρ = 0.25 mm
TESTING SPAN (S) = 40 mm

Figure 2.25 Dimensions and notation of a standard size Charpy V-notch specimen (Server, 1978)

The ability of a material to absorb energy has been noted to decrease with decreasing temperature. The decrease of absorbed energy with decreasing temperature is mostly the case for low strength steels that have a BCC crystal structure (Callister & Rethwisch, 2008).

To assess this phenomenon, the Charpy impact test is done at different temperatures and the range of temperatures over which the *ductile to brittle transition temperature* (DBTT) of a material occurs is determined. The DBTT has a strong dependency on the microstructure and alloy composition as illustrated in Figure 2.26. In addition, the appearance of the specimen fracture surface can also be used to determine the transition temperature based on the *fracture-appearance-transition temperature* (FATT) method. A fibrous surface is indicative of ductile fracture (shear failure), whereas a granular surface indicates brittle fracture (cleavage fracture).

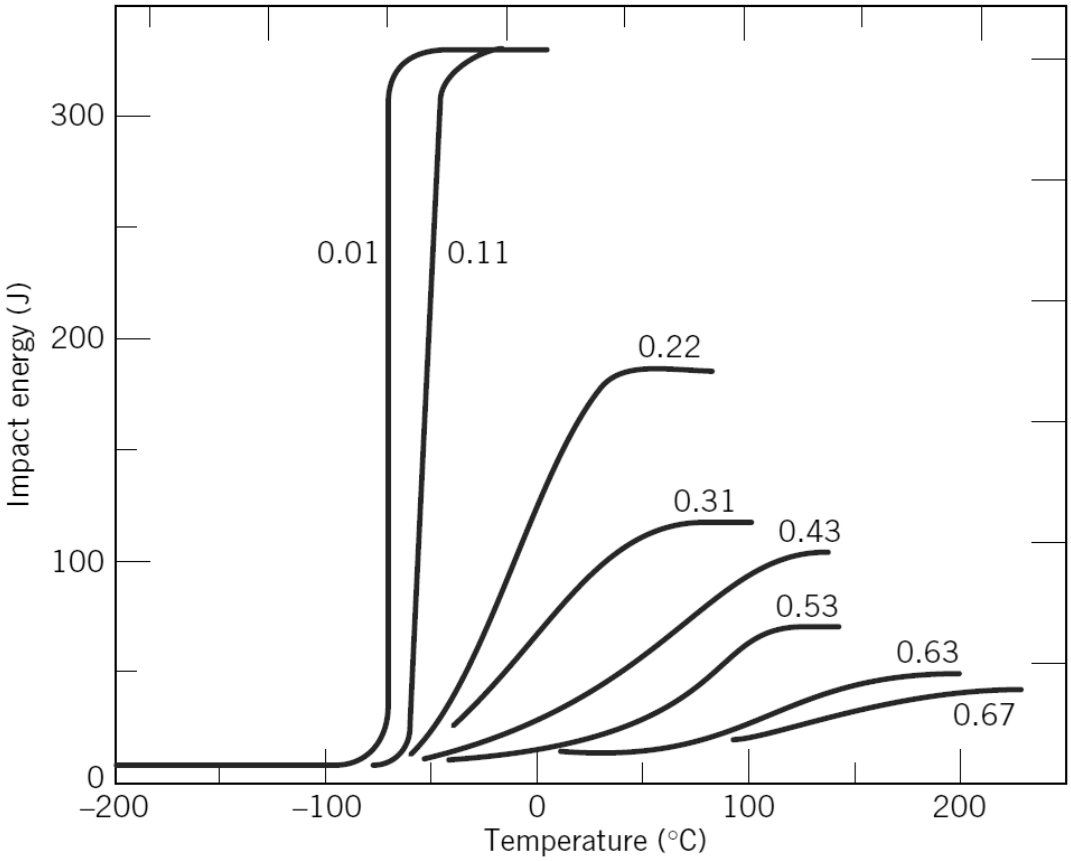

Figure 2.26 Dependency of ductile-brittle transition temperature on carbon content for steel (Callister & Rethwisch, 2008)

Several transition temperatures can be determined from any set of Charpy impact test results by using different criteria. The different criteria that are usually used to define the transition temperature of a material are as shown in Figure 2.27 (Viswanathan, 1989). The transition temperature (T_1) can be determined based on the specified level of impact energy (E_1) *e.g.* the 27 J transition temperature. Alternatively, the transition temperature can be determined based on the specimen fracture appearance, which is indicative of shear fracture percentage (Viswanathan, 1989).

The FATT is the temperature (T_2) at which the fracture surface appears to be 50% brittle and 50% ductile. Generally, T_2 is chosen at the midpoint of the impact energy transition region as it can be measured with relative ease. Lastly, the transition temperature (T_3) can be selected as the temperature at maximum energy for fracture. The temperature at maximum energy for fracture is the highest and most conservative transition temperature. Above the temperature T_3, the specimen has a completely ductile fracture surface. The lower and upmost parts of the S-shape of the transition curve are denoted as the lower-shelf and upper-shelf, respectively. The lower-shelf region is characterised by low temperature and completely brittle fracture, whereas the upper-self is the region above T_3. The energy levels in these regions are also

denoted as the lower-shelf energy and the upper-shelf energy, respectively. The characteristic S-shape of the transition curve can also be divided into three regions that relate to the ease or difficulty of crack initiation and propagation as shown in Figure 2.27.

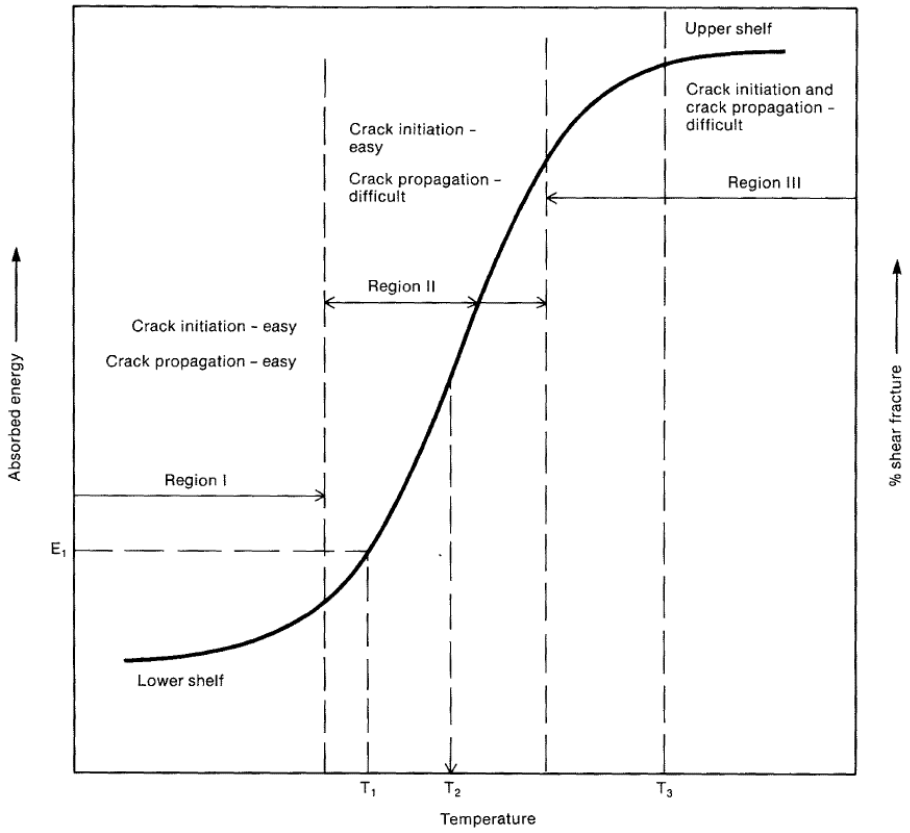

Figure 2.27 Charpy transition temperature curve (Viswanathan, 1989)

Charpy impact testing can also be done on a machine that is equipped with measuring instruments. Instrumented impact testing of metallic materials can be traced back to the late 1980s, where it was used by several industries for quality control in their manufacturing processes (Varma & Loveday, 2002; Bohme, 2002; Server, 2002). The standard (ISO 14556) for the instrumented Charpy impact test was first published in 2000 and currently in its second edition (British Standards Institution, 2015). Nevertheless, Server (2002) details the history and development of techniques that were used for instrumenting the striker of a Charpy machine and measuring the load-time response, dating to 1929. The energy absorbed by the specimen in the instrumented Charpy impact test can be measured from the area under the load-displacement curve. Measuring the load-time response during the impact test allows for the impact energy required for crack formation and propagation to be quantified separately, including the shear lip formation energy as shown in Figure 2.28.

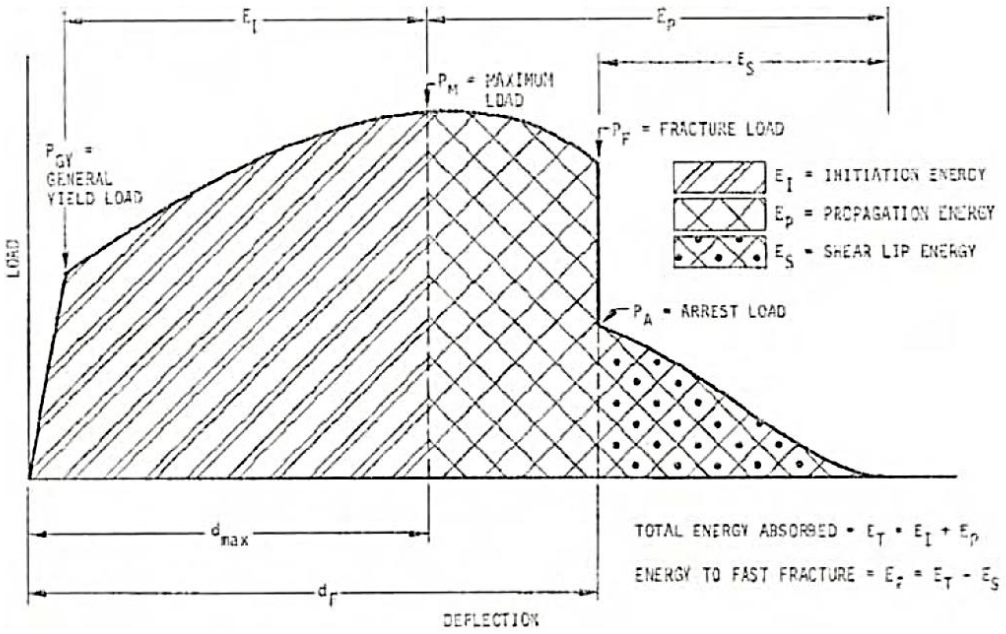

Figure 2.28 Force-displacement curve showing the partitioning of initiation, propagation and shear lip energy (Server, 2002)

Different materials can have the same impact energies and identical areas under their curves. However, the load-displacement curves can be quite different for each material and temperature. Considerable information about the behaviour of specimens in high strain loading rates can be obtained from different segments of the instrumented Charpy test if the force-displacement curves are divided into characteristic parts as illustrated in Figure 2.29.

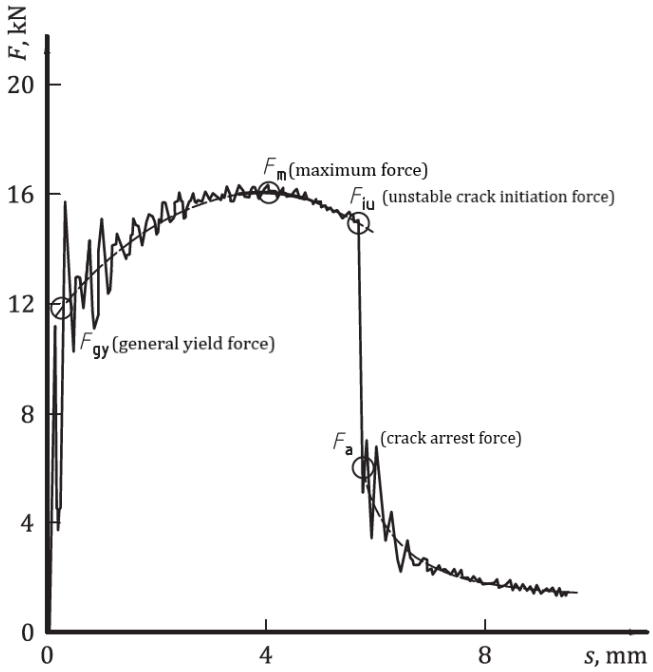

Figure 2.29 Identification of the characteristic forces in the instrumented Charpy impact test (British Standards Institution, 2015)

For instance, the characteristic forces can be used to approximate the value of the proportion of ductile fracture surface, *i.e. percentage of shear fracture* (PSF), which can be determined by using any of the four formulae prescribed by ISO 14556 (Bohme, 2002; Fang & Ding, 2009; British Standards Institution, 2015). Equation 2.22 has been found to give satisfactory results for pressure vessel steels, with a standard deviation of approximately 10% between the measured and calculated values of the PSF. Server (1978) derived Equation 2.23 for estimating the dynamic general yield strength (σ_{gyd}) of Charpy V-notch specimens and it can be used once the general yield force (F_{gy}) is known (Bohme & Schindler, 2000; Fang & Ding, 2009). Likewise, the dynamic fracture toughness (J_d) can be estimated using the modified Rice expression given in Equation 2.24. Rice developed the *J integral* parameter in 1968 to describe nonlinear material behaviour near a crack (Anderson, 2005).

$$\boldsymbol{PSF = \left[1 - \frac{F_{iu} - F_a}{F_m + 0.5(F_m - F_{gy})}\right] \times 100\%} \tag{2.22}$$

$$\boldsymbol{\sigma_{gy,d} \approx 3F_{gy} \frac{S}{4B(W-a)^2}} \tag{2.23}$$

$$\boldsymbol{J_d = \frac{kE}{B(W-a)}} \tag{2.24}$$

Where

k – modification coefficient, k = 1.46 for standard Charpy V-notch specimen with a/W = 0.2

E – impact absorbed energy at any point of interest

The Charpy V-notch impact test is also widely used to assess the toughness and impact properties of weldments, especially during the qualification of WPS (Easterling, 1992). It is recommended that the notch be cut at 1 mm to 2 mm from the fusion line to test HAZ impact properties and at the centreline to test the weld metal (British Standards Institution, 2012). The absorbed energy of the tested area is assessed against the impact properties of the parent material.

2.17 Small Punch Testing

The need for characterising the actual mechanical properties of welded components by direct testing methods has led to development of novel techniques based on miniaturised specimens (Milicka & Dobe, 2004; Dorazila, et al., 2015; Craddock Dyson, et al., 2016). Small punch testing is a mechanical testing method currently used to obtain tensile, fracture and creep data from very small volumes of experimental material, extracted from the surface of actual components which are still in service. The effect of long-term creep exposure on the empirical correlations for determination of yield strength, tensile strength and FATT of 14MoV6-3 has been investigated previously in comparison to the results of standardised tensile, impact and small punch tests.

The small punch testing technique allows for economical evaluation of the ductility of steel and welded joints that have been in service well over 100,000h (Zeman, 2003). Furthermore, it makes it possible to determine a practical safe operational time limit since the level of safety for continued service and maintenance planning is done based on the gathered information.

2.18 Surface Replication

Surface replication is a well-developed metallography method that is used to take in situ microstructure measurements of power generating plants components (Marder, 1989). The surface replica technique relies on copying the surface topography of the component being examined. Surface replication is extensively used in power generating plants for assessing creep damage of components operating in high temperature conditions (Morige, 2015). It can be carried out in the plant without the need to remove the component from service and is considered as a *non-destructive examination* (NDE) technique. Furthermore, the need for cutting large samples from a component for testing in the laboratory is also eliminated. This is particularly useful when frequent testing of the component is required over its lifetime. Hardness of the material, the type and composition of the alloy and surface conditions are key material parameters that must be known for successful application of the surface replication technique. Some of the equipment that are required to perform surface replication are outlined in Table 2.8 (Morige, 2015).

Table 2.8 Equipment required to performing surface replication (Morige, 2015)

Grinding and polishing	Etching	Replication
• Portable motorised handheld grinder/polisher • Rubber disc holder • Adhesive backed abrasive discs (80, 120, 320, 500, 800 & 1200 grit) • Discs of polishing cloths • Polishing compound (Diamond paste of 9, 6, 3 & 1μm) • Cleaning solvent (Methanol) • Cotton wool for swabbing and cleaning	• Etchants • Cotton wool for swabbing • Rubber gloves	• Sheets of cellulose acetate film • Acetone • Standard glass slides • Adhesive tape

The surface replication technique involves grinding coarse grit papers, polishing with finer compounds, cleaning and flushing with methanol and a cotton wool swab, and applying a chemical etchant to reveal the microstructure. Nital, a mixture of nitric acid and alcohol, is commonly used for iron, carbon, and alloy steels. The concentration of nitric acid varies from 1-10%, with 3-5% solution most common for low alloy steel. A double or triple etch-polish-etch procedure is generally followed to reveal microstructural features like creep voids. To take a surface replica, an acetate filmstrip is dipped in acetone for two seconds, placed on the polished and etched surface, dried, and secured to a glass microscope slide as shown in Figure 2.30. The surface replica can be evaluated directly under an optical microscope or in an electron microscope after some preparation (Marder, 1989; ASM International, 2004; Ngoasheng, 2017).

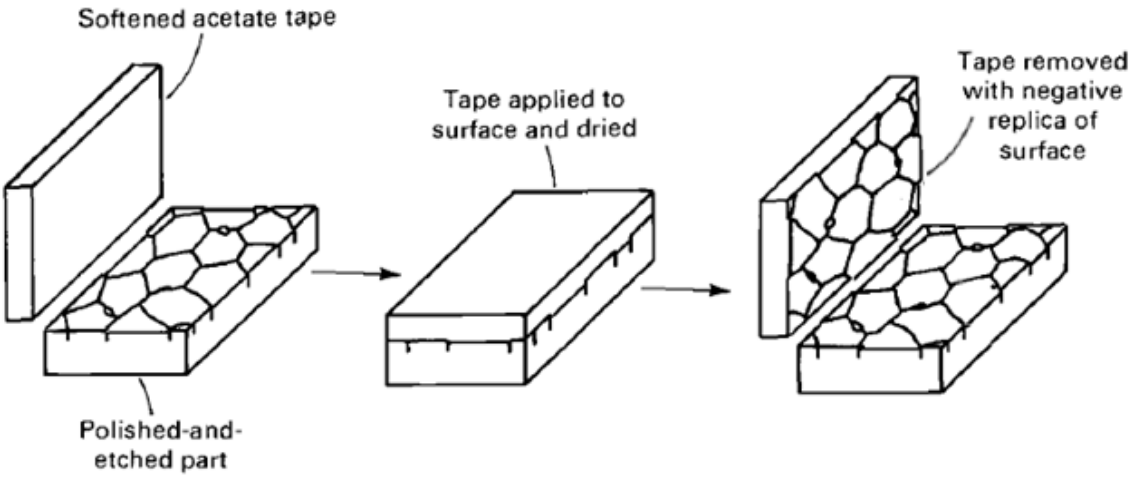

Figure 2.30 Schematic of the surface replica technique (Marder, 1989)

The evaluation of replica slides involves two steps. Firstly, the replica slide is assessed for quality to avoid incorrect or inaccurate assessments of creep damage level in the component. Then, creep voids are counted to quantify the creep void density of the material being assessed. A 1 mm stage micrometre is typically used to calibrate the microscope area and determine the ocular calibration factor prior to evaluating replica slides (Ngoasheng, 2016). The evaluation of replicas is generally done at 500× or 400× magnification on the optical microscope. Surface replication can also be used to assess creep damage in power plant steels based on the evolution of carbides. In steels with bainitic and pearlitic microstructure, the level of creep damage can be correlated to the degree of spheroidization of carbides (Furtado & Le May, 2004). This is because the degree of spheroidization of carbides provides a good indication of the extent of thermal exposure the material has undergone.

2.19 Remaining Life Estimation

The surface replication method is a valuable tool in the estimation of remaining life of creep-damaged components as it can be combined with analytical methods to classify the damage and estimate remaining life of creep exposed components (Viswanathan, 1989).

The method developed by Neubauer and Wadel in the 1980s is used extensively in the classification of creep damage in steam piping as shown in Figure 2.31 (Viswanathan, 1989; Marder, 1989; Furtado & Le May, 2004; Hodzic & Hajro, 2007; Dobrzanski, et al., 2011). The Neubauer and Wadel model can also be used to estimate the time for continued safe operation and component replacement time and condition.

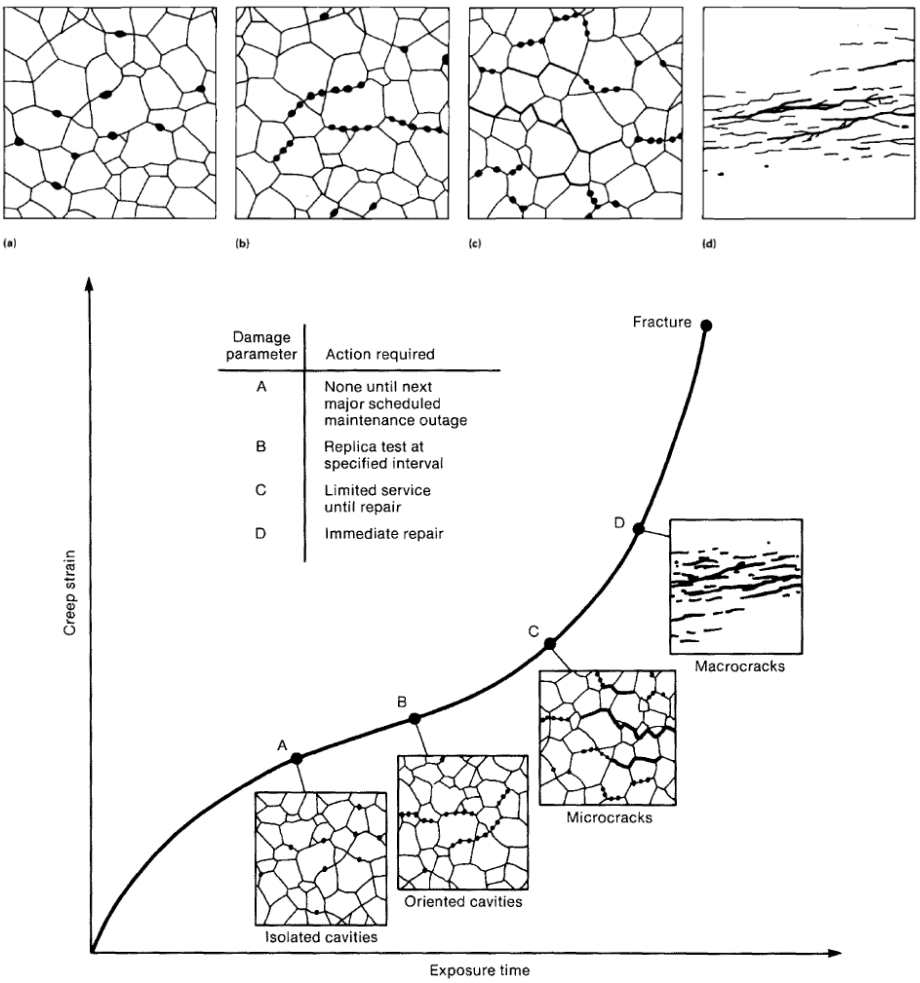

Figure 2.31 Formation of creep cracks. Small voids (a), coalesce over time (b), form intergranular cracks (c) and ultimately macrocracks (d) (Marder, 1989; Viswanathan, 1989; Dobrzanski, et al., 2011)

Creep damage models are widely used as the basis of RLE in South African power generating plants (Bezuidenhout, et al., 2010). The RLE considers the active failure mechanisms with contribution of material properties, stress, temperature and environment as the common damage drivers. Surface replication is complemented with hardness testing and chemical analysis to explain anomalies and probable causes of damage.

The damage models rely on data recorded during the evaluation of metallographic replicas under the optical microscope, where micro void damage is quantified at 500× (or 400×) magnification since creep voids with diameters <0.1 μm begin forming at around 10% creep life of a material (van Zyl, 1997). Some creep voids grow to approximately 1 μm and become visible under 400× magnification, typically in low alloy and 12CrMoV steels where the strain rate is below 10^{-6} h^{-1} and the consumed *life fraction* (LF) of 0.2 to 0.5 (van Zyl, et al., 2005).

Creep damage is expressed in terms of void density and has the units of voids per square millimetre. Metallographic void damage is classed in intervals of 50 up to 200 voids.mm^{-2} and thereafter in steps of 100 up to 1,000 voids.mm^{-2}. The damage model used in South African power plants is shown in Equation 2.25 (van Zyl, 1997).

The remaining life or residual life can be calculated from Equation 2.26 and it corresponds to the time to crack initiation for the component, not failure. A conservative value of 1,000 voids.mm^{-2} for the number of voids at fracture (N_f) has been suggested by van Zyl (1997). This value could evolve to a few thousand voids per square millimetre (in practice) before micro crack formation and crack development occur in a component.

$$\boldsymbol{LF = {t}/{t_r} = \left[1 - \left(1 - \frac{N}{N_f}\right)^{\gamma}\right]} \quad \textbf{(2.25)}$$

$$\boldsymbol{t_{rem} = \frac{t \times (1 - LF)}{LF} = t_r(1 - LF)} \quad \textbf{(2.26)}$$

Where

t – exposure time (time in service) (hr)

t_r – rupture time (hr)

t_{rem} – remaining time to rupture (remaining life) (hr)

N – number of voids (voids.mm^{-2})

N_f – number of voids at fracture (voids.mm^{-2})

γ – material creep ductility parameter

Inspection intervals and appropriate interventions are recommended based on the RLE classification based on the calculated remaining life as shown in Table 2.9 (Smit, 2015).

Table 2.9 Remaining life estimate classification (Smit, 2015)

RLE CLASS	DEFAULT RECOMMENDATIONS
CLASS 1 Component at the end of its useful life Not manageable inside outage philosophy High risk of failure with continued operation	**1. Replace immediately. Do not operate further.** Note: Risk assessment for further operation for limited time under special mitigation measures.
CLASS 2 Component approach end of its useful life Still manageable inside outage philosophy Plan replacement and operate within design	**1. Replace within 3 years** (with 18 months inspection for borderline components) 2. Investigate all excursions and dynamic events
CLASS 3 Damaged component with significant remaining life Safely manageable by inspections	**1. Inspect within 3 years** 2. Operate within design & maintain within Eskom Philosophy
CLASS 4 Component with onset or no damage Manageable within outage intervals	**1. Inspect within 6 years** 2. In exceptional cases inspection interval could be extended

If remaining years calculated is <3 years then class 1
If remaining years calculated is 3–9 years then class 2
If remaining years calculated is 12–18 years then class 3
else class 4 with onset of damage

ECCC master curve equations are also used in the RLE of power plant components operating in the creep regime. Equation 2.27 is the master curve formula for ½Cr-½Mo-¼V steel (12MoCrV6-2-2) that is used to estimate the specimen rupture time in a uniaxial creep test (Spindler, 2017).

$$\boldsymbol{P(\sigma) = \ln(t_r^*) - a - eT - \frac{f}{T} = blog\sigma_0 + c\sigma_0 + d\sigma_0^2} \qquad \textbf{(2.27)}$$

Where:

$P(\sigma)$ – creep rupture parameter,

t_r^* – predicted rupture time (h),

T – absolute temperature (K)

σ_0 – stress (N/mm^2), and

a, b, c, d, e and f – constants (see Table 2.10).

The master curve equation was produced from stress rupture data of over seven million testing hours, 500 data points, and 46 heats of ½Cr-½Mo-¼V steel. Table 2.10 shows the values of the constants that are required for the ½Cr-½Mo-¼V steel master curve equation.

Table 2.10 Constants a, b, c, d, e and f values for ½Cr-½Mo-¼V steel master curve equation

a	−39.7658730
b	−8.43513298
c	−0.00186616660
d	-2.91037377×10^{-5}
e	0.00935613085
f	49662.4102

Dobrzanski et. al. (2011) designed RLE models for microstructural changes that occur in low and high chromium steels during long-term operation in creep conditions and also came up with a method of classifying and assessing the conditions of these materials.

The actual microstructure degradation class is assigned based on the partial examinations of the changes in the pearlite/bainite/martensite areas, advancing precipitation processes, internal defects and the degree of material degradation as shown in Figure 2.32. The microstructural degradation, internal defects and the results of the creep test are correlated to determine the residual life of the component being assessed.

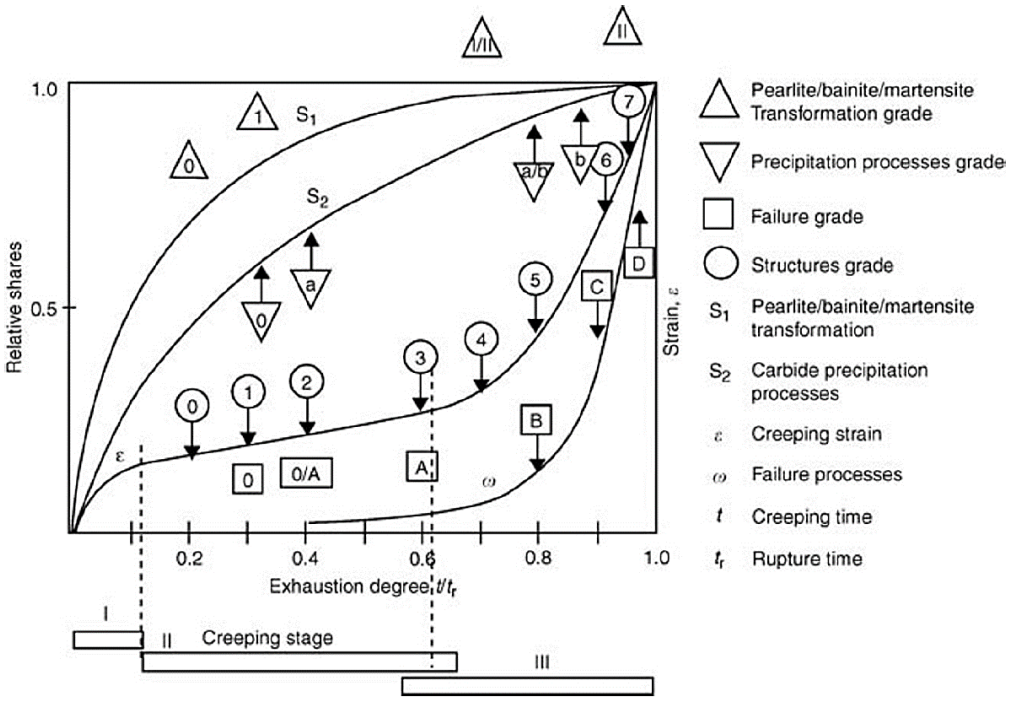

Figure 2.32 Model for classification of material condition based on microstructural changes and internal damage that occur during long-term operation under creep conditions (Dobrzanski, et al., 2011).

Dobrzanski et. al. (2011) have also developed diagrams to represent the changes in microstructure of ½Cr-½Mo-¼V steel during long-term service in the creep regime where the degree of exhaustion is based on the strain resulting from creep.

Figure 2.33 shows the diagrams for assessing ½Cr-½Mo-¼V materials after service in creep conditions without internal defects.

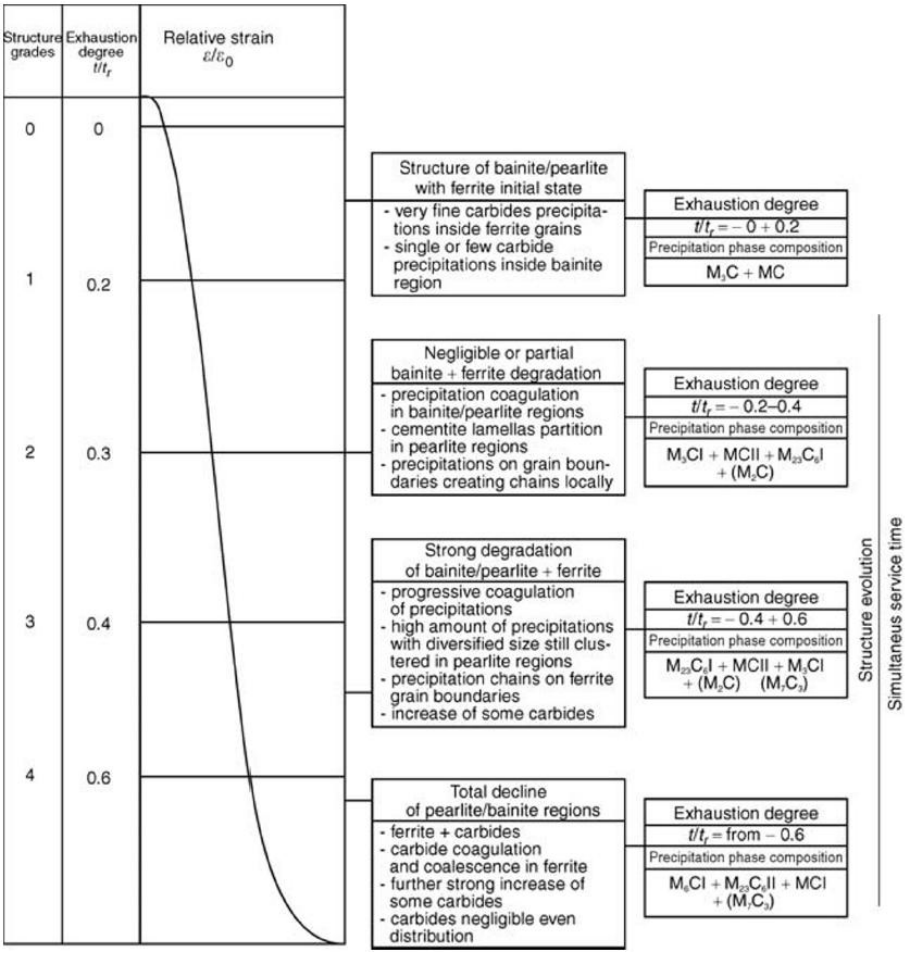

Figure 2.33 Classification of microstructure changes in ½Cr-½Mo-¼V steel during long -term services without internal damage (Dobrzanski, et al., 2011)

Figure 2.34 shows the diagrams for assessing ½Cr-½Mo-¼V materials having internal defects and correlates with Neubauer and Wadel method.

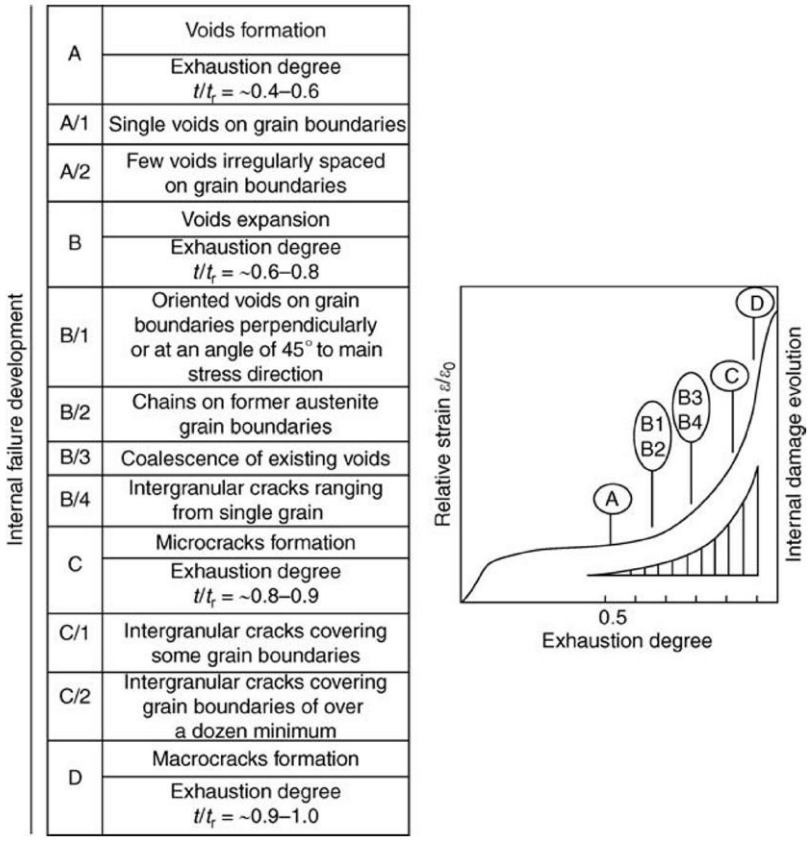

Figure 2.34 Classification of creep damage in ½Cr-½Mo-¼V steel based on the degree of exhaustion (Dobrzanski, et al., 2011)

Dobrzanski et. al. (2011) also present micrographs that show chronological stages of changes that occur in the microstructure and development of internal defects in ½Cr-½Mo-¼V steel after prolonged operation in creep conditions.

2.20 Chapter Summary

High temperature, creep-resistant materials remain a crucial part of coal-fired power plants in South Africa. The low alloy steel 14MoV6-3 is among the widely used steels in steam pipes and other components of the boiler. These components are required to withstand long periods of operation at elevated temperature and pressure (creep regime). It has become critical to understand the structural integrity, failure mechanisms and remaining life of the currently installed components for continued safe operation since many coal-fired power plants in South Africa and around the world are now being operated beyond their original design life. Nevertheless, 14MoV6-3 remains a viable material for continued service and life extension of coal-fired power plants. However, the degradation of the material needs to be closely monitored and managed, especially that of welded components since weldments have been identified to be the weakest link of creep exposed components. Remaining life

estimations require an integrated approach that combines metallurgical evaluation, mechanical testing and operational data to be effective. Continued safe operation of creep exposed material can be achieved if it is supported by holistic inspection and testing programmes that incorporates real time conditions of materials in service into remaining life estimation models.

Although 14MoV6-3 still features prominently in South African coal-fired powered plants, understanding of its behaviour in service and further characterisation has been significantly affected by the prioritisation of more advanced materials, notably 9-12% Cr steels that are currently being used to replace older materials (Molokwane, 2013; Mphaphathi, 2016; Marx, 2016). Hence, some research gaps can be noted in the literature. For instance, there is limited consensus on the presence and role of carbides such as M_7C_3 in degraded 14MoV6-3, existing models and RLE methods lack integration of real-time operational data and multiaxial stress effects. There is limited interest in exploring alternative methods e.g., small sample testing and abridged creep testing, which could offer viable alternatives for monitoring of creep-aged components while they are still in service.

Additionally, even though weldments have been identified as life-limiting features in creep exposed components, there is minimal effort to quantify material strength reduction factors that can be reliable applied to account for the welding thermal cycle and prior creep damage of material in service when doing repairs or partial replacements.

The next chapter give details of the research methodology. It will include the details of all the experiments and tests that were done, and the tools and equipment that were used.

Chapter 3: Experimental Procedure

This chapter outlines the sampling strategy and preparation of samples from sections of steam pipes that are used in the boiler of coal-fired power plants. The chapter gives details of the material chemical analysis, surface replication, metallography, mechanical testing, thermodynamic phase modelling, Gleeble physical simulation and testing. Furthermore, the suite of techniques that were used for material characterization are also described.

3.1 Materials

Normalised and tempered virgin and service-exposed 14MoV6-3 steel samples extracted from the steam pipeline system of a coal-fired power plant were used in this research. The service-exposed pipe shown in Figure 3.1 was removed from the hot reheat system of the boiler plant after a service life of more than 200,000 hours.

Figure 3.1 Service-exposed 14MoV63 pipe

The creep damage of the service-exposed pipe was classified through microstructural and surface replica techniques. The creep damage history of the service-exposed pipe is summarised in Table 3.1.

Table 3.1 Creep damage history of service-exposed material

Area Identification	Remaining Life Estimation
Butt weld, RB01-106 (2013)	Class 4 – Component with onset or no damage manageable within outage intervals
Butt weld, RB01-107 (2016)	Class 2 – Component approach end of its useful life, still manageable inside outage philosophy.
Parent material (in-between)	Class 4 – Component with onset or no damage manageable within outage intervals

Table 3.2 shows the dimensions, operating conditions, and design information of the service-exposed pipe (Eskom, 1985). A pipe with similar specifications was procured, designed to operate for 200,000 hours, and conforming to EN 13480, while also meeting BS EN 10216-2 material specifications and mechanical properties (British Standards Institution, 2007; van Zyl E. , 2013; British Standards Institution, 2017). The virgin material has an ID of 540 mm and a wall thickness of 25 mm

Table 3.2 Steam piping data (Eskom, 1985)

Pipe Sizes	Material	Temperatures (°C)		Pressures (MPa)		Design	Operating hours	
		Design	Operating	Design	Operating	Code	Design	Actual
540mm ID × 18mm WT	DIN 14MoV6-3 (BS 3604 HFS 660)	540	540	4.3	3.75	BS 806	100 000	277 452

3.1.1 Preparation of Bulk Sample

Two sections of approximately Ø540×200 mm were extracted from the service-exposed pipework using a horizontal band saw, and a coolant was applied during the cutting process to minimise thermal effects. The samples for mechanical tests were cut from the bulk pipework into round and square bars.

3.1.2 Chemical Analysis

Chemical analysis of the composition of both the service-exposed and new materials was performed on the weld metal and PM on either side of the weld metal. Analyses were performed at an accredited laboratory, Scrooby's Laboratory Service Close Cooperation. The chemical analysis results were compared with the requirements specified in BS EN 10216-2 (British Standards Institution, 2007). The composition of the virgin material was also checked

against the material specifications of the original equipment manufacturer (OEM) (Wyman-Gordon Forgings, 2011). The chemical composition was within the range of the 14MoV6-3 steel specification, as shown in Table 3.3. However, the weld metal contents of Mn, Mo, and V were slightly higher than the one prescribed by BS EN 10216-2. Exceeding the limits of vanadium content increases the risk of reheat cracking (Bailey, 1994). The chemical analysis data were also used with Thermo-Calc software for thermodynamic calculations of equilibrium phases.

The chemical analysis also shows that the filler metal closely matched the 14MoV6-3 steel. The welding process used to join the pipe during fabrication is unknown. However, power stations currently use the GTAW process for welding the root and SMAW for welding the hot and intermediate weld passes. The 2.25Cr1Mo filler metal is normally used, and the welding is typically followed by PWHT, with preheat done prior to welding (Dlamini, 2013)

Table 3.3 Chemical analysis results (in weight %) for the 14MoV6-3 samples used for research

Element	**Material No: 1.7715**	**Samples**			
	BS EN 10216-2	Virgin Parent Material	Ex-service Weld Metal	XSPM_14MoV63 (upstream of weld)	XSPM_14MoV63 (downstream of weld)
C	0.10 - 0.15	0.15	0.14	0.11	0.10
Mn	0.40 - 0.70	0.50	0.91	0.47	0.43
S	0.020 (max)	≤ 0.005	0.008	0.014	0.017
P	0.025 (max)	0.009	0.014	0.016	0.010
Si	0.15 - 0.35	0.22	0.32	0.21	0.20
Cr	0.30 - 0.60	0.54	0.44	0.41	0.35
Mo	0.50 - 0.70	0.58	0.87	0.55	0.53
Ni	≤0.30	0.21	0.10	0.20	0.05
Cu	≤0.30	0.14	0.09	0.09	0.10
Al	≤0.040 (tot)	0.028	0.009	0.024	0.037
V	0.22 - 0.28	0.24	0.52	0.29	0.28
Nb	-	≤ 0.005	≤ 0.005	≤ 0.005	≤ 0.005

Element	Material No: 1.7715	Samples			
	BS EN 10216-2	Virgin Parent Material	Ex-service Weld Metal	XSPM_14MoV63 (upstream of weld)	XSPM_14MoV63 (downstream of weld)
B	-	≤ 0.0005	0.0005	≤ 0.0005	≤ 0.0005
Ti	-	≤ 0.005	0.017	≤ 0.005	≤ 0.005
Co	-	0.009	0.020	0.009	0.011
Fe	Matrix	Matrix	Matrix	Matrix	Matrix

3.2 Through-wall Thickness Surface Replication

Replicas were taken lengthwise in the forming direction of the pipe to include the weld metal and the PM and HAZ on either side of the weld as show in Figure 3.2 (Ngoasheng, 2017). A block sample was cut at an arbitrary location to assess the virgin material.

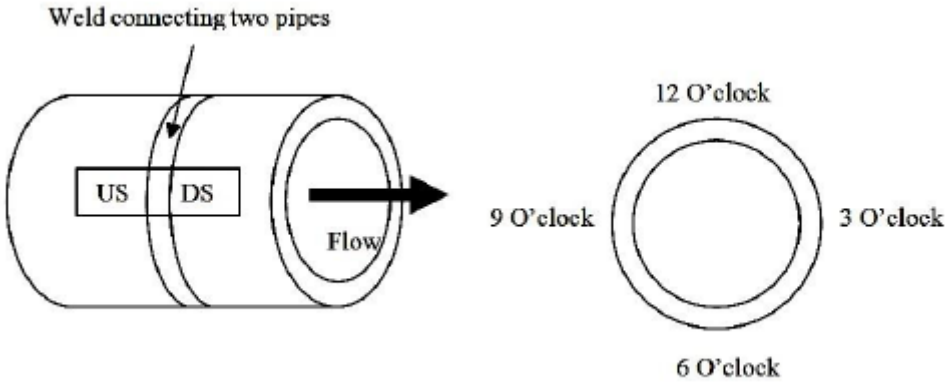

Figure 3.2 Surface replication of butt weld (Ngoasheng, 2017)

The surfaces of all the materials were prepared in the same manner. A portable motorised handheld grinder was used to grind the surface with successively finer grades of 320, 500, 800, and 1200 grit size silicon carbide paper.

The surface was polished to a mirror finish using woven wool discs of polishing cloth, with 6 µm, 3 µm and 1 µm diamond paste. The surface was cleaned with methanol between the polishing steps. A freshly mixed 5% nital etchant (95% vol. ethanol and 5% vol. nitric acid) was applied to the polished surface to reveal the microstructure. Two (2) surface replicas were lifted from the etched surface using a 12 × 40 mm 50 µm thick cellulose acetate film dipped in acetone. The surface replicas were obtained in two steps. The first replica was lifted

immediately after etching the surface followed by lifting of a duplicate replica taken at the same place as the first one. Surface replica films were mounted on a glass slide and marked accordingly.

The replicas were analysed by a replica evaluation metallurgist for quality and defects revealed by the replicated microstructure. The analysis of replicas was performed under an optical microscope at up to 500× magnification using Zeiss Axio Lab.A1 laboratory microscope. The number of voids was counted to determine the void density of the component. The remaining life was estimated using the damage model presented in Equation 2.25.

ImageJ software was used estimate the size of voids as observed from the replica micrographs. Boundary conditions were set to analyse particles of specific size range and circularity, as shown in Table 3.4. The obtained void sizes (irregular-shaped area) were converted to equivalent circular diameter using Equation 3.1. The original micrograph was used to distinguish creep voids from other circular microstructural features that may meet the set criteria of boundary conditions and get included in the result of particle analysis (van Zyl, et al., 2005).

$$\boldsymbol{d = 2 \times \sqrt{A/\pi}} \tag{3.1}$$

Where

A – measured particle size

Table 3.4 Creep void features boundary conditions

Boundary condition	Size [µm^2]	Circularity
Range	0.20 – infinity	0.60 – 1.00

3.3 Metallography

Sectioned specimens were mounted in black conductive SEM resin (Aka-resin phenolic) at 200°C using an Opal 410 hot mounting press. The SAPHIR 520 grinding and polishing machine was used for surface preparation. Grinding of the specimens was done under running water using 200, 500, 800, and 1200 grit size successively. The specimens were polished to

3 µm finish with a polycrystalline diamond suspension. Polished samples were etched using 3% Nital etchant (97% vol. ethanol and 3% vol. nitric acid).

3.4 Mechanical Testing

This section describes the different mechanical tests performed in this study. The Vickers hardness method was used for hardness measurements, uniaxial tensile test at room and elevated temperatures were used to evaluate tensile properties, and the Charpy V-notch impact test was used for assessing impact properties. The creep properties of the service-exposed parent material were assessed using an isothermal creep test.

3.4.1 Hardness Testing

Through-wall thickness hardness measurements were taken at 1 mm depth intervals around the pipe circumference of the service-exposed parent material and weld joint samples, as shown in Figure 3.3. Twenty-five indentations were made at 1 mm intervals along the replica lifting area. Hardness measurements were performed on the virgin parent material on a block sample at similar depth intervals. The Vickers hardness test was performed using the EMCO TEST DURASCAN hardness testing machine with the load of 10 kgf (HV_{10}).

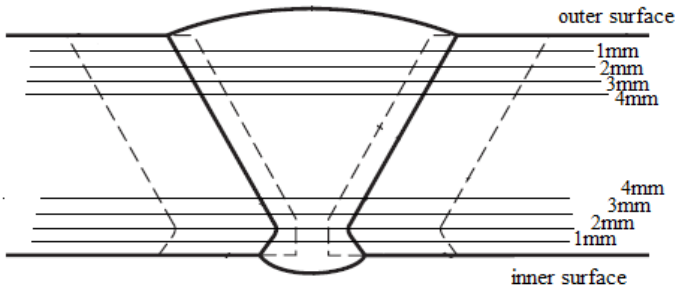

Figure 3.3 Through the wall thickness surface intervals with reference to the pipe inner and outer surfaces

Micro-hardness measurements were taken using the Future-tech FM-700 machine. A 300 gf load with a 15 s dwell time was used. Indentations were made normal to the weld across the area covering the base metal, HAZ, and weld metal, as shown in Figure 3.4. The distance between the indentations was measured to estimate the locations of the various HAZ sub-regions.

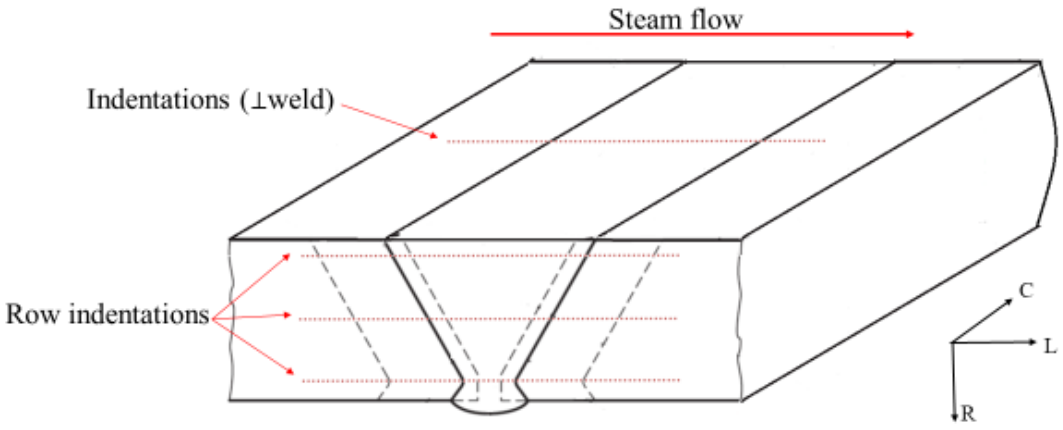

Figure 3.4 Schematic of micro indentations on the service-exposed weldment

3.4.2 Tensile Testing and Elevated Temperature Tensile Testing

Uniaxial tensile testing was performed on tensile specimens with a round gauge length at ambient (23°C) and at elevated temperature (500°C, 540°C and 560°C) in accordance with ISO 6892-1 and ISO 6892-2, respectively (International Organisation for Standardization, 2011; International Organisation for Standardization, 2016). A strain rate of 2.5×10^{-4} s^{-1} was used for all tensile tests.

The dimensions of the specimens are shown in Figure 3.5 for room temperature tests and Figure 3.6 for elevated temperature tests, respectively (Tshamano, 2017).

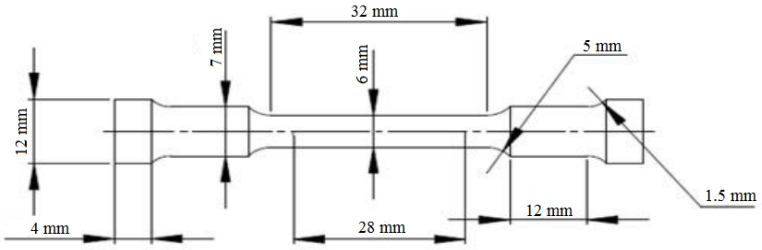

Figure 3.5 Room temperature tensile test specimen (Tshamano, 2017)

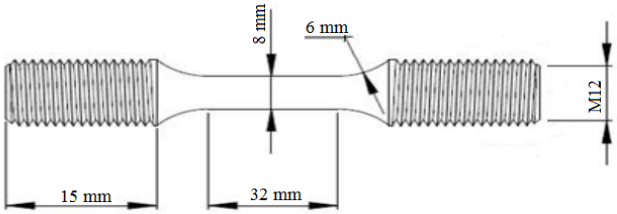

Figure 3.6 Elevated temperature tensile test specimen (Tshamano, 2017)

Type-K thermocouples were attached at the centre of the sample to control the furnace temperature. Samples were heated to the test temperature and soaked for 30 min before the test load was applied. The Instron 5582 universal testing machine shown in Figure 3.7 was used to carry out the tensile tests at room and elevated temperatures.

(1) Cross head, (2) Temperature controller, (3) Remote control
(4) Clamp/Chunk with loadcell, (5) Heating furnace
(6) Computer and (7) Test frame

Figure 3.7 Instron 5582 universal testing machine set up for hot tensile test (Tshamano, 2017)

3.4.3 Impact Testing

Impact testing was conducted on specimens machined from both the service-exposed and virgin parent materials, as well as from the service-exposed weldment. The Charpy V-notch test was conducted in accordance with ASTM E23–12c (ASTM International, 2013). All specimens were taken in the longitudinal direction with the notch machined in the radial direction (i.e., in the L-R direction).

The aim was to determine the impact properties of these materials and assess their ductile to brittle transition behaviour in presence of a flaw and fast loading conditions. The Charpy V-notch test method was done in accordance with ASTM E23 – 12c (ASTM International, 2013). All specimens were taken in the longitudinal direction with the notch machined in the radial direction, *i.e.* in the L-R direction.

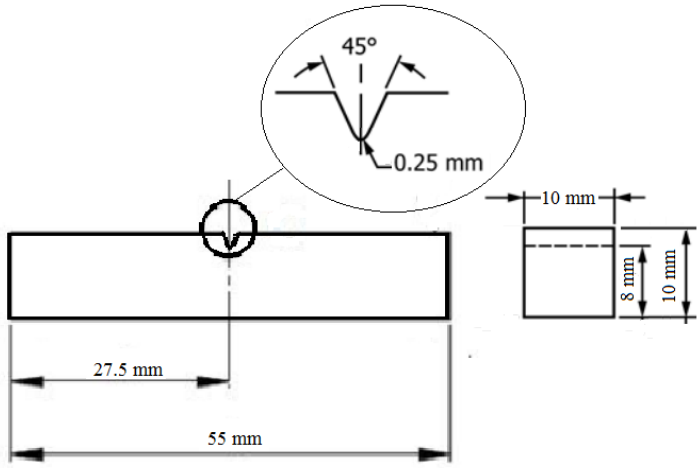

Figure 3.8 Charpy V-notch impact test specimen (ASTM International, 2013)

The impact testing of specimens was done on the Instron SI series motorised pendulum impact testing machine (Model SI-1M). The specimens were tested at -30, 0, 20, 50, 100, and 200°C to evaluate the DBTT and FATT temperatures of the material. All tests were conducted with a constant impact velocity of about 5.29 m/s. At least two (2) specimens were tested at each temperature for all the materials. Specimens tested at or below room temperature were soaked in Thermal H5 bath fluid for 30 min in the Julabo F32-HE refrigerated and heating circulator.

The energy required for crack initiation and crack propagation was determined using the instrumented impact test force *vs.* time and energy *vs.* time plots as shown in Figure 3.9 (Zrilic & Aleksic, 2003; Ibrahim, 2011; ASTM International, 2013).

Lateral expansion was measured using a 150 mm Mitutoyo digital Vernier calliper (ASTM International, 2013). The Boltzmann function in the Origin graphing software was used to fit a curve to each dataset of the research materials. This function produces a sigmoidal curve with the characteristic *S-shape*. This fitted curve represents the upper- and lower-shelf energy, as well as the DBTT regions of the specimen.

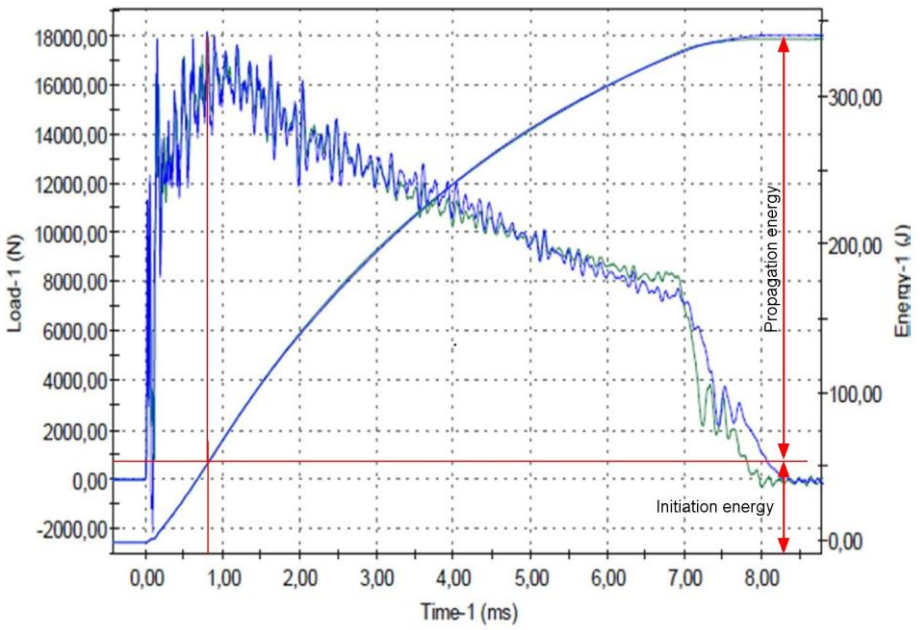

Figure 3.9 Typical load-time curve and energy-time curve generated by an instrumented Charpy impact-testing machine

The measurements of the width and thickness (termed dimensions A and B) of the unstable fracture region were taken using the digital Vernier calliper and the percent shear was determined from Table A4.1 of ASTM E23 (ASTM International, 2013). Furthermore, the fracture surfaces of the specimens were analysed under the Nikon AZ100M motorised multipurpose zoom microscope to determine the percentage of brittle fractures.

$$\%\boldsymbol{Shear\ area} = \frac{\boldsymbol{Total\ fracured\ area - Unstable\ fracture\ area}}{\boldsymbol{Total\ fracured\ area}} \times \mathbf{100} \qquad \textbf{(3.2)}$$

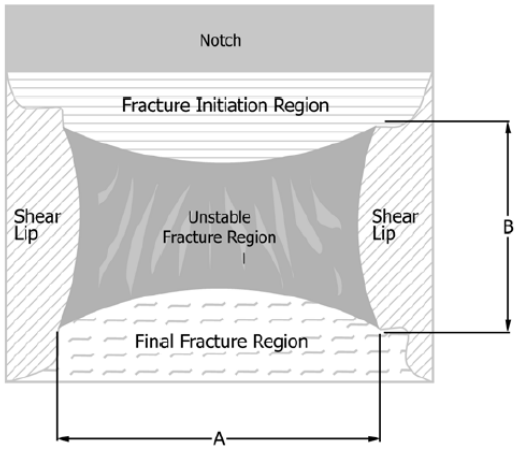

Figure 3.10 Fracture surface of a Charpy V-notch impact test specimen showing the various region of fracture (ASTM International, 2013)

3.4.4 Creep Testing

The Applied Testing Systems (ATS) WinCCS Lever Arm Tester (Series 2330) was used to conduct the creep tests, as shown in Figure 3.12 (a). The specimens were loaded onto the extensometer frame, and two thermocouples (type-K) attached at each end, as shown in Figure 3.12 (b). The thermocouples measured and controlled the temperature at the top and bottom of the split furnace are shown in Figure 3.12 (c), while the extensometer measured the specimen deformation.

A temperature control of $\Delta T = 5°C$ was set between the bottom half and top half of the furnace to ensure uniform distribution of heat, limit temperature excursion, and eliminate the possibility of the chimney effect phenomenon. The chimney effect may lead to a bias in fracture location, as the top half of the furnace will be hotter than the bottom half. ASTM E139 (2003) recommends two thermocouples for specimens with the length of the reduced section less than 50 mm.

For specimens with the length of the reduced section that is greater than 50 mm, three thermocouples must be attached. The third thermocouple must be attached near the centre of the specimen. The ATS machine is equipped with two high temperature extensometers rated at 1100°C. The system automatically averages the results to obtain better creep data. The isothermal creep testing method was followed, in which the specimens are subjected to a constant temperature (600°C) and different loads in an argon inert gas environment.

A gauge length of ~47 mm was marked on the reduced length of the specimen. A ramp rate of 100°C/h was used to heat the specimen to the test temperature. Once the temperature was reached, the specimen was soaked for one hour before applying the pre-load (~10% of total load) and running the test. The initial test stress (σ_0) was estimated using the reference stress method that is based on the modified Von Mises Equation 2.14 (van Zyl, 1997).

The ECCC master curve equation for ½Cr-½Mo-¼V steel (12MoCrV6-2-2) was used to estimate the test duration (rupture time), as shown in Equation 2.27. All specimens were tested at stresses of 60, 80, and 100 MPa. However, only a test at 60 MPa and 600°C was successfully done due to challenges with the testing frame. The test was performed using the service-exposed PM specimen.

The test stresses were factored by ± 20% to account for the lower and upper scatter bands of the ECCC master curve (Dobrzanski, 2020). The ruptured creep specimen was sectioned as shown in Figure 3.13 for analysis of the effect of load and temperature on the load bearing section compared with the sections that did not carry any load but experience high temperature.

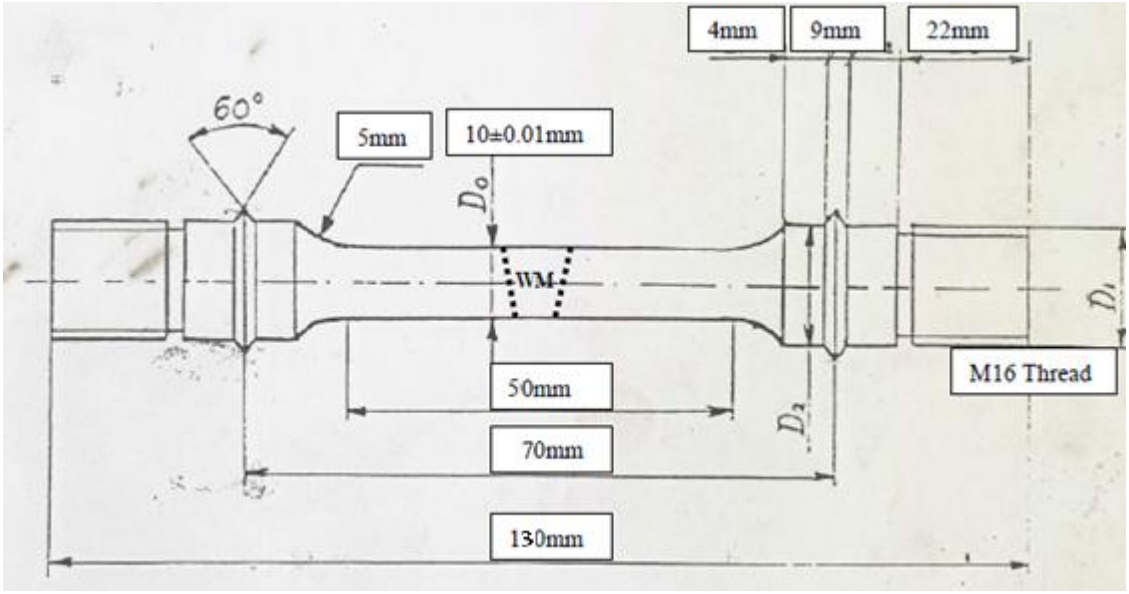

Figure 3.11 Cross-weld creep specimen (Molokwane, 2013)

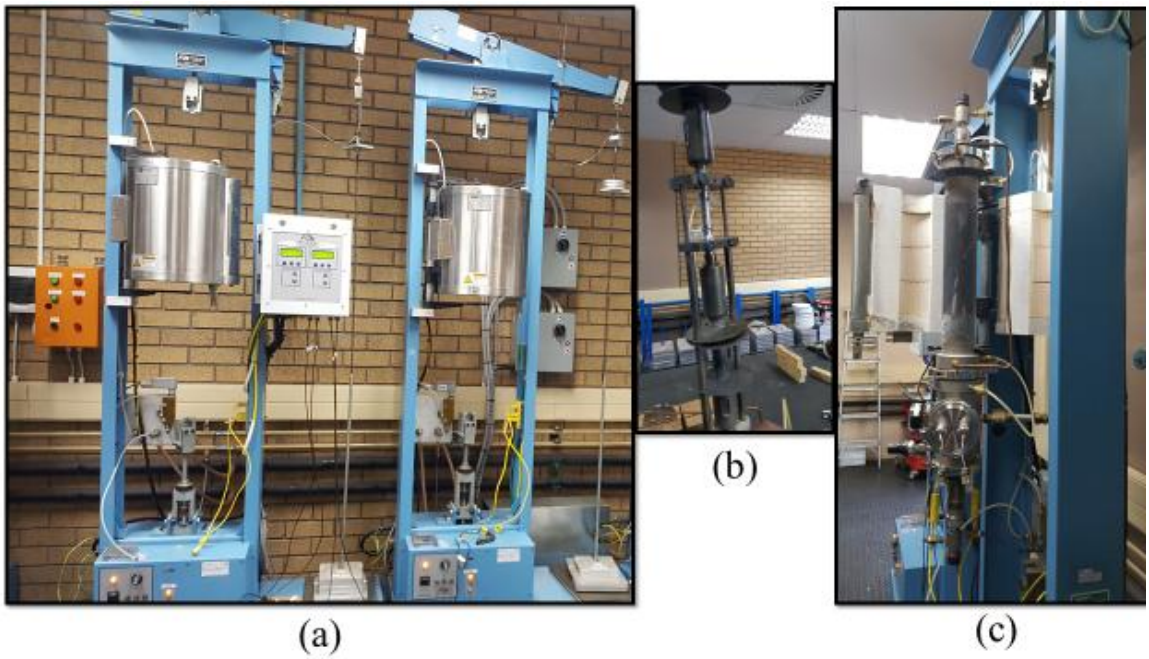

Figure 3.12 Creep testing machine and associated equipment: (a) testing frame, (b) extensometer frame and (c) spilt furnace

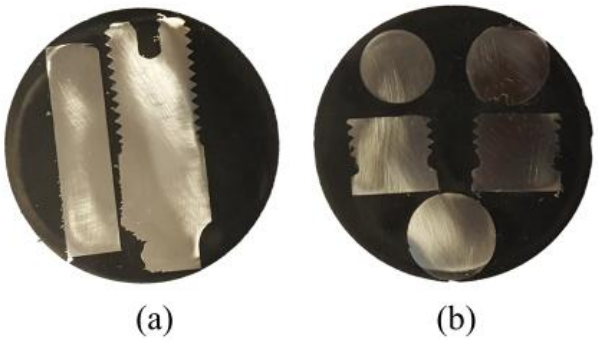

Figure 3.13 Ruptured creep specimen, sectioned to analyse the temperature and load effects on the (a) longitudinal section of the threaded-end and reduced section of the specimen and (b) transverse section of the specimen threaded-end

3.5 Thermodynamic Modelling of Phases with Thermo-Calc

Thermo-Calc thermodynamic calculations were performed over the temperature range 273 to 1873°C using the TCFE5 database, which is the Steels and Fe-alloys database version 5 of the Thermo-Calc software. The chemical composition presented in Table 3.3 was employed in the simulation analysis.

The Thermo-Calc thermodynamic calculations provided the required phase transformation temperatures for the HAZ simulations. As shown in Figure 3.14, the simulated processes included the solidification process, relative stability of matrix phases, and precipitation of secondary phases in 14MoV6-3 steel as a function of temperature. Thermo-Calc was also used to evaluate the equilibrium phases at a service temperature of 540°C. The average formulas (CEF) and empirical formulas of these phases were estimated from the phase compositions.

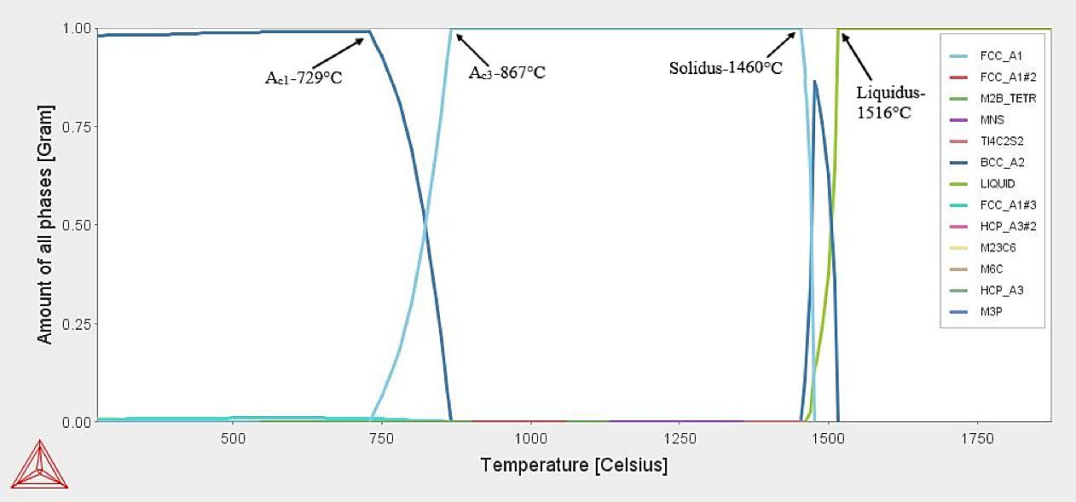

Figure 3.14 Typical Thermo-Calc thermal equilibrium transformation property diagram showing the equilibrium phases as a function of temperature for a composition of 14MoV6-3 steel with the A_{c1}, A_{c3}, solidus and liquidus temperatures indicated

3.6 Process Simulation and Material Testing with the Gleeble

The Gleeble® 3500 thermal-mechanical simulator was used to conduct weld HAZ simulation and hot tensile test. The HAZ simulation was performed to study the microstructure, mechanical properties and behaviour of individual HAZ regions. A hot tensile test was conducted to assess the tensile properties of the test materials compared to conventional tensile testing method. Type-K thermocouples were used for temperature monitoring and temperature profile recording in both experiments. The thermocouples were attached in the middle of the specimens by spot welding at 32 V using the DSI 35200 Thermocouple Welder as shown in Figure 3.15. Table 3.5 shows the operating parameters of type-K thermocouples.

Table 3.5 Thermocouples operating parameters

Thermocouple Type	Description (polarity)	Operating range [°C]	Peak Temperature [°C]	Max. time at peak temperature
Type-K	Ni-Cr (+); Ni-Al (-)	0 – 1250	1350	1 sec.
			1300	3 sec.
			1200	30 sec.

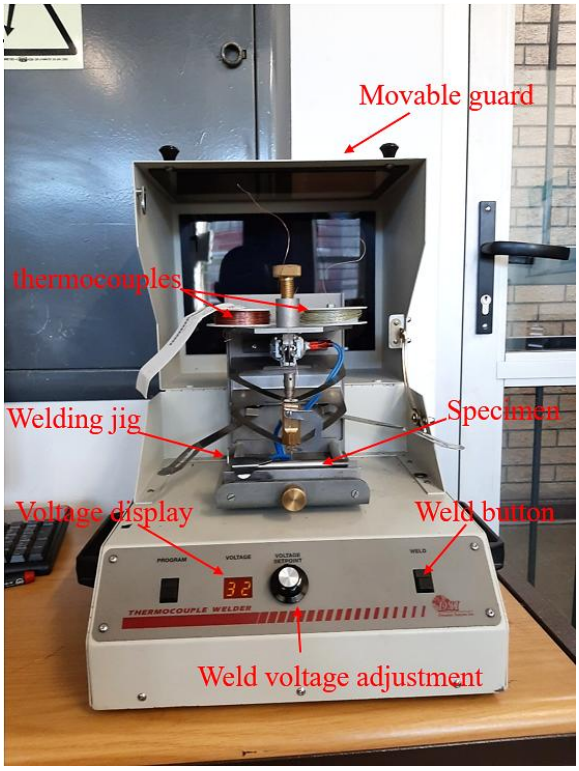

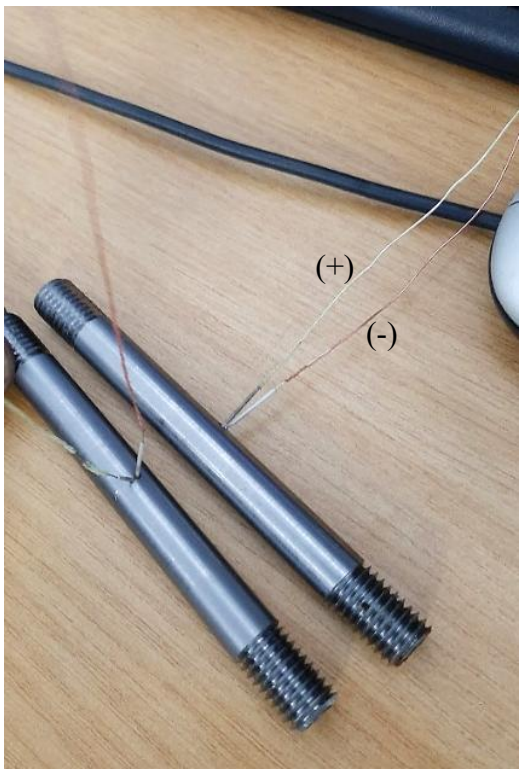

(a) (b)

Figure 3.15 Photo of (a) DSI 35200 Thermocouple Welder and (b) welded thermocouples on hot tensile specimens

3.6.1 Heat Affected Zone Simulation on the Gleeble®

Figure 3.16 shows the approximate location of the simulated microstructure on the phase diagram and the actual position on a weldment.

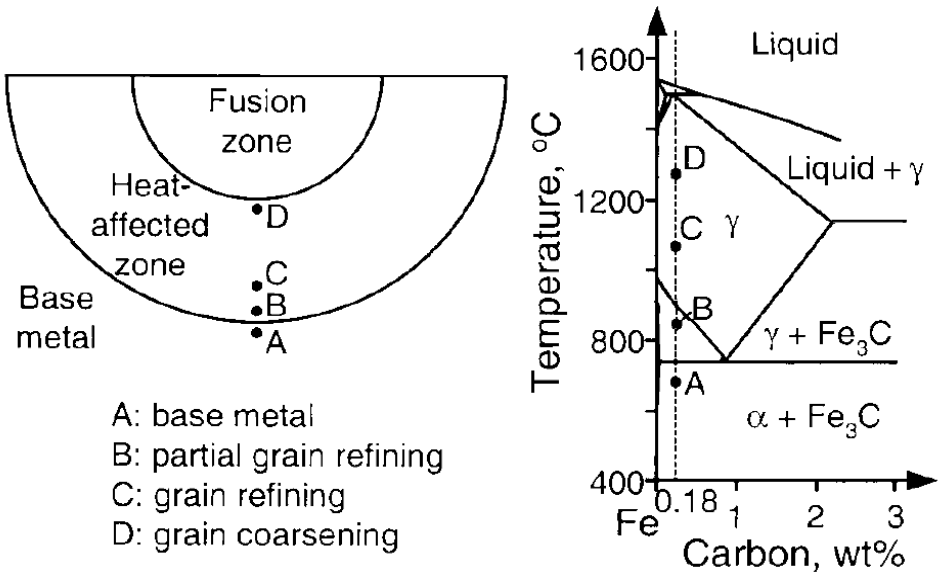

Figure 3.16 Locations and phases of the simulated microstructure (Kou, 2003)

The critical temperatures of A_{C1} and A_{C3} were estimated from the Thermo-Calc equilibrium simulation shown in Figure 3.14. In addition, Equations 3.3 and 3.4 were used to calculate transformation temperatures and compared them to the temperatures obtained in Thermo-Calc (Lomozik, 2013).

$$A_{C1} = 723 - 10.7 \times Mn - 16.9 \times Ni + 29.1 \times Si + 16.9 \times Cr + 290 \times As + 6.38 \times W \quad (3.3)$$

$$A_{C3} = 910 - 203 \times C^{1/2} - 15.2 \times Ni + 44.7 \times Si + 104 \times V + 31.5 \times Mo + 13.1 \times W - (30 \times Mn + 11 \times Cr + 20 \times Cu - 700 \times P + 400 \times Al - 120 \times As - 400 \times Ti) \quad (3.4)$$

Table 3.6 and Table 3.7 present the estimated A_{C1} and A_{C3} transformation temperatures of the virgin and service-exposed PM, respectively. The bainite transformation start of the virgin material and the service-exposed material were estimated to be 677°C and 714°C, respectively, using Equation 2.1 (ASM International, 2012).

Table 3.6 Comparison of critical temperature estimations for virgin 14MoV6-3 steel samples

Transformation temperature	Location on Fe-C phase diagram	Thermo-Calc [°C]	Lomozik Equation [°C]	ΔT [°C]
A_{c1}	A_1 < 800	728	729	~1
A_{c3}	800 < A_3< 1000	866	877	~10

Table 3.7 Comparison of critical temperature estimations for service-exposed 14MoV6-3 steel samples

Transformation temperature	Location on Fe-C phase diagram	Thermo-Calc [°C]	Lomozik Equation [°C]	ΔT [°C]
A_{c1}	A_1 < 800	768	727	~41
A_{c3}	800 < A_3< 1000	889	898	~10

The cooling time from 800°C to 500°C was calculated using Equation 2.3 (Blondeau, 2008). The input data were obtained from an existing WPS, which recommended a preheat

temperature of 200°C and an average heat input of 1.3 kJ/mm. However, the effect of preheat and mechanical constraints was not considered during the simulation. Table 3.8 summarises the HAZ simulation parameters.

Table 3.8 Peak temperatures and cooling time from 800°C to 500°C

HAZ Sub Region	Location	Peak Temperature	Cooling Time
		T_p [°C]	Δt_{8-5} [sec.]
ICHAZ	$A_{c1} < T_p < A_{c3}$	860	7.5
FGHAZ	$A_{c3} < T_p < 1100$	1080	7.5
CGHAZ	$A_{c3} << T_p < 1495$	1280	7.5

During the simulation, a heating rate of 50°C/s was used for all specimens, and the exponential cooling HAZ simulation program was selected. The program is based on Equation 3.5.

$$\boldsymbol{T = T_{max} e^{(\frac{-0.47}{\Delta t} t)}} \quad \textbf{(3.5)}$$

Where:

T_{max} – peak temperature, °C

Δt – cooling time from 800°C to 500°C, seconds

After the welding simulation, the specimens were subjected to a PWHT, where samples were heated to 730°C at a heating rate of 300°C/h and soaked for two (2) hours. Samples underwent both annealing and normalizing heat treatments. The furnace-cooling rate was set to 600°C/h (~0.2°C/s). Table 3.9 summarises the PWHT parameters used for simulated HAZ specimens of all the research materials. The PWHT cycle is schematically illustrated in Figure 3.17.

Table 3.9 Post-weld heat treatment parameters used for simulated HAZ specimens

Cooling Environment	Initial Temperature (°C)	Peak Temperature (°C)	Holding Time (Hrs)	Heating Rate (°C/s)	Cooling Rate (°C/s)
Furnace	RT	730	2	300	600
Ambient air	RT	730	2	300	–

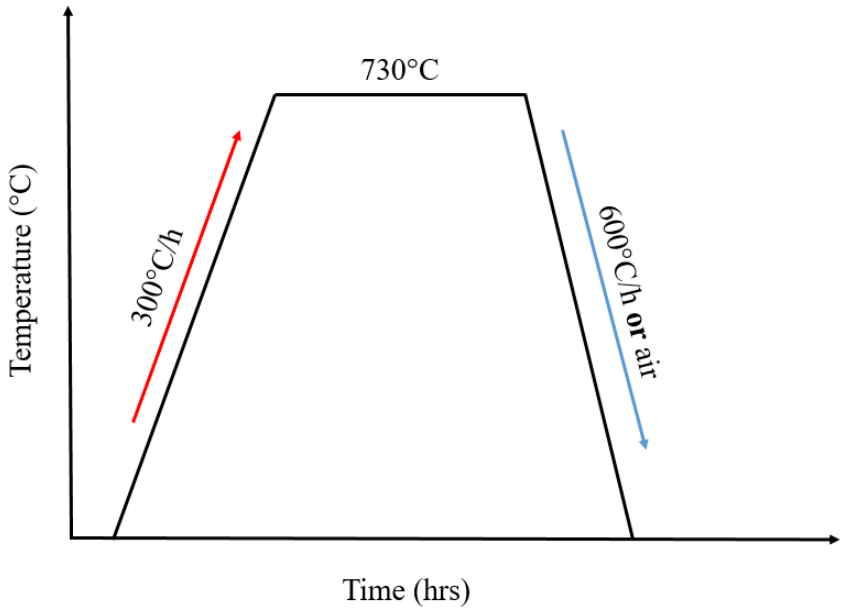

Figure 3.17 Schematic illustration of the post weld heat treatment cycle of simulated HAZ specimens

3.6.2 Gleeble Hot Tensile Test

Samples were first deformed at a slower strain rate of about 1% strain to make provision for the elastic region of the material. Samples are rapidly heated to the test temperature and then held at this temperature for 60 seconds. The test load is then applied, and the specimen is pulled until it fractures. The stress-strain results are recorded by the QuickSim software and can be readily analysed on the Origin software. Dimensional changes are directly measured from the specimen (post-test) for further analysis of material behaviour. Figure 3.20 shows the QuickSim program that was used in this experiment.

Table 3.10 Strain rate ranges of different tensile tests (Davis, 2004)

Type of tensile test	Strain rate range (s^{-1})
Pseudo static tensile test	10^{-5} to 10^{-1}
Dynamic tensile test	10^{-1} to 10^{2}

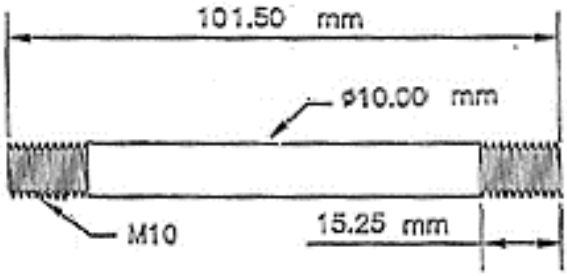

Figure 3.18 Round bar hot tensile test specimen with threaded ends (Dynamic Systems Inc., 2014)

$$\boldsymbol{m} = \left(\frac{\partial \ln \sigma}{\partial \ln \dot{\varepsilon}}\right)_{\varepsilon,T} = \left(\frac{\Delta \log \sigma}{\Delta \log \dot{\varepsilon}}\right) \tag{3.6}$$

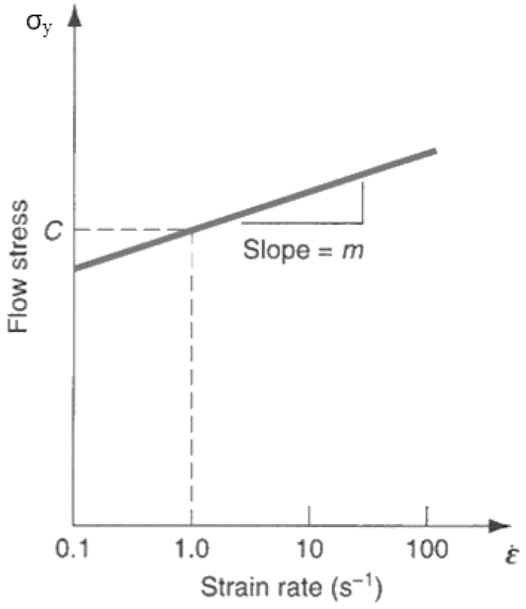

Figure 3.19 Flow stress dependency on strain rate

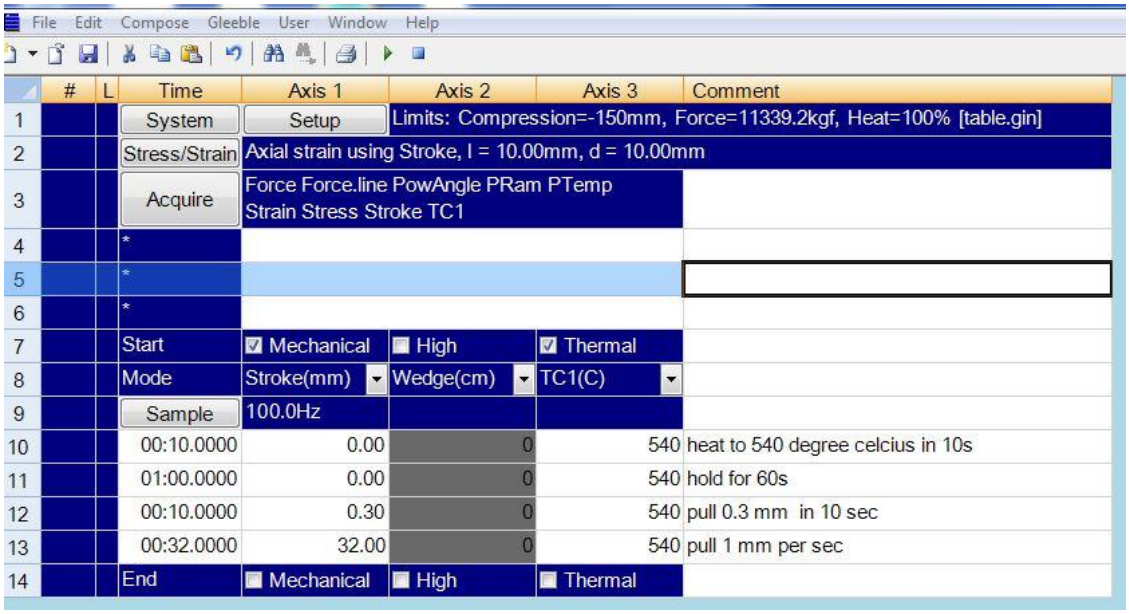

Figure 3.20 QuickSim program for hot tensile testing on the Gleeble®

3.7 Material Characterisation

Analytical techniques such as the optical microscopy, SEM, and XRD were used to analyse the microstructures and phases formed in as received, welded samples and HAZ simulated samples.

3.7.1 Optical Microscopy Analysis

The OM analyses were performed at the Eskom Research & Innovation Centre (ERIC) and Wits University facilities using the Zeiss Axio Lab.A1 and Olympus GX41 laboratory microscopes, respectively. These optical microscopes were used to analyse the microstructure of all the research materials. Micrographs of areas of interest were taken at magnifications of 200× and 500× from various specimens. Creep and HAZ simulated samples were also examined to study the fracture locations and microstructural features.

The average grain sizes of all samples were determined using the mean lineal intercept method (Avner, 1974; ASTM International, 2010). The intercepting lines were then counted on each line. The procedure was performed using ImageJ software with micrographs taken at magnification of 200×. The average grain size was determined for the array using Equation 2.28. Alternatively, several grains were traced (one grain at a time) using the freehand area selection tool in ImageJ. The equivalent circular diameter of each area was calculated from Equation 3.1 to determine the size of each grain. The average grain size was calculated as the average of all measurements.

3.7.2 Scanning Electron Microscopy Analysis

SEM analysis was carried out using a Zeiss SIGMA Field Emission SEM at Wits University, a JEOL JSM 7001F SEM at the Centre for High-Resolution Transmission Electron Microscopy (CHRTEM) at the Nelson Mandela University (NMU) and an FEI Quanta 600 at the ERIC facilities. SEM analysis of the virgin and service-exposed PM and weldment was carried out at ERIC and Wits facilities using the BSE and SE techniques. EDS was used for elemental analysis. In addition, the BSE and SE techniques were applied to study the composition and morphology of carbides in the virgin and service-exposed PM and on the service-exposed weldment.

Fractography of tensile samples was conducted at Wits using the Zeiss SIGMA Field Emission SEM. All fractography were taken at the bottom of the cup-and-cone fractures. At NMU, the virgin PM specimens were cut and mounted using bakelite resin. All the examinations were performed using the JEOL JSM 7001F SEM with magnifications of 250× to 5000×. The EBSD and TKD techniques were also applied in this analysis.

Table 3.11 shows the settings used for the EBSD and TKD analysis. A Nordlys HKL EBSD Detector was used for the analysis. Data processing and analysis were performed using the Aztec Acquisition and Channel5 HKL Processing Software packages.

Table 3.11 SEM parameters for EBSD and TKD analysis

Mode	Accelerating Voltage [kV]	Specimen Tilt [°]	Current [nA]	Step size [µm]	Magnification
EBSD	15	70	11	0.20	500×
TKD	30	-20	11	0.05	5000×

Various orientation maps were generated based on the orientation of the specimen. Maps of band contrast, inverse pole figures, and Euler angles were generated to represent the EBSD data. In an orientation map, the specimen orientation data are used to determine the colour of each point. Therefore, grains with the same orientation share the same colour. The BC is a measure of the EBSD pattern quality that is acquired from the average intensity of the Kikuchi bands with respect to the overall intensity within an EBSD pattern (Kang, et al., 2013). The higher the value (the brighter the colour in this case) the better the pattern. A greyscale image can be mapped based on the detected brightness. Grain boundaries and

deformed regions are darker than fully recrystallized regions. The IPF allows the crystallographic directions to be evaluated relative to the specimen axes, i.e., rolling, traverse, and normal directions. The colouring scheme of the IPF corresponds to different orientations that are given in an asymmetric pattern unit (APU) or orientation unit triangle.

Three Euler angles (ϕ_1, Φ and ϕ_2) are used to describe the orientation of the sample relative to the crystal. The orientation is transformed into RGB colour (Red, Green, and Blue) for mapping in Euler colouring. In the Channel5 software, the Euler angles are also used to describe the orientation relationships between other coordinate systems. The All-Euler option was used to create orientation maps that display different orientations as different colours. In this component, all three Euler angles are combined into a single colour and used for each point in the map.

3.7.3 X-Ray Diffraction Analysis

The Bruker D2 Phaser XRD diffractometer shown in Figure 3.21 was used to analyse the phase and composition of carbides in the virgin and service-exposed PM, weld metal and the HAZ. The instrument uses an X-ray generator with a voltage of 30 kV and current of 10 mA with the Cu Kα wavelength (λ) of 1.54 Å. It is fitted with the 1-dimensional SSD160 detector. DIFFRAC.SUITE software is used for data control and analysis. The other scanning parameters are listed in Table 3.12.

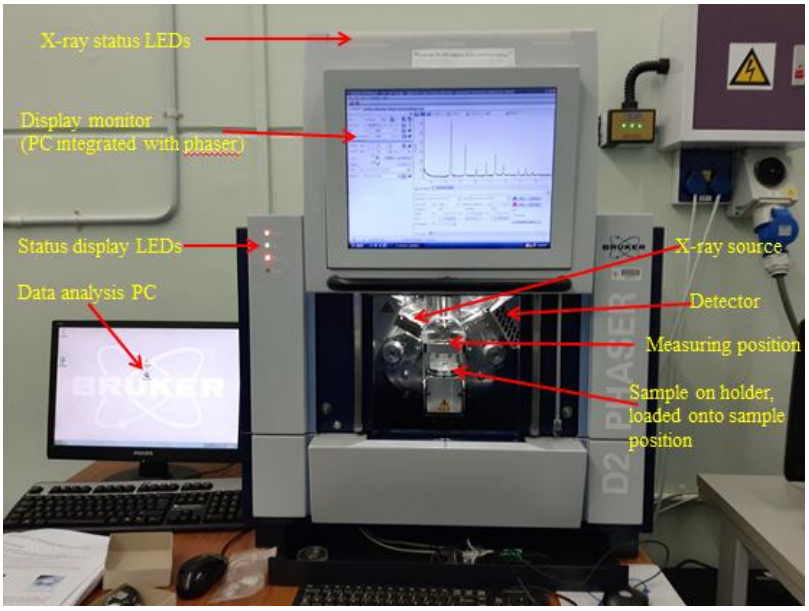

Figure 3.21 Benchtop XRD diffractometer

Data acquisition was performed using the DIFFRAC.MEASUREMENT software module. The DIFFRAC.EVA software module was used for data processing and matching the obtained peak patterns to reference PDF database. Peak matching was done using PDF-4+ 2019 database. OriginPro software was used to plot the peak patterns and analyse the crystal structure of the research materials.

Table 3.12 XRD analysis scanning parameters

Type	Range [°]	Steps	Increment [°]	Time [s]
2Theta	5 – 90	3227	0.026	0.36

The Scherrer formula (Equation 3.7) was used to determine crystallite size (D) and other associated parameters, such as the dislocation density (δ) (Equation 3.8) and the micro strain (ε) (Equation 3.9), for all the materials (Langford and Wilson, 1978; Monshi et al., 2012; Abbaschian et al., 2009; Cullity and Stock, 2014;). These parameters contribute to the profile (peak broadening) of the observed peak pattern because the peak width (β) is inversely proportional to crystallite size (D). The diffraction peak profile's peak width is measured at half-maximum height resulting from small crystallite size and is defined as the Full Width at Half Maximum (FWHM). The Scherrer constant (k), also known as the constant of proportionality (shape factor), is taken as 0.9 for FWHM of spherical crystals with cubic unit cells. However, the actual value of the Scherrer constant varies from 0.62 to 2.08 depending on the peak width, crystallite shape, and crystallite size distribution.

$$\boldsymbol{D = \frac{k\lambda}{\beta cos\theta}} \tag{3.7}$$

$$\boldsymbol{\delta = \frac{1}{D^2}} \tag{3.8}$$

$$\boldsymbol{\varepsilon = \frac{\beta}{4tan\theta}} \tag{3.9}$$

Monshi *et al.* (2012) proposed a modified Scherrer equation that can be used to estimate the average crystallite size more accurately as shown in Equation 3.10. This formula is obtained using the least-squares method to mathematically decrease the source of errors and finding the average crystallite size through all or any number of selected peaks. By rearranging the

formal Scherrer equation and taking natural log on both sides, the result of lnβ can be plotted against ln(1/cosθ) to obtain a straight line with unity slope and an intercept of about ln(kλ/L). The least-squares method gives the best slope and most accurate value of this intercept. The expression (Equation 3.11) can be used to calculate the average crystallite size (L) from the exponential of the intercept.

$$\boldsymbol{ln(\beta) = ln\left(\frac{k\lambda}{D}\right) + ln\left(\frac{1}{cos\,\theta}\right)} \quad \textbf{(3.10)}$$

$$\boldsymbol{e^{ln\frac{k\lambda}{L}} = \frac{k\lambda}{L}} \quad \textbf{(3.11)}$$

Furthermore, the XRD data was used in the assessment of remaining life of the research materials as proposed by Dobrzanski et al. (2011) in a method that relies on the fact that the size, shape and composition of carbides in 14MoV6-3 steel change over time in service. The results of all the experiments and analyses performed on the virgin and service-exposed PM and the weld metal are presented and discussed in the next chapter.

Chapter 4: Results and Discussion

4.1 Material Characterisation

4.1.1 Introduction

Samples of both new and service-exposed 14MoV6-3 parent material, as well as service-exposed butt-weld, were analysed to characterise microstructural evolution resulting from long-term service under creep conditions. Microstructural analysis was performed using optical microscopy and scanning electron microscopy. Mechanical properties were evaluated through hardness, tensile, impact testing and creep testing. The results were assessed for compliance with the requirements specified in BS EN 102162-2 (British Standards Institution, 2007). A summary of the experimental tests is provided in Tables 4.1 and 4.2.

The results presented in Table 4.1 are discussed in the subsequent sections. This includes the creep life assessment and damage analysis of the virgin parent material, the service-exposed parent material and the weldment. Subsequent sections present HAZ simulations and Gleeble® tensile testing, thermal equilibrium simulations, XRD analysis and the discussion of all the test results.

Table 4.1 Summary of samples and the test methods used in the study

	Test/observation Method										
Sample	Vickers Hardness Testing	Tensile Testing		Charpy V-notch Impact Testing		Creep Testing	Surface Replicas	OM	SEM	XRD	TCS
		RT	Elevated	RT	DBTT						
Virgin PM	✓	✓	✓	✓	✓	–	✓	✓	✓	✓	✓
Ex-service PM	✓	✓	✓	✓	✓	✓	✓	✓	✓	✓	✓
Ex-service Weld Joint	✓	✓	✓	✓	✓	–	✓	✓	✓	✓	✓
xGleeble	✓	–	✓	✓	✓	–	✓	✓	✓	–	–

Table 4.2 Details of Ductile Brittle Transition Temperature testing matrix

Sample Area	V-notch location on sample	Test Temperature (°C)						
		-30	0	20	23	50	100	200
Virgin PM	Centre	✓	✓	✓	–	✓	✓	✓
Ex-service PM	Centre	✓	✓	✓	✓	✓	✓	✓
Butt weld	Mid-weld	✓	✓	✓	✓	✓	✓	✓
HAZ 1	up-stream of butt weld	–	✓	✓	–	✓	–	✓
HAZ 2	down-stream of butt weld	✓	–	✓	–	✓	✓	–
xGleeble	ICHAZ; FGHAZ & CGHAZ	–	–	✓	–	–	–	–

4.2 Assessment of Virgin Parent Material

4.2.1 Hardness Results

The virgin parent material exhibited an average hardness of 164 HV10, as shown in Table 4.3. This value falls within the acceptable range for 14MoV6-3 steel at room temperature, which is specified to be between 140 and 192 HV_{10} (British Standards Institution, 2007; Hodzic & Hajro, 2011; Junek & Janovec, 2015).

Table 4.3 Vickers hardness of the new 14MoV6-3 pipe

	Hardness (HV_{10})	
Data	Measured	OEM
Average	**164**	**160**
Std. Dev.	5.6	4.2

The OEM hardness values were converted from Brinell hardness (HBS) to Vickers using Equation 4.1 and used for comparison (ASTM International, 2013). The OEM values are also within the acceptable hardness range of 14MoV6-3 steel and in agreement with the measured values.

$$\boldsymbol{HV10 = 8.52592 \times 10^{-2} + 9.82889 \times 10^{-1}(HBS) + 1.89707 \times 10^{-4}(HBS)^2} \quad \textbf{(4.1)}$$

The hardness profile of the virgin material, as measured through the pipe wall thickness, is shown in Figure 4.1. The difference in measured hardness may be attributed to the hot finished seamless pipe manufacturing process and subsequent heat treatment. The higher

hardness may be due to secondary hardening phenomenon as the steel was tempered at a temperature higher than 700°C (Totten, 2007). The distribution of hardness through the pipe wall thickness is shown in Figure 4.2 and ranges from 154 to 190 HV_{10}.

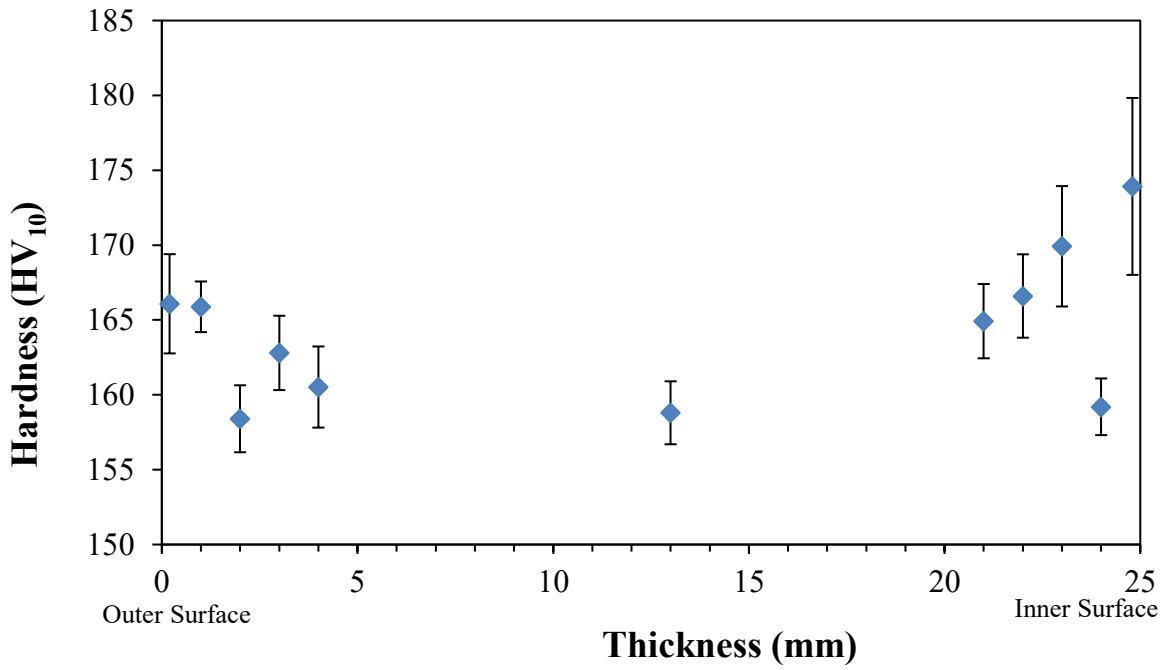

Figure 4.1 Through-wall thickness hardness (HV10) profile of virgin 14MoV6-3 parent material

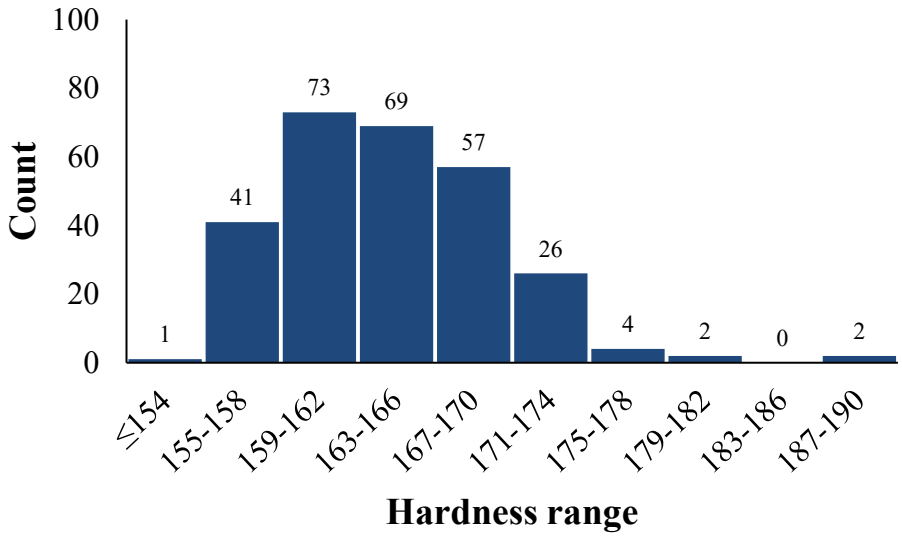

Figure 4.2 Through-wall thickness hardness range of the virgin parent material

4.2.2 Room Temperature Tensile Properties

The room temperature tensile properties of the virgin parent material are shown in Table 4.4. The average lower and upper yield strengths were found to be approximately 385 and 392 MPa, respectively. The listed tensile properties meet the acceptability criteria of BS EN 10216-2 for 14MoV6-3 steel (British Standards Institution, 2007). The obtained strength values were slightly higher than those reported by the OEM. The difference in the strength values is attributed to dissimilarities in the location, orientation, size (geometry) and preparation of the sampled material, and type of tensile testing machine. Nonetheless, the virgin parent material exhibited excellent strength and ductility at room temperature.

Table 4.4 Room temperature tensile properties of virgin parent material

Test Temperature [°C]	Yield Strength [MPa]	Tensile Strength [MPa]	Elongation [%]	Reduction in Area [%]
23	381	553	34	51
Std. Dev.	6.0	2.3	2.4	1.4

The SEM fracture surface of the virgin parent material is shown in Figure 4.3 (a). The surface is typical of ductile material and characterised by a grey, fibrous appearance (Dieter, 1961; Davis, 2004; Callister & Rethwisch, 2008;). The fractograph reveals an irregular surface that features many spherical dimples, which is typical for plastic deformation. Callister et al. (2008) suggested that these dimples are one-halves of micro voids that form, coalescence and ultimately separate during the fracture process. The areas that consist of fine, small dimples were found to contain Mn and Cr as shown on the EDS spectrum in in Figure 4.3 (b).

(a)

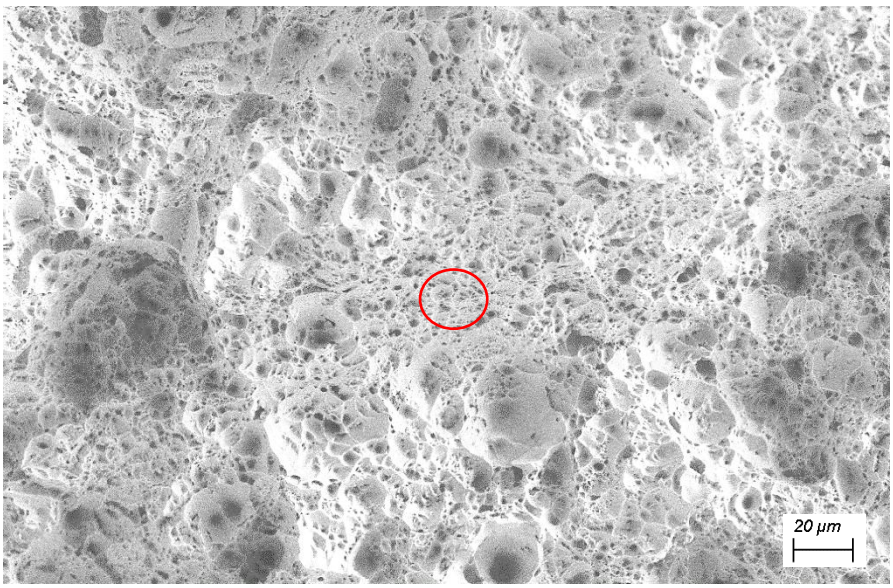

(b)

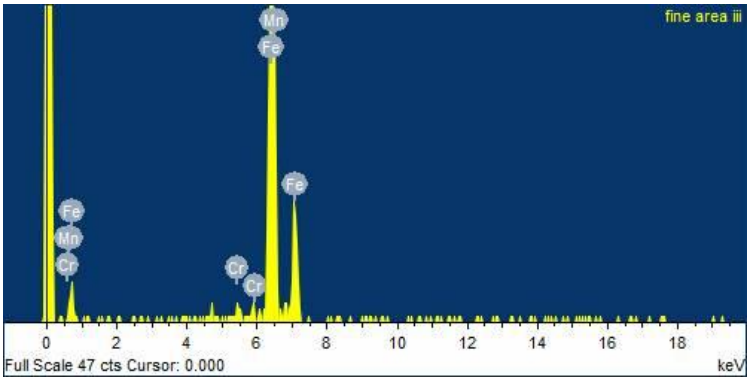

Figure 4.3 Typical fracture surface appearance of the virgin parent material (room temperature specimen) under SEM (a) and EDS analyses of inclusions and microvoids (b).

4.2.3 Elevated Temperature Tensile Properties

Tensile properties of virgin parent materials were conducted at different temperatures ranging from 500°C to 560°C as shown in Table 4.5. The proof strength of the virgin parent material at each temperature was above the minimum proof strength specified by BS EN 10216-2 at elevated temperatures (British Standards Institution, 2007). The yield and tensile strength decreased with increasing temperature, with the yield and tensile strength at 560°C reported to be 247 MPa and 348 MPa, respectively.

Table 4.5 Elevated temperature tensile properties of virgin parent material

Test Temperature [°C]	Yield Strength [MPa]	Tensile Strength [MPa]	Yield-Tensile Ratio	Elongation [%]	Reduction in Area [%]
500	264	425	0.62	23	83
540	256	370	0.69	27	84
560	247	348	0.71	26	88

Typical stress-strain curves of the virgin parent material at 500°C, 540°C and 560°C test temperatures are shown in Figure 4.4. The stress-strain curves are characteristic of ductile material with a gradual transition from the elastic to the plastic region.

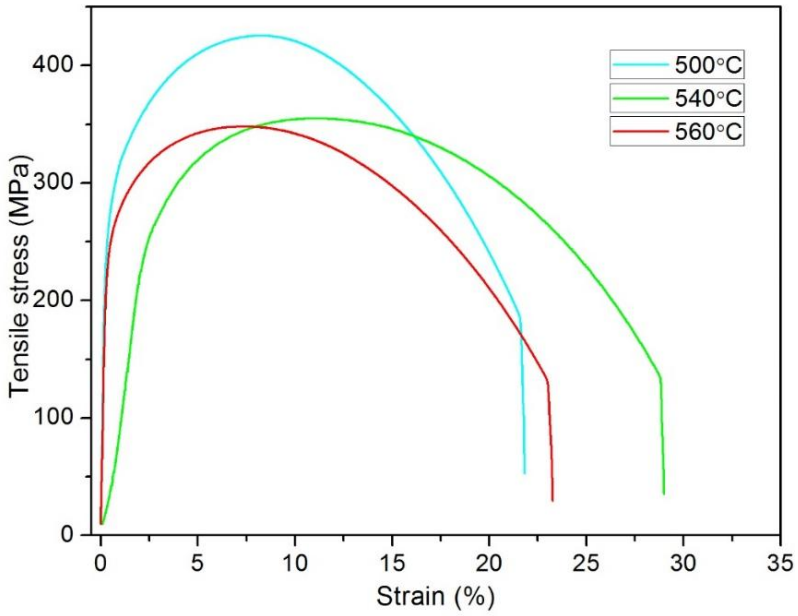

Figure 4.4 Typical elevated temperature stress-strain plot of the virgin parent material

The variation in YS, UTS and the yield tensile ration (YTR) as a function of temperature are shown in Figure 4.5 (a). The YTR increases with temperature but remains sufficiently low for plastic deformation. The reduction of strength with temperature is typical of low alloy steels such as 14MoV6-3 steel (Davis, 2004). In addition, the yield strength is higher than the specified minimum strength at elevated temperature and in general, the virgin parent material maintained its good mechanical properties at elevated temperature.

Figure 4.5 (b) shows the change in ductility with increasing temperature. The ductility increases as the temperature increases but slight drops at 560°C. The reduction in area does not show any significant variation between 500°C and 540°C. However, a sharp increase in reduction in area is observed at 560°C.

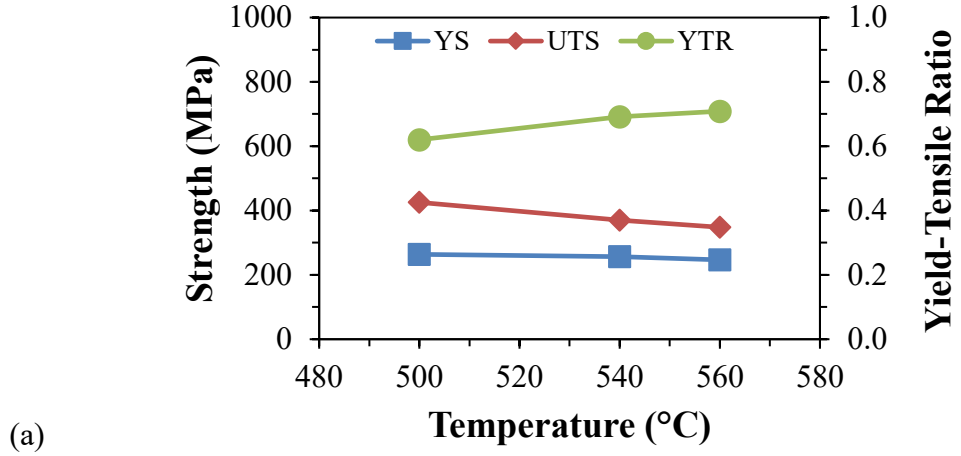

(a)

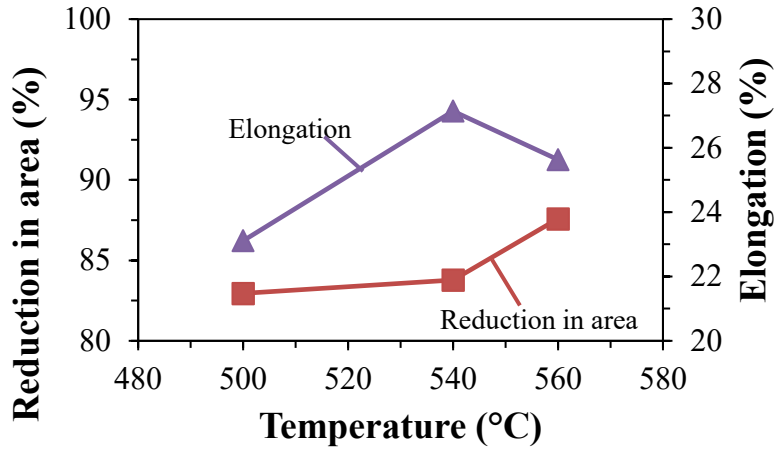

(b)

Figure 4.5 (a) Variation of Yield strength, UTS and Yield-Tensile ratio as a function of temperature. (b) Variation of reduction in area and elongation with temperature.

The correlation of the YTR to the elongation and reduction in area is shown in Figure 4.6. The ductility of the virgin material shows a relatively small change of approximately 4% as the YTR changes. This could be an indication that the material has a wide safety margin when it comes to plastic collapse failures.

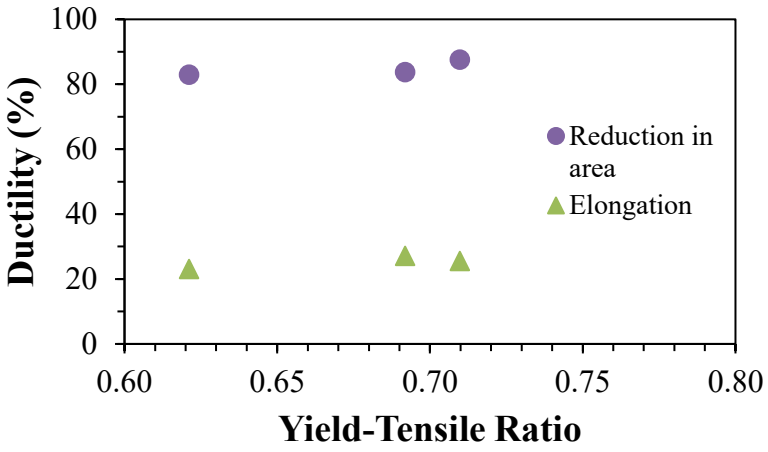

Figure 4.6 Yield-Tensile Ratio versus ductility at elevated temperature

The variation of the Young's modulus with temperature is shown in Figure 4.7. The Young's modulus of the virgin parent material was found to decrease with increasing temperature, consistent with the observed reduction in both yield and tensile strengths. The temperature dependence of Young's modulus is due to increased atomic activity driven by higher kinetic energy (Abe, et al., 2008). As temperature increases, atomic bonds are more easily displaced, reducing the stiffness of material and results in a lower Young's modulus.

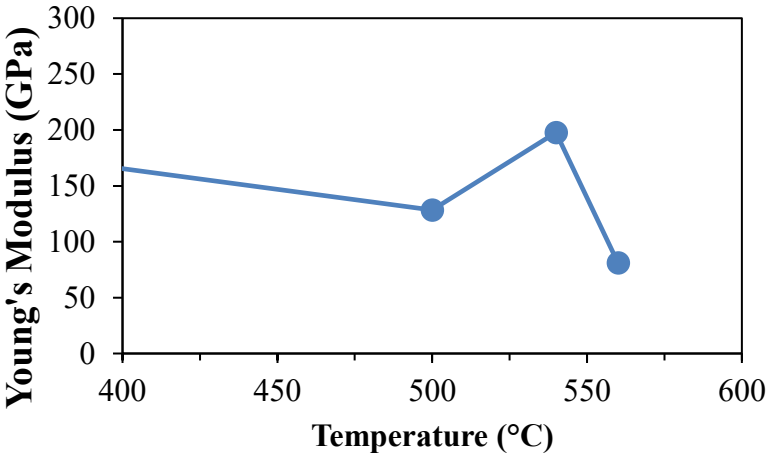

Figure 4.7 Variation of the Young's modulus as a function of temperature

The ductile fracture surface appearance of the virgin parent material at elevated temperature is shown in in Figure 4.8 (a) and (b). Large and small inclusions were observed on the fracture surface, as indicated by red and yellow arrows, respectively. The EDS analysis of these inclusions is presented in in Figure 4.8 (c). Al and Mo are the major elements detected in the analysis.

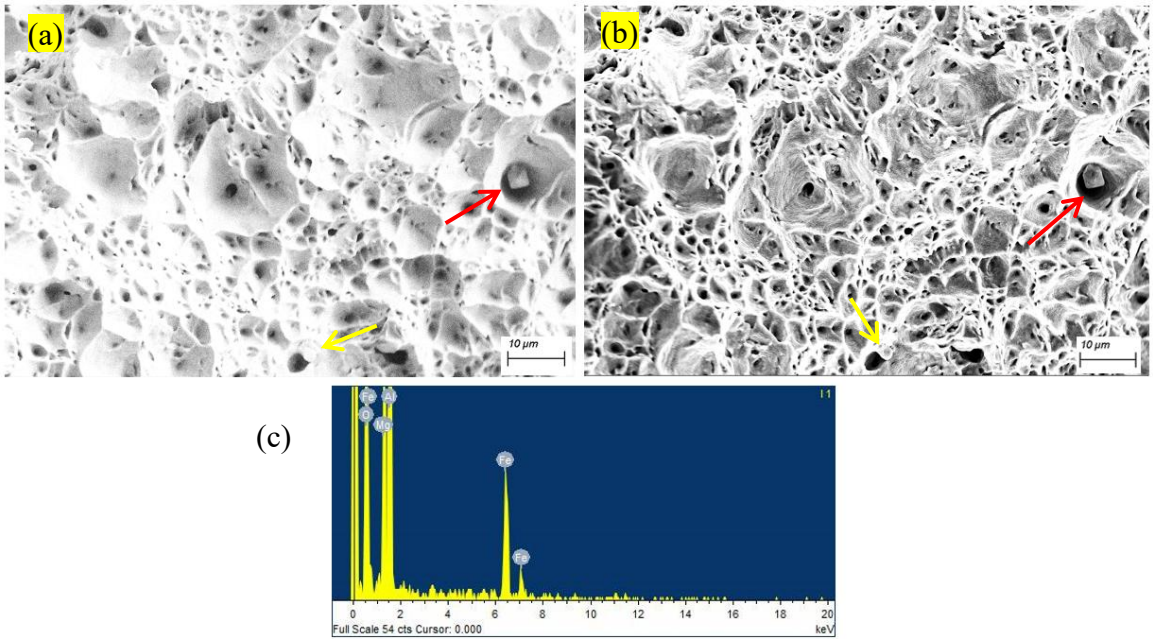

Figure 4.8 Typical fracture surface appearance of the virgin parent material (elevated temperature specimen) under SEM (a) SE2 and (b) InLens. EDS analyses of inclusions and microvoids (c).

4.2.4 Impact Properties

The impact properties of the virgin parent material at different testing temperatures are summarised in Table 4.6. The average impact energy of 368 J obtained at room temperature significantly exceeds the minimum longitudinal (40J) and transverse (27J) values specified by BS EN 10216-2 (British Standards Institution, 2007). The impact toughness is within acceptable limits across a broad temperature range, with testing conducted from -30 °C up to 200 °C. However, the criteria for impact properties at elevated temperatures and low temperatures are not specified for 14MoV6-3 in BS EN 10216-2. The impact energy required for crack initiation did not vary significantly with temperature, suggesting that crack initiation is primarily dependent on the stress conditions at the crack tip (Cvetkovski, et al., 2002). The impact toughness results presented in Table 4.6 are comparable to results obtained in literature (Zrilic & Aleksic, 2003; Hodzic & Hajro, 2010).

Table 4.6 Impact toughness properties of virgin parent material at different temperatures

Test temperature [°C]	Total absorbed energy [J]	Energy required for crack [J]	
		Initiation	Propagation
-30	61	27	34
0	288	46	242
20	368	27	341
50	353	53	301
100	353	50	303
200	330	41	290

The fractured surfaces of virgin parent material at different test temperatures are shown in Figure 4.9. The specimen fracture surface appears fibrous at the temperatures of 20, 50, 100 and 200°C. The observed fracture surfaces at temperatures above 20°C are characteristic of shear failure. In addition, the samples did not fracture completely due to high ductility of the material, as indicated by impact properties such as lateral expansion.

Samples tested at 0°C and -30°C showed brittle fracture and the FATT was observed to occur between 0°C and 20°C.

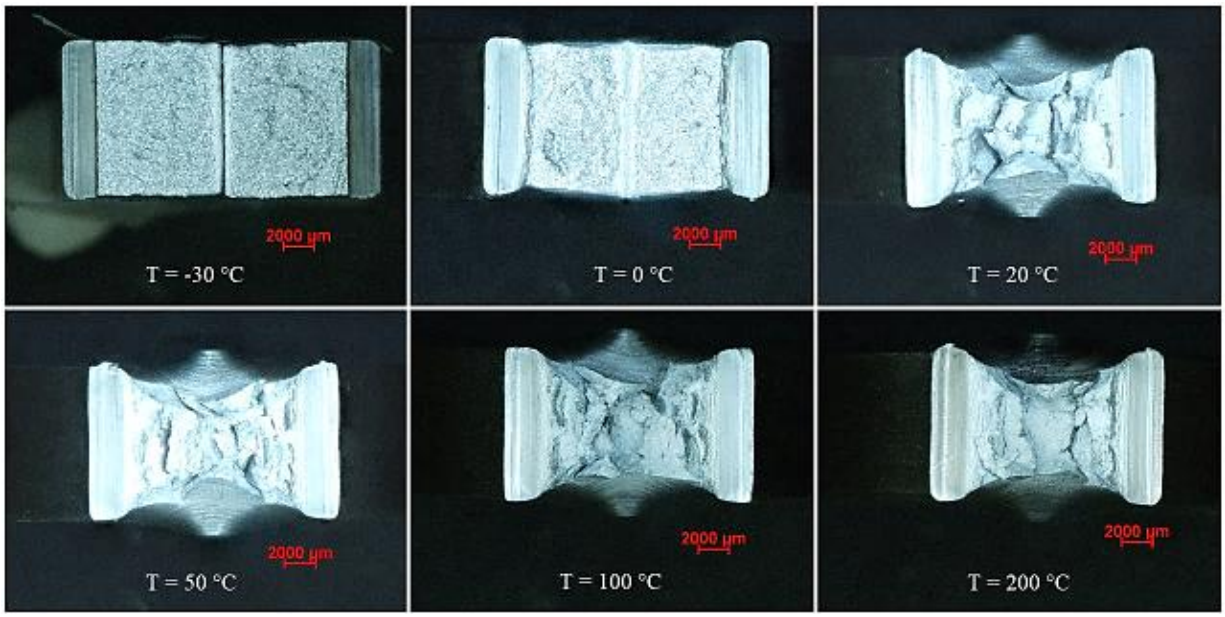

Figure 4.9 Fracture appearance of virgin material specimens at various temperatures

The change in impact energy, percentage of shear fracture and lateral expansion, as a function of temperature, is shown in Figure 4.10 (a), (b) and (c). The material exhibits an abrupt decrease in total energy with decreasing temperature, indicating a ductile-to-brittle transition around 0°C. The upper-shelf energy associated with ductile fracture, was recorded as 350 J at 20°C, while the lower-shelf energy indicative of brittle fracture was observed around 60 J at -10°C.

Although the standard 27 J transition temperature is not directly observed in this dataset, it can be inferred to occur below -30 °C. Based on the lateral expansion versus temperature curve, the key transition points are located at 0 °C (ductile-to-brittle transition temperature, DBTT), 20 °C (upper-shelf), and -30 °C (lower-shelf). The fracture mode is estimated to be 100% shear between 20 °C and 200 °C, as shown in Figure 4.10. At 0 °C, a mixed-mode fracture was observed, while a fully brittle fracture (0% shear) occurred at -30 °C.

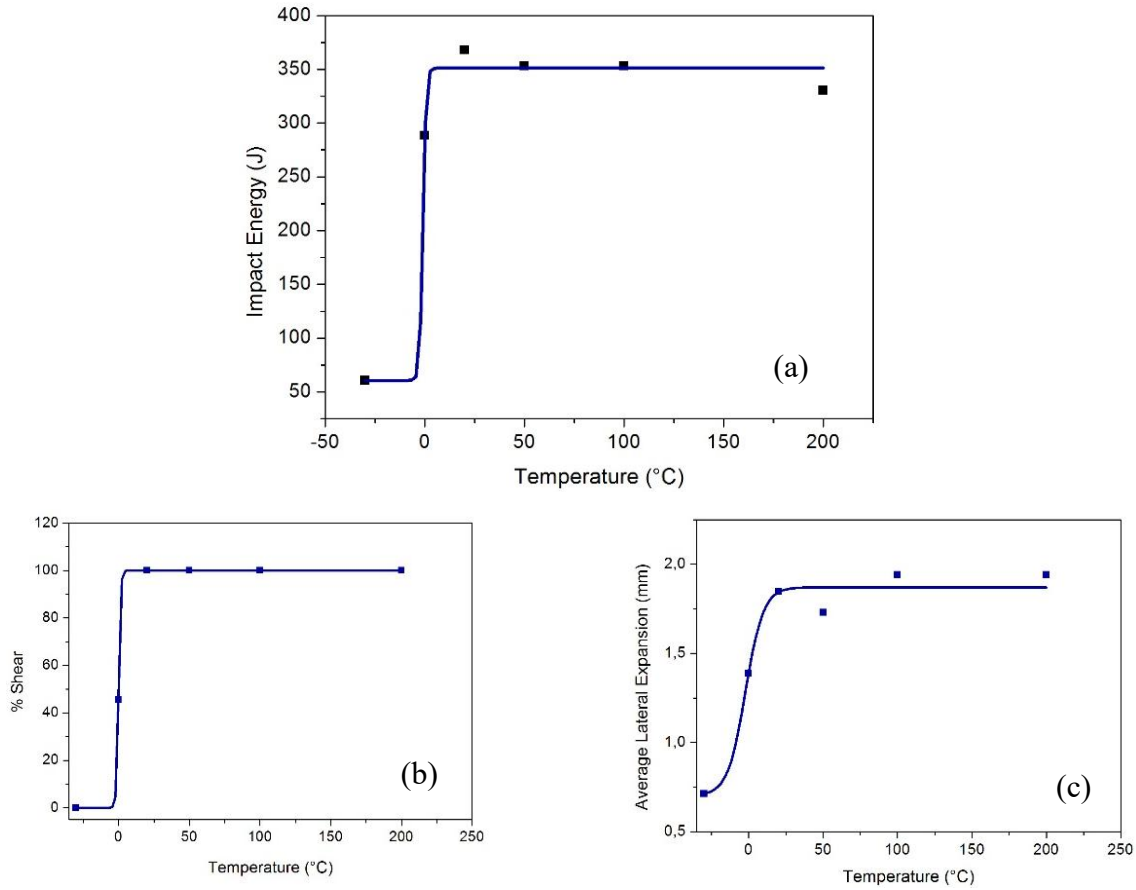

Figure 4.10 Ductile-Brittle Transition Temperature of virgin parent material evaluated against (a) impact energy, (b) percentage of shear fracture and (c) lateral expansion

Figure 4.11 shows the maximum load that was recorded at the temperatures of -30, 0, 20, 50, 100 and 200°C. The applied load remained relatively constant across the temperature range, except for a notable deviation at 200 °C due to thermal softening. A similar trend was observed for the required crack initiation energy.

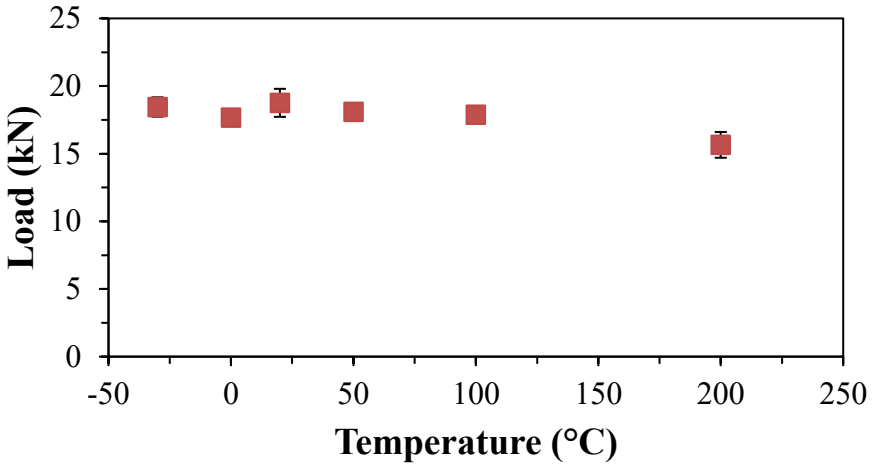

Figure 4.11 Maximum load as a function of temperature for the virgin parent material

4.2.5 General Microstructure of the Virgin Material

This section presents the analysis of the microstructure of the virgin parent material. The overview of the microstructure from the observations made under the optical and scanning electron microscopes are discussed. The SEM analyses were performed using the basic BSE and SE techniques, which were supplemented advanced techniques such as EBSD and TKD.

4.2.5.1 Optical Microscopy Analysis

The optical microstructure of the virgin parent material is shown in Figures 4.12 and 4.13. The virgin parent material exhibited a dual phase microstructure consisting of ferrite and bainite, which is typical of the initial microstructure of 14MoV6-3 alloy steel (Wyman-Gordon Forgings, 2011). The lighter-etching phase with equiaxed grains was identified as ferrite, while the darker phase appearing as islands of ferrite-carbide aggregates, was identified as bainite.

The average grain size and phase fraction of the virgin parent material is shown in Table 4.7. The grain size was estimated using the lineal intercept method and the phase fraction was

determined by ImageJ software (ASTM International, 2010). An average grain size of 9.6 µm was reported.

Table 4.7 Average grain size of virgin parent material

Line Length [µm]	Average No. of intercepts	Average grain size [µm]	ASTM grain size number [G]	Ferrite/Bainite phase fraction [%]
400	42	9.6	10.1	78/22

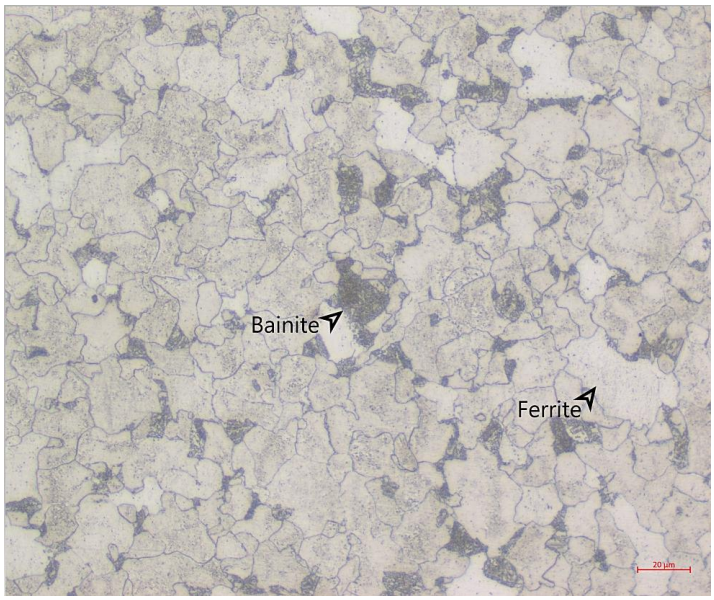

Figure 4.12 Initial ferrite-bainite microstructure of virgin parent material that was chemically etched with 5% Nital

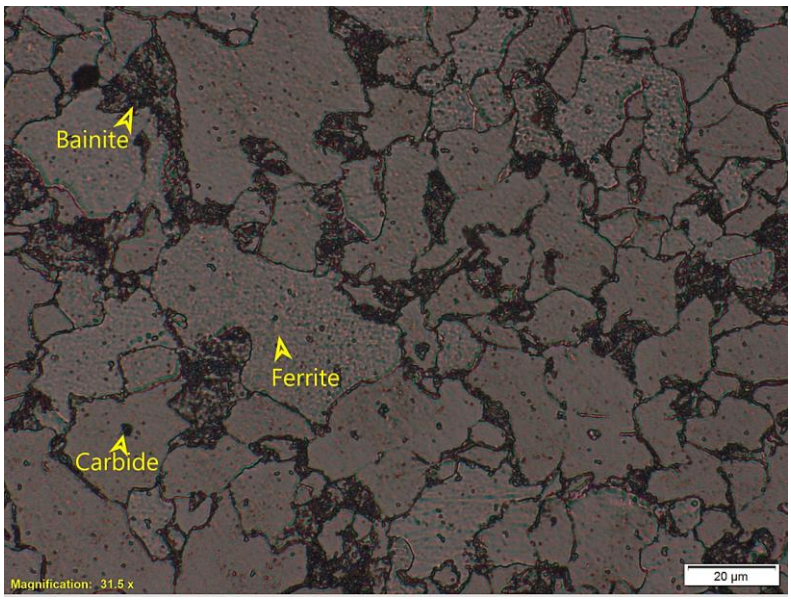

Figure 4.13 Initial ferrite-bainite microstructure of virgin parent material that was chemically etched with 3% Nital

4.2.5.2 Scanning Electron Microscopy Analysis

The SEM backscatter micrograph (Figure 4.14) shows the microstructure of the virgin parent material that consists of ferrite and bainite. An insert at higher resolution highlights the presence of large carbides precipitates along grain boundaries, as well as fine carbides dispersed within the ferrite grains (indicated by white arrows). Bainite grains appearing as ferrite-carbide aggregates are marked with yellow arrows.

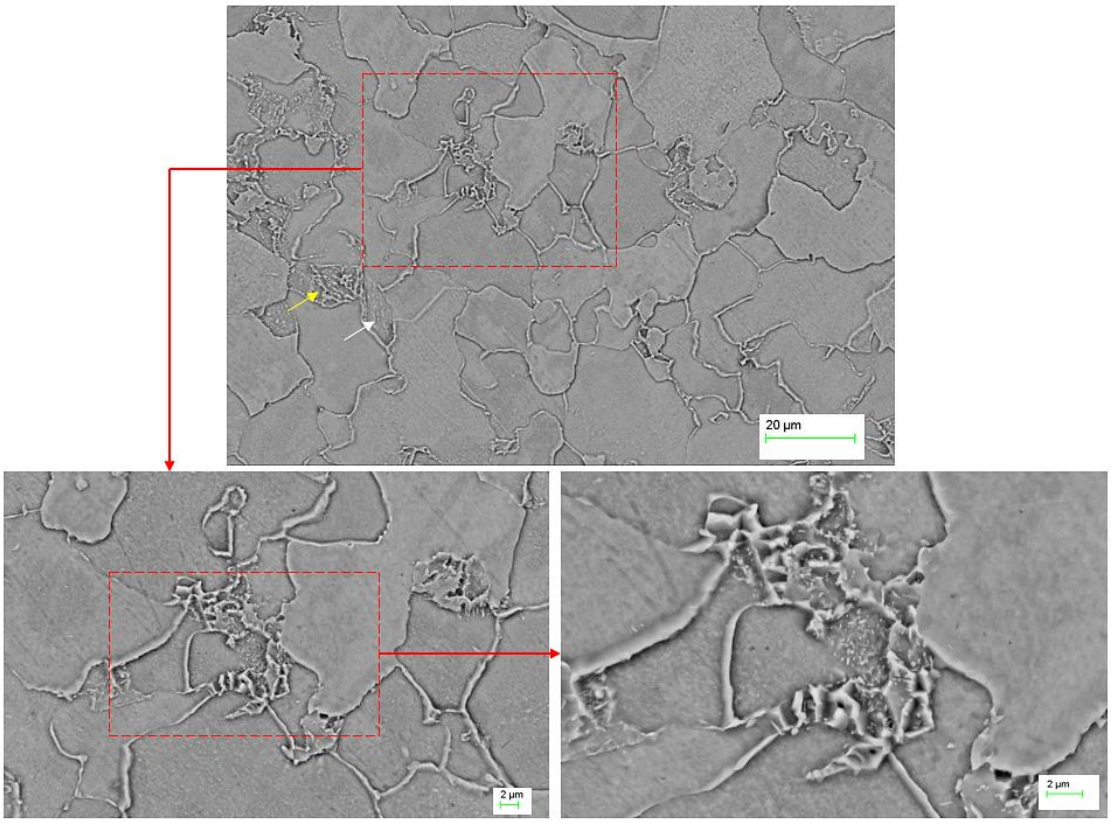

Figure 4.14 Microstructure of the virgin parent material observed with BSE at up to 5000× magnification

The EDS analysis of the virgin parent material is shown in Figure 4.15. The detected elements (Fe, Cr, Mn, Ni, and Mo) are consistent with the chemical composition of 14MoV6-3 steel.

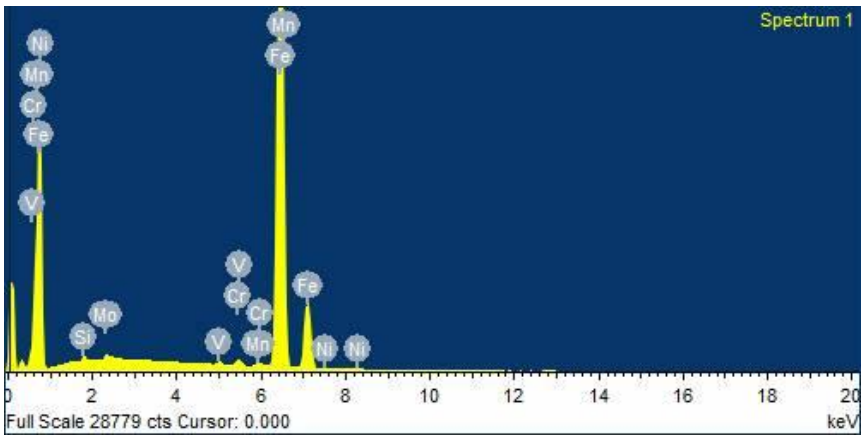

Figure 4.15 SEM EDS spectrum of the virgin parent material

Figure 4.16 shows SEM secondary electron micrographs of the virgin parent material at different magnifications. The details of the microstructural features are highlighted in the enlarged inserts.

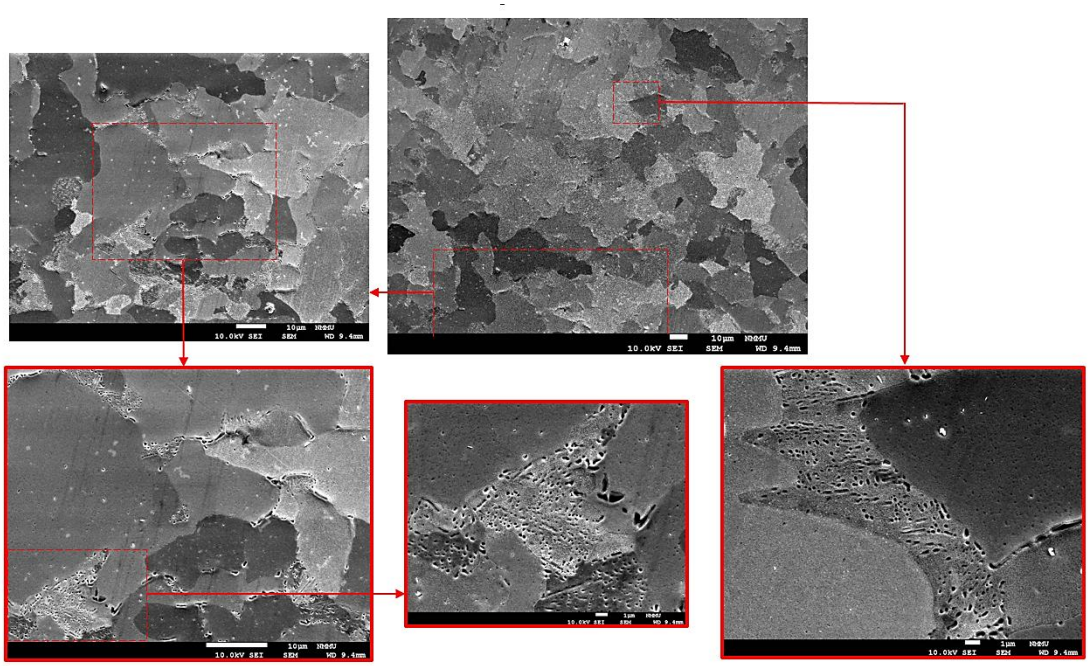

Figure 4.16 Details of microstructural features of the virgin parent material, observed with SE at up to 5000× magnification

Various microstructural features and phases are clearly distinguished in the band contrast (BC) images by differences in brightness as shown in Figure 4.17. The ferrite phase appears as a bright region, while bainite is observed as a darker, fine-grained aggregate. Dark particles along grain boundaries are identified as inclusions. The observed grain-to-grain brightness variation may be attributed to differences in crystallographic orientation (Kang, et al., 2013). The IPF_Z0 maps show grain orientations relative to the Z0 direction, corresponding to the standard unit triangle or APU. Grains exhibit a random orientation distribution, with similarly oriented grains appearing in the same colour. The Euler angle maps show grain orientations according to the Euler colour scale, where similar colours indicate similar crystallographic orientations.

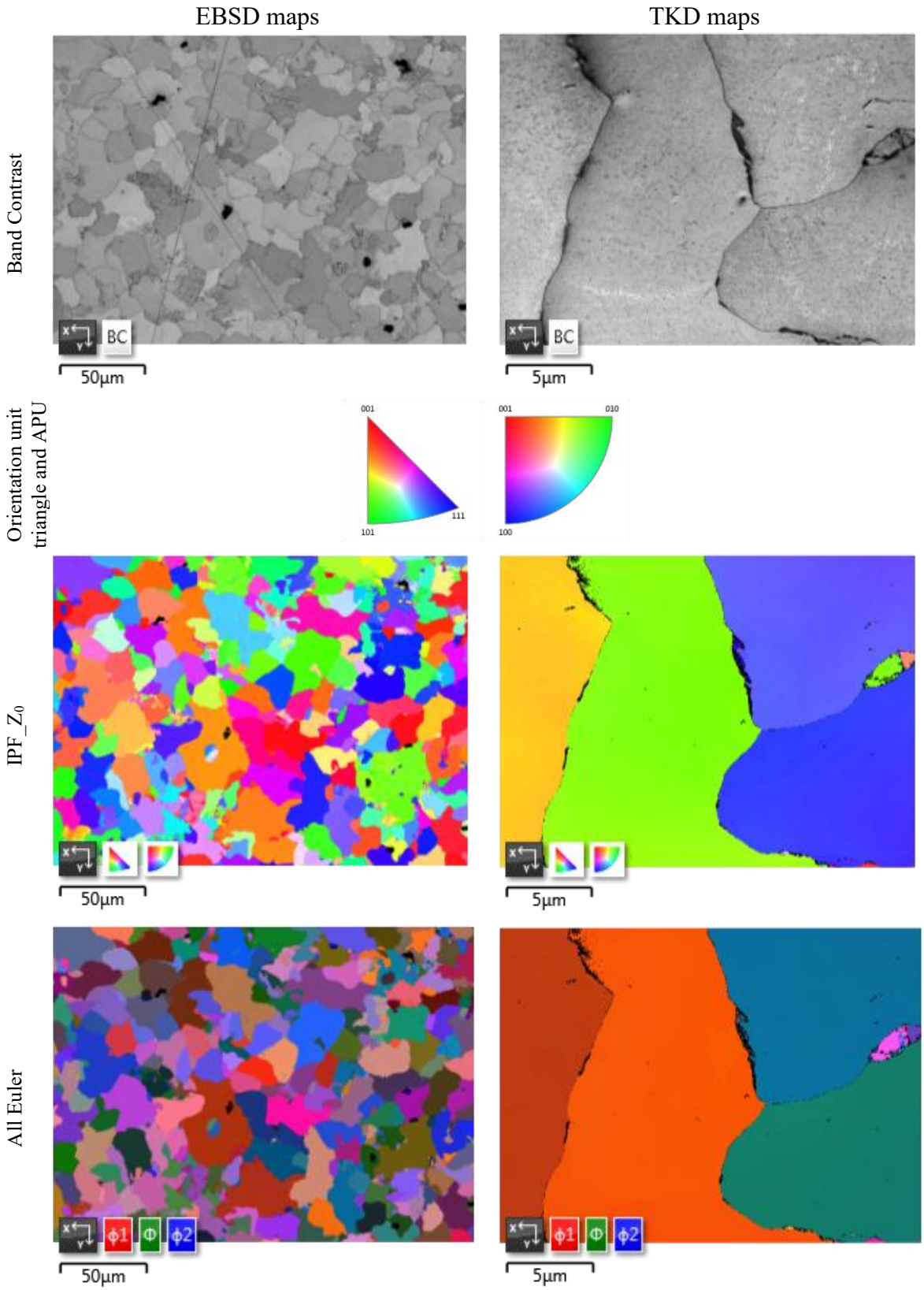

Figure 4.17 Band Contrast, Inverse Pole Figure and All Euler maps of the virgin parent material as obtained by SEM EBSD and TKD

The phase fractions determined in this analysis are shown in Figure 4.18. The observed area consists of ferrite with the Fe_3C phase along the grain boundaries.

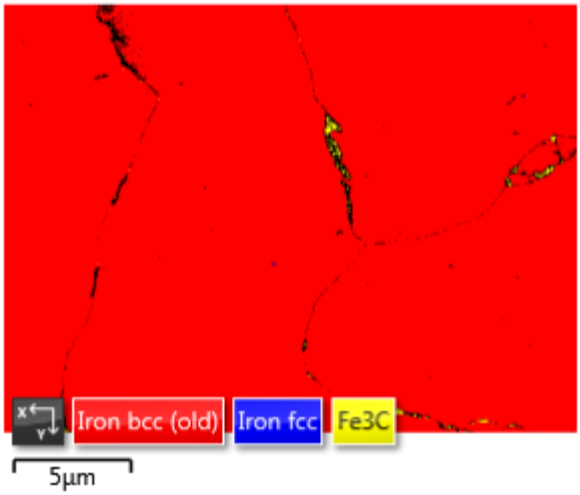

Figure 4.18 Identification of phases present on the virgin parent material by SEM TKD

4.2.5.3 Carbide Precipitation in the Virgin Parent Material

The morphology and composition analysis of carbides on the virgin parent material conducted using the FEI Quanta 600 SEM. The composition and morphology of the observed carbides and microstructure is shown in Figure 4.19. From Table 4.8, it was not possible to distinguish the composition of carbides from the matrix because of the very small size of carbides. Additionally, the morphologies could not be associated with a specific type of precipitates, aside from the general tendency to form along grain boundaries. A more detailed analysis of the composition and morphology of these carbides would require higher-resolution microscopy techniques, such as TEM.

Table 4.8 Chemical composition of the identified carbides

Element	Si	V	Cr	Mn	Fe	Ni	Cu	Mo
wt.%	0.36	0.34	0.81	0.7	96.04	0.2	0.19	1.38

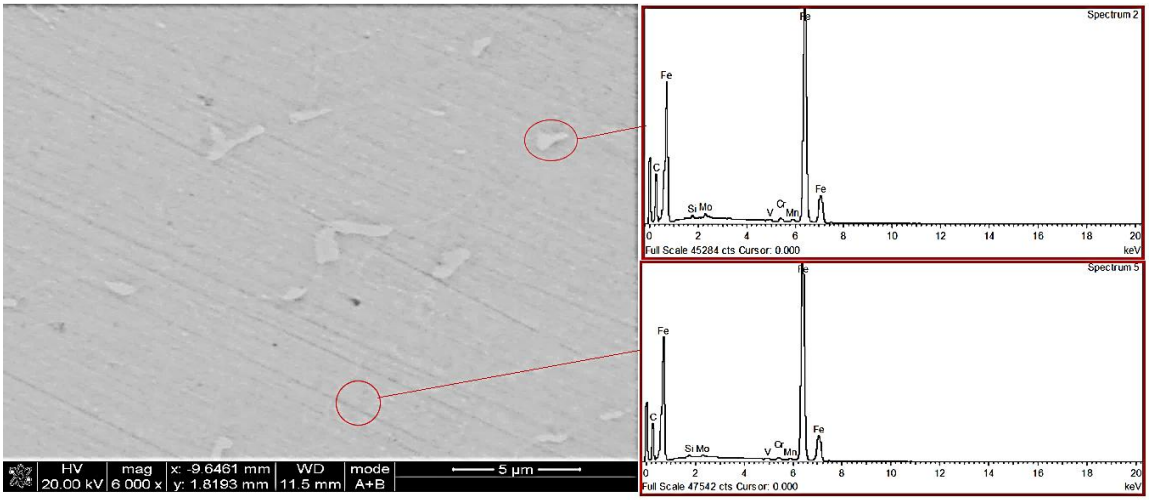

Figure 4.19 Carbide morphology and composition of the virgin parent material

4.3 Evaluation of the Service-exposed Material Behaviour

4.3.1 Assessment of Service-Exposed Parent Material

In this section, the mechanical properties and microstructural analysis of service-exposed parent material are presented.

4.3.1.1 Hardness Results

The average hardness values of the service exposed parent material are summarised in Table 4.9. The hardness of the service-exposed parent material was found to be within acceptable range of 14MoV6-3 steel despite being in service for over 200 khr (British Standards Institution, 2007). However, the hardness of the service-exposed parent material is lower than the virgin parent material. The difference in hardness between the two materials may be attributed to variations in their thermal or service history.

Table 4.9 Average hardness of the service-exposed parent material

	Hardness [HV10]			
Position	12 o'clock	3 o'clock	6 o'clock	9 o'clock
Average	**151**	**155**	**156**	**155**
Std. Dev.	3.7	3.3	2.5	5.9

The plots of hardness that was measured through the wall thickness at 12 o'clock, 3 o'clock, 6 o'clock and 9 o'clock positions are shown in Figure 4.20 to Figure 4.23. The maximum and minimum hardness values were noted at the inner surface of the pipe and located at 9 o'clock and 12 o'clock positions, respectively. However, the hardness profile of each position shows that there are no significant differences in the hardness of the outer surface and inner surface.

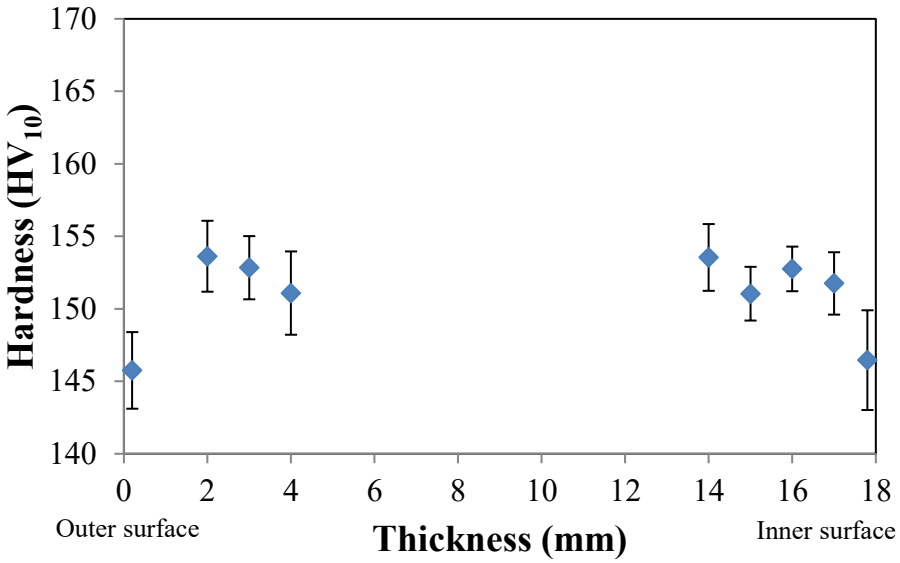

Figure 4.20 Through-wall thickness hardness profile of service-exposed 14MoV6-3 at 12 o'clock

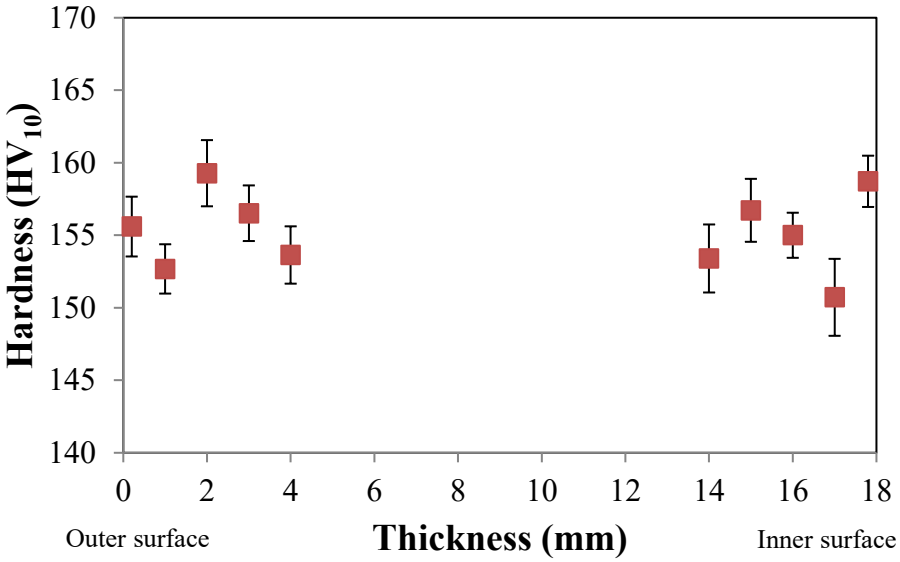

Figure 4.21 Through-wall thickness hardness profile of service-exposed 14MoV6-3 at 3 o'clock

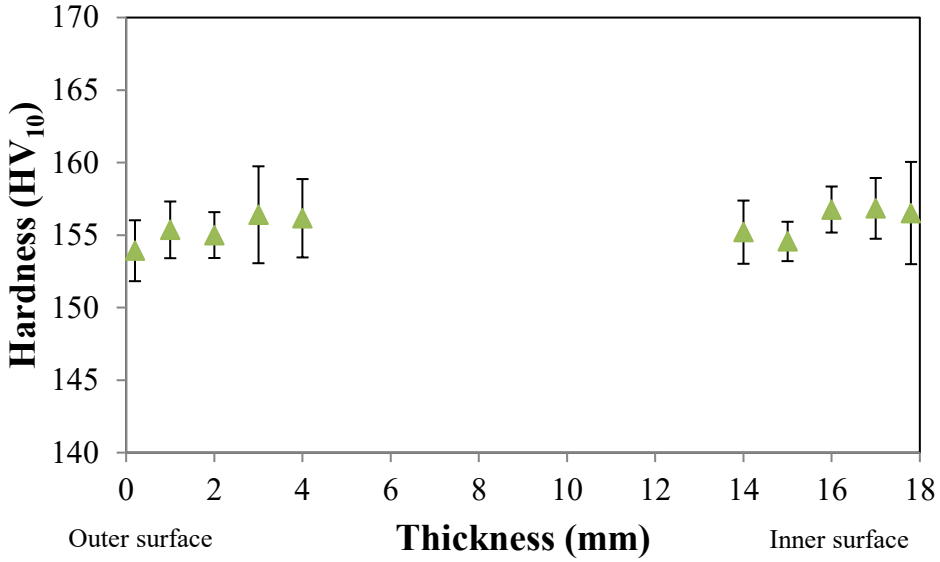

Figure 4.22 Through-wall thickness hardness profile of service-exposed 14MoV6-3 at 6 o'clock

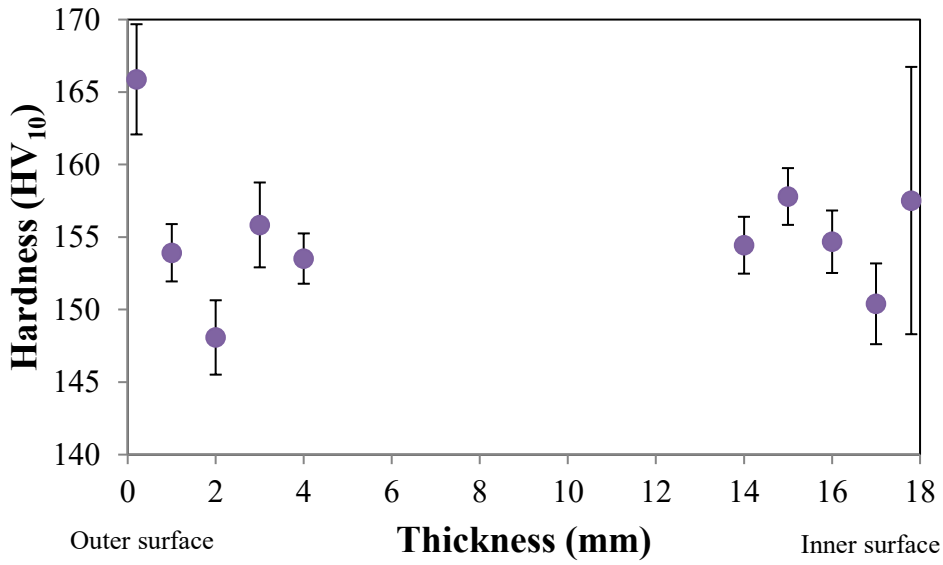

Figure 4.23 Through-wall the thickness hardness profile of service-exposed 14MoV6-3 at 9 o'clock

The distribution of the measured hardness values is shown in Figure 4.24. The hardness varied from 139 to 182 HV10 through the pipe wall thickness and around the pipe circumference.

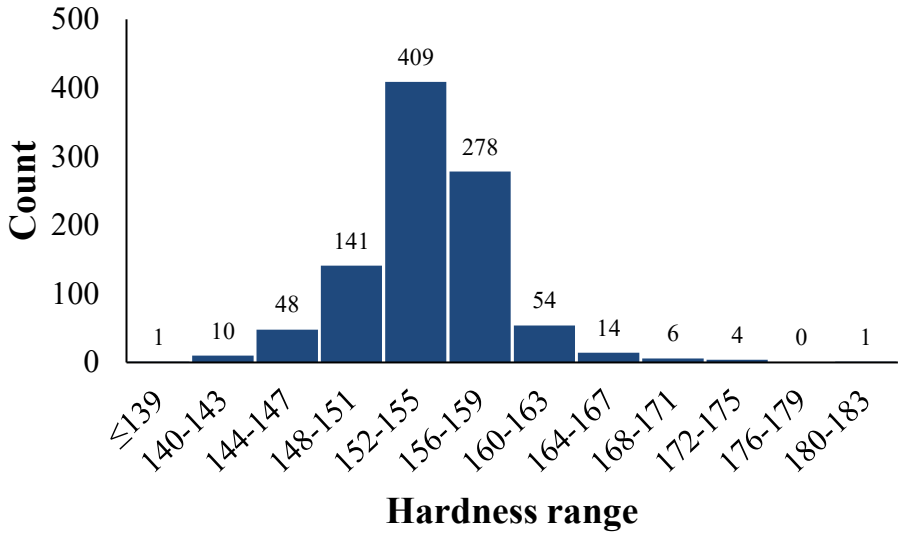

Figure 4.24 Through-wall thickness hardness range of the service-exposed parent material

4.3.1.2 Room Temperature Tensile Properties

The room temperature tensile properties of the service-exposed parent material are shown in Table 4.10. The tensile properties are within the acceptability criteria of BS EN 10216-2 (British Standards Institution, 2007). However, the yield strength and ductility values fall within the lower bound of the acceptable values of 14MoV6-3 steel and are lower than the tensile properties of the virgin parent material. The difference in material properties may be explained as the deterioration of mechanical properties due to long-term service under creep conditions. The service-exposed parent material has YT ratio of 0.6 at room temperature.

Table 4.10 Room temperature tensile properties of service-exposed parent material

Test Temperature [°C]	Yield Strength [MPa]	Tensile Strength [MPa]	Elongation [%]	Reduction in Area [%]
23	326	516	30	47
Std. Dev.	7.5	2.4	1.64	1.09

The fracture surface of the service-exposed parent material tested at room temperature is shown in Figure 4.25(a). The fracture surface exhibited a dimpled topography, which is characteristic of ductile fracture. Additionally, small sulphur-containing inclusions were

observed on the fracture surface. The EDS analysis shown in Figure 4.25(b) confirmed the presence of (Fe, Mn)S inclusions.

(a)

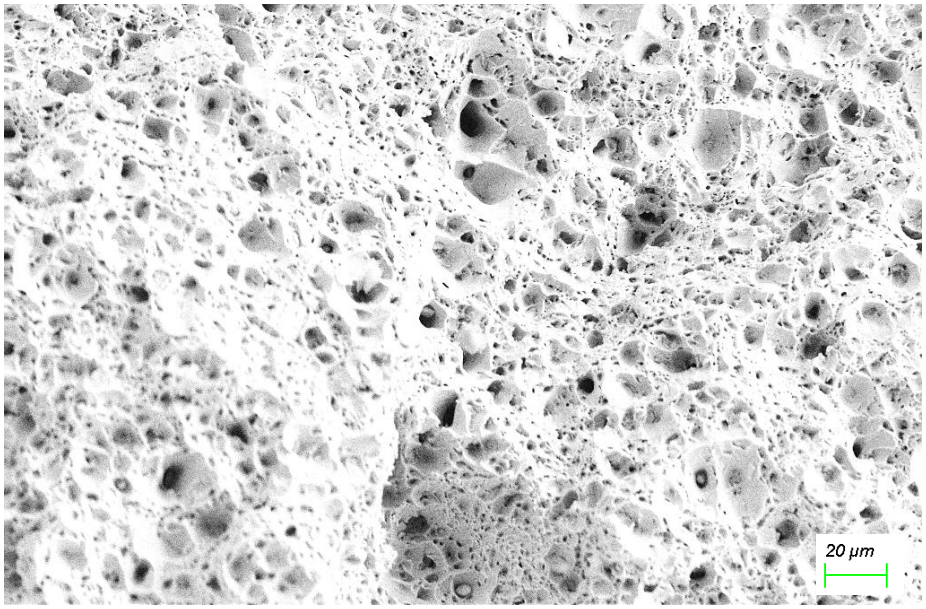

(b)

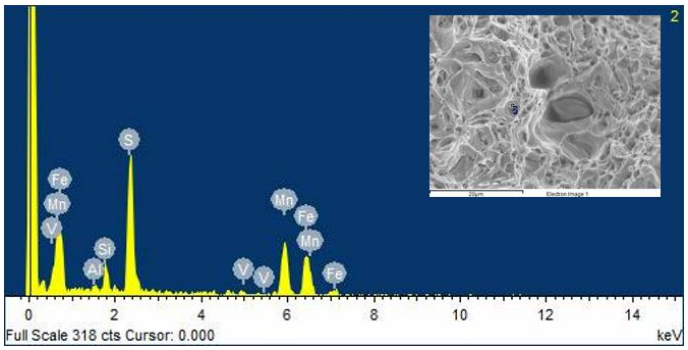

Figure 4.25 Typical fracture surface appearance of the service-exposed parent material (room temperature specimen) under SEM (a) and EDS analyses of inclusions and microvoids (b).

4.3.1.3 Elevated Temperature Tensile Properties

The tensile properties of the service-exposed parent materials at 500°C, 540°C and 560°C are presented in Table 4.11. The yield strength was 223 MPa and 190 MPa at 500°C and 560°C, respectively. The yield strength values are within the minimum requirements specified for steel 14MoV6-3 at elevated temperatures (British Standards Institution, 2007). Representative stress-strain curves corresponding to high temperatures are shown in Figure 4.26. The results demonstrate a clear temperature dependence of the tensile properties, which is typical for low-alloy steels.

Table 4.11 Elevated temperature tensile properties of service-exposed parent material

Test Temperature [°C]	Yield Strength [MPa]	Tensile Strength [MPa]	Yield-Tensile Ratio	Elongation [%]	Reduction in Area [%]
500	223	330	0.68	27	79
540	200	282	0.71	33	82
560	190	257	0.74	31	84

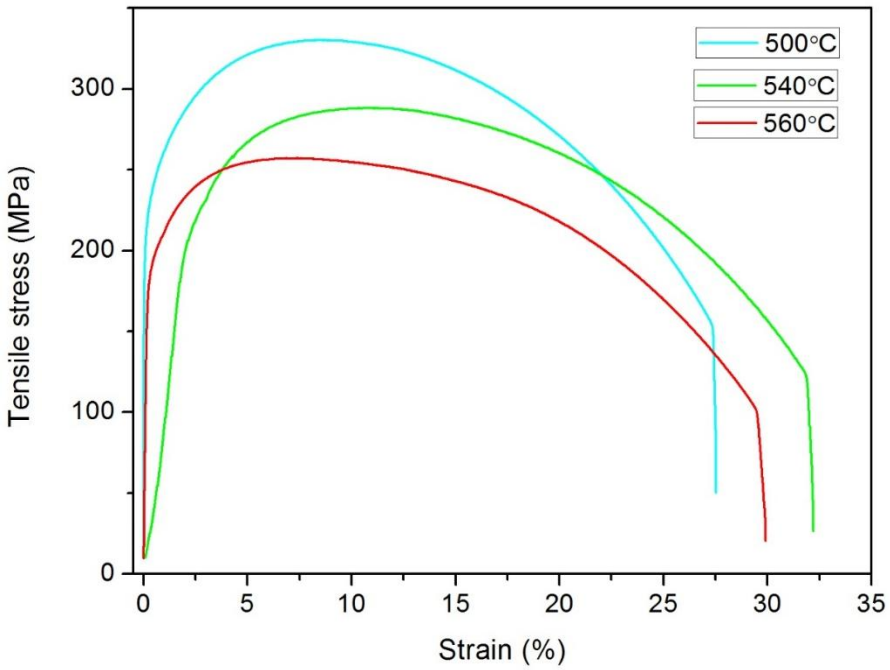

Figure 4.26 Typical stress-strain plot of the service-exposed parent material at elevated temperature

The variation in YS, UTS and YTR as a function of temperature for the service-exposed parent material is shown in Figure 4.27(a). A reduction in strength is observed with increasing temperature, with the most notable decline occurring in the UTS. Despite this, both YS and UTS exhibit a similar downward trend, consistent with the expected behaviour of low-alloy steels at elevated temperatures.

The YTR remains relatively stable between 500 °C and 540 °C, but shows a noticeable increase at 560 °C. This shift may suggest an increased susceptibility to plastic deformation under conditions of elevated temperature and loading beyond design specifications.

Nonetheless, the material demonstrates good ductility across the tested temperature range, as illustrated in Figure 4.27 (b). The reduction in area increases with temperature, indicating

enhanced plasticity. Elongation shows a sharp increase between 500 °C and 540 °C, followed by a slight decrease at 560 °C.

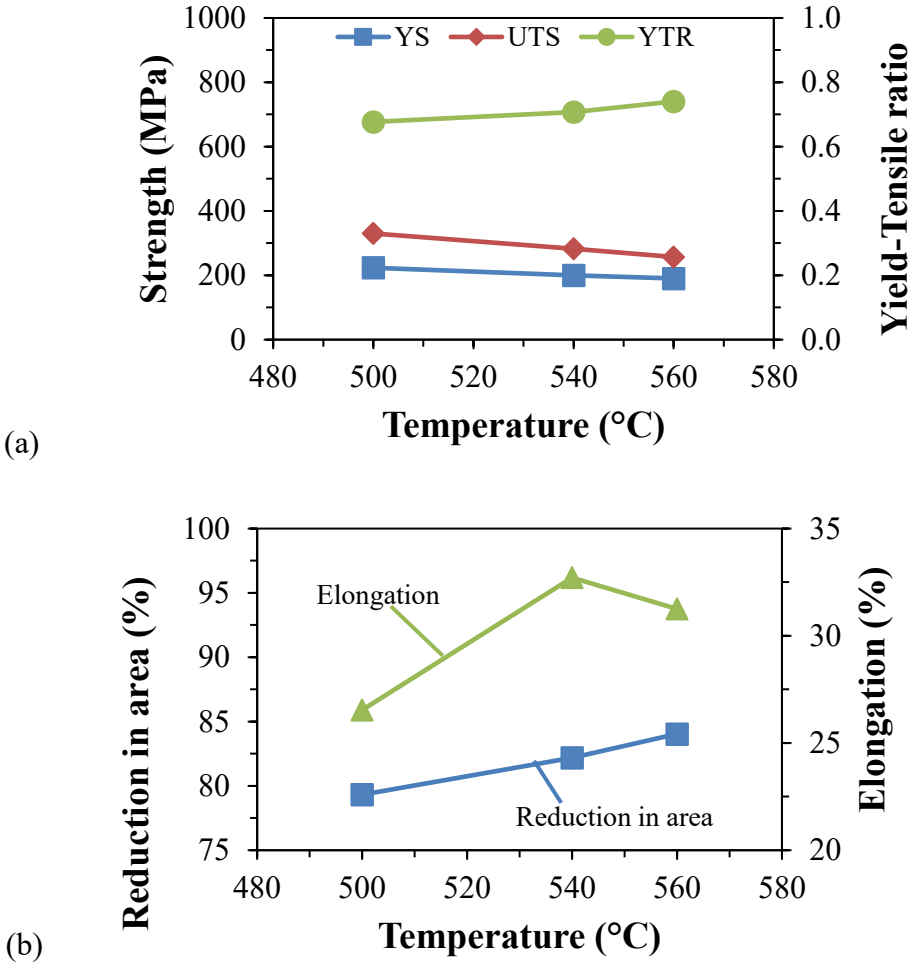

Figure 4.27 (a) Variation of Yield strength, UTS and Yield-Tensile ratio as a function of temperature. (b) Variation of reduction in area and elongation with temperature.

The correlation between the YT ratio and ductility parameters (elongation and reduction in area) is shown in Figure 4.28. A slight increase in ductility of approximately 4% is observed in the service-exposed parent material as the YT ratio increases. A similar trend was also observed in the virgin parent material.

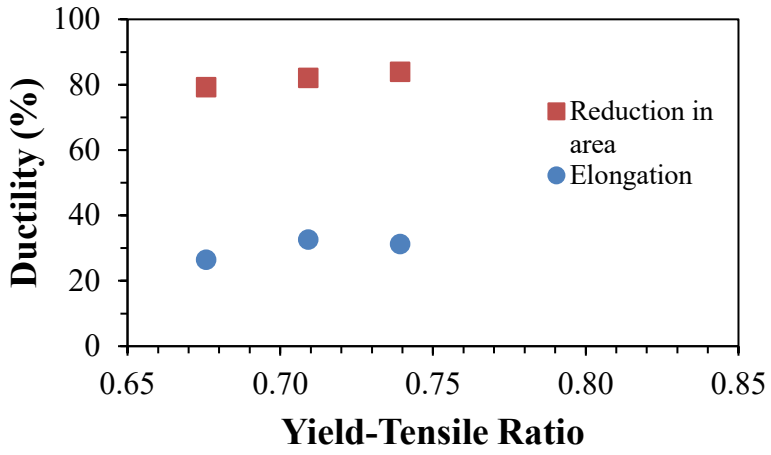

Figure 4.28 Yield-Tensile ratio versus ductility at elevated temperature

The variation of Young's modulus with temperature is estimated from the stress–strain data, with results shown in Figure 4.29. The Young's modulus decreases with increasing temperature, and the behaviour is consistent with typical material behaviour at elevated temperatures. A similar temperature dependence was observed in the virgin parent material. However, it was noted that the Young's modulus of the service-exposed parent material was consistently higher than that of the virgin material at all test temperatures.

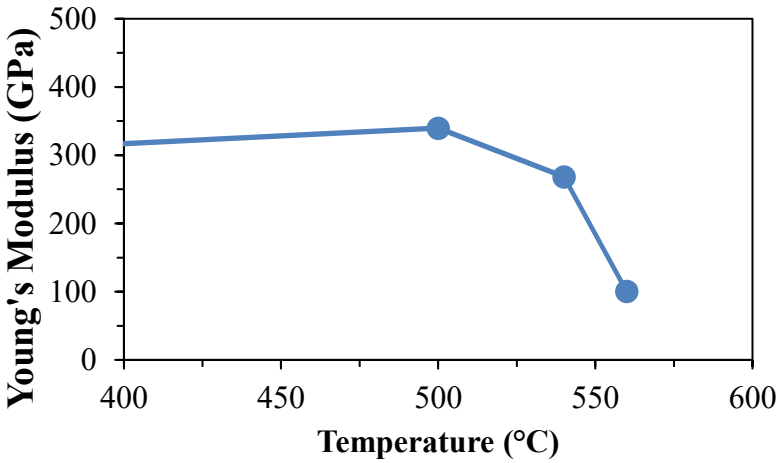

Figure 4.29 Variation of the Young's modulus as a function of temperature

Figure 4.30 shows the SEM fracture surface and the composition of inclusions observed on the service-exposed parent material. The fracture surface is characteristic of ductile fracture, exhibiting numerous small equiaxed dimples.

(a)

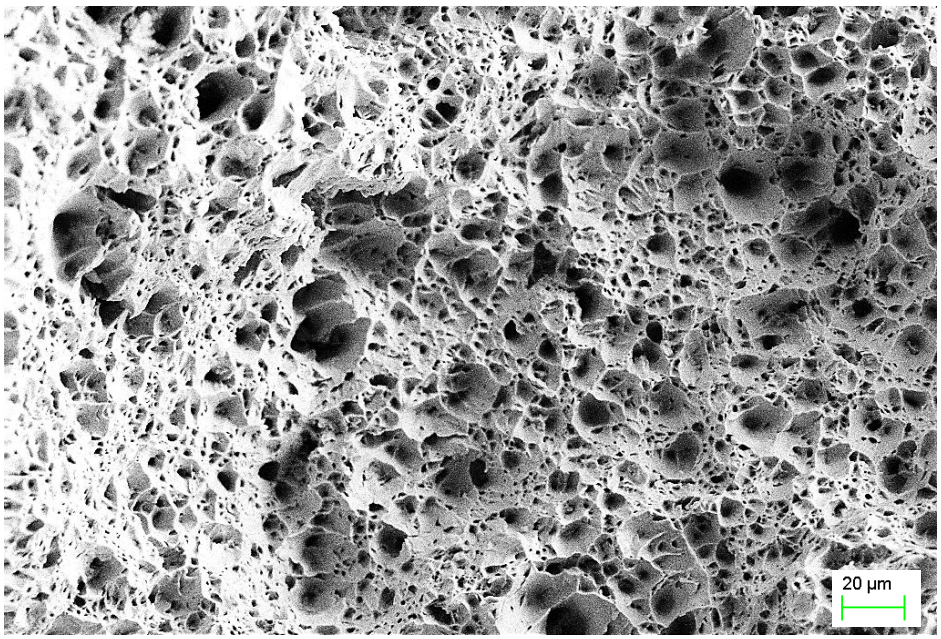

(b)

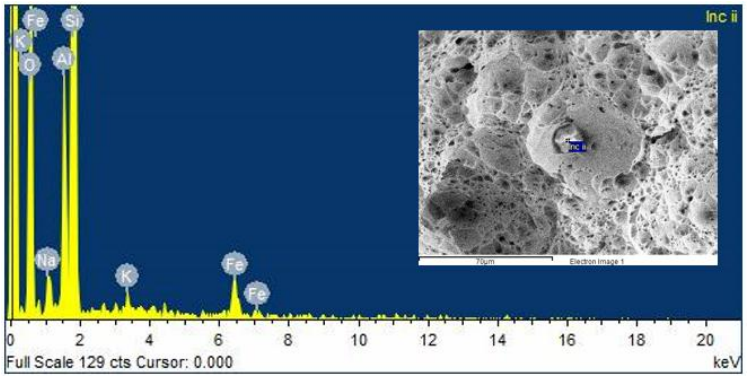

Figure 4.30 Typical fracture surface appearance of the service-exposed parent material elevated temperature specimens tested at 540°C under SEM (a) and EDS analyses of inclusions and microvoids (b).

4.3.1.4 Impact Properties

Table 4.12 presents the absorbed impact energy of the service exposed parent material at -30°C, 0°C, 20°C, 23°C, 50°C, 100°C and 200°C. The average absorbed energy at room temperature is significantly lower than the minimum specified for 14MoV6-3 steel (British Standards Institution, 2007). Moreover, at -30°C, 0°C, 20°C, and 50°C the impact properties of the service-exposed material were deemed unacceptable. At these temperatures, the energy required for crack initiation was comparable to that for crack propagation. This is an indication that samples were fractured with minimal resistance, which is characteristic of a brittle fracture.

This poses a potential risk during boiler start-up operations, particularly if the pipework is subjected to high dynamic loads, such as water hammer, at temperatures below 100°C. In contrast, specimens tested at 100°C and 200°C fractured in a ductile manner, exhibiting acceptable levels of absorbed energy.

Additionally, it is evident that the energy associated with crack initiation does not vary significantly with temperature, indicating that it is primarily influenced by the local stress conditions at the crack tip. This behaviour was also observed in the virgin parent material.

Table 4.12 Impact properties of service-exposed parent material at different temperatures

Test temperature [°C]	Total absorbed energy [J]	Energy required for crack [J]	
		Initiation	Propagation
-30	3	2	1
0	6	3	3
20	12	6	6
23	12	6	7
50	38	23	15
100	137	22	115
200	173	36	137

A plot of the maximum load that was recorded at temperatures of -30°C, 0°C, 20°C, 50°C, 100°C and 200°C is shown in Figure 4.31. A noticeable change in the load required to fracture the samples was observed with varying testing temperature, indicating a transition temperature between 50°C and 100°C.

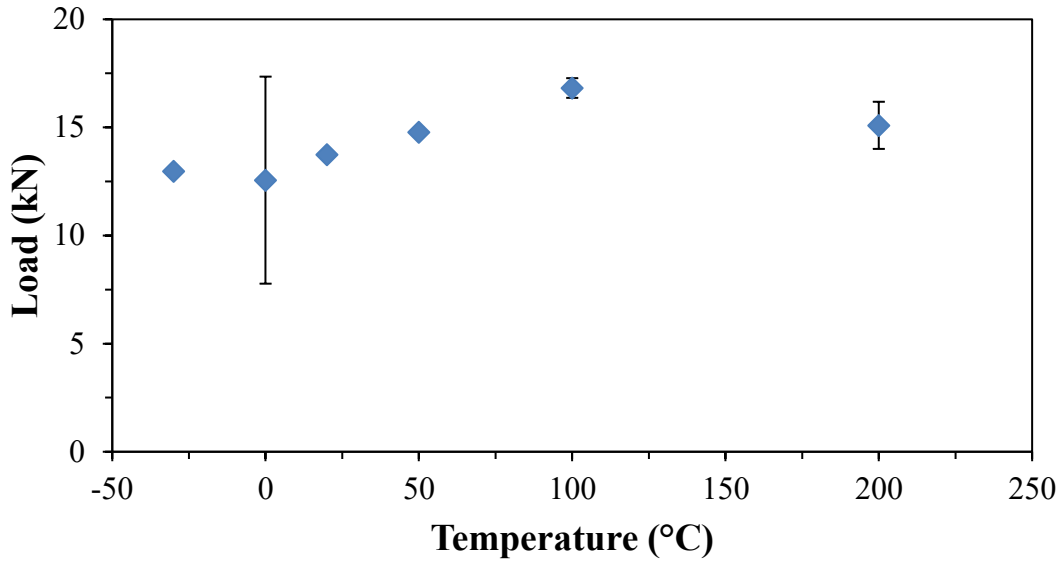

Figure 4.31 Maximum load as a function of temperature for the service-exposed parent material

The SEM fracture surface of the service-exposed parent material specimens tested at -30°C, 0°C, 20°C, 50°C, 100°C and 200°C are shown in Figure 4.32. The specimens tested at temperatures of -30°C, 0°C, and 20°C exhibited flat fracture surfaces with a crystalline appearance (granular), which is indicative of brittle fracture. At 50°C, the fracture surfaces began to show a mixed mode fracture appearance. Fracture mode transitioned from brittle to ductile shear fracture when the temperature increased, this was evidenced by a reduction in the granular (cleavage) area and an increase in lateral contraction at the notch in specimens tested at 100°C and 200°C. Based on the fracture surface observations, the fracture appearance transition temperature (FATT) is estimated to be between 50°C and 100°C.

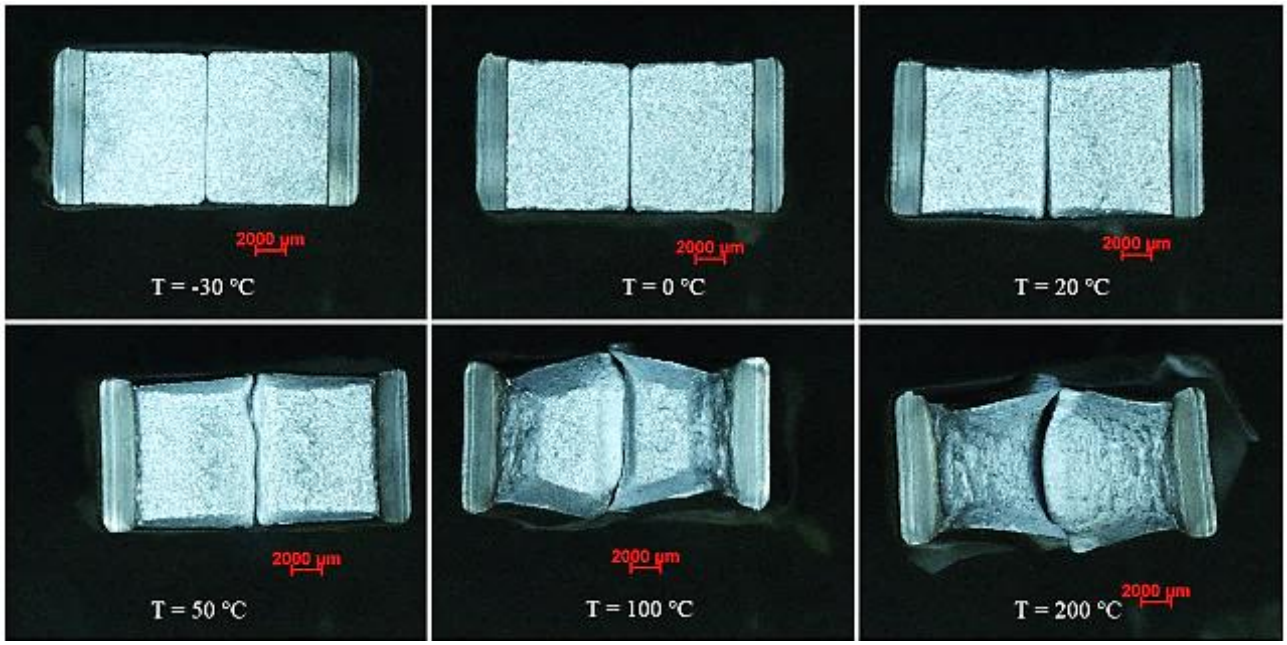

Figure 4.32 Fracture surface appearance of the service-exposed parent material specimens at various temperatures

Figure 4.33 shows the DBTT of the service-exposed parent material evaluated against impact energy (a), percentage of shear fracture (b) and lateral expansion (c). From the impact energy curve in Figure 4.33(a), the DBTT is approximately 75°C, corresponding to an absorbed energy of about 80 J. The lower and upper-shelf transition temperatures are observed at 12J and 163J, occurring at 20°C and 125°C, respectively. The transition temperature corresponding to an absorbed energy of 27 J is estimated at ~41°C. Figure 4.33 (b) shows that the fracture appearance transition temperature (FATT) was estimated at approximately 75°C. Similarly, the lateral expansion vs. temperature curve in Figure 4.33(c) indicates a DBTT of ~75 °C, with lower- and upper-shelf transition temperatures estimated at approximately -11 °C and 150 °C, respectively.

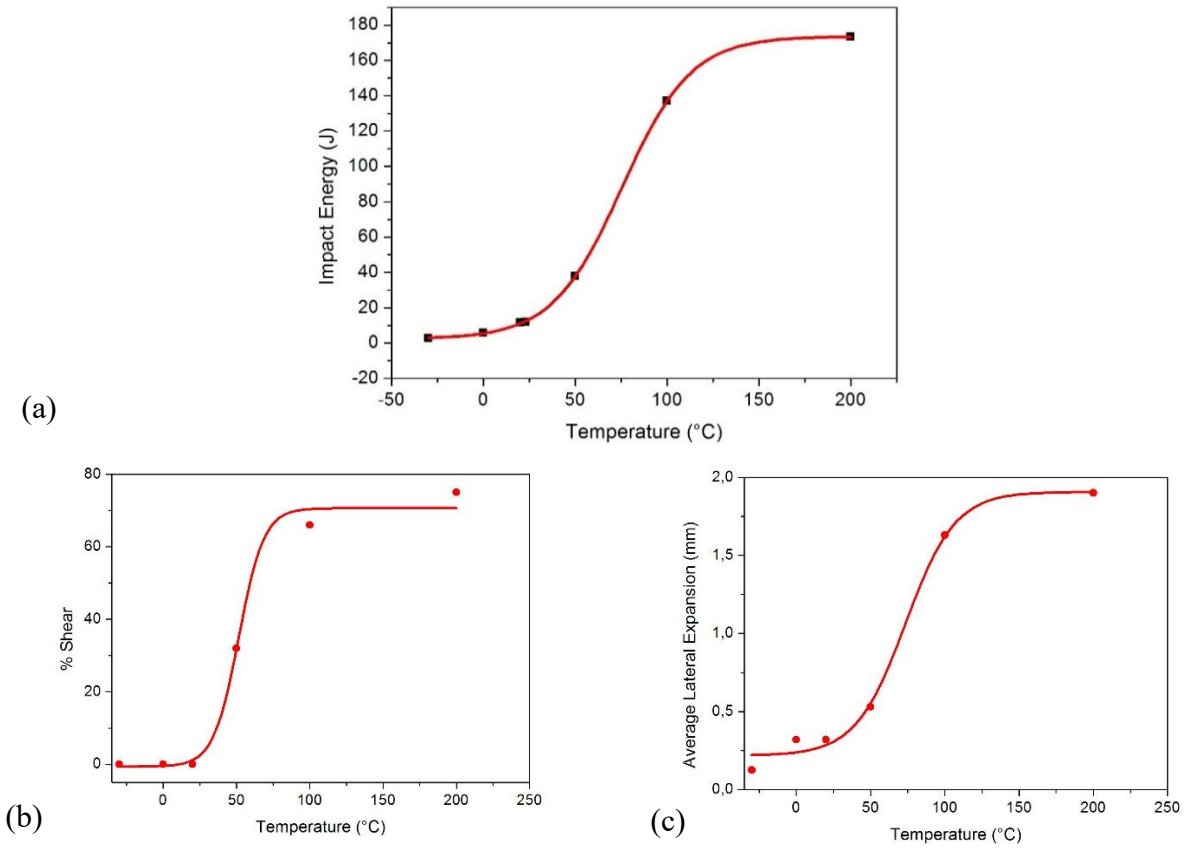

Figure 4.33 Ductile-Brittle Transition Temperature of service-exposed parent material evaluated against (a) impact energy, (b) percentage of shear fracture and (c) lateral expansion

4.3.1.5 General Microstructure of the Service-Exposed Parent Material

This section presents the microstructural analysis of the service-exposed parent material. Optical microscopy and scanning electron microscopy (SEM) were employed to characterise the microstructure. In addition, detailed SEM results of carbides formed during long-term service under creep conditions are presented.

4.3.1.5.1 Optical Microscopy Analysis

The microstructures of the service-exposed parent material are shown in Figures Figure 4.34 and Figure 4.35. The microstructure exhibits signs of prolonged exposure to high temperature and creep. The microstructure consists predominantly of ferrite containing fine carbides (FC) withing the grains and large carbides (LC) along the grain boundaries. The bright regions correspond to ferrite grains, while the grey regions represent a mixed phase of ferrite and pearlite or bainite. The dark areas are identified as iron-carbon carbide (M_3C). Both clustered and isolated inclusions are observed throughout the microstructure, as indicated in the micrographs. Additionally, occasional voids that are fewer than 50 voids/mm² are distributed

across the wall thickness of the service-exposed parent material. The observed damage, primarily at grain boundaries, is characteristic of creep degradation.

Table 4.13 shows the average grain size and phase fraction (%area) of the service-exposed parent material as estimated with the ImageJ software. From the results, it can be noted that the average grain size for the service exposed material is 8.8 µm. The phases are categorised according to level of brightness.

Table 4.13 Average grain size of service-exposed parent material calculated with the lineal intercept method

Line Length [µm]	Average No. of intercepts	Average grain size [µm]	ASTM grain size number [G]	Ferrite/Mixed/Carbide phase fraction [%]
400	45	8.8	10.5	15/53/32

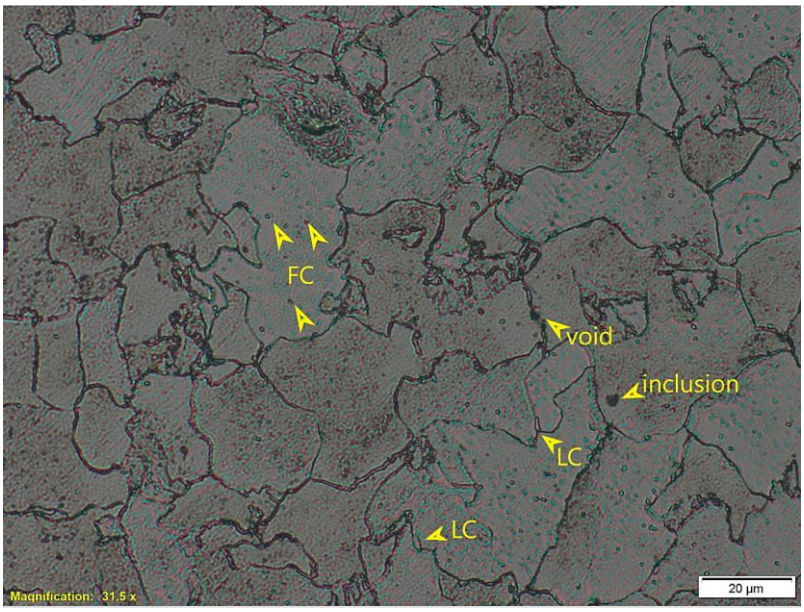

Figure 4.34 Microstructure of the service-exposed parent material etched with 3% nital, showing fine and large carbides visible at 500×

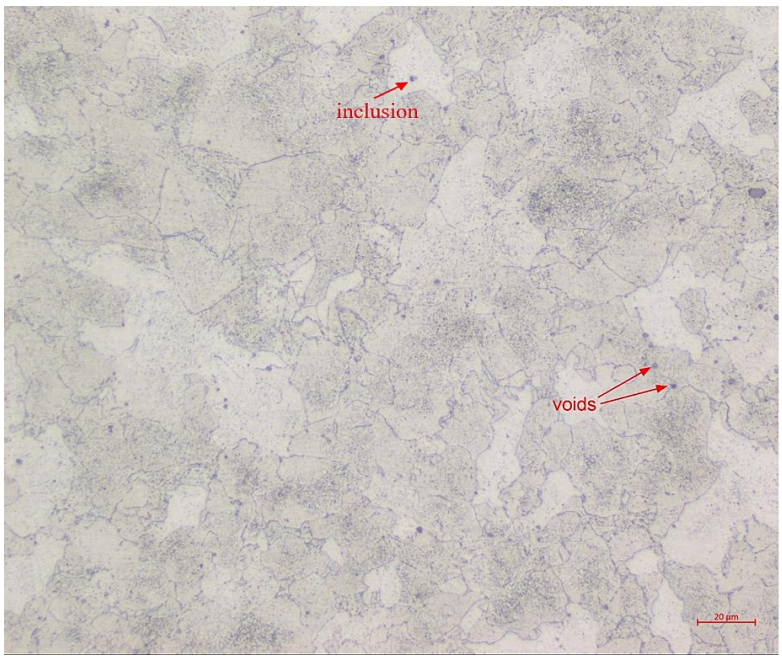

Figure 4.35 Microstructure of service-exposed parent material etched with 5% nital, showing creep voids and inclusions

Figure 4.36(a) shows a replica micrograph of the service-exposed parent material, in which creep voids and inclusions are clearly distinguishable. Creep voids appear as darker features with a globular morphology, predominantly located along grain boundaries. In contrast, inclusions that are removed are brighter and often surrounded by a thick, dark boundary. Both fine and large carbides are also visible in the replica micrographs. There was no evidence of void linkage or micro-cracking in any of the replicated areas.

The micrograph of the service-exposed parent material was processed using ImageJ by converting it to a binary image and applying a threshold to facilitate void size analysis, as shown in Figure 4.36(b). Selected creep voids are highlighted in red. The analysed area was approximately 0.06 mm². Void sizes ranged from 0.5 µm to 2 µm, with an average diameter of 1.3 ± 1 µm. The estimated void density was approximately 32 voids/mm². This level of creep damage corresponds to an exhaustion degree of t/tr ≈ 0.4–0.6, aligning with Class 4-A/1 of the classification model proposed by Dobrzański et al. (2011), which is characterised by isolated voids along grain boundaries.

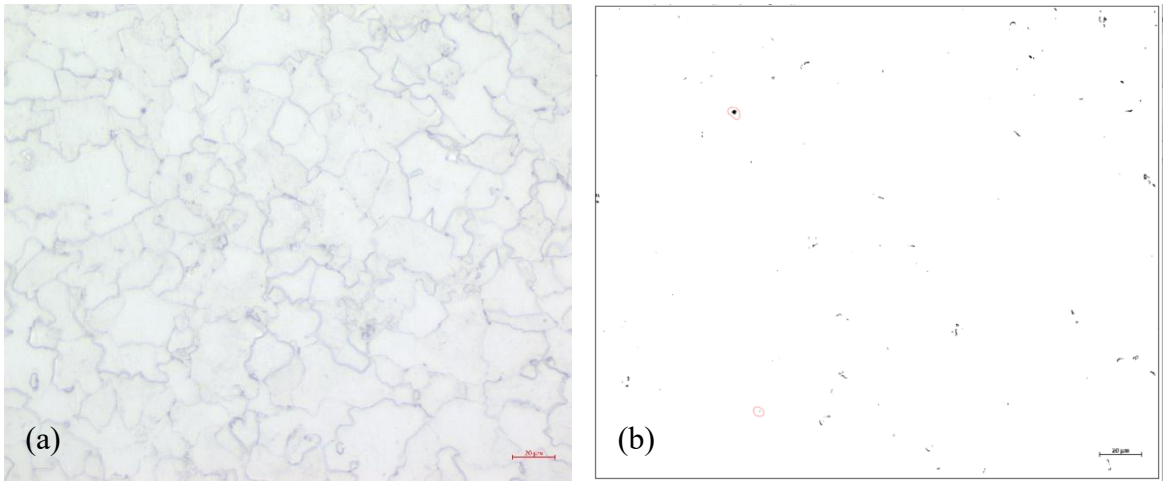

Figure 4.36 Micrograph of the service-exposed parent material replica and the corresponding threshold image.

4.3.1.5.2 Scanning Electron Microscopy Analysis

The SEM microstructure of the service-exposed parent material is shown in Figure 4.37. From the microstructure large carbides can be seen along the grain boundaries and finely dispersed particles dispersed within the grains. The bainite/pearlite areas exhibit significant decomposition as a result of service exposure. Scattered micro voids are observed at the grain boundaries as indicated by white arrow. Inclusions indicated by orange arrow were noted within the grains.

According to the classification proposed by Dobrzanski et al. (2011) for microstructural degradation in ½Cr-½Mo-¼V steels under creep conditions, the observed microstructure corresponds to Class 4-A/1. The class is defined by the presence of single voids along ferrite grain boundaries with an exhaustion degree of 0.4 to 0.6. However, the observed microstructural features are similar to class 1 (150–160 HV10), which is also correlated by the hardness results discussed earlier in Section 4.3.1.1. Class 1 microstructures are characterised by partially decomposed bainite/pearlite, with coagulated M_3C precipitates of varying sizes, fine MC carbide precipitates within ferrite grains, and chains of $M_{23}C_6$ carbides along the ferrite grain boundaries. Components that have an exhaustion degree of 0.4 to 0.6 show a strong microstructural degradation of M_3C, MC, $M_{23}C_6$ and sometimes M_2C and M_7C_3 precipitates.

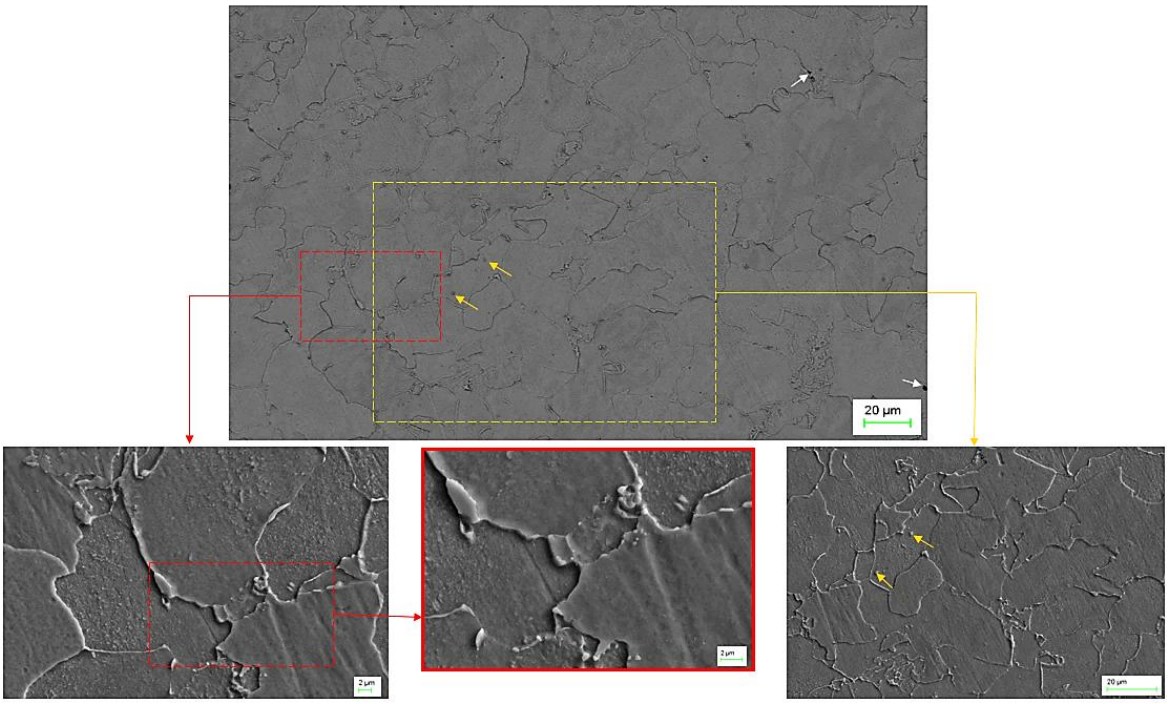

Figure 4.37 Microstructure of the service-exposed parent material with some details of microstructural features

The EDS analysis of the service-exposed parent material shown in Figure 4.38 is in good agreement with the chemical composition of 14MoV6-3 steel.

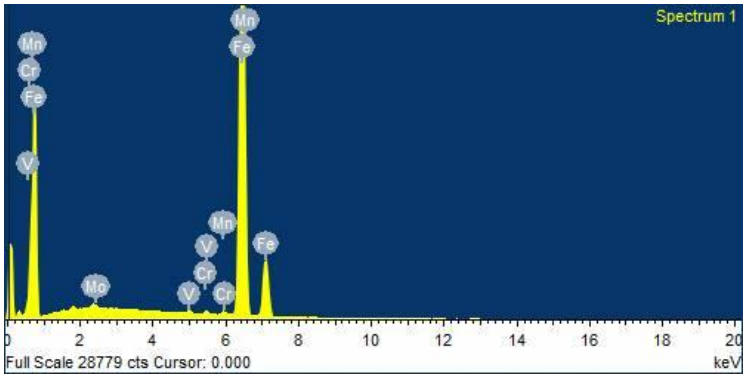

Figure 4.38 SEM EDS spectrum of the service-exposed parent material

4.3.1.5.3 Carbide Precipitation in the Service-Exposed Parent Material

The morphology and composition analysis of carbides on the service-exposed parent material was carried out using the FEI Quanta 600 SEM. The composition and morphology of the observed carbides and microstructure are shown in Figure 4.39. Large and small carbide precipitates were observed along the grain boundaries. These precipitates are characteristic of iron carbide (Fe, Cr, Mn, Mo, etc.)$_3$C and molybdenum-rich (Fe, Mo, Mn, Cr)$_{23}$C$_6$ carbide.

The formation of carbide $(Mo)_2C$, is unlikely due to the relatively high amounts of other elements. Mo_2C carbides are occasionally present in low alloy steels with life fraction of 0.2 to 0.6 and are known to cause secondary hardening, which improves creep strength in low alloy steels. The M_3C carbides appear relatively large and irregular in shape and are located along the grain boundaries. $M_{23}C_6$ carbides were also observed at the grain boundaries and typically exhibited an elongated morphology. Creep voids were observed in the microstructure, as indicated by the orange arrows. Additionally, the analysis revealed the presence of sulphur-rich inclusions, shown in Figure 4.40. Inclusions were identified as manganese sulphides (MnS).

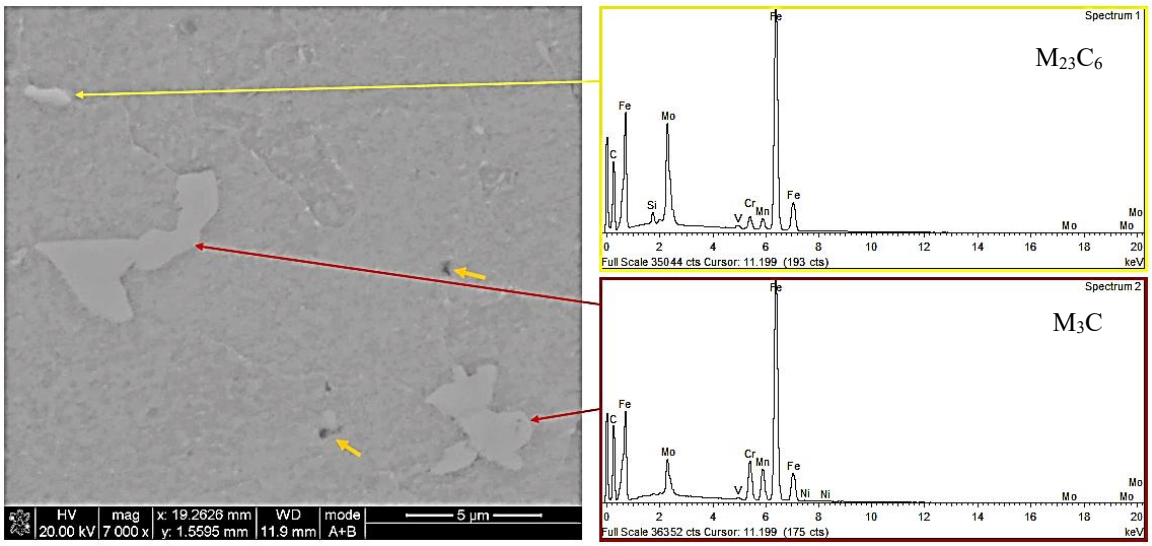

Figure 4.39 Carbide morphology and composition of the service-exposed parent material

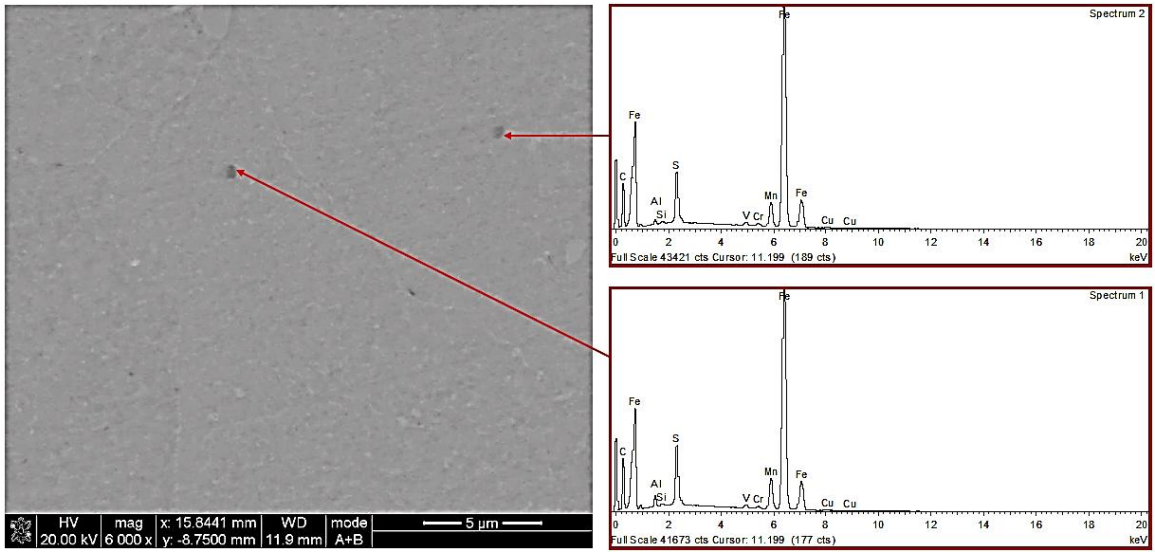

Figure 4.40 Sulphur-containing inclusions observed on the service-exposed parent material

4.3.2 Assessment of Service-exposed Weldment/Weld-joint

In this section, the mechanical properties and microstructure of the service-exposed weldment are discussed. The weldment includes the weld metal, HAZ and the parent material adjacent to the HAZ. The mechanical properties and microstructure of the weld metal, HAZ and parent material were assessed either individually or as weldment unit. The weldment experienced fabrication process related temperatures and the service temperatures.

4.3.2.1 Hardness of the Service-exposed Weldment

4.3.2.1.1 Hardness (HV_{10}) Results

Vickers hardness testing (HV_{10}) of the service-exposed weldment was carried out in the same manner as the service-exposed parent material. Measurements were taken across the surface of the weldment to include the HAZ, weld metal and the parent material for both upstream and downstream butt weld, and through the pipe wall thickness. The average hardness results are summarised in Table 4.14. The average hardness results are within the acceptable hardness range of 14MoV6-3 steel, although the upper bound values fall outside the acceptability criteria of BS EN 10216-2 (British Standards Institution, 2007). Noticeably, the average hardness data is symmetrical on opposite sides of the pipe.

Table 4.14 Through-wall thickness hardness profile measured on the service-exposed weld joint

	Hardness (HV_{10})			
Position	12 o'clock	3 o'clock	6 o'clock	9 o'clock
Range	153 – 245	148 – 227	146 – 234	148 – 245
Average	**186**	**174**	**181**	**175**
Std. Dev.	24.1	19.3	21.8	19.3

The hardness profiles of the service-exposed weldments are shown in Figure 4.41. The lowest hardness values were recorded in the parent material, while the highest hardness values were measured adjacent to the fusion line, corresponding to the coarse-grained heat affected zone (CGHAZ). The hardness in the CGHAZ exceeds the recommended values for the 14MoV6-3 parent material.

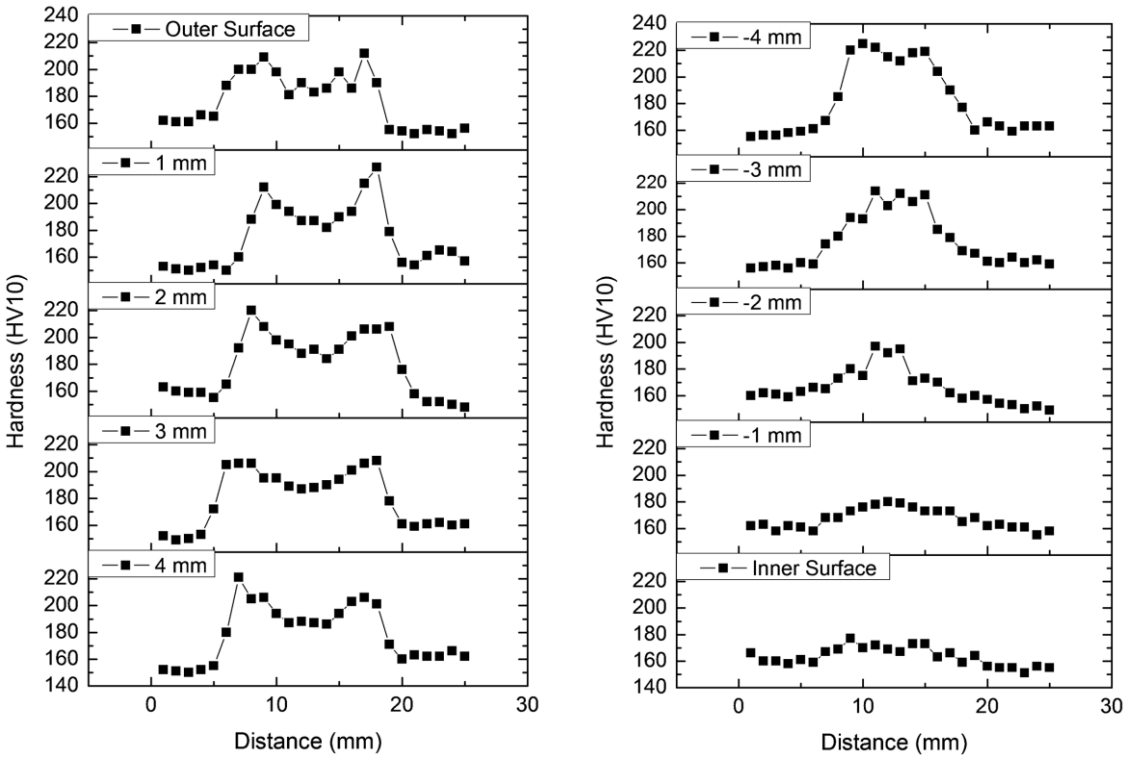

Figure 4.41 Typical hardness profile of the service-exposed weldment, measured across the weld joint and through the pipe wall thickness

Figure 4.42 shows the distribution of the hardness measurements recorded in the service-exposed weldment. The hardness measurements varied from 146 to 245 HV_{10} across the weldment, through the pipe wall thickness and around the pipe circumference. The skewed distribution of the hardness values is indicative of the hardness gradient observed across the weldment.

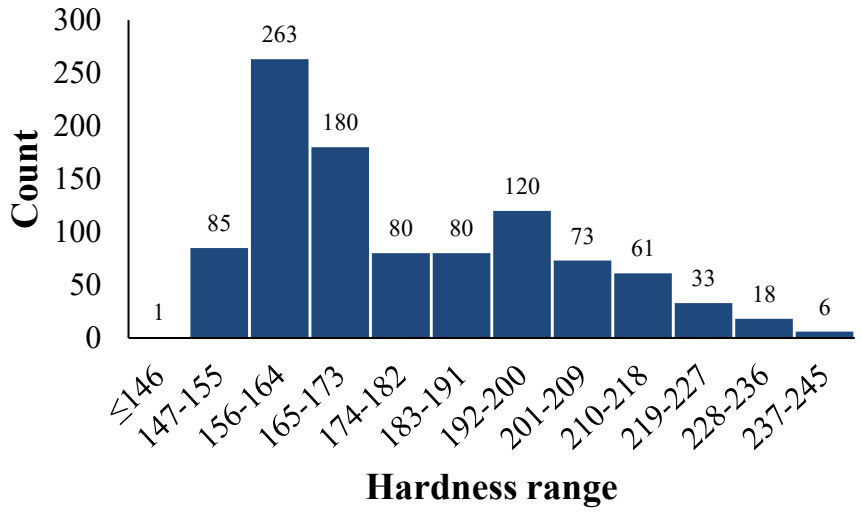

Figure 4.42 Through-wall thickness hardness range of the service-exposed weldment

4.3.2.1.2 Hardness (HV_3) Profile of the Weld Joint

Micro indentation hardness test conducted on the service-exposed weldment for improved results. Hardness measurements were performed using an EMCO Vickers hardness-testing machine with a 3 kgf load (HV_3). The test was conducted on a transverse section of the service-exposed weld joint, taken on three rows. In addition, several individual indentations were taken arbitrarily taken along the HAZ. The hardness range and average value are presented in Table 4.15, and the hardness profile shown in Figure 4.43. The highest average hardness of 192 HV_3 was obtained on the top of the sample, and the lowest hardness of 170 HV_3 was obtained on the bottom row.

Table 4.15 Hardness range and average hardness of row and individual indentations traverse to the service-exposed weldment

	Hardness (HV_3)			
Row	Top	Middle	Bottom	HAZ
Range	151 – 240	155 – 228	160 – 189	154 – 203
Average	**192**	**186**	**170**	**174**
Std. Dev.	24.1	24.6	7.8	14.6

An area with the lowest hardness was identified as the inter-critical heat affected zone (ICHAZ). In contrast, an area with the highest hardness corresponds to the CGHAZ. The FGHAZ lies between ICHAZ and CGHAZ sub-zones. The different regions are highlighted in red in Figure 4.44. A large inclusion of approximately 250 μm in diameter was also observed in the weld metal highlighted by the yellow circle.

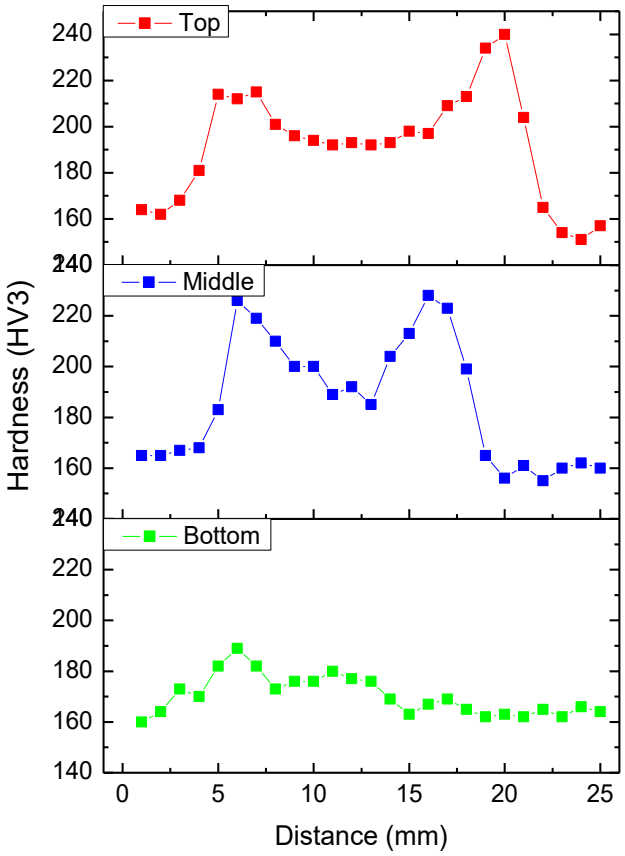

Figure 4.43 Hardness profile of the service-exposed weldment, measured traverse to the weld joint

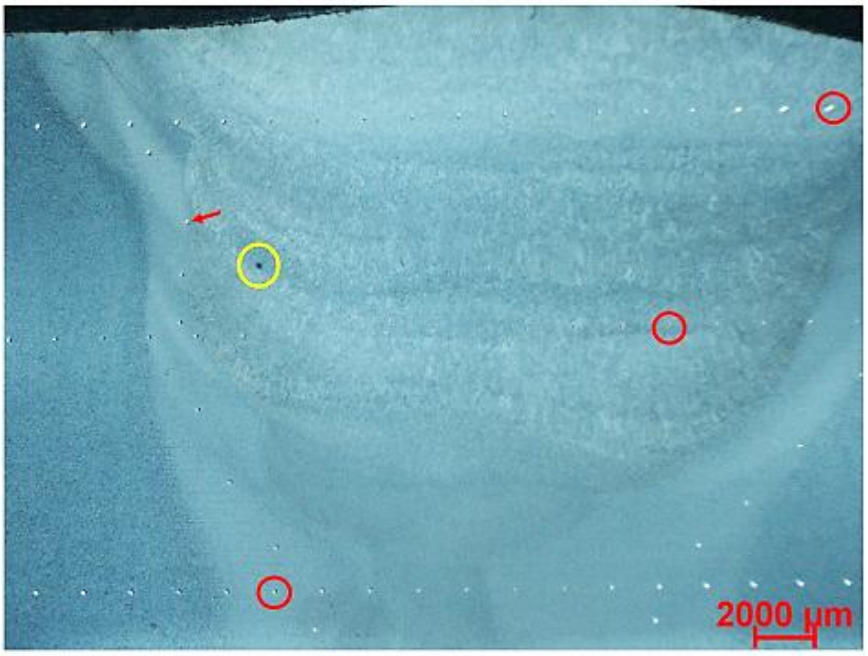

Figure 4.44 Row indentation and arbitrary hardness measurements on the service-exposed weld joint

Figure 4.45 shows the variation of hardness with depth, measured transversely across the weldment. The hardness variation is more pronounced in the HAZ, which can be attributed microstructural gradient.

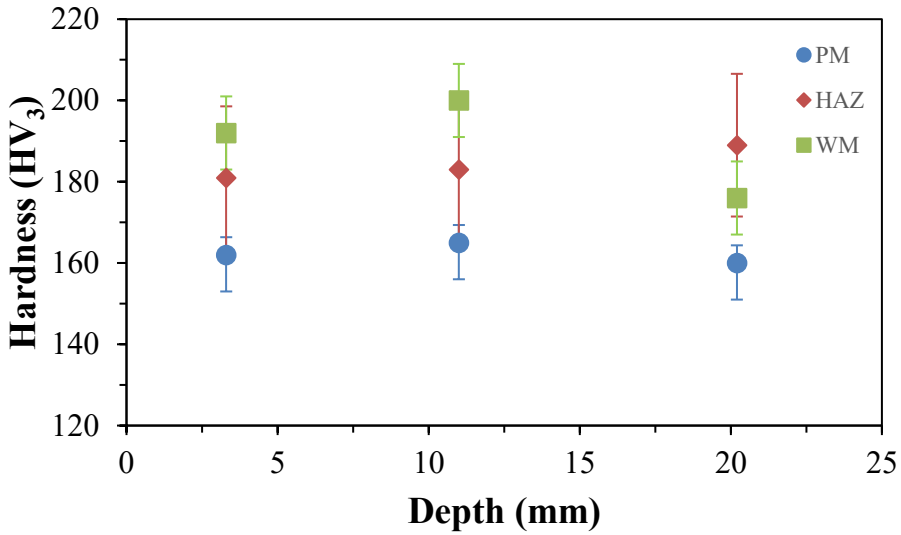

Figure 4.45 Variation of hardness with depth in the service-exposed parent metal, HAZ and weld metal

4.3.2.1.3 Hardness ($HV_{0.3}$) Profile of the Weld Joint

Micro hardness testing was also performed across the weld joint using a load of 0.3 kgf ($HV_{0.3}$) to obtain a higher resolution of the hardness profile for the service-exposed weldment. The results of the hardness measurements for each section of the weld joint are presented in Table 4.16. The weld metal recorded the highest average micro- hardness of 217 $HV_{0.3}$, while the lowest average micro-hardness of 150 $HV_{0.3}$ was reported for the parent metal.

Table 4.16 Microindentation hardness range and average of the service-exposed weldment

	Hardness ($HV_{0.3}$)		
Area	Parent metal	HAZ	Weld metal
range	132 – 169	151 – 218	182 – 242
average	**150**	**174**	**217**
Std. Dev.	9.2	17.9	13.8

The micro hardness profile of the service-exposed weldment is shown in Figure 4.46. From the results, the location of the tempered, inter-critical, fine-grained and coarse-grained sub-

regions can be estimated. The tempered zone is located at the start of the HAZ and has relatively similar hardness throughout. The tempered zone, located at the of the HAZ shows a relatively uniform hardness distribution. A region showing a sudden decrease in hardness is the ICHAZ. The highest hardness is observed in the CGHAZ. The FGHAZ is identified by its intermediate hardness, that is between the ICHAZ and the CGHAZ. Figure 4.47 shows micro indentations made across the specimen.

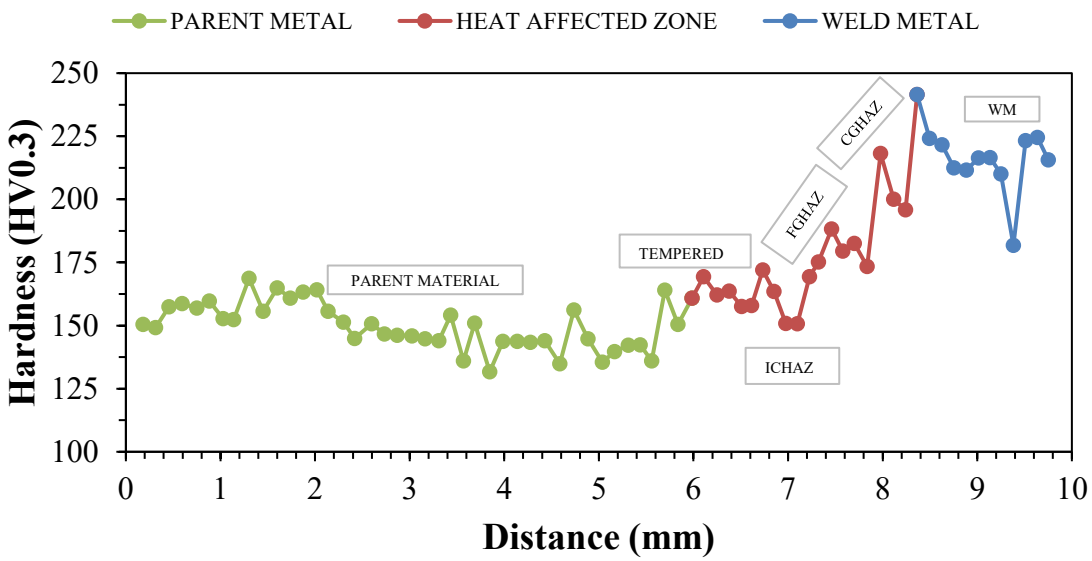

Figure 4.46 Micro indentation hardness (HV0.3) of the service-exposed weldment

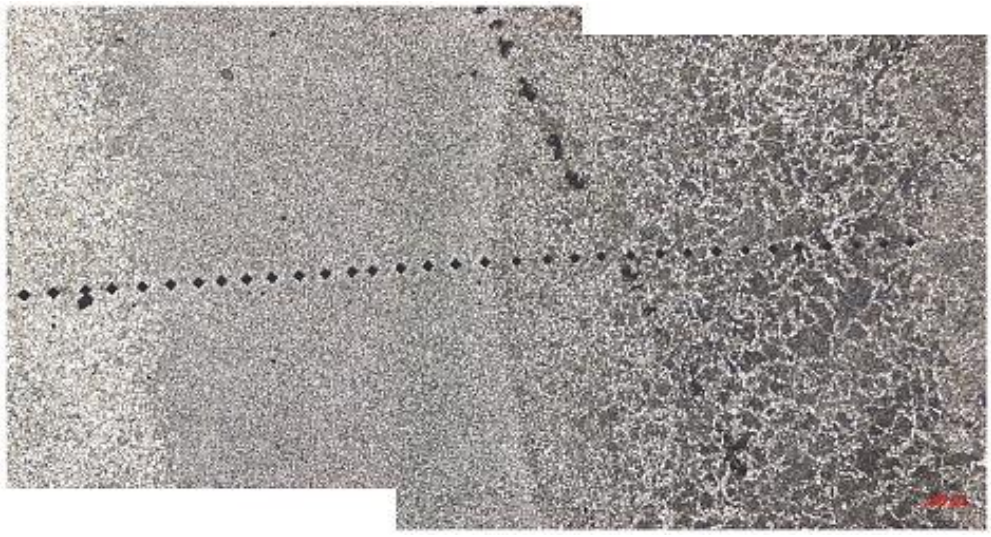

Figure 4.47 Stitched image of microhardness indentations on the service-exposed weld joint at 500× magnification

4.3.2.2 Room Temperature Tensile Properties

The room temperature tensile properties of the service-exposed weldment are summarised in Table 4.17. The tensile properties of the service-exposed weldment met the acceptability criteria specified in the BS EN 10216-2 for 14MoV6-3 steel at room temperature (British Standards Institution, 2007). However, this was expected as it is a common engineering practise to use filler materials with superior mechanical properties than the parent material. However, the weldment exhibited ductility that falls below the minimum threshold defined by BS EN 10216-2 standard. The reduction in ductility may be attributed to the degradation of material properties caused by high thermal cycles during welding and prolonged exposure to high temperature and stress during service. Nonetheless, the observed YT ratio of 0.7 is consistent with the results of the parent materials. The yield and tensile strength of the service exposed weldment is 371 MPa and 530 MPa, respectively.

Table 4.17 Room temperature tensile properties of service-exposed weldment

Test Temperature [°C]	Yield Strength [MPa]	Tensile Strength [MPa]	Elongation [%]	Reduction in Area [%]
23	371	530	17	49
Std. Dev.	23.2	7.6	1.5	2.6

4.3.2.3 Elevated Temperature Tensile Properties

The tensile properties of the service-exposed weldment at 540°C are presented in Table 4.18. The weldment was only tested at 540°C due to limited material. The results show that the yield and tensile strength are 250 MPa and 301 MPa, respectively. At elevated temperature, the yield strength of the service-exposed weldment was noticeably reduced although it remained within the acceptable limits specified in BS EN 10216-2 for 14MoV6-3 steel. A slight increase in ductility was observed compared to room temperature results, and material toughness was retained. However, the higher YT ratio suggests that the weldment may exhibit a more brittle or catastrophic failure mode than the parent material since the margin of safety is reduced.

Table 4.18 Elevated temperature tensile properties of service-exposed weldment

Test Temperature [°C]	Yield Strength [MPa]	Tensile Strength [MPa]	Yield-Tensile Ratio	Elongation [%]	Reduction in Area [%]
540	250	301	0.83	19	79
Std. Dev.	8.7	6.9	0.03	1.6	2.9

The fracture surface of the service-exposed weldment is shown in Figure 4.48. The surface exhibited a dimpled topography, characteristic of ductile fracture. Inclusions containing sulphur and manganese were observed on the fracture surface, with their composition confirmed by EDS spectrum analysis. The inclusions were identified as MnS, which is known to promote reheat cracking in low alloy steels (Shibli, 2014).

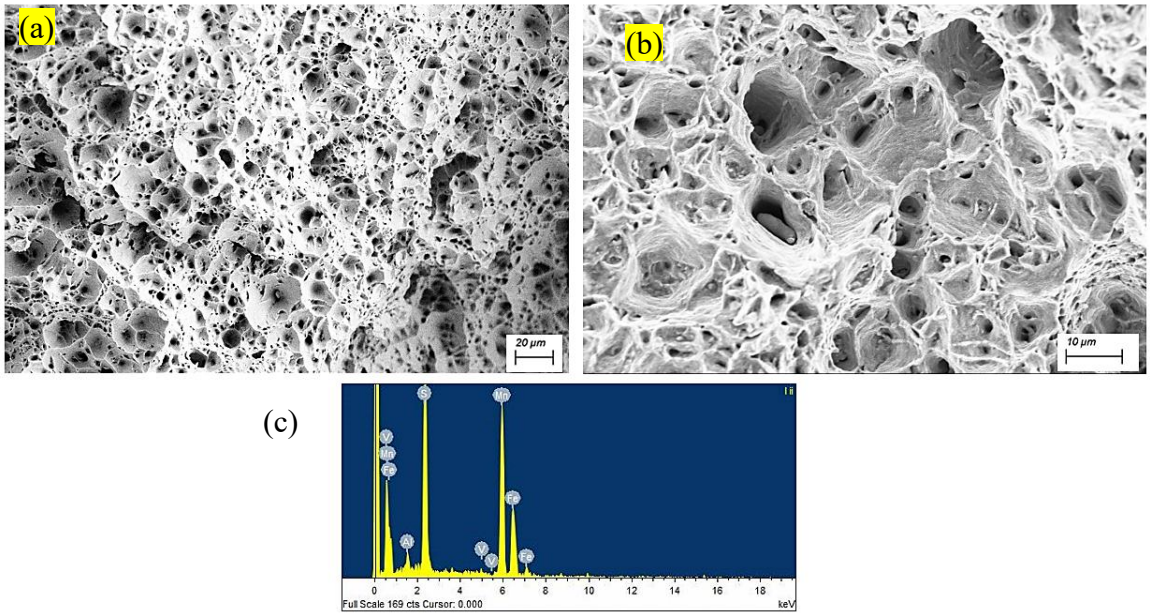

Figure 4.48 SEM fracture surface of the service-exposed weldment (elevated temperature specimen) (a) and (b). EDS analyses of inclusions and micro voids (c).

4.3.2.4 Impact Properties

The impact properties of the service-exposed weldment were evaluated against the acceptance criteria for 14MoV6-3 parent material as specified in BS EN 10216-2 (British Standards Institution, 2007). Test specimens were sectioned to access the three regions of the weldment.

Test specimens were designated as US HAZ (upstream) and DS HAZ (downstream), respectively. Due to a limited number of available specimens, testing temperatures were staggered across the range between the two HAZ regions. This approach was justified by the fact that identical materials were joined during the original pipe installation.

4.3.2.4.1 Impact Properties of the Weld Metal

The impact properties of the weld metal tested at -30°C, 0°C, 20°C, 23°C, 50°C, 100°C and 200°C are listed in Table 4.19. The impact energy measured at room temperature falls below the minimum average absorbed energy specified for 14MoV6-3 steel. The energy required for crack initiation shows minimal variation with temperature. However, the energy required for crack propagation increases with increasing temperature.

Table 4.19 Impact properties of service-exposed weld metal at various temperatures

Test temperature [°C]	Total absorbed energy [J]	Energy required for crack [J]	
		Initiation	Propagation
-30	15	5	10
0	11	5	6
20	35	20	15
23	26	16	10
50	50	24	26
100	57	13	45
200	112	30	82

Figure 4.49 shows the maximum load recorded during impact testing of the weld metal at temperatures of -30°C, 0°C, 20°C, 23°C, 50°C, 100°C and 200°C. No significant variation in maximum load was observed across the tested temperature range.

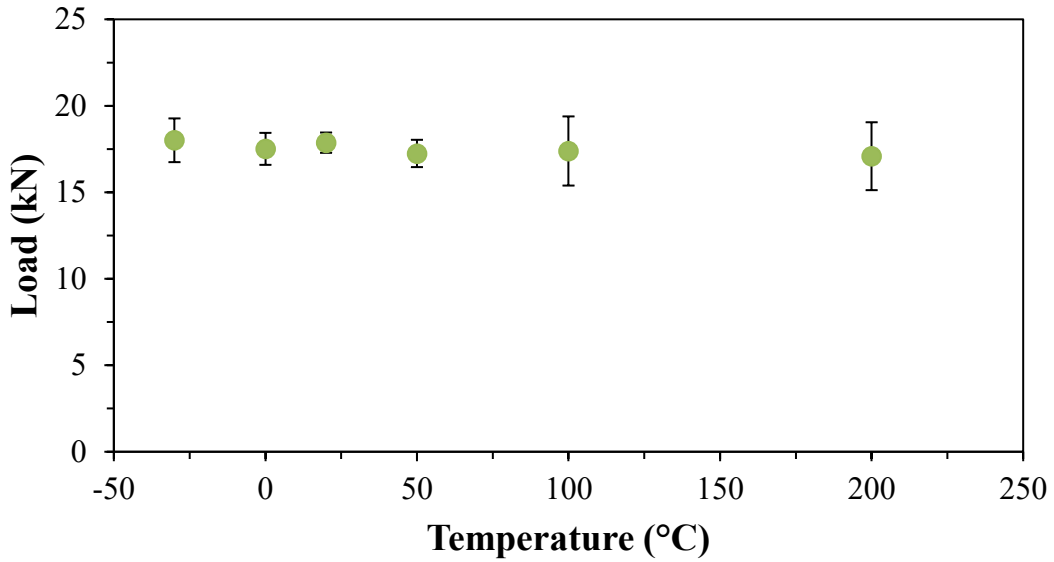

Figure 4.49 Maximum load vs. temperature for service-exposed weld metal

The variation in impact properties of the weld metal as a function of testing temperature is shown in Figure 4.50 (a). Figure 4.50 (b) shows the lateral expansions. The impact energy of gradually decreases with decreasing temperature, showing a linear behaviour, which is characteristic of steels with carbon content exceeding 0.6 wt.% (Callister & Rethwisch, 2008). The weld metal has a CE value of 0.67. The absence of a pronounced transition in ductile to brittle behaviour may be attributed to the specific microstructure and alloy composition of the weld metal. The DBTT is estimated to occur at approximately 90°C, corresponding to an impact energy of about 60 J. The 27 J transition temperature is estimated to be ~15°C. The upper shelf and lower shelf properties are not clearly defined within the tested range. The lateral expansion vs temperature curve correlates with the absorbed energy trend. Overall, the impact energy values across the temperature range are relatively low, indicative of brittle fracture behaviour.

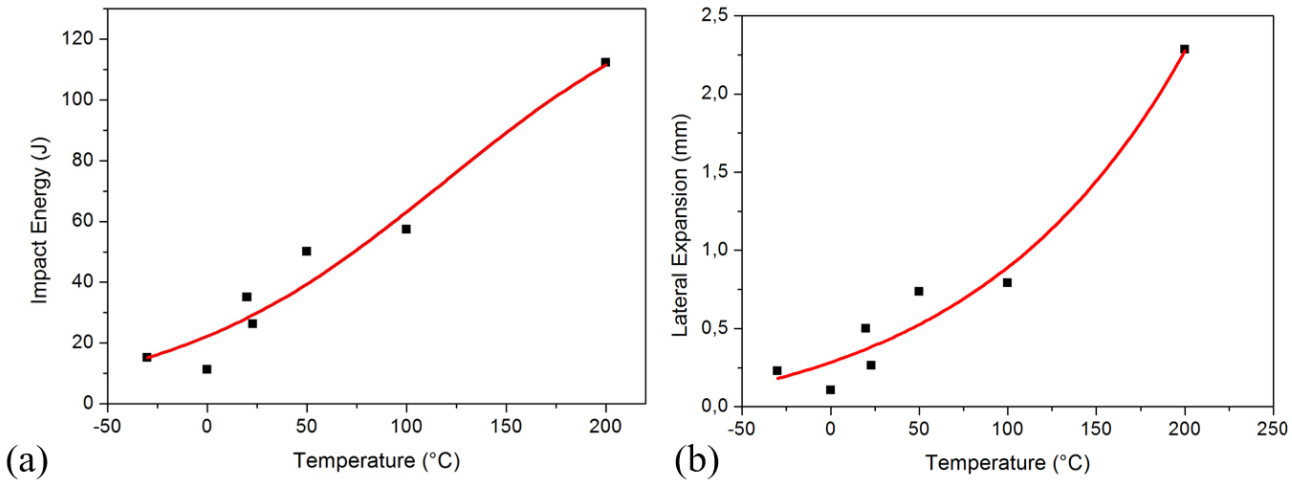

Figure 4.50 Ductile-Brittle Transition Temperature of weld metal versus (a) impact energy and (b) lateral expansion

The fracture appearance of the weld metal specimens tested at -30 °C, 0 °C, 20 °C, 50 °C, 100 °C and 200°C are shown in Figure 4.51. At -30 and 0°C, the specimens showed a flat fracture surface with a granular appearance that is characteristic of brittle fracture. As the testing temperature increased, the extent of the granular (brittle) region decreased, and a mixed-mode fracture appearance became evident in specimens tested between 20 °C and 200 °C, indicating a transition toward a more ductile fracture behaviour.

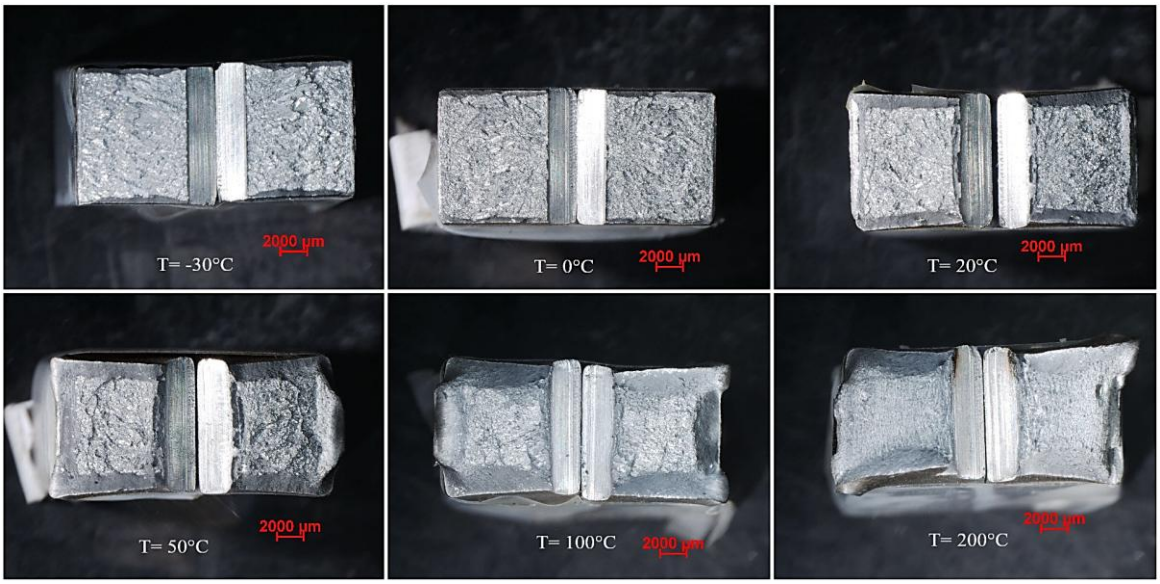

Figure 4.51 Fracture appearance of the service-exposed weld metal specimens at different temperatures

4.3.2.4.2 Impact Properties of the Heat Affected Zones

The impact properties of the US HAZ at 0 °C, 20 °C, 50 °C and 200°C are presented in Table 4.20. The impact energy of the US HAZ met the minimum requirements specified for 14MoV6-3 steel (British Standards Institution, 2007). At 0 °C, 50 °C and 200°C, the total absorbed energy was predominantly associated with crack propagation. However, at room temperature most of the energy was absorbed during the crack initiation process. Nevertheless, the energy required for crack initiation remained relatively constant across the tested temperature range.

Table 4.20 Impact toughness properties of service-exposed US HAZ at different temperatures

Test temperature [°C]	Total absorbed energy [J]	Energy required for crack [J]	
		Initiation	Propagation
0	63	26	37
20	67	44	24
50	167	51	116
200	142	39	103

Table 4.21 presents the impact properties of DS HAZ at -30 °C, 20 °C, 50 °C, and 100 °C. The DS HAZ impact energy at room temperature meets the acceptability criteria specified in BS EN 10216-2 (British Standards Institution, 2007). The energy required for crack initiation showed a slight increase with increasing test temperature. In all DS HAZ specimens, more than 50% of the total absorbed energy was associated with crack propagation.

Table 4.21 Impact toughness properties of service-exposed DS HAZ at different temperatures

Test temperature [°C]	Total absorbed energy [J]	Energy required for crack [J]	
		Initiation	Propagation
-30	51	23	28
20	110	30	80
50	146	53	94
100	178	50	128

Figure 4.52 shows the variation of maximum load with temperature for the US HAZ and DS HAZ tested at -30°C, 0°C, 20°C, 50°C, 100°C, and 200°C. The maximum loads recorded for both HAZ regions were comparable and remained relatively constant across the tested temperature range.

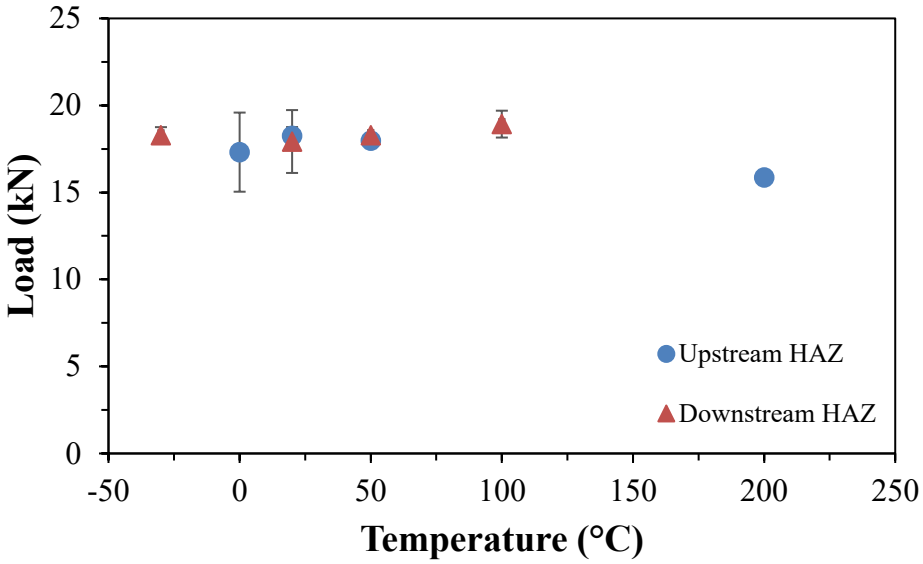

Figure 4.52 Maximum load versus temperature of the service-exposed HAZ

The transition temperature behaviour of the US HAZ is shown in Figure 4.53. The DBTT of the US HAZ was estimated to be approximately 35°C, corresponding to an impact energy of around 110 J, as shown in Figure 4.53(a). The lower shelf energy could not be observed from the dataset. However, the upper shelf impact energy of 147 J and a transition temperature of ~85°C was measured. The transition temperatures indicated by the lateral expansion versus temperature curve in Figure 4.53(b) closely correlate with those determined from the impact energy data.

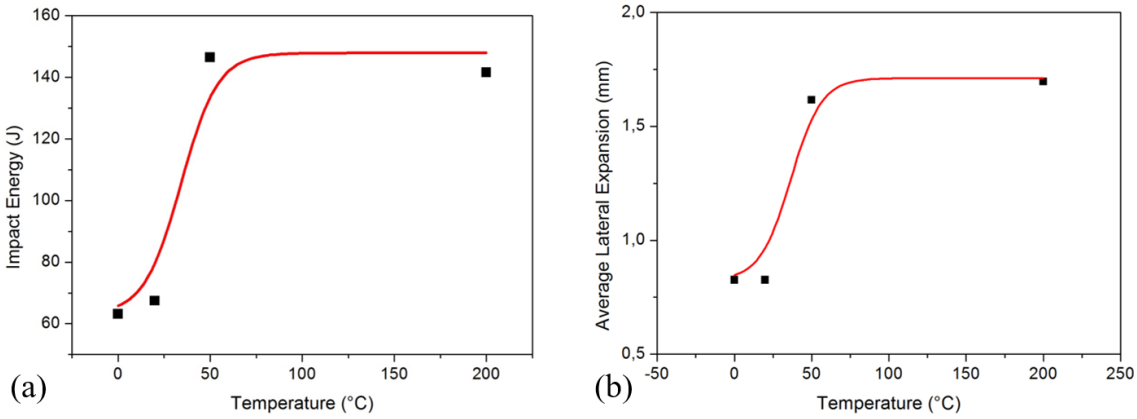

Figure 4.53 Ductile-Brittle Transition Temperature of the service-exposed US HAZ versus (a) impact energy and (b) lateral expansion

Figure 4.54 shows the transition temperature of the DS HAZ evaluated at -30°C, 20°C, 50°C and 100°C. A DBTT of approximately 25°C was estimated, corresponding to an impact energy of ~113 J, as shown in Figure 4.54(a). The lower and upper shelf energies were observed to be 51 J and 178 J, occurring at the transition temperatures of approximately 15°C and 65°C, respectively. Similar transition temperatures were identified from the lateral expansion versus temperature plot, as shown in Figure 4.54(b).

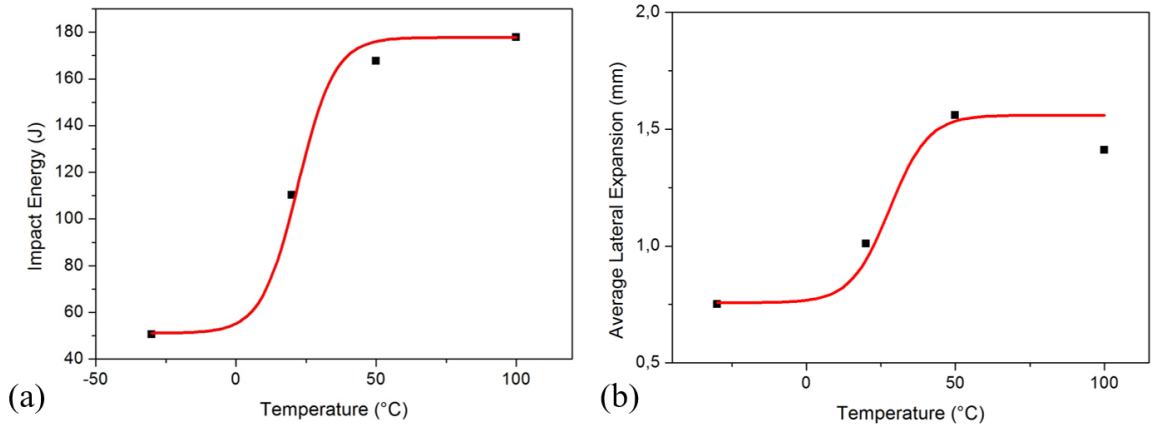

Figure 4.54 Ductile-Brittle Transition Temperature of the service-exposed DS HAZ versus (a) impact energy and (b) lateral expansion

The fracture appearance of the DS HAZ and US HAZ at -30°C, 0°C, 20°C, 50°C, 100°C and 200°C are shown in Figure 4.55. Samples tested at -30°C and 0°C exhibit fracture surfaces typical of brittle fracture, characterised by flat and granular features. With increasing test temperature, the fracture appearance transitions to a mixed-mode fracture, as evidenced by

the progressive reduction in the granular (brittle) region on specimens tested at 20 °C and up to 200°C.

Figure 4.55 Fracture appearance of the service-exposed HAZ specimens at different temperatures

Figure 4.56 shows the variation in impact energy test conducted at 20°C and 50°C. Results show that the region of higher impact toughness surrounds a localised area of lower toughness within the weldment. This mismatch in toughness may contribute to stress concentration and increase the likelihood of crack initiation and propagation under service conditions.

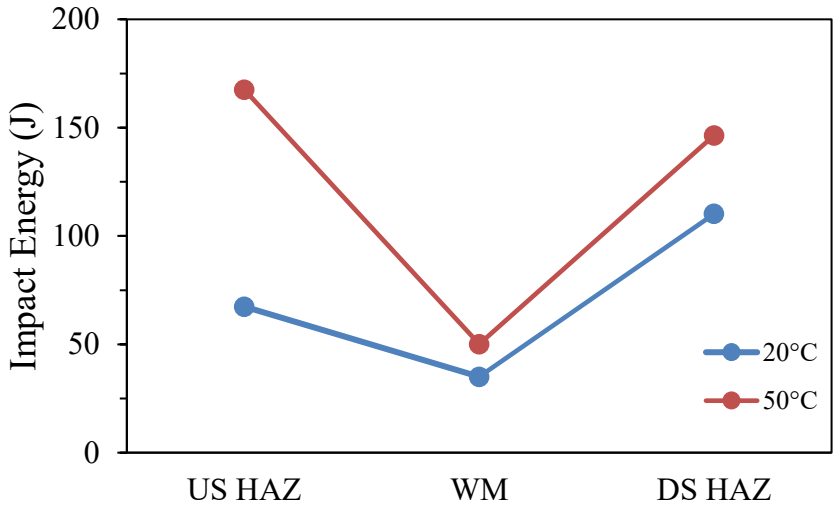

Figure 4.56 Impact energy as a function of temperature and in relation to the specimen location in the service-exposed weldment

4.3.2.5 Microstructure analysis

This section discusses the microstructure analysis of the service-exposed weldment. The assessment was done using OM and SEM analysis. Carbides that are present across the weldment, after long-term service, were also examined using SEM analysis and are discussed accordingly.

4.3.2.5.1 Optical Microscopy Analysis

The microstructure of the service-exposed weldment is shown in Figure 4.57 and consists of the weld metal and HAZ. The weld metal had complex recrystallized microstructure that consisted of acicular ferrite as shown in Figure 4.57(a). The HAZ consists of decomposed ferrite (equiaxed grains) with scattered voids and inclusions, as observed in Figure 4.57(b).

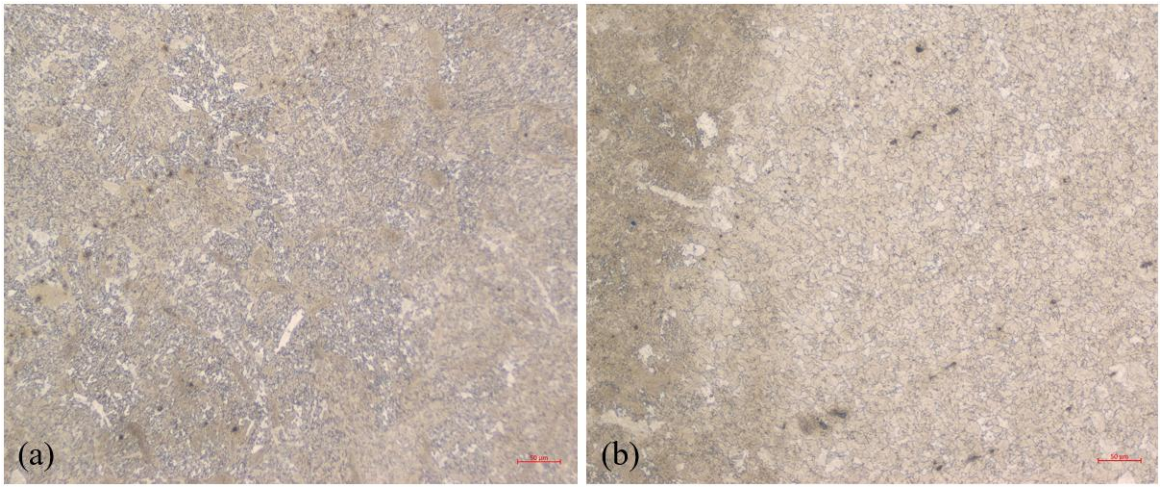

Figure 4.57 Microstructure of the service-exposed weldment at 500×, where (a) is weld metal and (b) is heat-affected zone

Table 4.22 summarises the details of the average grain size of the HAZ. The grain sizes were estimated using ImageJ software. The average grain size of the service exposed HAZ was measured to be 5.5 µm.

Table 4.22 Average grain size of service-exposed heat-affected zone

Line Length [µm]	Average No. of intercepts	Average grain size [µm]	ASTM grain size number [G]	Ferrite/Mixed/Carbide phase fraction [%]
400	72	5.5	11.7	33/56/11

Replica micrographs of the HAZ and parent material, taken from the service-exposed weldment, are shown in Figure 4.58. The micrographs were converted to binary image and threshold in ImageJ to analyse size of creep voids across the weldment. The sampled area of each micrograph was approximately 0.06 mm^2, with creep voids identified by red circles in Figure 4.58.

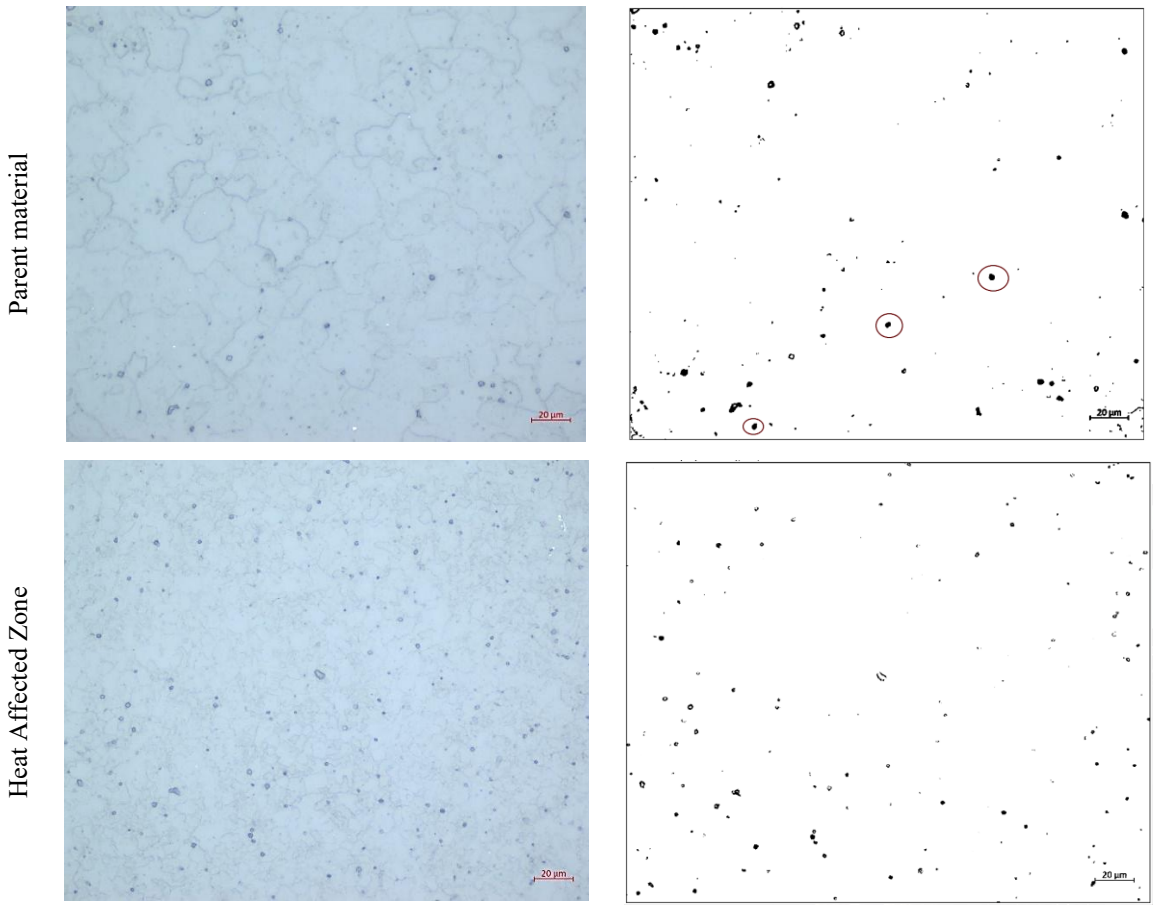

Figure 4.58 Micrographs of the service-exposed parent material replica (adjacent to the HAZ), ICHAZ replica, and their corresponding threshold images.

The size distribution of creep voids estimated in the service-exposed parent material is shown in Figure 4.59. The size of the creep voids was estimated to vary from approximately 0.6 µm to 3.6 µm with an average of 1.9 (±0.9 µm). The parent material has an estimated void density of approximately 236 voids/mm^2. Table 4.23 presents the estimation of the service-exposed parent material life exhaustion, time to rupture and remaining life. The remaining life of 21 and 11 years was estimated for the parent material, which was classified as RLE class 4 and class 3, respectively. These findings correlate with the measurements that were taken while the component was still in service, as presented in Table 3.1.

Table 4.23 Remaining life estimation for the service-exposed parent material

creep ductility parameter (γ)	Life Fraction, t/t_r	Time to rupture, t_r (hrs)	Remaining life, t_{rem} (hrs)	Damage class
3.4	0.60	462 745	185 293	Class 4
5	0.74	375 085	97 633	Class 3

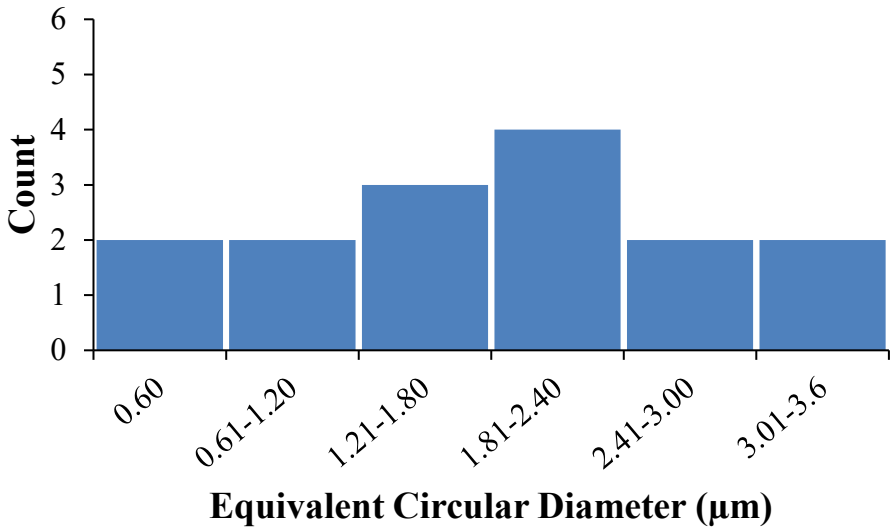

Figure 4.59 Size distribution of voids measured on the service-exposed parent material, immediately adjacent to the HAZ

Figure 4.60 shows the size distribution of creep voids estimated in the ICHAZ of the service-exposed weldment. The size of the creep voids in the ICHAZ was estimated to range from about 0.5 µm to 2.6 µm with an average void size of 1.5 (±0.6 µm). The void density in this area was estimated to be approximately 715 voids/mm^2. The life exhaustion, time to rupture and remaining life estimation for the ICHAZ are listed in Table 4.24. The remaining life of the weld ligament was estimated to be less than 1 year, classified as RLE class 1. The classification imply that creep damage will no longer be manageable within the outage philosophy and the pipework needs to be repaired or replaced. The results are in agreement with the service history of the material presented in Table 3.1, further justifying the decision to replace the component due the high risk of failure with continued operation.

Table 4.24 Remaining life estimation for the service exposed HAZ

creep ductility parameter (γ)	Life Fraction, t/t_r	Time to rupture, t_r (hrs)	Remaining life, t_{rem} (hrs)	Damage class
3.4	0.99	281 395	3 943	Class 1
5	1.00	277 975	523	Class 1

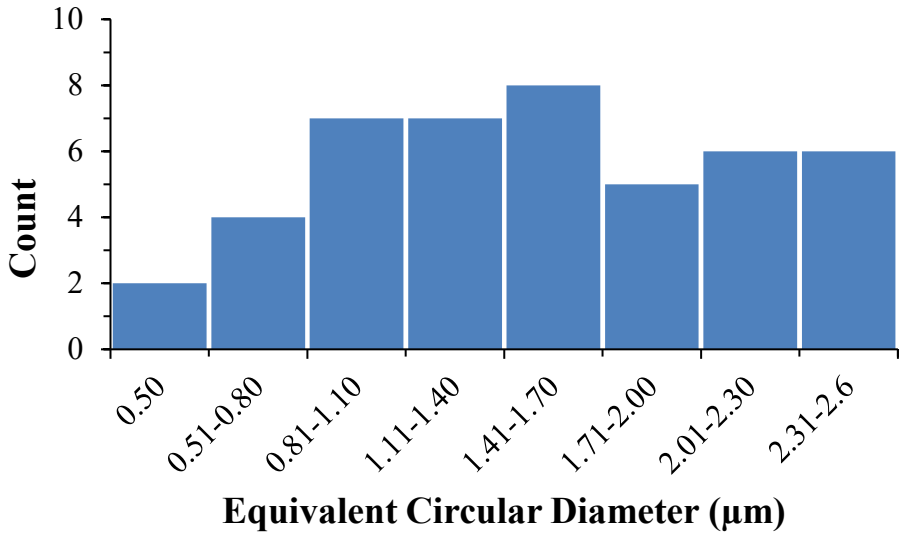

Figure 4.60 Size distribution of voids measured on the service-exposed ICHAZ

4.3.2.5.2 Scanning Electron Microscopy analysis

The ferritic microstructure of the service-exposed weld metal is shown in Figure 4.61, with carbide precipitates and creep voids are dispersed along the grain boundaries. The composition of the weld metal is shown in the EDS spectrum in Figure 4.62. The EDS analysis confirmed that a matching filler metal was used in making the weld as initially detected by the chemical analysis. A relatively high content of Mo and Mn was noted from the EDS analysis. Both Mo and Mn are known to lower the solidification cracking tendency of weld metals and hinder graphitisation (Bailey, 1994; Kou, 2003).

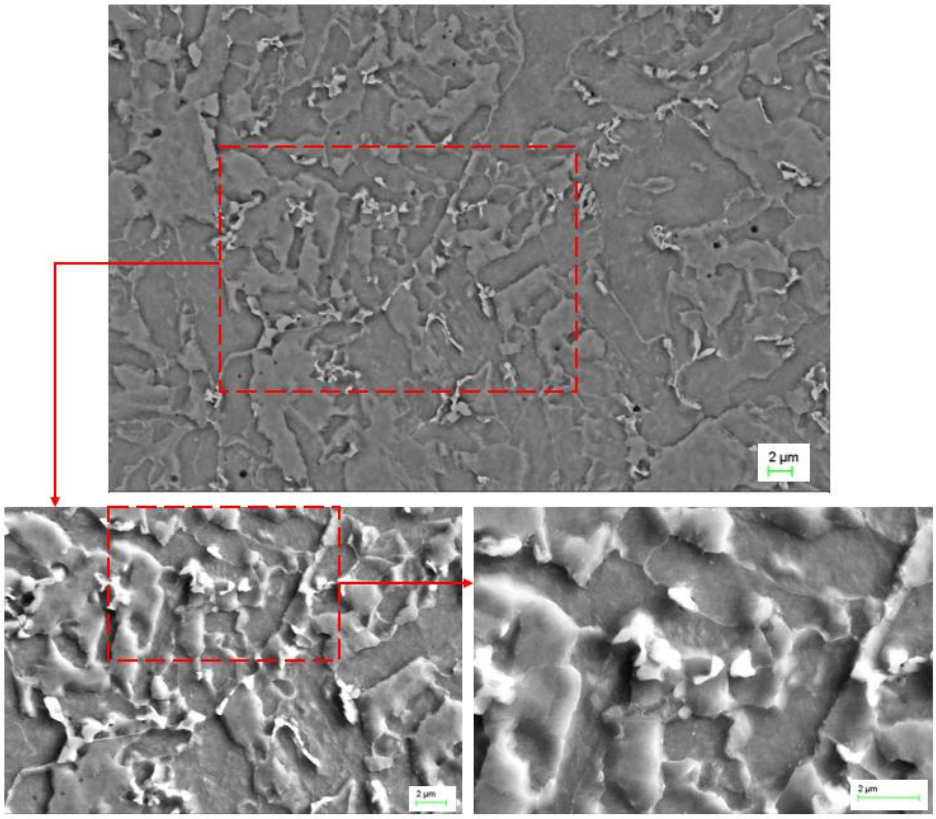

Figure 4.61 Microstructure of the service-exposed weld metal with detail of some carbide features

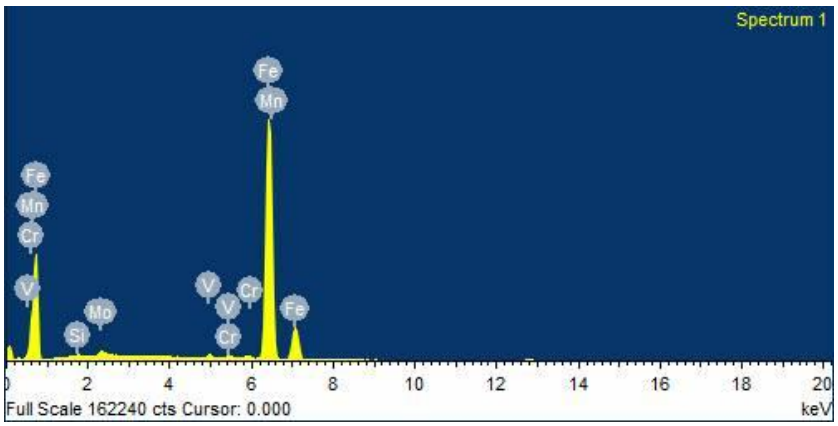

Figure 4.62 EDS spectrum of the service-exposed weld metal

The microstructure of the HAZ is shown in Figure 4.63. The microstructure consists of ferrite and carbides with voids dispersed along the grain boundaries. The HAZ microstructure was categorised as class 4-A/2 using the classification proposed by Dobrzanski et al. (2011).

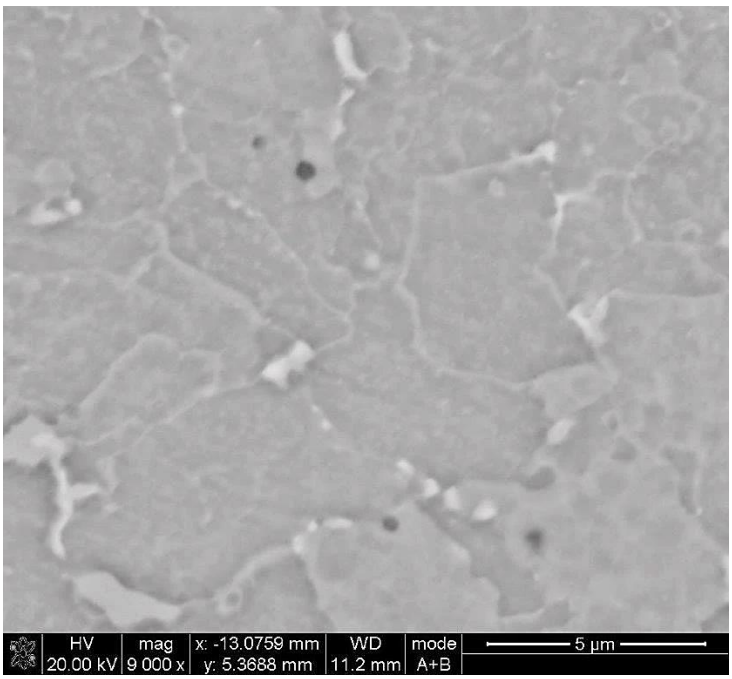

Figure 4.63 Microstructure of the service-exposed HAZ with scattered voids observed on grain boundaries

4.3.2.6 Carbide Precipitation in the Service-Exposed Weldment

SEM analysis was conducted on the service-exposed weldment to identify carbides present within microstructure. Locations of the analysed areas are shown in Figure 4.64. Microstructural examination of the weld metal, HAZ and parent material revealed two distinct types of carbides that were either rich in iron or molybdenum. As shown in Figure 4.65, the molybdenum-rich carbides contain relatively high silicon content, while the iron carbides also contain appreciable amounts of molybdenum and silicon, but with minimal vanadium and chromium. The Mo-rich carbides exhibit a string-like morphology and are primarily located along the ferrite grain boundaries, consistent with the description of $M_{23}C_6$ carbide (Dobrzanski, et al., 2011). In contrast, the Fe-rich carbides display an irregular, droplet-like shape and are also found along grain boundaries throughout the weldment, characteristic of M_3C-type carbides, though slightly smaller in size. Additionally, several micro voids were observed along the grain boundaries, as indicated by arrows in the micrographs.

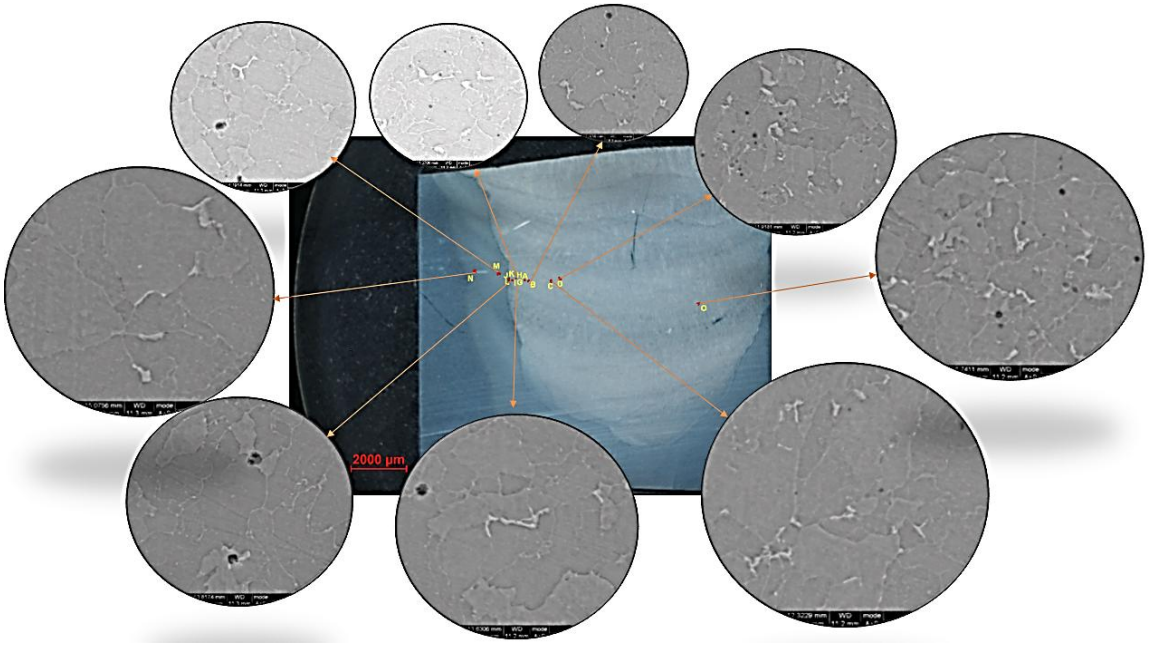

Figure 4.64 Locations of the areas sampled for the SEM microstructure assessment of the service-exposed weldment

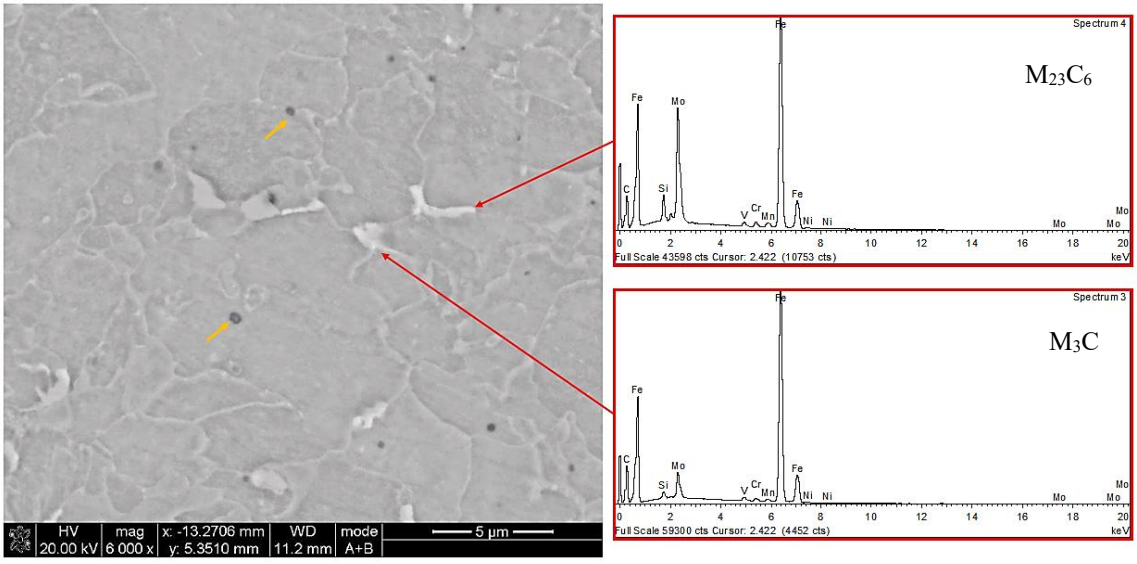

Figure 4.65 Morphology and composition of carbides observed across the service-exposed weldment

4.4 Life Assessment and Creep Damage Analysis

This section presents the results of the remaining life estimation and prediction of time to rupture for the pipe that removed from service after long-term operation in the creep regime. Additionally, the deformation behaviour of the service-exposed parent material under creep test conditions is discussed.

4.4.1 Remaining Life Estimation

The remaining life of the service-exposed pipe were estimated based on its service history and operating parameters as listed in Table 4.25. These inputs were applied together with the ECCC master curve for 12MoCrV6-2-2 as previously presented in Equation 2.27. The analysis yielded maximum life exhaustion of 32%, corresponding to the lower bound life prediction, defined as the mean curve plus 25% reference stress on the ECCC master curve.

Table 4.25 Life estimate of service-exposed 14MoV6-3 pipework based on ECCC master curve

Service history & operating parameters			%Life exhaustion	
Time [hrs]	**Ref. Stress [MPa]**	**Temperature [°C]**	**ECCC + 20%**	**ECCC – mean**
277 452	50	540	32	15

Based on a creep rupture strength of 50 MPa and an operating temperature of 540°C, the estimated time to rupture is approximately 250 years (2 183 862 hrs) as per BS EN 10216-2 (British Standards Institution, 2007). Using this data, a mean life exhaustion of 12.7% was calculated, with a corresponding product life and mean stress (PLM), P_{LM} value of 20600.79. The value for the constant C was taken as 19.

The remaining life estimates for the investigated material were also conducted using void density measurements obtained from surface replicas and of the research material were also done using the void count from the surface replicas and creep damage model described in Equation 2.25. Surface replicas were lifted and evaluated following procedures outlined in Section 3.2. Creep damage was quantified by measuring the density of creep voids on both the new and service-exposed material. As expected, no creep voids were detected on the virgin parent material, which has not been exposed to creep conditions. Measurements taken from the service-exposed parent material showed minimal damage, with only occasional voids observed and a void density of less than 50 voids/mm², which is in agreement with service history results shown in Table 3.1. However, measurements taken approximately 5 mm from the ICHAZ revealed an average void density of 150 voids/mm². The highest level of creep damage was recorded within the ICHAZ, with an average void density of 392 voids/mm². Figure 4.66 shows the through-wall creep damage profile of the service-

exposed parent material adjacent to the HAZ, highlighting that the peak void density was located in the ICHAZ, approximately 4 mm below the inner surface.

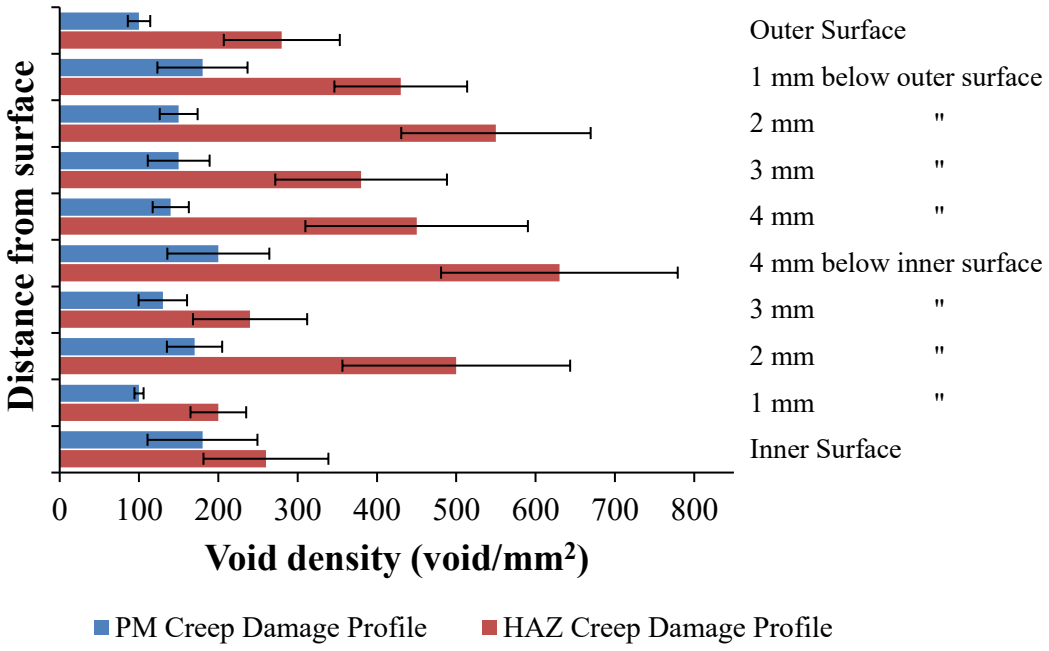

Figure 4.66 Through-wall creep damage profile of the service-exposed parent material and Heat Affected Zone

Figure 4.67 shows micrographs of the creep damage that was observed on the service-exposed parent material (a) and on the ICHAZ (b). Noticeably, the creep voids on this material are not distributed homogeneously but are scattered randomly along the grain boundaries. This phenomenon has been attributed to the system loading that occurs during the boiler system shutdown and start up (Molokwane, 2013).

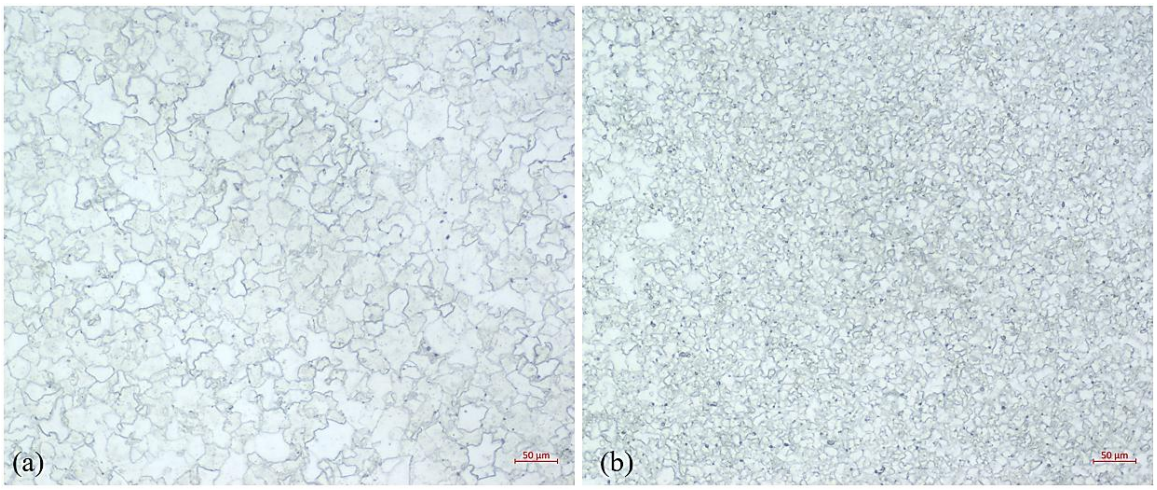

Figure 4.67 Replica micrographs of the service-exposed weldment showing (a) parent material and (b) HAZ at 200×

Table 4.26 shows the remaining life estimation of the service-exposed weldment estimated using the creep damage model. Based on the maximum creep void density, a remaining life of approximately 22 years was calculated for the parent material, while the HAZ was found to have reached the end of its useful life. The average void density resulted in remaining life of approximately 36 years for the parent material and three (3) years for the HAZ. The pipework would be barely manageable within the outage philosophy of the coal-fired power plants shown in RLE classification in Table 2.9.

Table 4.26 Remaining life estimates for service-exposed 14MoV6-3 weldment

Sample Location	%Life exhaustion at λ=3.4/5	Remaining Life (yrs.)	Damage Class
		maximum/average void density	
PM	59/69	~22/36	4/4
HAZ	100/100	~0/3	1/2

A more conservative approach to estimating the remaining life based on average void density involves determining the damage class using the average of the remaining life values calculated with λ=3.4 and λ=5. This method yields an estimated remaining life of approximately two (2) years for the HAZ and 29 years for the parent material. These results confirm that continued operation of the pipework without risk mitigation, weld repair or complete replacement would be unsafe. Accordingly, the weldment, specifically the HAZ has been identified as the life-limiting feature of this component.

4.4.2 Prediction of Time to Rupture

The rupture time of the service-exposed parent material under creep conditions was estimated using the ECCC master curve data sheet for ½Cr-½Mo-¼V (Spindler, 2017). This master curve is based on creep test data obtained from virgin materials with no prior service history. The predicted life range (time to rupture) for a sample tested at 60 MPa and 600°C is shown in Table 4.27. The tested sample, however, ruptured significantly earlier after approximately 4375 hrs, which is outside the predicted life range of 11 – 57 khrs. This premature failure is attributed to prior long-term service under creep conditions. Figure 4.68 shows the stress versus time to rupture results of the creep test, superimposed on the ECCC master curve predicted behaviour curve. The observed material behaviour aligns with the lower bound of the ECCC dataset, which is consistent with the mechanical properties of the service-exposed parent material, most of which fall within the lower bounds of their respective acceptance criteria. Nonetheless, additional test data are required to establish a more reliable trend and accurately position the material performance relative to the ECCC master curve. It is important to note that an exact correlation at the same stress and temperature conditions is not expected due to the inherent scatter in creep data. A rupture time of approximately 19,000 hours was also estimated using BS EN 10216-2, which is in reasonable agreement with the ECCC data.

Table 4.27 Estimation of time to rupture

Prediction parameters		**Estimated Rupture Time [hrs]**			
Ref. stress [MPa]	Temperature [°C]	ECCC + 20%	ECCC mean	ECCC - 20%	BS EN 10216-2
60	600	11 350	23 704	57 009	19 063

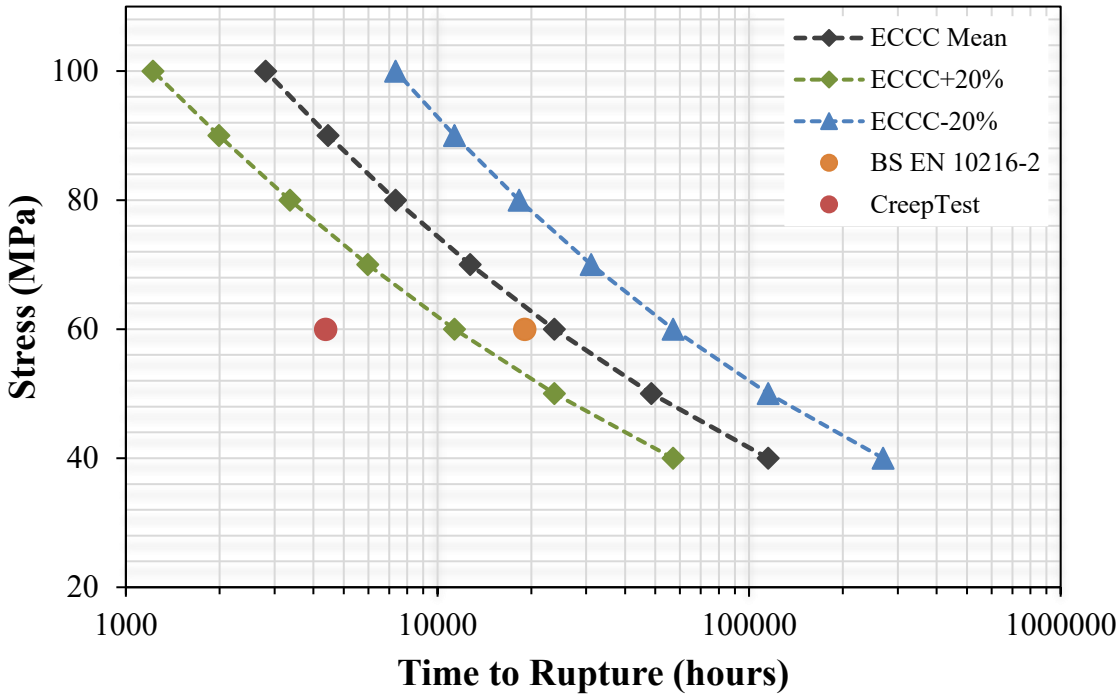

Figure 4.68 Stress vs time to rupture curve of the service-exposed parent material

The ECCC master curve data was used to determine the P_{LM} curve as a function of the creep strength as shown in Figure 4.69. The P_{LM} values of the service-exposed parent material at 60 MPa were estimated to be 20406.22, 20323.61 and 19765.61 from the data of the ECCC-mean, BS EN 10216-2 and creep test, respectively.

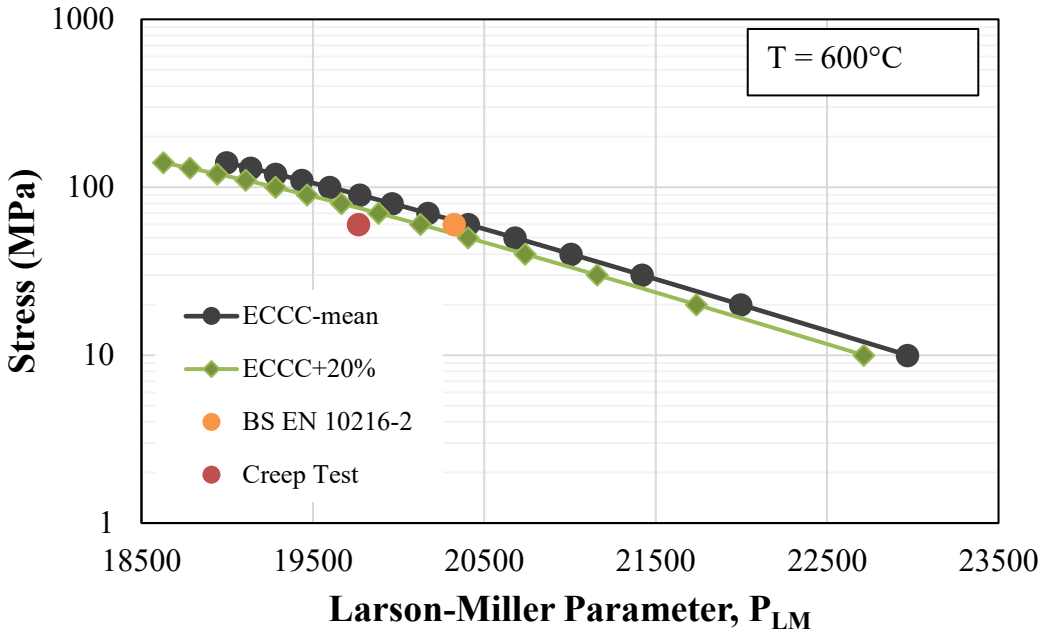

Figure 4.69 Estimation of time to rupture of the service-exposed parent material in terms of Larson-Miller parameter

Given the known time to rupture at 600°C, it is possible to estimate the time to rupture across a range of temperatures at the same applied stress, assuming the P_{LM} and constant C remain unchanged. These estimations are shown in Figure 4.70. The extrapolated time to rupture of 205,068 hrs corresponds to the residual life of the service-exposed parent material at service temperature of 540°C. The useful life, defined as the disposable residual life available for safe continued operation is estimated to be 123,041 hrs (14 years), corresponding to a life exhaustion of 58%. This estimated life exhaustion aligns with the results obtained from creep void density measurements using surface replicas and the creep damage model.

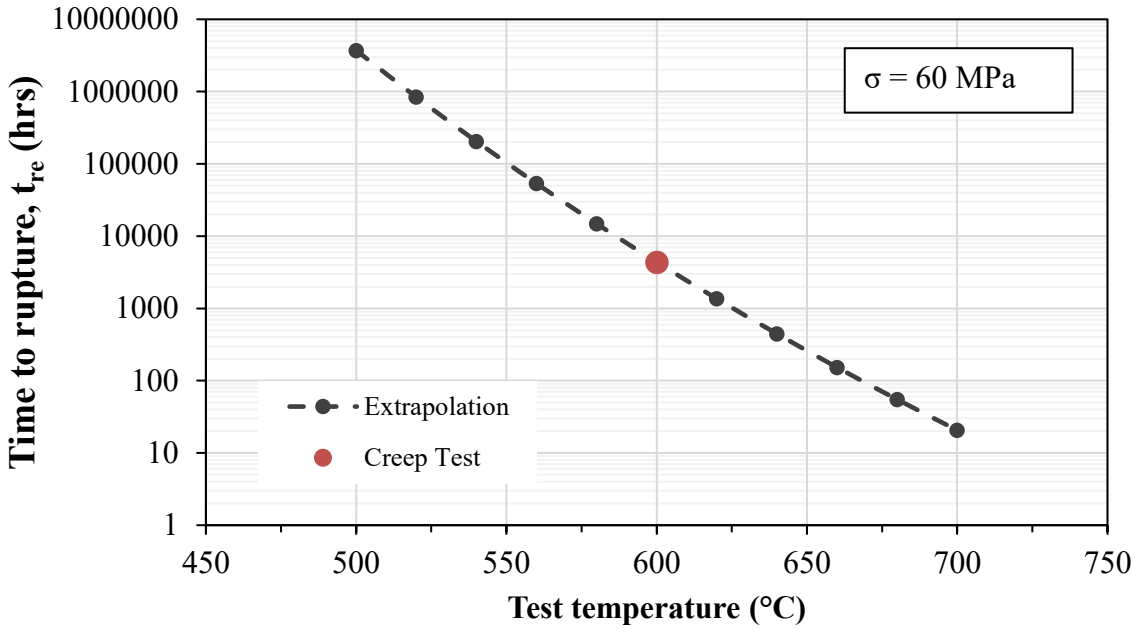

Figure 4.70 Extrapolation of time to rupture for the service exposed material creep test at various temperatures and constant stress of 60 MPa

4.4.3 Material Behaviour under Creep Test

The results of the creep test done on the service-exposed parent material and the testing conditions are summarised in Table 4.28. The test was run continuously without interruption until the sample ruptured. An average creep rate of 1×10^{-9} s^{-1} and strain of ~1% was recorded at test duration.

Table 4.28 Creep test results of the service-exposed parent material

Test conditions			Results		
Temperature [°C]	**Stress [MPa]**	**Media**	**Duration [hrs]**	**%Elongation**	**%RA**
600	60	Argon	4375	12	20

A smoothed three-stage creep curve of the service-parent material is shown in Figure 4.71. The sample experienced minimal primary creep deformation, where the creep rate decreased with time. The decrease in creep rate during the primary creep stage is associated with strain hardening or the decrease in free/mobile dislocations (Abe, et al., 2008). Much of the test duration took place at a steady-state creep rate (3.2×10^{-6} h^{-1}) before entering tertiary stage. The creep rate remains constant during the secondary creep stage, which is normally attributed to the state of equilibrium between strain hardening and rate of recovery

(softening). This state of equilibrium is shown on the creep rate curve in Figure 4.72. During the primary stage of creep, the strain rate is observed to decrease with time, although it remains higher than that of the secondary stage. The tertiary stage is characterised by the rapid increase in creep rate leading up to sample rupture. The sudden increase in creep rate, observed at approximately 1% strain as shown in Figure 4.73, may be attributed to material softening mechanism such as microstructural degradation or cavity formation.

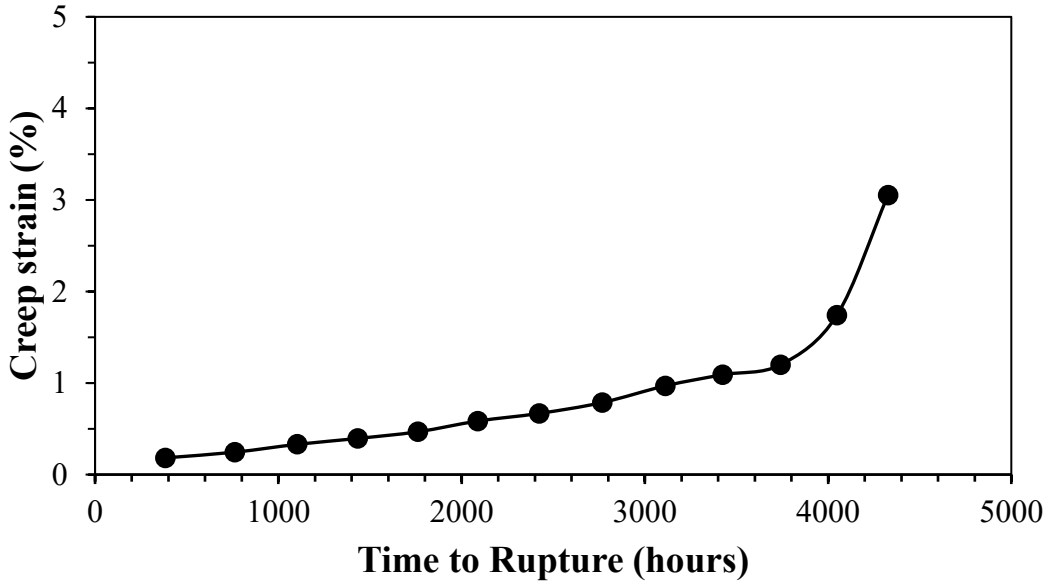

Figure 4.71 Creep curve of the service-exposed parent material tested at 600°C and 60MPa

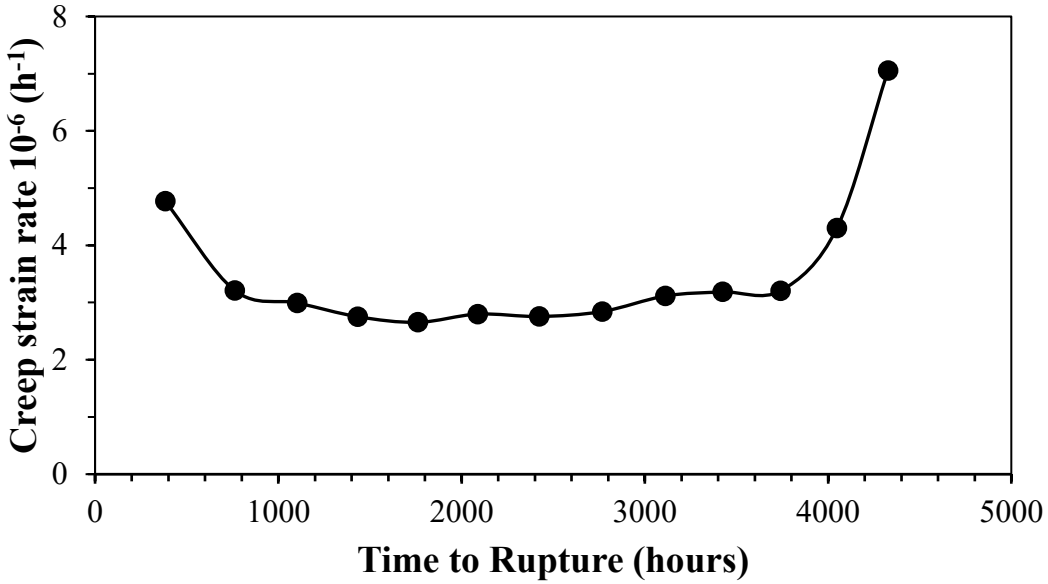

Figure 4.72 Creep rate curve of the service-exposed parent material tested at 600°C and 60MPa

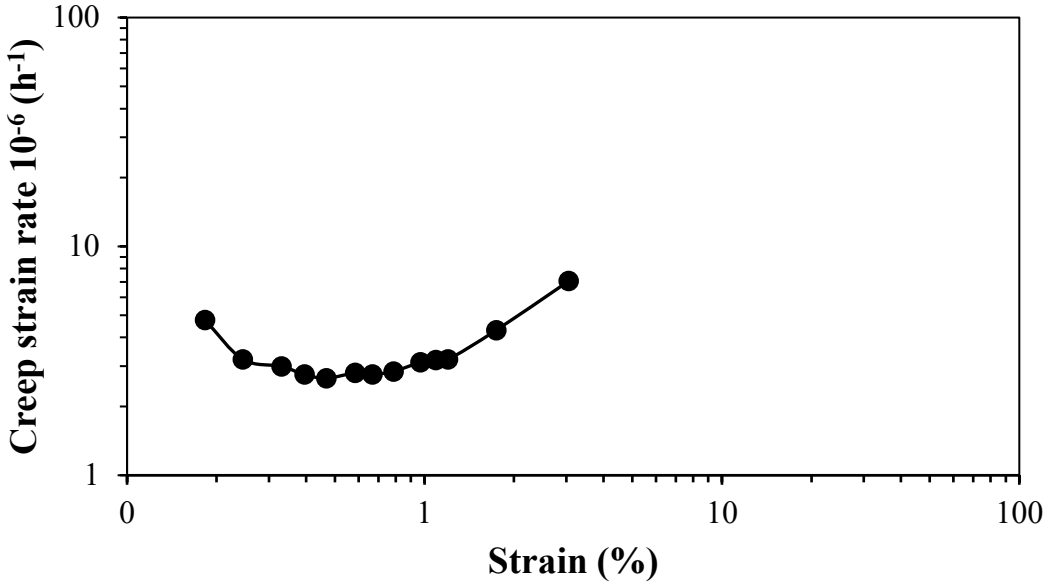

Figure 4.73 Creep rate versus strain curve of the service-exposed material tested at 600°C and 60MPa

The ruptured creep specimen of the service-exposed material is shown in Figure 4.74. The fracture location is approximately at the centre of the specimen, which is an indication that the specimen was heated and loaded uniformly during the creep test. Furthermore, no scaling was observed on the ruptured specimen. The post-test dimensional changes are given in Table 4.28.

Figure 4.74 Ruptured creep specimen of the service-exposed parent material

The microstructure of the ruptured specimen is shown in Figure 4.75. The micrographs shown were taken on the gauge length near the failure location (a) and on the top side grip end (b) as shown in Figure 3.13. Some scattered voids were observed along the grain boundaries of a rather decomposed ferrite microstructure as detailed in (c). A similar structure

was observed throughout the specimen, including the grip ends that only experienced high temperature and very little to no stress. The specimen grip end that was positioned at the top end of the furnace was further analysed for any evidence of the chimney effect, which was not apparent. This is in good agreement with the measured temperature difference of <1°C between the top and bottom half of the furnace during the creep test.

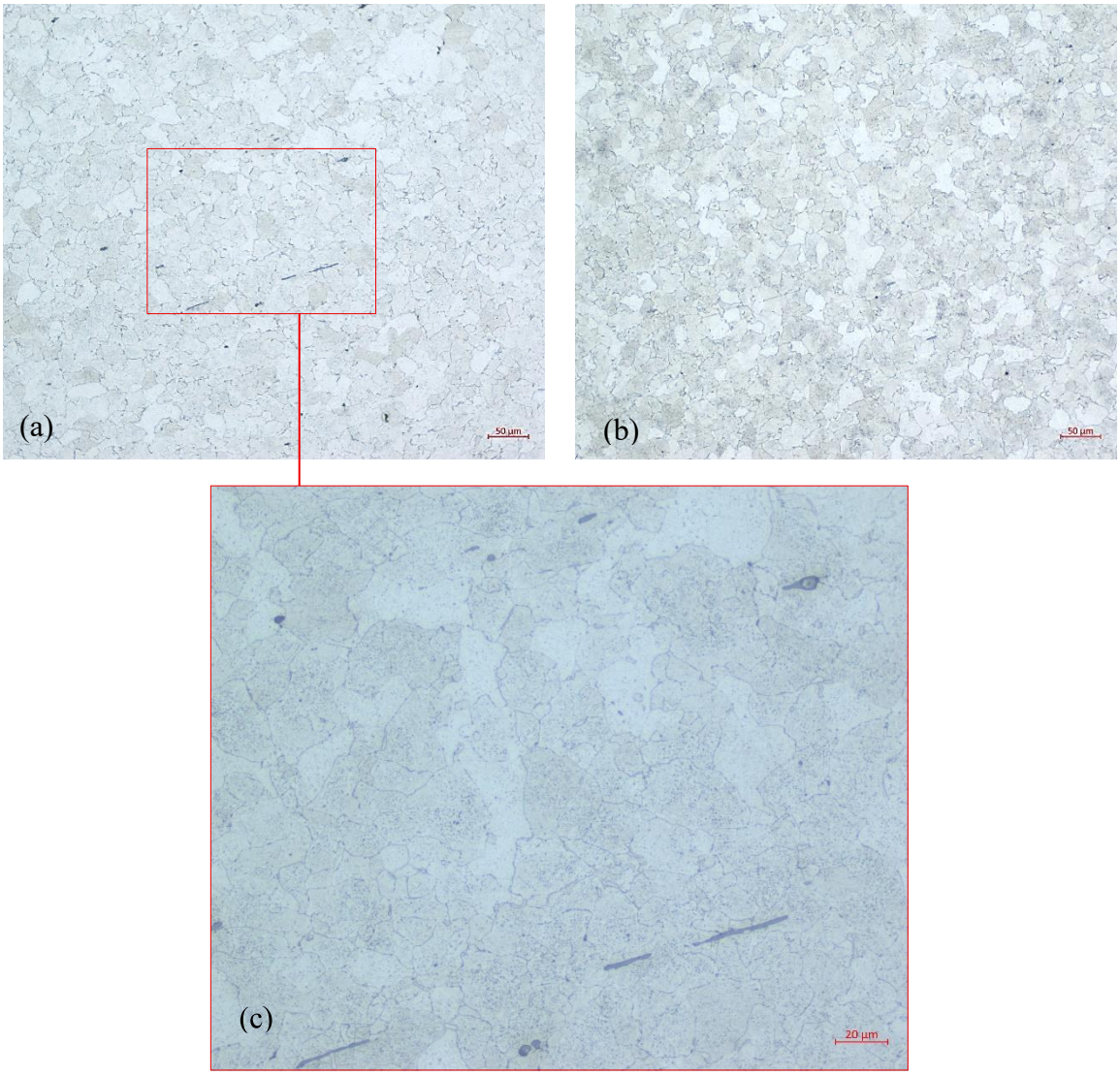

Figure 4.75 Micrographs of the creep test specimen taken at fracture location along the gauge length and at the grip ends

4.5 Heat Affected Zone Simulation and Hot Tensile Testing Using the Gleeble®

The Gleeble thermo-mechanical simulator was used to do the HAZ simulation and tensile testing of the virgin and service-exposed parent materials. The following sections discuss the results of the HAZ simulation and hot tensile tests on the virgin and service-exposed parent materials.

4.5.1 Simulation of Heat Affected Zone Sub-regions

A single thermal cycle was used to simulate thermal history experienced by each HAZ region in a single pass weld. Figure 4.76 shows the thermal cycle curves of the simulations at 860°C (a), 1080°C (b) and 1280°C (c).

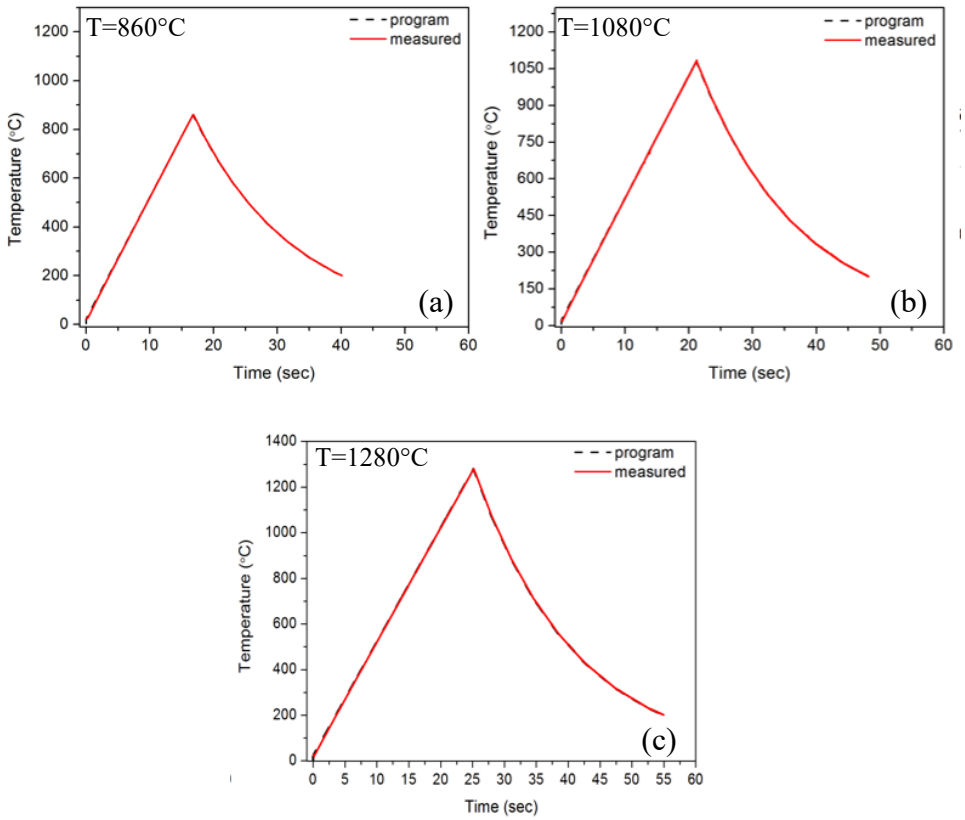

Figure 4.76 Typical welding thermal cycles of the HAZ simulation for peak temperatures corresponding to the predicted ICHAZ (a), FGHAZ (b) and CGHAZ (c)

The peak temperatures were selected to correspond with the predicted HAZ regions of the service-exposed and virgin parent materials. A heating rate of 50°C/s and cooling time of 7.5

seconds from 800°C to 500°C were used for all the specimens. The program and measured temperatures matched well for both the heating and cooling cycles for all peak temperatures.

4.5.2 Microstructure Characterisation of Simulated HAZ Regions

The microstructure of the simulated HAZ are evaluated as a function of peak temperature, PWHT and cooling conditions.

4.5.2.1 Microstructure of the HAZ regions simulated on virgin parent material

The grain sizes of the virgin parent material simulated HAZ regions were estimated using the lineal intercept method on the ImageJ software and summarised in Table 4.29. The fraction of the ferrite and bainite phases were also estimated for each peak temperature and sample condition.

Table 4.29 Grain size of virgin parent material simulated HAZ regions as a function of peak temperature and cooling condition

Peak Temperature (sample condition) [°C]		Line Length [µm]	Average No. of intercepts	Average grain size [µm]	ASTM grain size number [G]	Ferrite/Bainite phase fraction [%Area]
RT	furnace	400	48	8.4	10.5	76/24
RT	air	400	47	8.6	10.4	74/26
860	as-weld	400	64	6.2	11.4	48/52
	furnace	400	45	8.9	10.3	75/25
	air	400	44	9.2	10.3	64/36
1080	as-weld	-	-	-	-	41/59
	furnace	400	14	28 (50)	7	56/44
	air	400	21	19.1	8.1	74/26
1280	as-weld	-	-	-	-	38/62
	furnace	-	-	-	-	49/51
	air	400	92	4.2 (33)	12.5	52/48

The as-received microstructure of the virgin parent material is ferrite and bainite as discussed in Section 4.2.5. The as-received virgin parent material was subjected to a heat treatment and cooled in either ambient air or furnace. Figure 4.77 shows the microstructure that was obtained after the heat treatment of the virgin parent material. The resulting microstructures

are highly similar and likely correspond to the tempered zone of the HAZ. This similarity is reflected in both grain size and phase fraction, which appear comparable across the examined regions. The consistent microstructural appearance may be attributed to the fact that any cooling rate from annealing temperatures below A_{c1} produces a similar microstructure and hardness (Dossett & Boyer, 2006; Totten, 2007).

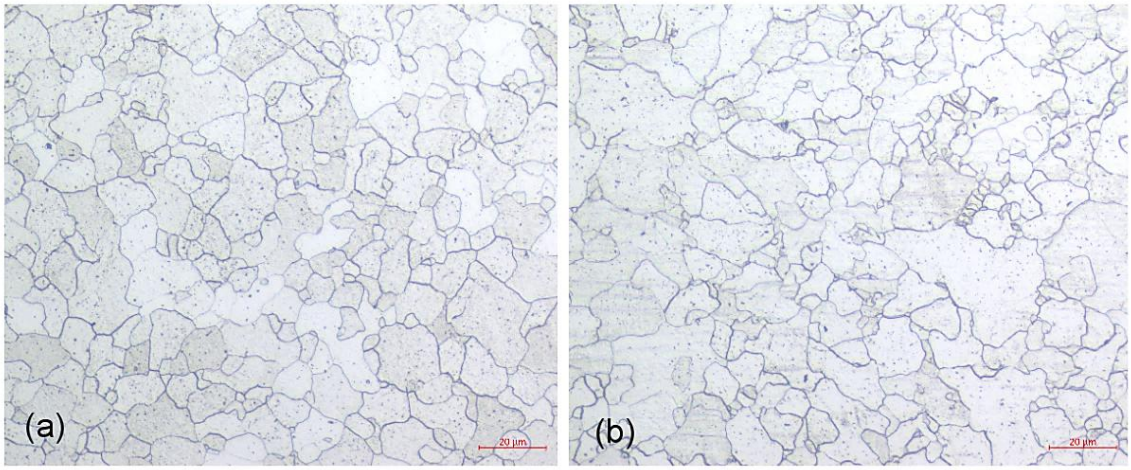

Figure 4.77 Microstructures of as-received virgin parent material after heat treatment and cooled in (a) furnace or in (b) air

The as-weld microstructure of simulated HAZ at peak temperature 860°C consists of ferrite (equiaxed) and bainite/pearlite (ferrite-carbide aggregate) as shown in Figure 4.78(a) and the close-up insert. Upper bainite generally etches brighter than pearlite due to the relatively large size of ferrite laths in bainite compared to the lamellar spacing of pearlite (Aliya & Lampman, 2004). The size of ferrite laths is normally used to determine the interparticle spacing of cementite in upper bainite. A bainitic microstructure was observed at peak temperatures 1080°C and 1280°C as shown in Figure 4.78(b) and (c), respectively. This microstructure is typical of upper bainite, which consists of aggregates of ferrite plates (acicular) separated by thin films of austenite, martensite or fine needles cementite (Totten, 2007; Burke, 2009). Optical microscopy is not sufficiently accurate to make a clear distinction between these bainite and martensite phases, but it is effective in distinguishing bainite from pearlite. The bainite phase is dominant in the as-weld microstructure and its fraction increased with the increase in peak temperature. This is due to the transformation that occurs when the steel is subjected to the different heat cycles and cooled quickly (~40°C/s) from 800 to 500°C of the various peak temperatures.

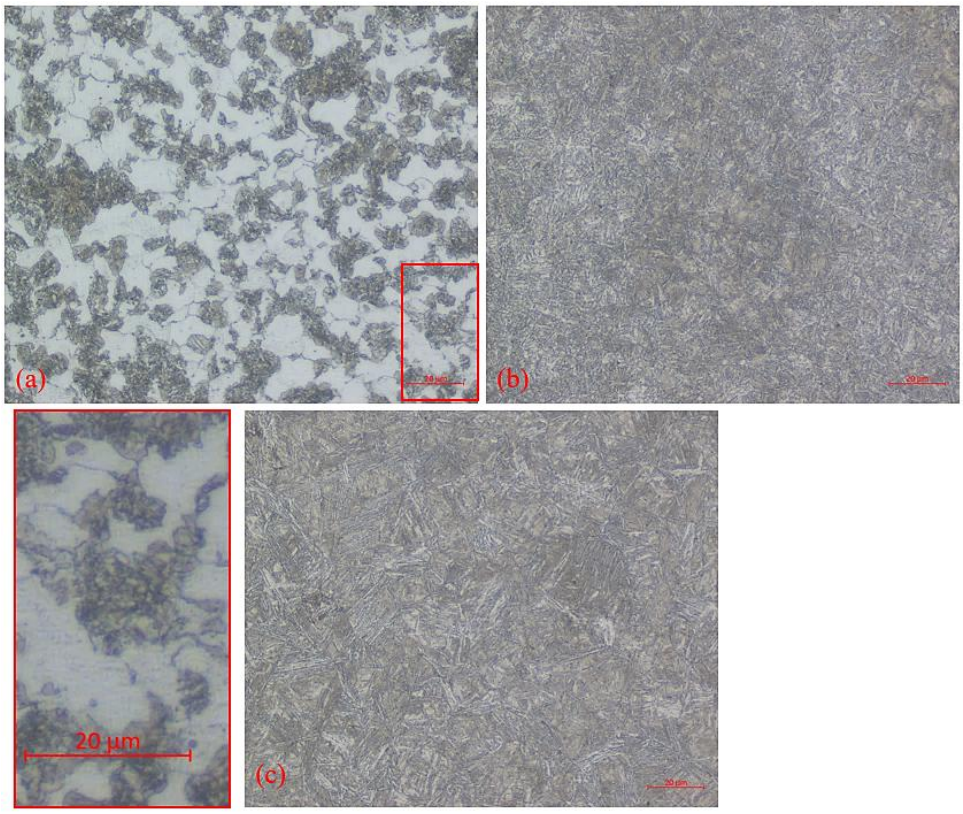

Figure 4.78 As-weld simulated HAZ microstructures of virgin material heated to different peak temperatures of (a) T_p=860°C, (b) T_p=1080°C and (c) T_p=1280°C

The microstructure of the HAZ that were simulated at 860, 1080 and 1280°C peak temperatures, subjected to PWHT and cooled at different rates/conditions are shown in Figure 4.79. At peak temperature 860°C, the microstructure of the specimens that were cooled in the furnace (a) and in air (b) appear similar regardless of the difference in cooling conditions. The furnace cooled HAZ that was simulated at peak temperature 1080°C (c) contains a mixture of coarse and fine grains (duplex grain structure). The average size of the grains was estimated to be about 50 µm and 4 µm for the coarse and fine grains, respectively. The air-cooled specimen (d), on the other hand, consisted of coarse grains throughout the structure. Ferrite was estimated to account for up to 74% of the area in the air-cooled specimen at peak temperature 1080°C. The microstructure of the 1280°C peak temperature HAZ specimen that was cooled in the furnace (e) consists of a bainite structure. The air-cooled specimen (f) had a similar appearance but with larger ferrite plates and scattered coarse grains of about 33 µm. In addition, air-cooled specimens contained coarse ferrite grains closer to the parent material that also had an average size of ~33 µm (G= ~2.5) and an area fraction of about 90% as shown in Figure 4.80. The average size of the fine aggregate grains in this area was estimated to be less than ~3 µm. The observed increase in the size of grains with increasing peak temperature is to be expected since for most Cr-Mo-V steels a

variation in the peak temperature between 955°C and 1390°C may result in an increase of the grain size from 20 µm to 200 µm (EPRI, 2008).

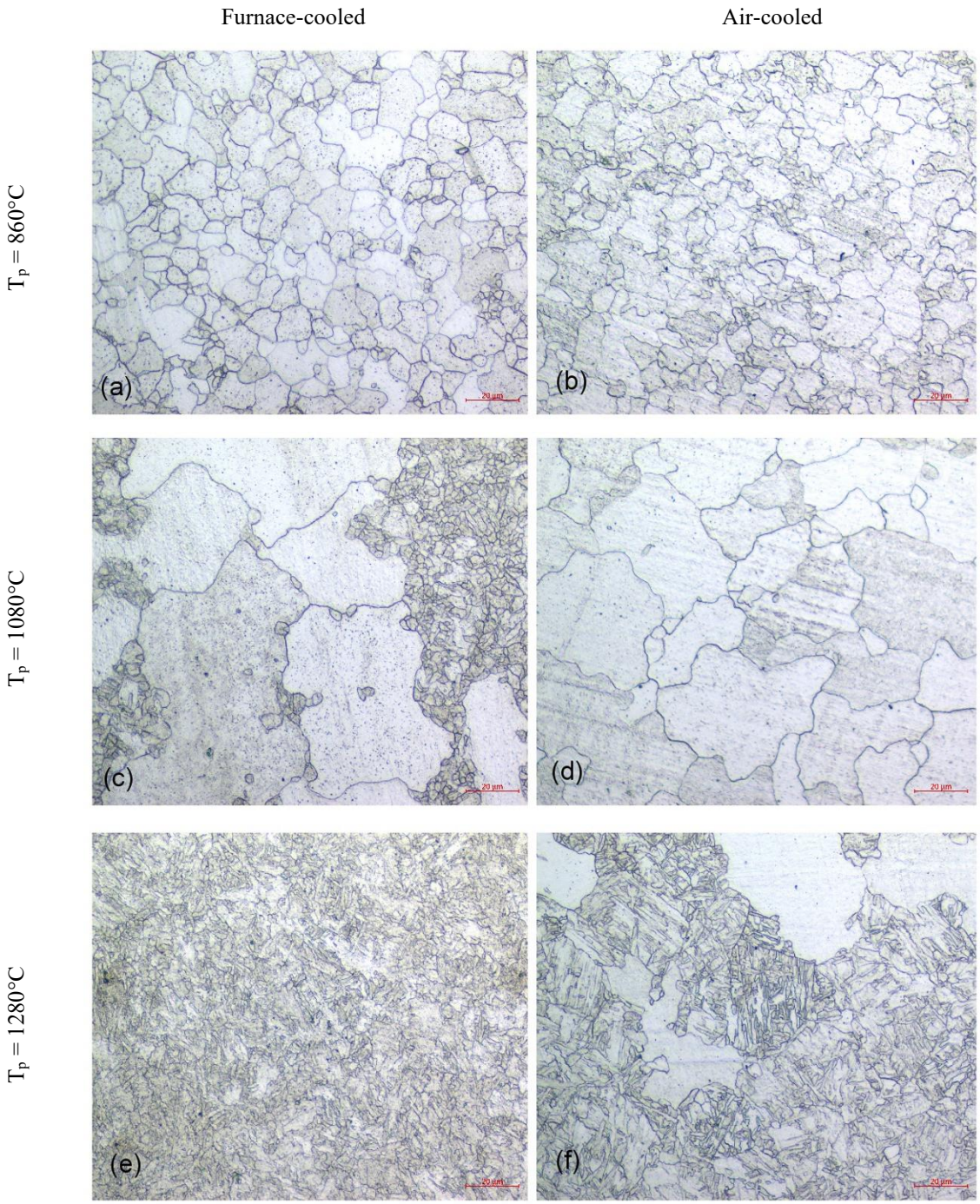

Figure 4.79 Microstructure of virgin material HAZ that was simulated at different peak temperatures, subjected to the same PWHT, and cooled in a furnace or in air.

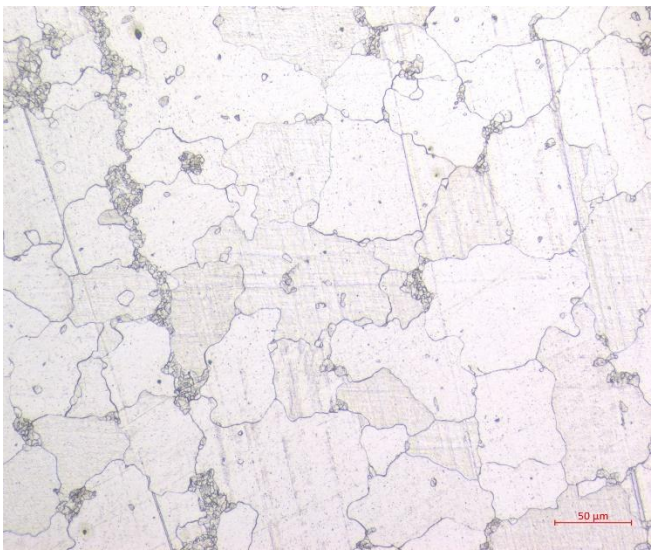

Figure 4.80 Coarse grains with fine aggregate observed on the air-cooled 1280°C peak temperature simulated HAZ specimen, next to the parent material

4.5.2.2 Microstructure of the HAZ regions simulated on service-exposed parent material

The average grain size and phase fractions that were observed on the simulated HAZ of the service-exposed material are presented in Table 4.30 as a function of HAZ simulation peak temperature and applied cooling conditions after PWHT. The results of grain size and phase fraction estimation are discussed in relation to the microstructure obtained at the various peak temperatures and cooling conditions.

Table 4.30 Grain size of service-exposed parent material simulated HAZ as a function of peak temperature and cooling condition

Peak Temperature (sample condition) [°C]		Line Length [µm]	Average No. of intercepts	Average grain size [µm]	ASTM grain size number [G]	Ferrite/Bainite/Carbide phase fraction [%Area]
RT	furnace	400	47	8.6	10.4	49/33/19
RT	air	400	45	9.0	10.3	34/38/28
860	as-weld	400	68	5.9	11.5	37/38/25
	furnace	400	47	8.5	10.5	60/21/19
	air	400	48	8.3	10.5	32/34/33
1080	as-weld	-	-	-	-	41/59
	furnace	400	-	-	-	38/19/43
	air	400	13	30.1	6.8	44/40/16
1280	as-weld	-	-	-	-	45/55
	furnace	-	-	-	-	30/26/44
	air	-	-	-	-	32/26/42

The microstructure of the service-exposed parent material is ferrite and carbide as discussed in Section 4.3.1. The microstructure that results from the service-exposed parent material being subjected to a heat treatment that is the same as PWHT and cooled either in furnace (a) or in air (b) are shown in Figure 4.81. The presented microstructure has very similar dimensional features, but with notable differences in phase fraction and appearance. The microstructure likely represents the tempered region of the HAZ. This may be due to the annealing temperature falling below A_{c1}, making the resulting microstructure independent of the cooling rate.

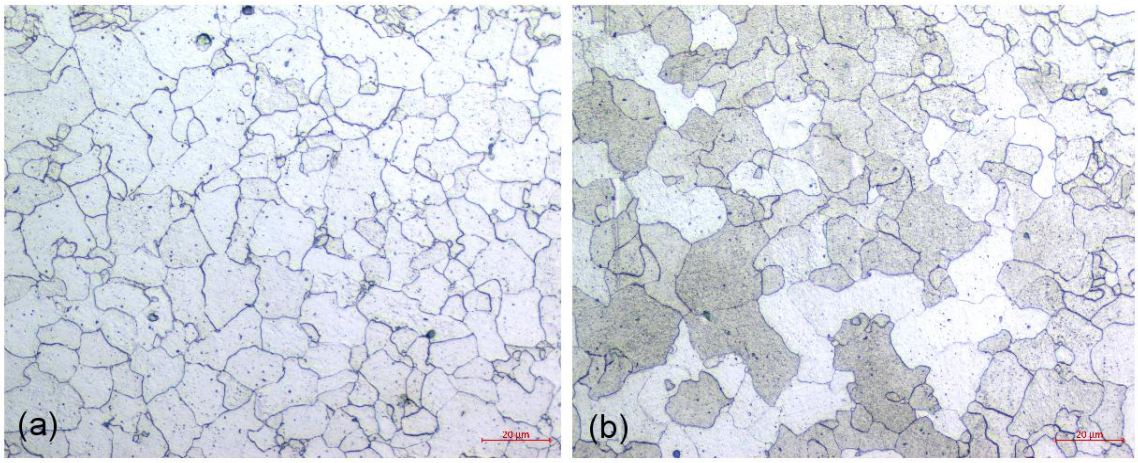

Figure 4.81 Microstructures of service-exposed parent material as heat-treated and cooled in (a) furnace or in (b) air

Figure 4.82 shows the as-weld microstructure of the service-exposed material simulated HAZ that was obtained at 860°C, 1080°C and 1280°C peak temperatures. At peak temperature 860°C (a) the microstructure is ferrite with pearlite/bainite carbide aggregate around the ferrite grains. A fine grain pearlitic/bainitic microstructure was obtained at peak temperature 1080°C (b). The 1280°C peak temperature (c) as-weld specimens showed a microstructure with bainitic sheaves and fine needles of carbide lamella (shown on insert).

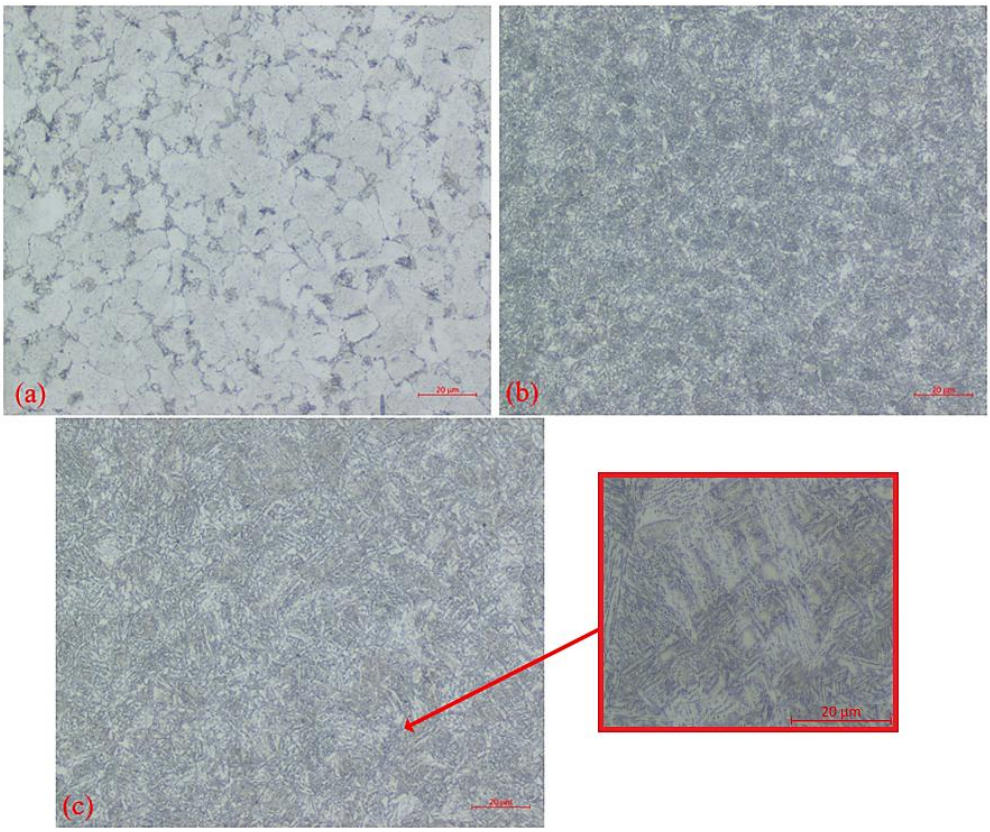

Figure 4.82 As-weld simulated HAZ microstructures of service-exposed material heated to different peak temperatures of (a) Tp=860°C, (b) Tp=1080°C and (c) Tp=1280°C

The microstructure of the HAZ simulated on the service-exposed parent material and subjected to PWHT and different cooling conditions is shown in Figure 4.83. The HAZ simulated at peak temperature 860°C, subjected to PWHT and cooled in the furnace (a) or in air (b) resulted in similar microstructure. However, there is noticeable difference in the phase fraction, which may be due to the different cooling conditions. The slower cooling rates in the furnace allow for more carbon diffusion and dissolution of carbides. The air-cooled simulated HAZ at peak temperature 1080°C (d) is characterised by large grains of different phases. The microstructure is likely that of massive ferrite, which typically observed when ferritic material is cooled rapidly from the austenitic temperature region. However, an area of fine grains (~27%) was also observed next to the parent material as shown in Figure 4.84(b). The size of these fine grains ranges from 2-6 μm. Very fine grains were observed on the furnace cooled HAZ simulated at peak temperature 1080°C (c). The size of these grains could not be measured accurately with the intercept method. In addition, an area of mixed coarse (69%) and fine grains (31%) was observed in samples shown in Figure 4.84(a). The duplex structure was located between the fine grain HAZ and parent material. The average size of the coarse grains was estimated to be ~42 μm and the fine grains were 4-6 μm. Scattered creep voids (~3 μm) were also noted throughout this microstructure. At peak temperature 1280°C, the air-cooled simulated HAZ (f) was observed to consist of acicular ferrite with pearlite/bainite carbide phase fraction. Farther away from this section, an area of fine grains (~4 μm) was noted next to the parent material. The furnace-cooled simulated HAZ (e) exhibits a microstructural appearance similar to that of the air-cooled HAZ, however, it lacks the fine-grained region observed in the air-cooled specimens.

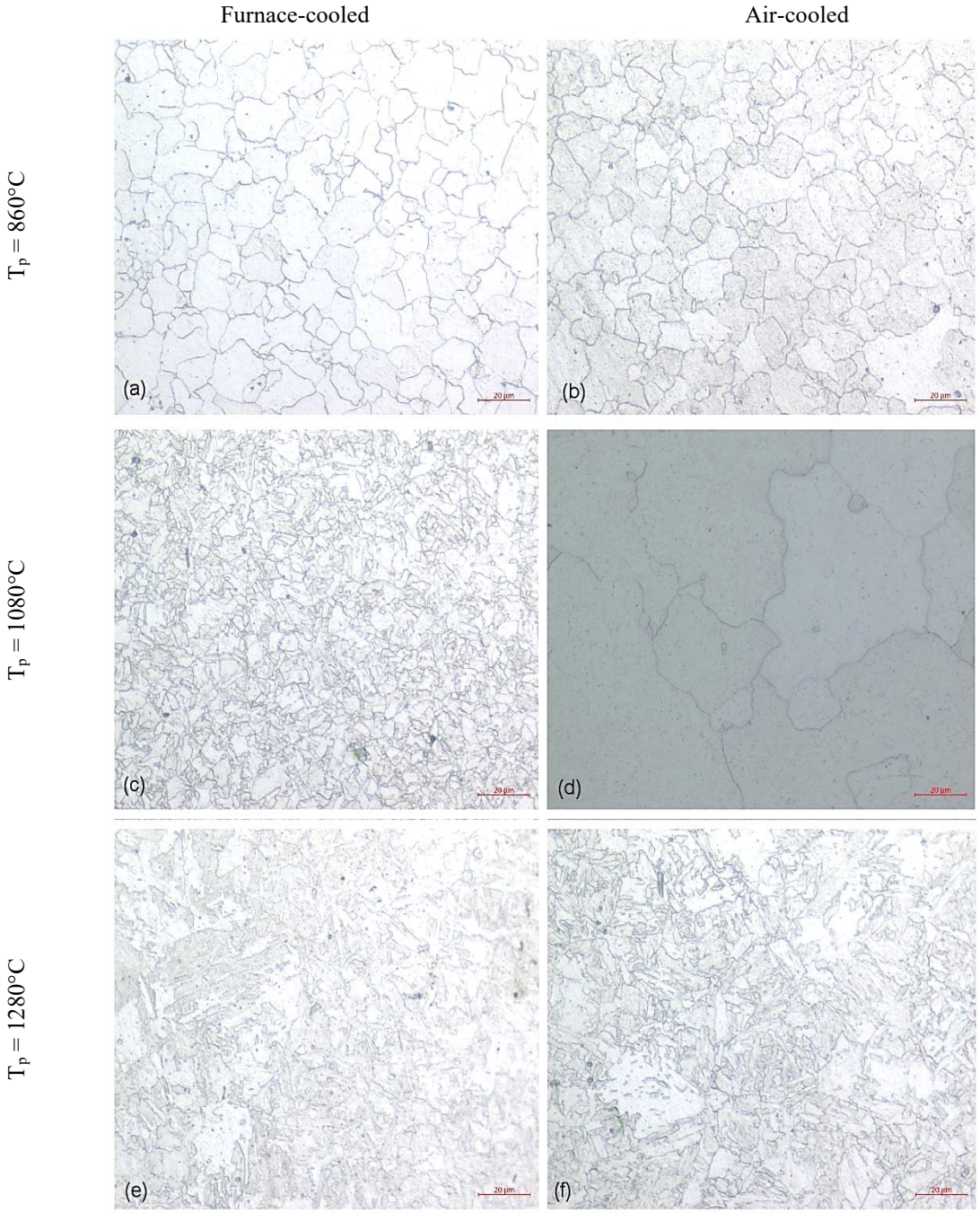

Figure 4.83 Simulated HAZ microstructures of service-exposed material heated to different peak temperatures and subjected to PWHT with different cooling conditions. Tp=860°C cooled in furnace (a) or in air (b), Tp=1080°C cooled in furnace (c) or in air (d) and Tp=1280°C cooled in furnace (e) or in air (f).

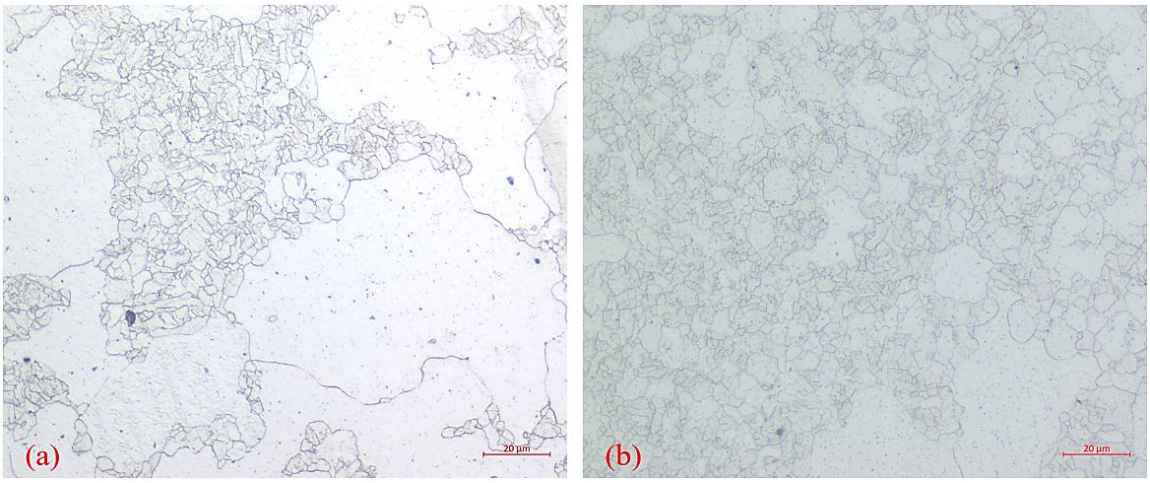

Figure 4.84 Areas of duplex grain size observed on the simulated HAZ microstructures of service-exposed material heated to 1080°C peak temperature and cooled in furnace (a) or in air (b) after PWHT

4.5.3 Assessment of Mechanical Properties of Simulated HAZ Regions

Mechanical properties of the simulated HAZ regions of the virgin and service-exposed parent materials are presented in this section. Hardness and impact properties of the simulated HAZ were assessed against the 860°C, 1080°C and 1280°C peak temperatures. In addition, the effects of PWHT and subsequent cooling rates on the hardness and impact properties of the simulated HAZ were evaluated.

4.5.3.1 Hardness Assessment of the virgin material simulated HAZ regions

The average hardness of the virgin parent material (as-received and heat-treated) and the HAZ simulated from the virgin parent material are shown in Figure 4.85 as a function of peak temperature and cooling conditions after heat-treatment.

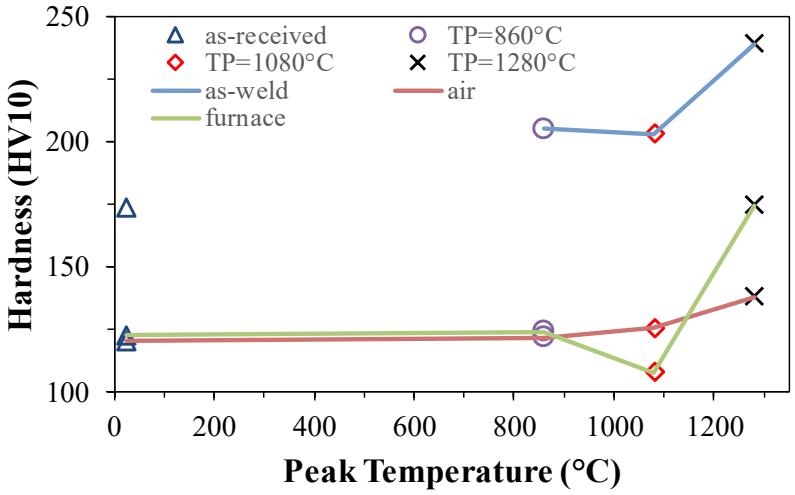

Figure 4.85 Hardness of virgin material simulated HAZ at different thermal cycles and subjected to different heat treatment cooling rates

The as-received parent material is within the acceptable hardness range of 14MoV6-3 steel (British Standards Institution, 2007). However, the hardness of the heat-treated (same as PWHT) parent material that was cooled in the furnace and the one that was cooled in air, fall well below the acceptable hardness range of 14MoV6-3 steel. The parent materials are seemingly not affected by the cooling rate, which correlates to the observations that were made on the microstructure as previously shown in Figure 4.77. The hardness and microstructure of the HAZ simulated at peak temperature of 860ºC and subject to PWHT was also not affected by the cooling rate as previously shown on the microstructure in Figure 4.79. A hardness of about 125 HV_{10} is achieved through the heat treatment, regardless of the prior state of the material and applied cooling rate. This is because any cooling rate from process annealing temperatures below A_{c1} results in the same microstructure and hardness (Dossett & Boyer, 2006; Totten, 2007). Also, the material was originally tempered at 715°C during manufacturing. This temperature was exceeded during this experiment, and that could lead to softening and loss of other mechanical properties (Bailey, 1994).

The simulated HAZ specimens that were not subjected to any PWHT (as-weld) showed the highest hardness values that fall outside the acceptable hardness range of 14MoV6-3 steel. The as-weld HAZ of peak temperature 1280ºC has an average hardness of approximately 240 HV_{10}. In general, the hardness of the simulated HAZ were observed to increase with the increase in peak temperature except for the furnace cooled HAZ at peak temperature 1080ºC where the lowest hardness was recorded. This softening may be due to the carbide spheroidization phenomenon (Arruabarrena, et al., 2011). The air-cooled simulated HAZ does not display this behaviour due to the relatively faster cooling rate applied after PWHT.

Nonetheless, the lowest hardness values were typically expected in the ICHAZ region due to the soft zone that occurs in this HAZ sub-region. All the simulated HAZ have the highest hardness at the peak temperature of 1280ºC, which correlates with the observed microstructure and the description of the CGHAZ.

The benefits of PWHT in achieving acceptable hardness are quite clear and that a controlled cooling environment is more favourable than cooling in open air. However, care must be taken to avoid the undesired softening effects that were observed on the furnace cooled simulated HAZ at peak temperature 1080ºC.

4.5.3.2 Impact properties of the virgin material simulated HAZ regions

The room temperature impact properties of the HAZ that were simulated from the virgin parent material are listed in Table 4.31. The average impact energy of the as-received, as-weld, furnace-cooled and air-cooled specimens of the virgin material were well above the specified minimum average impact energy of 14MoV6-3 steel at room temperature (British Standards Institution, 2007). However, when assessing each peak temperature, the as-weld specimens at peak temperature 860ºC showed poor impact properties and had a total impact energy that is below the minimum criteria. Nonetheless, in all the tested specimens, most of the energy was absorbed during the crack propagation process except for the air-cooled HAZ at peak temperature 860ºC.

Table 4.31 Charpy impact toughness properties of virgin material at room temperature

Specimen Condition	Peak temperature [°C]	Energy required for crack		Absorbed energy	
		Initiation [J]	Propagation [J]	Total [J]	Average [J]
As-received	PM	27	341	368	368
As-weld	860	4	14	18	
	1080	54	74	128	139
	1280	79	191	270	
Furnace Cooled	PM	–	–	–	Not tested
	860	3	375	378	
	1080	57	309	366	373
	1280	6	370	375	
Air Cooled	PM	59	272	331	331
	860	56	29	85	
	1080	51	172	223	235
	1280	51	347	398	

Figure 4.86 shows the variation of total absorbed energy with peak temperature for the HAZ specimens as tested at room temperature. An average of 368 J was recorded for the as-received parent material, and this was slightly reduced to 331 J on a parent material specimen that was subject to heat treatment (same as PWHT) and allowed to cool in air. The HAZ simulation without any PWHT drastically reduced the impact energy of the virgin material, especially at peak temperature of 860ºC. The furnace cooled HAZ specimens showed a more uniform behaviour, which may be attributed to the effect of PWHT and the slower cooling rate that results in a homogeneous microstructure. There is a noticeable decrease in impact toughness of the as-weld and air-cooled HAZ specimens in the region of the ICHAZ microstructure at peak temperature of 860ºC. The as-weld and air-cooled HAZ specimens showed similar behaviour of increasing impact toughness with peak temperature. However, the air-cooled specimens have higher values of impact toughness. The largest difference (~128 J) is observed at peak temperature of 1280ºC. This difference may be attributed to the PWHT and subsequent cooling rate of the simulated HAZ. The lowest value in impact toughness is observed on the as-weld HAZ at peak temperature of 860ºC. Moreover, the low impact toughness values of the as-weld and air-cooled ICHAZ specimens coincide with the

region where type IV cracking is likely to occur. The low impact energy values are seemingly avoided by cooling the specimen at slower rates, in a controlled environment.

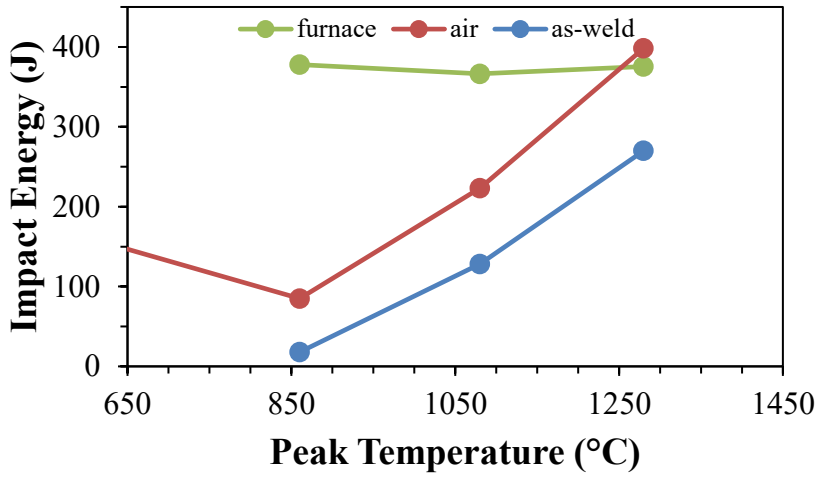

Figure 4.86 Impact energy vs peak temperature of different specimens of the virgin parent material simulated HAZ regions

4.5.3.3 Hardness Assessment of the service-exposed material simulated HAZ regions

Figure 4.87 shows the average hardness of the as-received and heat-treated service-exposed parent material together with that of the service-exposed simulated HAZ, as a function of peak temperature.

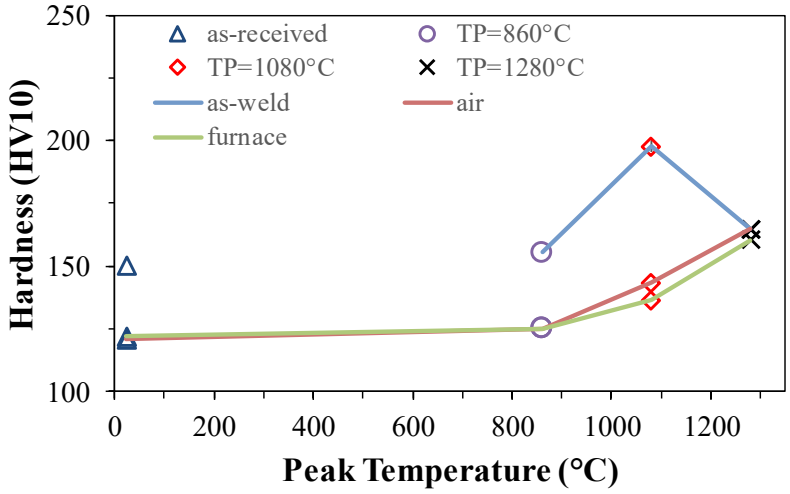

Figure 4.87 Hardness of service-exposed material simulated HAZ at different thermal cycles and subjected to different heat treatment cooling rates

The as-received service-exposed parent material had acceptable hardness at room temperature (British Standards Institution, 2007). The hardness of the service-exposed material was observed to drop to unacceptable level when the material was heat treated and cooled in either air or furnace. On the other hand, the hardness of the simulated HAZ was observed to vary with PWHT and cooling conditions. The hardness of the material only increased slightly when subject to peak temperature of 860°C with no PWHT. This was followed by an increase of up to 198 HV_{10} at peak temperature1080°C. The hardness then decreased to 165 HV_{10} at peak temperature of 1280°C. The hardness at peak temperature of 1080°C falls outside the acceptable hardness range of 14MoV6-3 steel.

The hardness of the simulated HAZ that was subject to PWHT, and different cooling conditions increased with the increase in peak temperature. However, the difference in cooling rate at peak temperature 860°C does not play a role in the decrease of hardness since the same hardness is obtained regardless of cooling conditions. There is only a slight difference in hardness of the PWHT simulated HAZ, which may be attributed to cooling conditions at peak temperature 1080°C. Noticeably, at the peak temperature of 1280°C, the hardness of the simulated HAZ hardly changes with the application of PWHT and subsequent cooling rate. The lowest hardness values were measured at the ICHAZ region, which is consistent with the expected behaviour of low alloy steels.

Overall, the current PWHT and subsequent cooling rate does not appear to be of benefit in the service-exposed material. Appropriate PWHT temperature and cooling conditions need to be evaluated and selected to achieve microstructure of acceptable hardness.

4.5.3.4 Impact properties of the service-exposed material simulated HAZ regions

The room temperature impact properties of the service-exposed material simulated HAZ regions are shown in Table 4.32.. The average absorbed energy of the service-exposed parent material (as-received) at room temperature is much lower than the specified minimum average absorbed energy of 14MoV6-3 steel (British Standards Institution, 2007). However, the average impact energy of the heat-treated parent material, as-weld, air-cooled and furnace-cooled HAZ are within the specification. There was noticeable improvement in impact energy when the parent material was heat treated and allowed to cool in either air or furnace. An average of 68 J and 364 J was obtained for the specimens cooled in air and in

the furnace, respectively. Most of the energy was absorbed during the crack propagation process in all the specimens.

Table 4.32 Charpy impact toughness properties of service-exposed material at room temperature

Specimen Condition	Peak temperature [°C]	Energy required for crack		Absorbed energy	
		Initiation [J]	Propagation [J]	Total [J]	Average [J]
As-received	PM	6	6	12	12
As-weld	860	51	72	123	
	1080	5	165	170	116
	1280	7	48	55	
Furnace Cooled	PM	51	313	364	364
	860	40	33	73	
	1080	36	361	398	251
	1280	39	243	282	
Air Cooled	PM	21	47	68	68
	860	29	40	70	
	1080	50	122	172	199
	1280	50	306	355	

Figure 4.88 shows the variation of total absorbed energy (at room temperature) with peak temperature for the different specimens of the service-exposed material simulated HAZ regions. The as-weld simulated HAZ impact energy did not vary much with temperature between the peak temperatures of 860°C and 1080°C. However, it decreased with increasing temperature up to peak temperature of 1280°C. The lowest value (55 J) in impact toughness of the as-weld simulated HAZ may be attributed to grain coarsening and formation of the upper bainitic structure. When the specimens were subjected to PWHT and cooled in air, the impact energy was observed to increase with increasing peak temperature. The highest impact energy was recorded at the peak temperature of 1280°C. The specimens that were cooled in the furnace following the PWHT recorded the highest value of impact energy at the peak temperature of 1080°C. The impact energy of the furnace cooled simulated HAZ was observed to first increase with increasing peak temperature between 860°C and 1080°C. It then decreased with increasing peak temperature up to peak temperature of 1280°C. Nevertheless, it is apparent that the applied PWHT had a regenerating effect on the impact

properties of the service-exposed material. The ICHAZ impact toughness values of all the specimens were observed to be relatively lower than those of other regions, except for the as-weld specimens at the peak temperature of 1280°C. The applied PWHT does not seem to resolve the susceptibility of the service-expose material to type IV cracking.

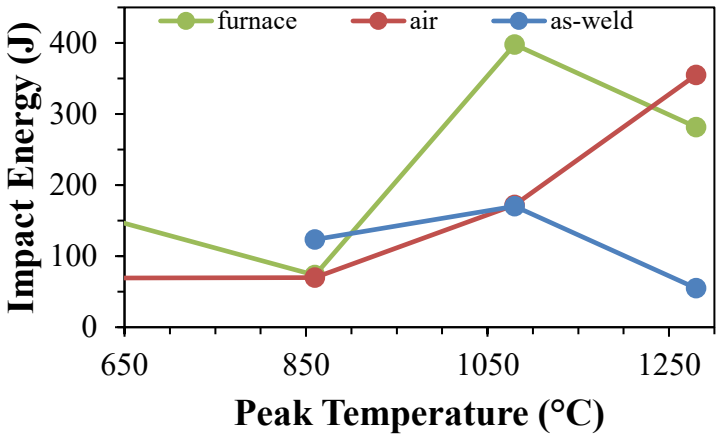

Figure 4.88 Impact energy vs peak temperature of different specimens of the service-exposed parent material simulated HAZ regions

4.5.4 Gleeble Hot Tensile Test

Gleeble hot tensile tests were done on the virgin and service-exposed parent materials at 500°C, 540°C and 560°C. The Gleeble hot tensile tests were done at a strain rate of 10^{-1} s^{-1}, which is higher than the strain rate used on the conventional tensile testing machine. The increase in strain rate has an effect of increasing the flow stress (Davis, 2004). Machine generated data was used to estimate the hot tensile properties of the virgin and service-exposed parent materials. The proof strength was estimated from the stress-strain results at an offset strain of 0.2% using linear regression as shown in Figure 4.89. The UTS, which is notably higher than that of the pseudostatic tensile test due to strain hardening, was taken as the highest stress value from the tensile test results since the experiment program was setup to output engineering stress-strain data. However, this approach does not cater for the strain rate dependency of the material. The strain dependency was quantified by taking the log of the relationship $\sigma_y = \dot{\varepsilon}^m$ as shown in Equation 3.6 (Davis, 2004; Khan, et al., 2008; Jankowski, et al., 2019). The slope of the linear fitted curve of the strain rate sensitivity (m) for 500, 540 and 560°C and strain rate of 2.5×10^{-4} and 10^{-1} s^{-1} are shown in Figure 4.90. The virgin material has a negative dependence of flow stress on strain at 500°C, 540°C and 560°C, i.e., strength increased with the increase in strain. The service-exposed material has a

negative dependency at 540°C and 560°C as the yield strength decreases with the increase in strain, except at 500°C where m is positive.

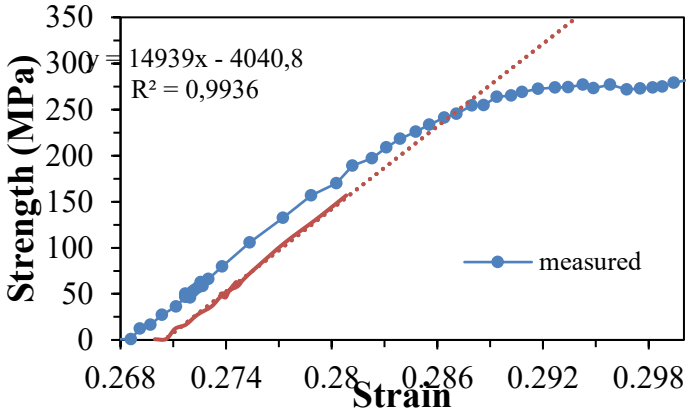

Figure 4.89 Estimation of Proof strength from stress-strain curve at 500°C

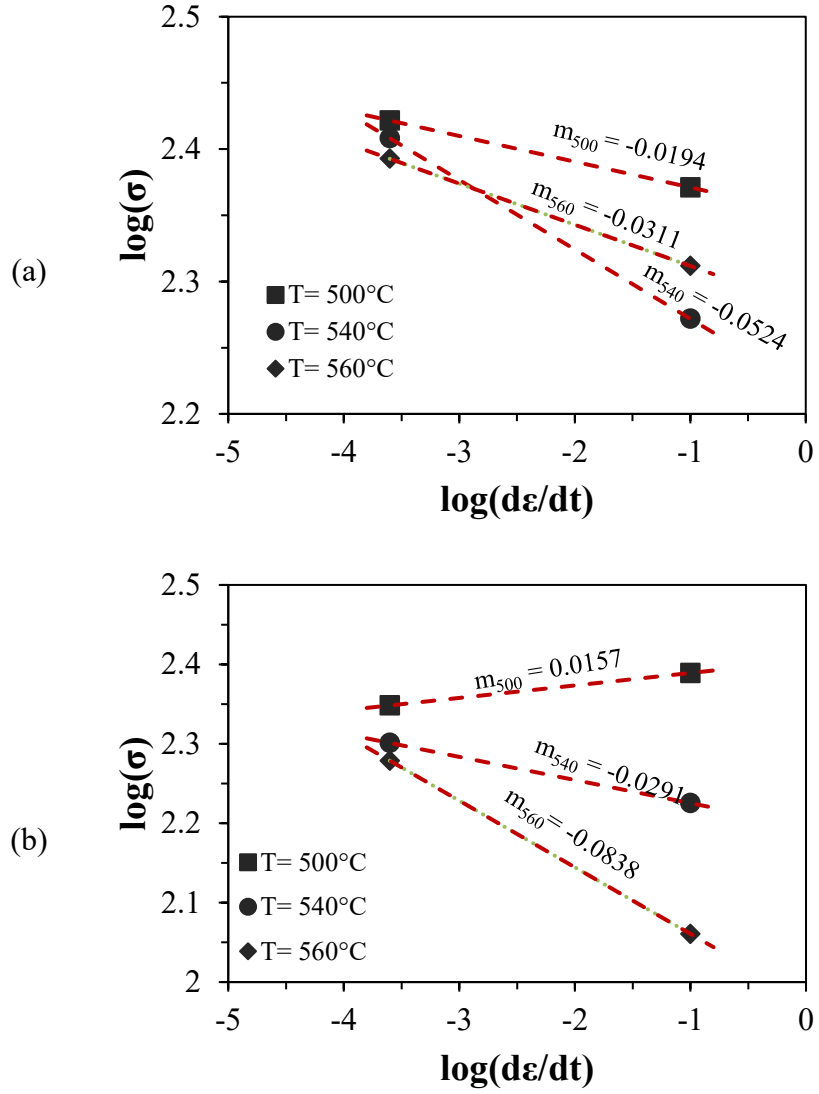

Figure 4.90 Strain rate sensitivity (m) of the (a) virgin and (b) service-exposed material at 500, 540 and 560°C and strain rate of 2.5×10^{-4} and 10^{-1} s^{-1}

The temperature dependency of stress for the virgin and service-exposed materials at the strain rate of 2.5×10^{-4} and 10^{-1} s^{-1} is shown in Figure 4.91. For the service-exposed material, the stress has a strong temperature dependency at the strain rate of 10^{-1} s^{-1} compared to the 2.5×10^{-4} s^{-1} strain rate. The slope of the linear fitted curve gives the relationship Q/Rn, where Q is the activation energy ($Jmol^{-1}$), R is the molar gas constant (8.3145 $Jmol^{-1}$ K^{-1}) and n is a material constant that is inversely proportional to the strain rate sensitivity (Yang, et al., 2021).

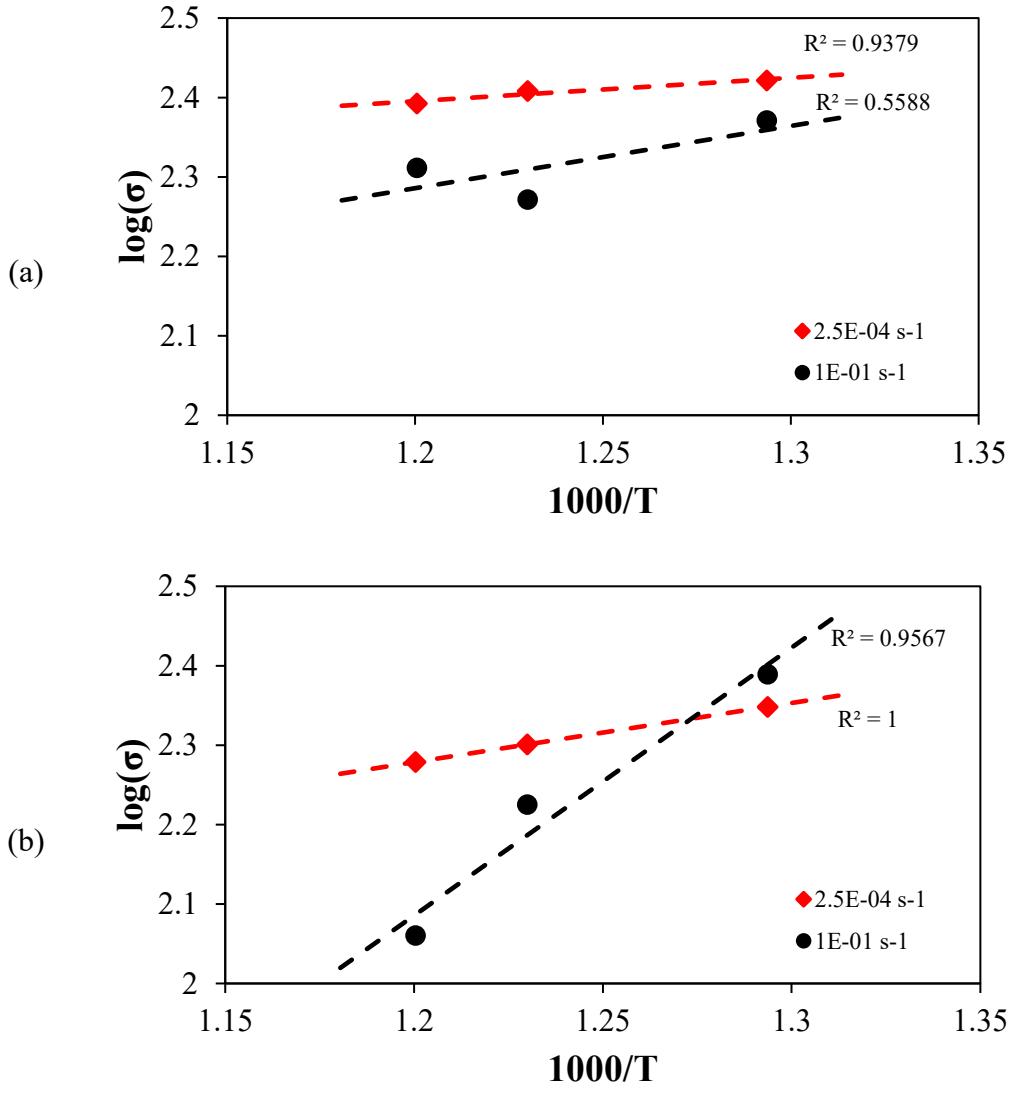

Figure 4.91 Temperature dependence of stress of the (a) virgin and (b) service-exposed material at different strain rates

4.5.4.1 Hot Tensile Properties of the Virgin Parent Material

Hot tensile properties of the virgin parent material are presented in Table 4.33. Figure 4.92 shows the stress-strain diagram of the virgin material. The specimens that were tested at 500°C were unbroken and did not undergo any dimensional changes, which could be explained by strain hardening. These specimens may have a higher UTS then reported.

Table 4.33 Gleeble hot tensile properties of virgin parent material

Test Temperature [°C]	Yield Strength [MPa]	Tensile Strength [MPa]	Yield-Tensile Ratio	Elongation [%]	Reduction in Area [%]
500	235	826	0.28	-	-
540	187	696	0.27	8	74
560	205	846	0.24	8	79

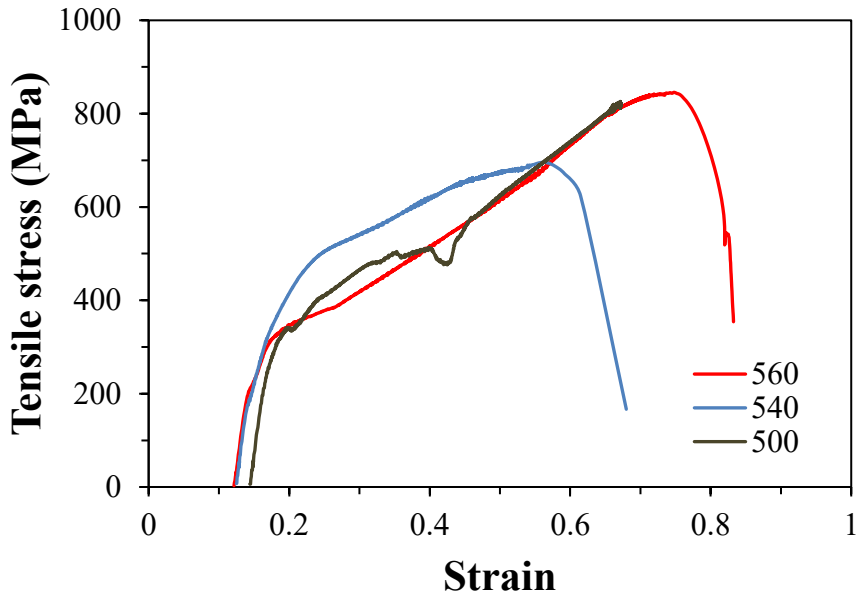

Figure 4.92 Stress-strain curve of the virgin material at 500, 540 and 560°C

Figure 4.93 shows the variation of tensile properties as a function of testing temperature. The material was observed to have good ductility that increased with increasing temperature. The proof strength of the material decreased with increasing temperature, which is characteristic of low alloy steels.

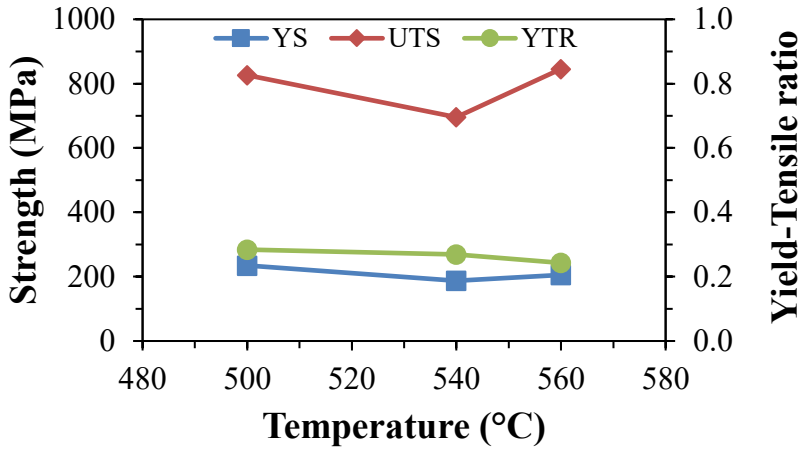

(a)

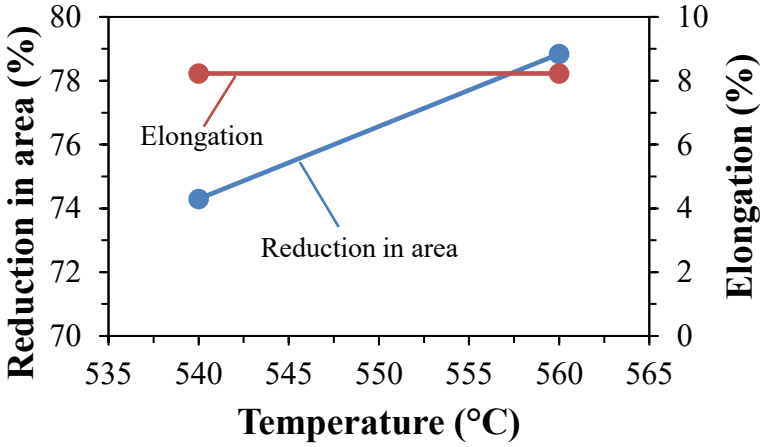

(b)

Figure 4.93 (a) Variation of virgin parent material Yield strength, UTS, Yield-Tensile ratio with temperature and (b) reduction in area and elongation with temperature.

The appearance of the fracture surfaces of the specimens that were tested at 540 and 560°C are shown in Figure 4.94. The fracture appearance is typical of ductile fracture.

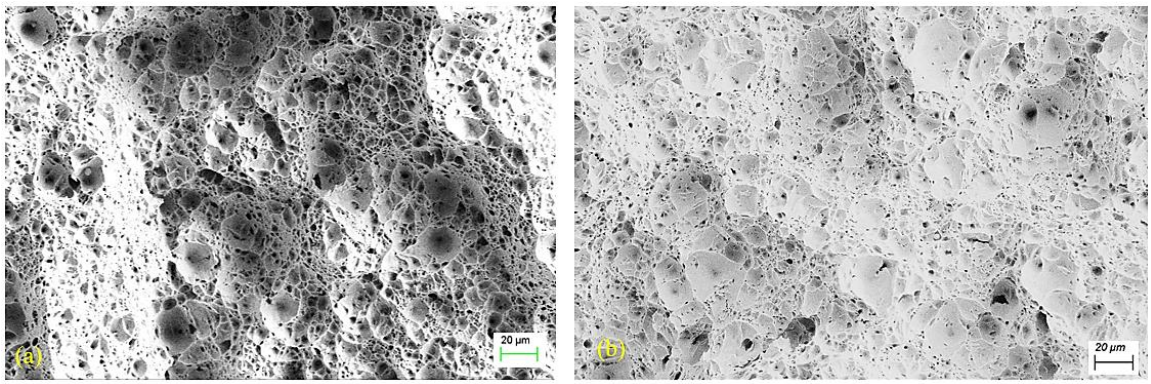

Figure 4.94 Fracture appearance of the specimens tested at (a) 540°C and (b) 560°C

A post-test Gleeble® hot tensile specimen, reassembled to measure dimensional changes, is shown in Figure 4.95. The reduction in area is more apparent than the elongation of the specimen.

Figure 4.95 Typical post-test Gleeble® hot tensile specimen of the virgin parent material

4.5.4.2 Hot Tensile Properties of the Service-exposed Parent Material

Hot tensile properties of the service-exposed parent material are listed in Table 4.34. Figure 4.96 shows the stress-strain diagram of the service-exposed parent material. The tensile stress was observed to decrease with the increase in temperature.

Table 4.34 Gleeble hot tensile properties of service-exposed parent material

Test Temperature [°C]	Yield Strength [MPa]	Tensile Strength [MPa]	Yield-Tensile Ratio	Elongation [%]	Reduction in Area [%]
500	245	890	0.28	7	67
540	168	665	0.25	6	69
560	115	558	0.21	8	69

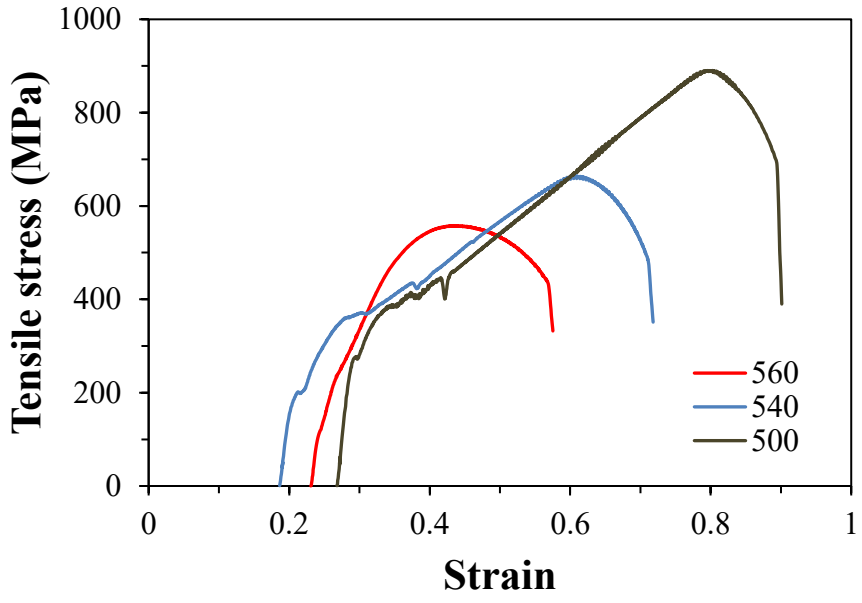

Figure 4.96 Stress-strain curve of the service-exposed parent material at 500, 540 and 560°C

The change in hot tensile properties of the service-exposed material as a function of testing temperature is shown in Figure 4.97. The decrease in strength with the increase in temperature is typical of 14MoV6-3 (British Standards Institution, 2007).

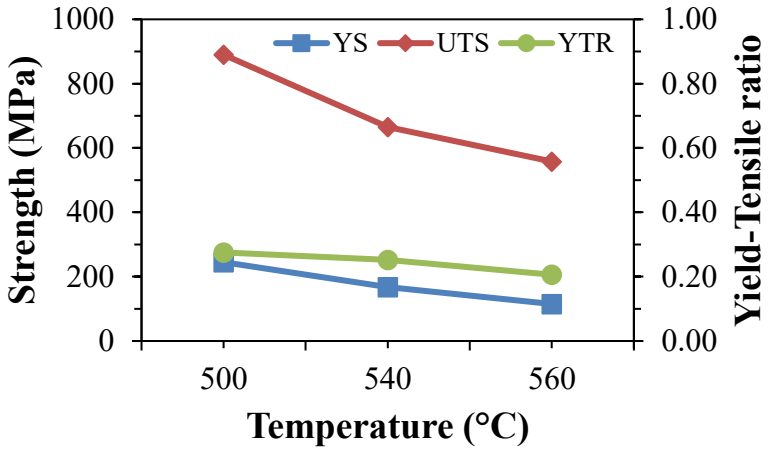

(a)

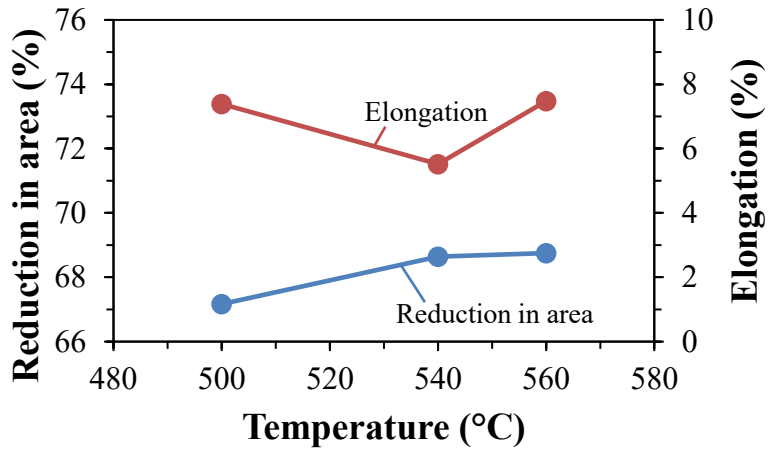

(b)

Figure 4.97 (a) Variation of service-exposed parent material Yield strength, UTS, Yield-Tensile ratio with temperature and (b) reduction in area and elongation with temperature.

The appearance of fracture surfaces of the service-exposed parent material specimens that were tested at 500°C, 540°C and 560°C are shown in Figure 4.98. The fracture surface was typical of ductile fracture with dimples and MnS inclusions observed in the specimens that were tested at 500°C, 540°C and 560°C. The fracture surface appears progressively rougher with increase in temperature, which correlates with the percentage reduction in area. This is an indication that an increased number of micro voids come in contact and coalesce as the temperature increases, which is evident from the micrographs. At 500°C (a) the fracture initiation sites (particles) are quite distinguishable, whereas at 560°C (c) the surface is micro void coalescence.

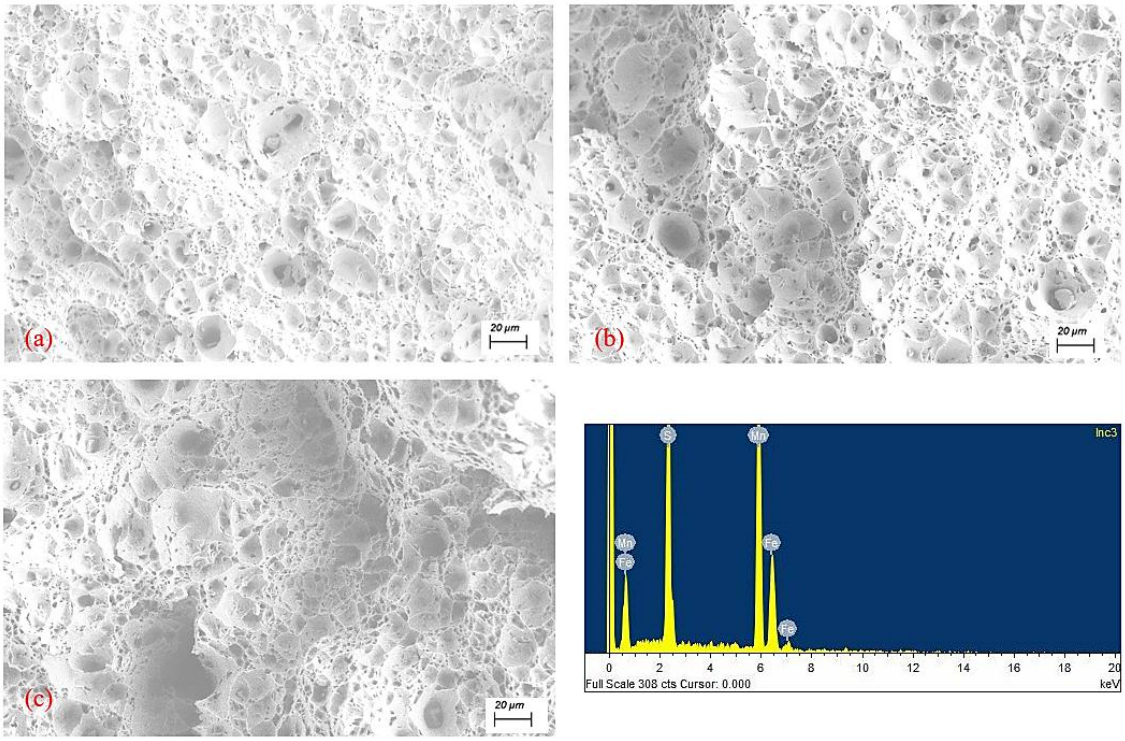

Figure 4.98 Fracture appearance of the specimens tested at (a) 500°C, (b) 540°C and (c) 560°C. Spectrum of inclusions observed in these specimens.

4.6 Thermo-Calc Thermal Equilibrium Simulation

This section presents the thermodynamics equilibrium simulations that were done for the virgin and service-exposed parent materials and the weld metal. The chemical composition of the virgin and service-exposed parent material and the weld metal presented in Table 3.3 were used as input data for the phase transformation simulation. The property diagrams obtained for the virgin parent material, service-exposed parent material and weld metal were very similar. The weight fraction of each phase, as a function of temperature, was noted to vary differently in these materials. Therefore, for each material, each phase and its composition was analysed over the range of temperature that it is present in. The evolution of equilibrium phases with temperature was examined and the composition of phases that are stable at service temperature of 540°C was also analysed in detail.

4.6.1 Transformation Simulation of Virgin Parent Material

The Thermo-Calc equilibrium plot of stable phase proportions of the virgin parent material are shown in Figure 4.99 as a function of temperature. The simulation shows the

transformation temperature A_{c1} and A_{c3} at approximately 729°C and 867°C, respectively. The solidus and liquidus temperatures are observed at 1460°C and 1516°C. The phases that nucleate and grow at specific temperatures under equilibrium conditions are presented together with the key transformation temperatures. The equal ratio of ferrite (BCC_A2) and austinite (FCC_A1) phases occurs at about 825°C.

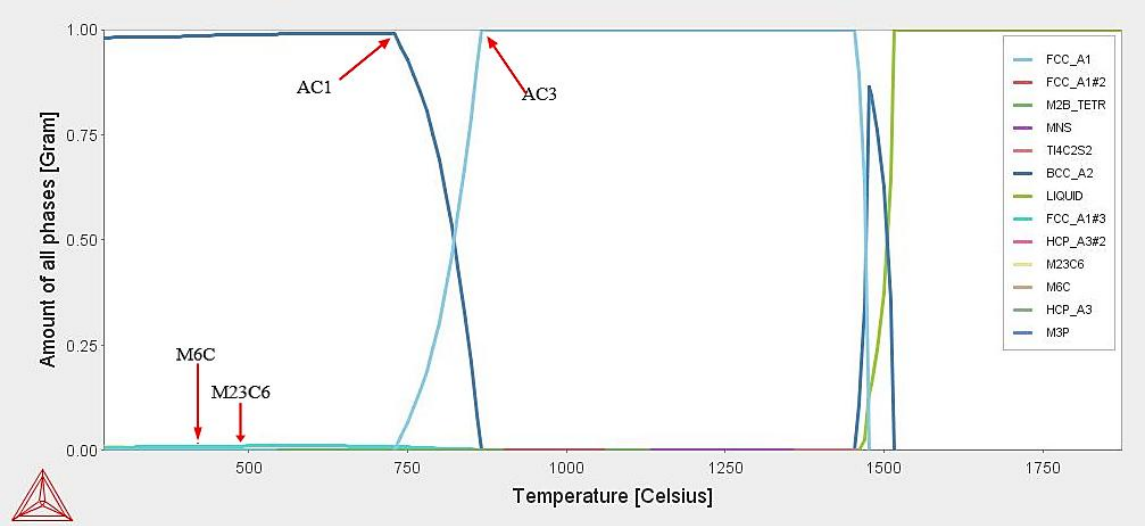

Figure 4.99 Thermo-Calc property diagram of the virgin parent material

The weight fraction of significant equilibrium phases that form around the operating temperature range are shown in Figure 4.100. The maximum weight fraction of $M_{23}C_6$ is approximately 0.86 wt.% at 273°C with a solvus temperature of about 468°C. This fraction increases with decreasing temperature. M_6C has a solvus temperature of approximately 416°C and its weight fraction first increases with decreasing temperature up to about 390°C. It then remains relatively stable until about 320°C, where it starts decreasing with temperature until it reaches a temperature of approximately 278°C and an estimated weight fraction of 0.0058 wt.%. The decrease is most likely due to the formation of HCP_A3 and a small fraction of M_3P, which both increase with decreasing temperature. The HCP_A3 phase reaches a maximum weight fraction of approximately 0.30 wt.% and M_3P reaches 0.021 wt.%. The maximum weight fraction of M_6C occurs at 324°C and is about 0.22 wt.%. Small amounts of MC, M_2B and MnS are stable throughout this temperature range. A small fraction of Cu-rich FCC is also present in this service temperature range. This may be due to the low solubility of copper in iron at low temperatures and the small Cu content in the material (Korzhavyi, et al., 2018).

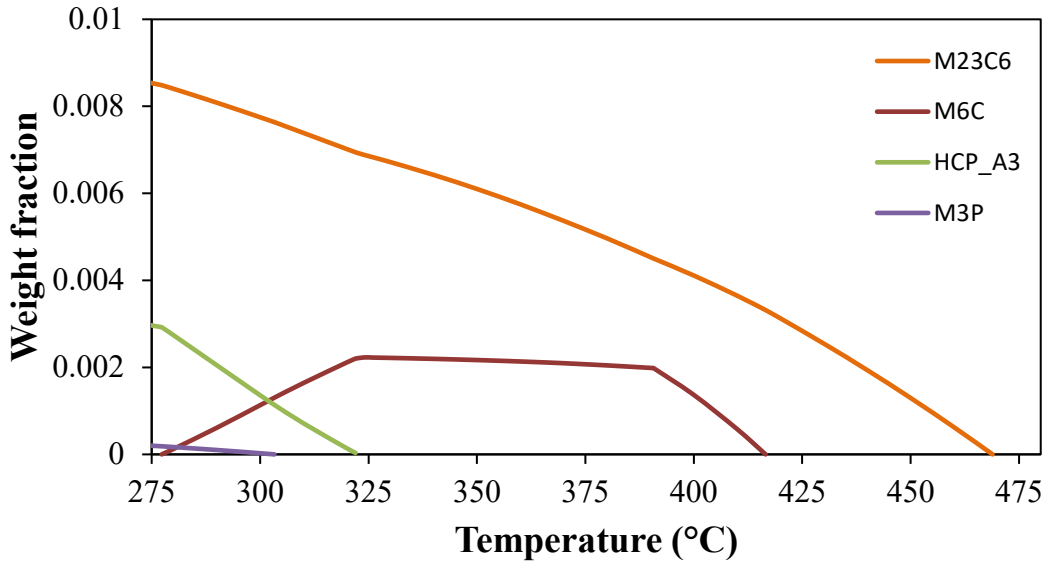

Figure 4.100 Plot of weight fraction vs temperature of the stable phases in virgin parent material

The stable phases that were present at the service temperature of 540°C were BCC, FCC (MC precipitate), the sulphide MnS, the boride M_2B and the Cu-rich FCC. The estimated average formulae and nominal compositions of the stable phases at operating temperature are given in Table 4.35.

Table 4.35 Estimated equilibrium phase composition of the virgin parent material at operating temperature of 540°C

Phase	Estimated Average Formula	Nominal Composition	Comment
BCC_A2	(Fe, Mn, Cr, Si, Mo, Ni, Cu, V, Co, P, Al, Ti, Nb, B, S)1C	Mainly Fe	Matrix
FCC_A1#2	(Fe, Mn, Cr, Si, Mo, Ni, Cu, V, Co, P, Al, Ti, Nb, B, S)1C	Mo, Cr and V rich $(Mo_{0.36}V_{0.37}Cr_{0.36})C_1$	MC precipitate
MnS	(Fe, Mn)1S1	MnS	Sulphide
M2B_TETR	(Fe, Cr, Mo, Ni)2B1	$(Fe_{1.14}Cr_{0.86})B_1$	Boride
FCC_A1#1	(Fe, Mn, Cr, Si, Mo, Ni, Cu, V, Co, P, Al, Ti, Nb, B, S)1C	Mainly Cu	Cu-rich precipitate

4.6.2 Transformation Simulation of Service-exposed Parent Material

Thermo-Calc equilibrium plot of stable phase proportions as a function of temperature for the service-exposed parent material are shown in Figure 4.101. The property diagram shows

the phases that nucleate and grow on cooling under equilibrium conditions. The key transformation temperatures are also indicated. The simulation shows the transformation temperature A_{c1} and A_{c3} at approximately 769°C and 889°C, respectively. The solidus and liquidus temperatures are observed at about 1418°C and 1520°C. Transformation of ferrite (BCC_A2) to austinite (FCC_A1) occurs in a slightly higher temperature in the service-exposed parent material compared to the virgin material with the ratio of the two phases equal at about 855°C.

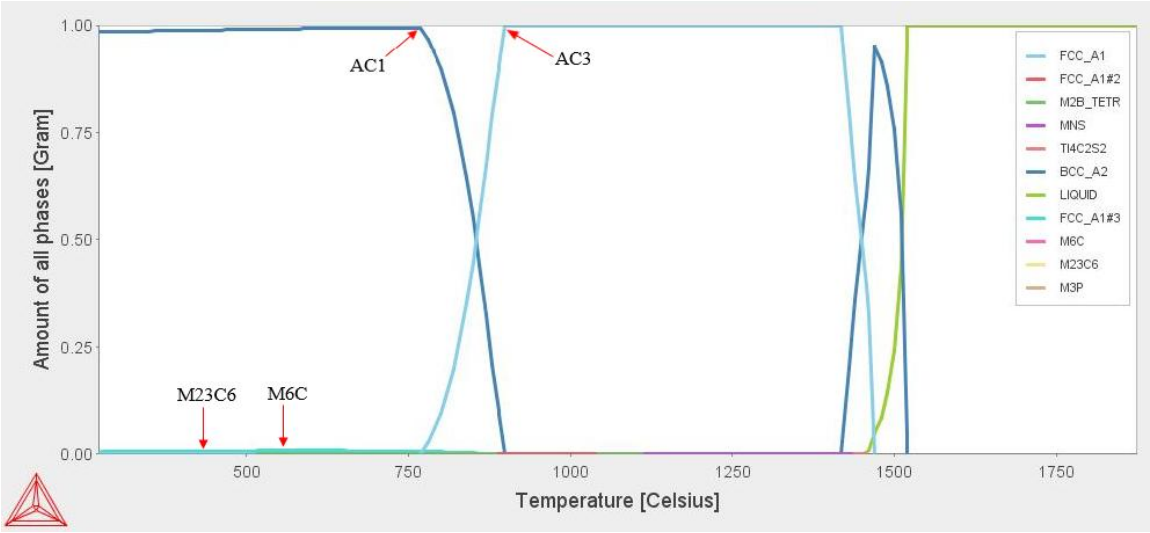

Figure 4.101 Thermo-Calc property diagram of the service-exposed parent material

The weight fraction of significant equilibrium phases that form around the operating temperature range in the service-exposed parent material are shown in Figure 4.102 The carbide M_6C forms at 555°C and increases with decreasing temperature until it reaches a maximum weight fraction of 0.45 wt.% at 273°C. This fraction increases with decreasing temperature. $M_{23}C_6$ forms at approximately 402°C and its weight fraction increases with decreasing temperature up to 0.47 wt.% at 273°C. A small fraction of phosphide M_3P appears at 339°C and is less than 0.1 wt.%. Small amounts of MnS and M_2B are stable throughout the service temperature range. In addition, small fractions of MC and Cu-rich FCC precipitates exist at lower temperatures.

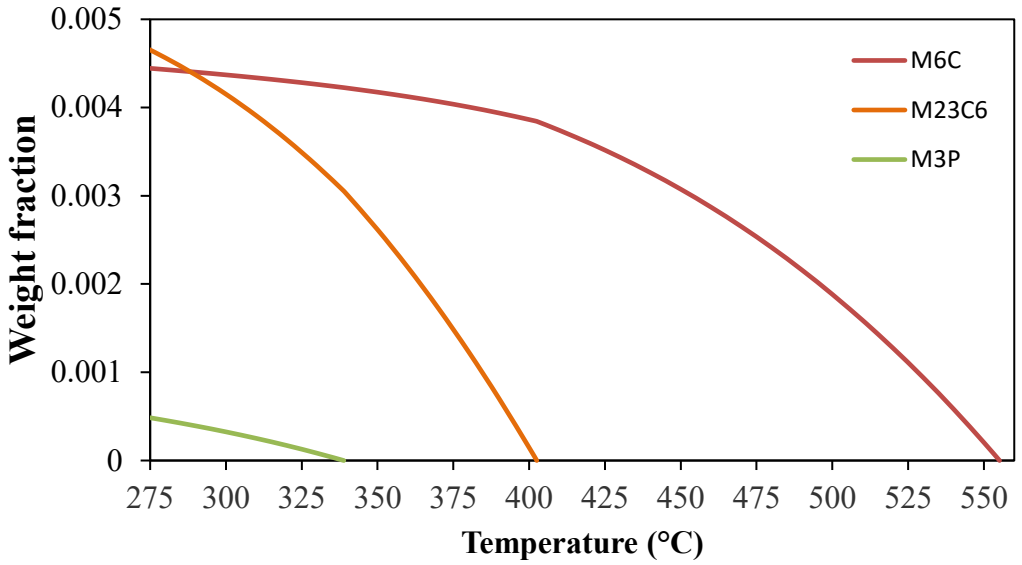

Figure 4.102 Plot of weight fraction vs temperature of the stable phases in service-exposed parent material

The phases that are estimated to be stable at the service temperature of 540°C are listed in Table 4.36. The estimated formulae and nominal composition of the stable phases are also given.

Table 4.36 Estimated equilibrium phase composition of the service-exposed parent material at operating temperature of 540°C

Phase	Estimated Average Formula	Nominal Composition	Comment
BCC_A2	(Fe, Mn, Cr, Si, Mo, Ni, Cu, V, Co, P, Al, Ti, Nb, B, S)C	Mainly Fe	Matrix
FCC_A1#2	(Fe, Mn, Cr, Si, Mo, Ni, Cu, V, Co, P, Al, Ti, Nb, B, S)C	V, Mo and Cr rich $(V_{0.62}Mo_{0.3}Cr_{0.19})C$	MC precipitate
M6C	$(Fe, Cr, Mo, Ni, V, Co, Nb)_6C$	$(Fe_2Mo_4)C$	Mo Carbide
MnS	(Fe, Mn)S	MnS	Sulphide
M2B_TETR	$(Fe, Cr, Mo, Ni)_2B$	$(Fe_{1.14}Cr_{0.86})B$	Boride

4.6.3 Transformation Simulation of Service-exposed Weld Metal

Figure 4.103 shows the property diagram of the service-exposed weld metal. The phases that nucleate and grow on cooling under equilibrium conditions are indicated together with key transformation temperatures on the property diagram. The simulation shows the

transformation temperature A_{c1} and A_{c3} at approximately 797°C and 902°C, respectively. The solidus and liquidus temperatures are observed at about 1416°C and 1512°C. Transformation of ferrite (BCC_A2) to austinite (FCC_A1) occurs in a higher temperature in the weld metal compared to the parent materials. The ratio of the two phases is equal at approximately 855°C.

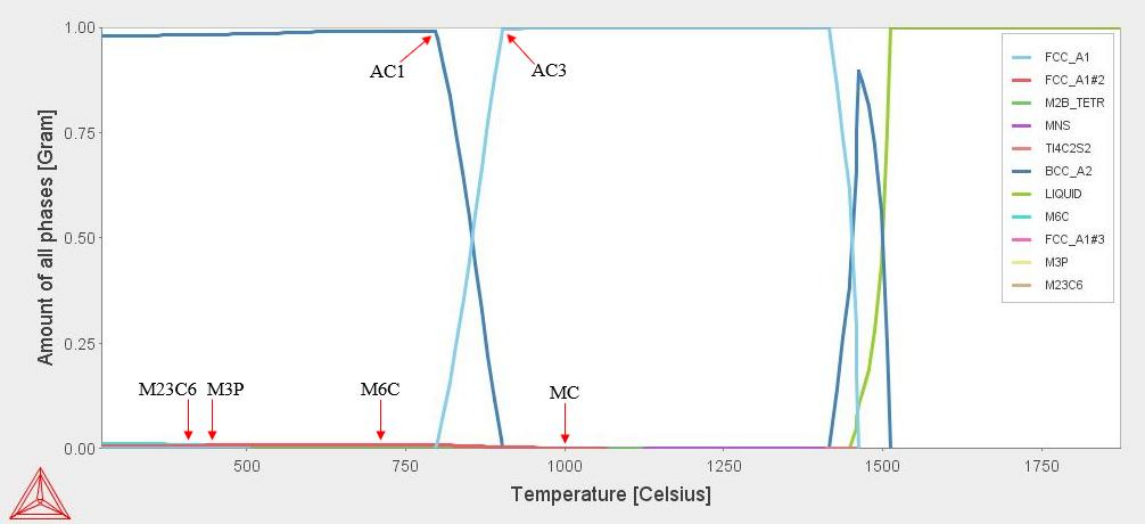

Figure 4.103 Thermo-Calc property diagram of the service-exposed weld metal

The notable phases that that are stable during service are shown in Figure 4.104. Precipitation of MC begins at 1065°C and increase with decreasing temperature up to a maximum weight fraction of about 0.96 wt.% at 626°C where the M_6C carbide starts forming. From this point, the MC precipitation decreases with temperature to a weight fraction of about 0.63 wt.% at 273°C. On the other hand, M_6C increases with the decreasing temperature until a maximum weight fraction of ~1.1 wt.% at 273°C. The formation of M_6C is likely responsible for slowing the rate of MC carbide precipitation.

At approximately 398°C the M_3P phosphide precipitates out of solution and slightly increases as the temperature decreases. The precipitation rate of M_3P is seemingly retarded by the formation of $M_{23}C_6$ at approximately 340°C. The maximum weight fraction of M_3P is approximately 0.08 wt.%, whereas $M_{23}C_6$ goes up to 0.15 wt.%. Nonetheless, both these precipitates are observed only in small quantities in the service temperature range, similar to the even smaller amounts of MnS and M_2B that are stable throughout the service temperature range.

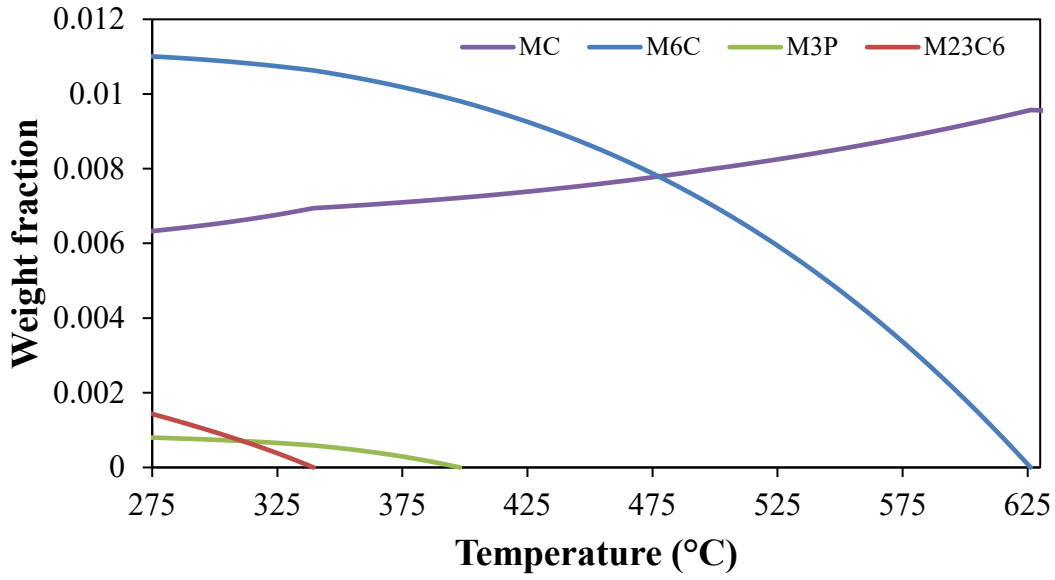

Figure 4.104 Plot of weight fraction vs temperature of the stable phases in service-exposed weld metal

Table 4.37 show the phases that are stable at the service temperature of 540°C in the weld metal.

Table 4.37 Estimated equilibrium phase composition of the service-exposed weld metal at operating temperature of 540°C

Phase	Estimated Average Formula	Nominal Composition	Comment
BCC	(Fe, Mn, Cr, Si, Mo, Ni, Cu, V, Co, P, Al, Ti, Nb, B, S)C	Mainly Fe	Matrix
FCC_A1#2	(Fe, Mn, Cr, Si, Mo, Ni, Cu, V, Co, P, Al, Ti, Nb, B, S)C	V, Mo, Cr and Ti rich $(V_{0.86}Mo_{0.18}Cr_{0.07}Ti_{0.03})C_1$	MC precipitate
M6C	$(Fe, Cr, Mo, Ni, V, Co, Nb)_6C$	$(Fe_2Mo_4)C_1$	Mo Carbide
MnS	(Fe, Mn)S	MnS	Sulphide
M2B_TER	$(Fe, Cr, Mo, Ni)_2B$	$(Fe_{1.13}Cr_{0.87})B_1$	Boride

4.6.4 Prediction of Equilibrium Phases at Service Temperature

The phases that are estimated to be present at service temperature for the virgin and service-exposed parent materials and the weld metal are shown Figure 4.105 as mass fraction of each material system. The balance phase (ferrite matrix) is not displayed. The MC carbide was predicted to be present in all the materials and appears to be slightly higher in the virgin material, possibly due to the higher carbon content of the virgin parent material. Small

quantities of the MnS and M_2B phases were predicted to be present in all the materials. A small quantity of Cu-rich FCC (FCC_A1#1) was only predicted to be present in the virgin material. The formation of Cu-rich precipitates is typically due to the low solubility of Cu in ferrite. The M_6C carbide was estimated on the service-exposed parent material and weld metal. The M_6C was estimated to be higher in the weld metal than in the service-exposed parent material, which may be attributed to the higher content of carbon and molybdenum in the weld metal.

The details of equilibrium phases and their respective chemical composition are given in Table 4.38 for the virgin and service-exposed parent materials and the weld metal.

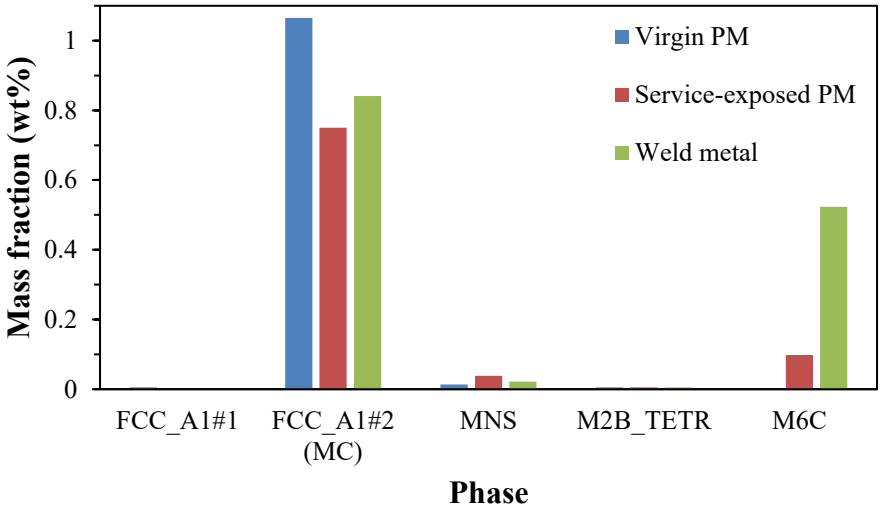

Figure 4.105 Estimation of equilibrium phases that are present in the virgin parent material, service-exposed parent material and weld metal at 540°C

Table 4.38 Composition of predicted equilibrium phases at 540°C (wt.%)

Material	Phase	Fe	Cr	Mo	V	Mn	C	Cu	S	B	Ti
Virgin	Ferrite	98.43	0.31	0.15	-	0.50	-	0.14	-	-	-
	MC	0.02	21.90	40.60	22.38	0.09	14.07	-	-	-	0.47
	Cu-rich	0.12	-	0.52	-	1.45	-	97.75	-	-	-
	MnS	-	-	-	-	63.14	-	-	36.86	-	-
	M_2B	53.35	37.37	0.23	-	-	-	-		9.05	
Service-exposed	Ferrite	98.45	0.32	0.22	-	0.45	-	0.09	-	-	-
	MC	0.01	11.85	34.77	37.66	0.05	14.33	-	-	-	0.67
	M_6C	24.79	0.83	71.64	0.32	-	2.43	-	-	-	-
	MnS	-	-	-	-	63.14	-	-	36.86	-	-
	M_2B	53.20	37.40	0.30	-	-	-	-		9.00	-
Weld Metal	Ferrite	97.77	0.40	0.32	0.04	0.91	-	0.09	-	-	-
	MC	-	4.34	22.16	55.72	0.04	15.12	-	-	-	2.02
	M_6C	24.18	0.73	71.21	1.43	-	2.44	-	-	-	-
	MnS	-	-	-	-	63.14	-	-	36.86	-	-
	M_2B	52.64	37.85	0.46	-	-	-	-	-	9.04	-

Figure 4.106 shows the estimated composition of the MC carbide at 540°C for the virgin parent material, service-exposed parent material and weld metal. The dominant element varied for each material and was estimated to be either molybdenum or vanadium.

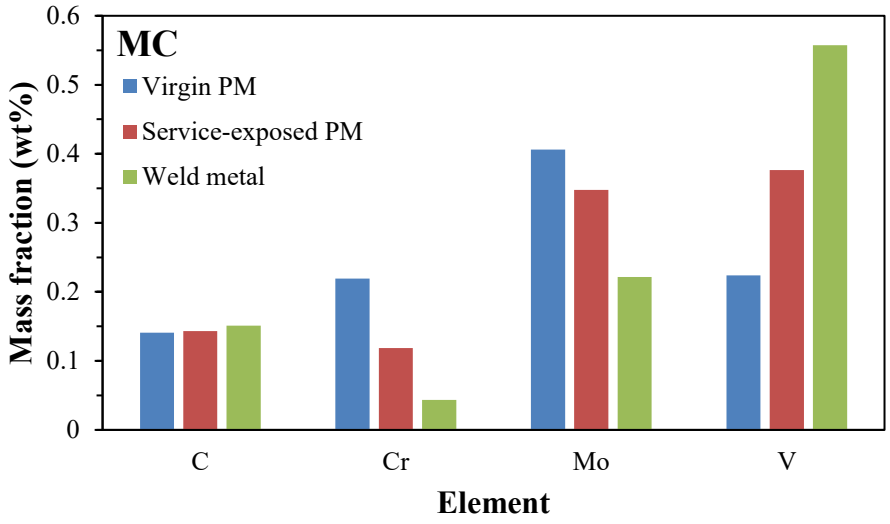

Figure 4.106 Estimation of the chemical composition of MC carbide in the virgin parent material, service-exposed parent material and weld metal at 540°C

Figure 4.107 shows the estimated composition of M_6C in service-exposed parent material and weld metal. The service-exposed parent material and weld metal had similar compositions of the M_6C carbide. Molybdenum was estimated to be the dominating element followed by iron. The general formula of the M_6C was estimated to be $(Mo, Fe, Cr, V)_6C$.

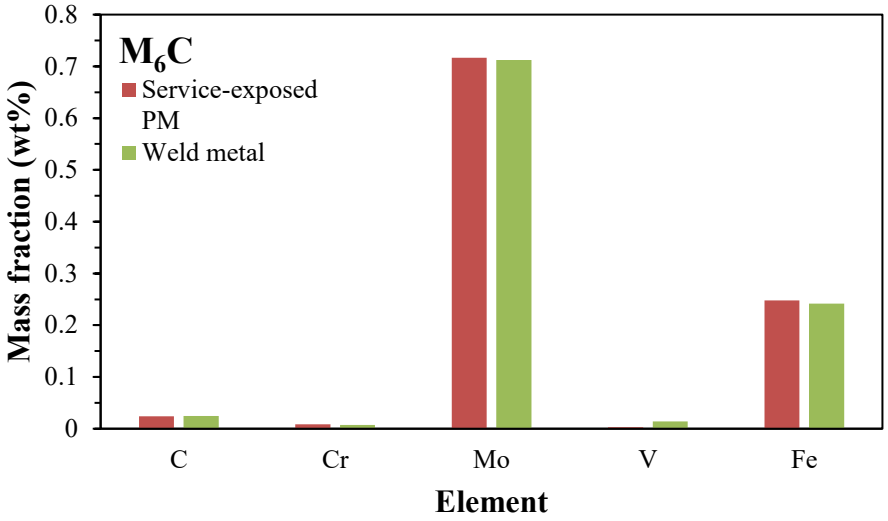

Figure 4.107 Estimation of the chemical composition of M6C carbide in the service-exposed parent material and weld metal at 540°C

4.7 Results of the X-Ray Diffraction Analysis

The XRD patterns of the service-exposed and virgin parent materials are shown in Figure 4.108 together with those of the weld metal and the HAZ. Similar patterns were obtained for all the samples. The patterns all have three acute diffraction peaks that belong to BCC crystal structure ferrite (α-Fe) and have interplanar spacings of approximately d_{110}=0.20, d_{200}=0.14 and d_{211}=0.12 nm. The lattice constant (a) was determined to be 0.286 nm for these materials. These parameters are in good agreement with the PDF values for iron.

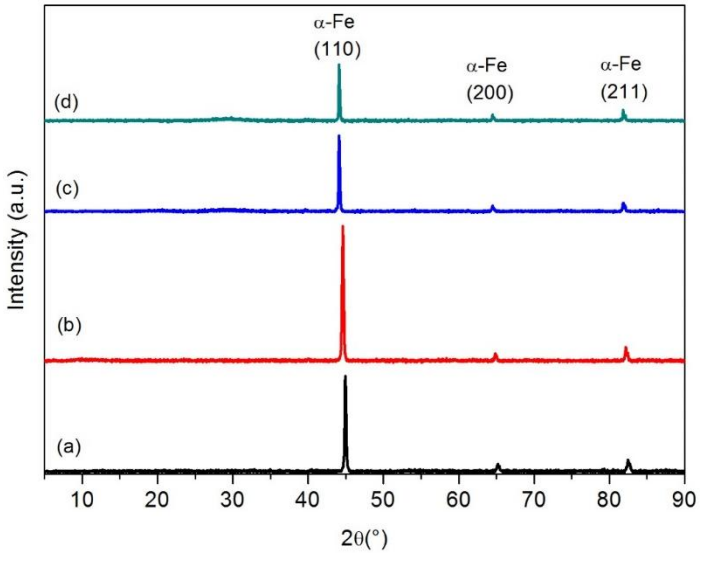

Figure 4.108 Diffraction patterns of the (a) service-exposed parent material, (b) virgin parent material, (c) weldmetal and (d) HAZ

Enlarged peaks of the virgin parent material are shown individually in Figure 4.109 to show evidence of peak broadening. Peaks (110), (200) and (211) show a broadening and are different from one another, which is an indication that there are strain and crystallite size differences in the virgin parent materials.

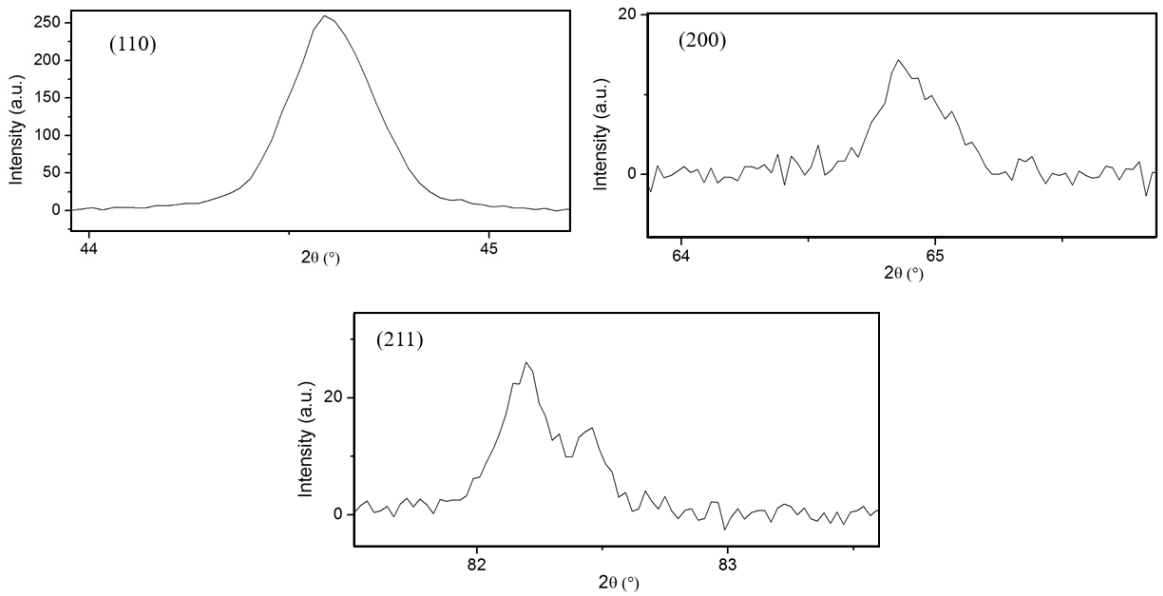

Figure 4.109 Diffraction patterns of individual peaks of the virgin parent material

4.7.1 Determination of the crystallite size, microstrain and dislocation density from XRD data using Scherrer Methods

The values of the peaks and peak broadening parameters are listed in Table 4.39 for the virgin parent material, Table 4.40 for the service-exposed parent material, Table 4.41 for the weld metal and Table 4.42 for the HAZ. It is apparent that as the peak gets broader the crystallite size gets smaller. Additionally, a different value of the crystallite size was obtained at each peak for all the specimens with the service-exposed parent material having the lowest average crystallite size. This is due to a systematic error that Monshi et al. (2012) confirmed to be inherent in the formal Scherrer equation. Hence, the modified Scherrer equation provides the benefit of decreasing the sum of absolute values of errors $\Sigma(\pm\Delta \ln\beta)^2$ and producing a single line through the points to give a single value of intercept.

Table 4.39 Values of 2Theta, FWHM, crystallite size, dislocation density and microstrain for the virgin parent material

Peak index	2θ (°)	β (°)	D (nm)	$\delta \times 10^{-3}(nm^{-2})$	$\varepsilon \times 10^{-3}$
110	44.61	0.257	33.35	0.899	2.739
200	64.90	0.303	31.12	1.033	2.076
211	82.24	0.407	25.89	1.490	2.036
Average			30.12	1.140	2.284
Std. Dev.			3.83	0.311	

Table 4.40 Values of 2Theta, FWHM, crystallite size, dislocation density and microstrain for the service-exposed parent material

Peak index	2θ (°)	β (°)	D (nm)	$\delta \times 10^{-3}(nm^{-2})$	$\varepsilon \times 10^{-3}$
110	44.95	0.246	34.91	0.821	2.598
200	65.21	0.421	22.39	1.995	2.873
211	82.53	0.469	22.54	1.968	2.331
Average			26.61	1.594	2.601
Std. Dev.			7.18	0.670	

Table 4.41 Values of 2Theta, FWHM, crystallite size, dislocation density and microstrain for the weld metal

Peak index	2θ (°)	β (°)	D (nm)	$\delta \times 10^{-3}(nm^{-2})$	$\varepsilon \times 10^{-3}$
110	44.13	0.218	39.32	0.647	2.347
200	64.52	0.341	27.55	1.318	2.358
211	81.91	0.404	26.04	1.476	2.031
Average			30.97	1.147	2.245
Std. Dev.			8,334	0,408	

Table 4.42 Values of 2Theta, FWHM, crystallite size, dislocation density and microstrain for the HAZ

Peak index	2θ (°)	β (°)	D (nm)	$\delta \times 10^{-3}(nm^{-2})$	$\varepsilon \times 10^{-3}$
110	44.14	0.19905	43.07	0.539	2.1421
200	64.54	0.30834	30.47	1.077	2.131
211	81.90	0.38511	27.31	1.341	1.936
Average			33.62	0.986	2.070
Std. Dev.			7.27	0,440	

The modified Scherrer equation was used to address the shortcomings of the original Scherrer equation and obtain one value that represents the average crystallite size for the (110), (200) and (211) peaks for each specimen. Figure 4.110 shows the linear plots of the modified Scherrer equation and Table 4.43 lists the obtained intercept, exponential of the intercept, average crystallite size and the average dislocation density.

Table 4.43 Average crystallite size and dislocation density calculated from modified Scherrer

Material	$ln\frac{k\lambda}{L}$	$e^{ln\frac{k\lambda}{L}}$	L (nm)	$\delta \times 10^{-3}(nm^{-2})$
Virgin PM	-5.5960	0.003713	37.35	0.717
Ex-service PM	-5.5982	0.003705	37.43	0.714
HAZ	-5.8523	0.002873	48.26	0.430
Weld metal	-5.7333	0.003236	42.84	0.545

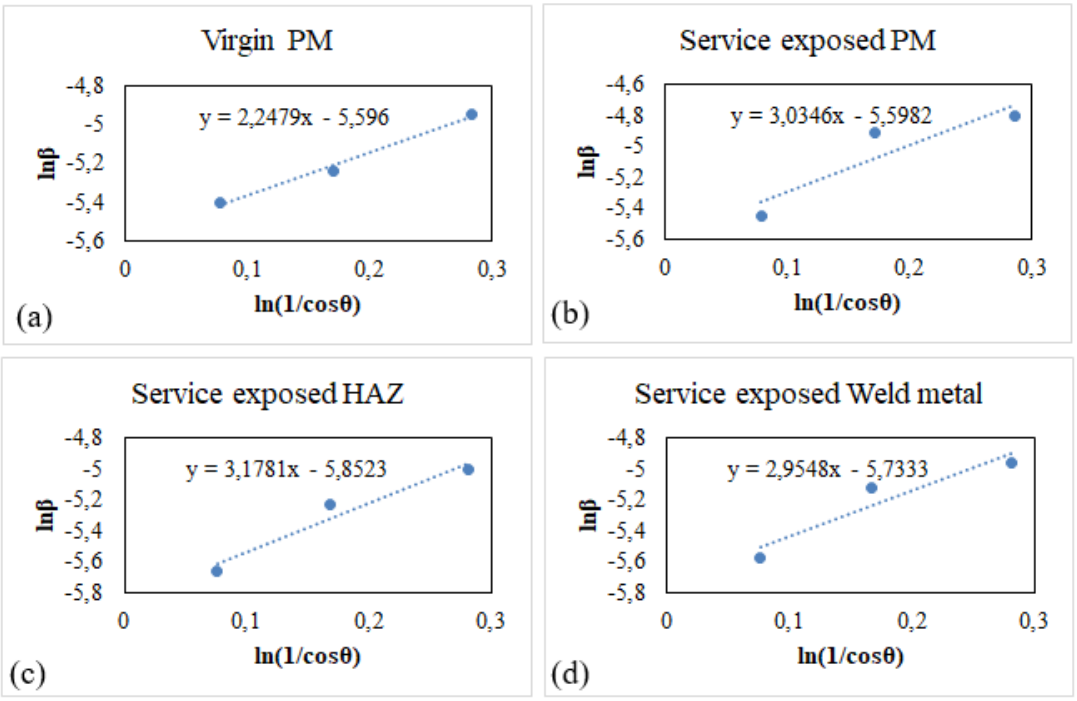

Figure 4.110 Linear plots of modified Scherrer equation and obtained intercepts for (a) virgin parent material, (b) service-exposed parent material, (c) HAZ and (d) weld metal

The service-exposed parent material was initially observed to have the lowest mean crystallite size, which corresponded to the highest dislocation density. However, when using the modified Scherrer approach, the parent materials were found to have an average crystallite size that is approximately the same. A possible indication that the crystallite size

of the material did not change or changed slightly over time in service and that the dislocation density remained relatively unchanged. It is known that during creep the dislocation density in a metal increases due to plastic deformation that is caused by dislocation multiplication and nucleation (Zhang, 2010; Sekido, et al., 2012; Di Gianfrancesco, 2017). The change in dislocation density can result in high creep strength if the steel is able to maintain a small subgrain size and a high dislocation density over a long period in creep conditions. Both the virgin and service-exposed steam pipes have not undergone any appreciable deformation of dimensions. On the other hand, the average crystallite size of the HAZ is much larger than that of the parent materials and a smaller dislocation density. This difference in crystallite size may be due to the different heat cycle experienced by the materials during the welding and PWHT of the steam pipe when it was put in service and the subsequent long term operation in creep service which is associated with the degradation of microstructure resulting in the reduction of the dislocation density (Vyrostkova, et al., 2011; Ennis, 2014). Nevertheless, more reliable measurements of the dislocation substructure are required for making comprehensive analysis and the TEM is the usually considered the proper technique for such analysis.

4.7.2 Estimation of Carbide phases and compositions from XRD data

Carbide phase diffraction peaks could not be clearly distinguished from the obtained patterns shown in Figure 4.108. However, the presence of candidate carbides and their composition could be estimated by matching of peaks with those available in the PDF database. Table 4.44 shows the probable phases that were obtained from the XRD analysis of virgin and service-exposed PM, as well as those of the HAZ and weld metal.

Table 4.44 Carbides detected by XRD analysis in the research specimens of 14MoV6-3

Sample	Carbide	Precipitate	Formula
Virgin PM	Chromium Carbide	M_3C_2, M_7C_3	Cr_3C_2, Cr_7C_3, $(Cr, Fe, Mo)_7C_3$
	Iron Carbide	M_3C	Fe_3C
	Manganese Carbide	$M_{23}C_6$, M_7C_3, M_3C	$Mn_{23}C_6$, Mn_7C_3, $(Mn, Fe)_3C$
	Molybdenum Carbide	M_2C, $M_{23}C_6$	Mo_2C, $(Fe, Mo)_{23}C_6$
	Vanadium Carbide	MC	V_4C_3, VC
	Chromium Iron Boride	M_2B	$(Fe, Cr)_2B$
Service-exposed PM	Chromium Carbide	$M_{23}C_6$, M_7C_3, M_3C, M_3C_2	$Cr_{23}C_6$, $(Cr, Mo)_{23}C_6$, Cr_7C_3, Cr_3C, Cr_3C_2
	Iron Carbide	M_3C, MC, M_7C_3, $M_{23}C_6$	Fe_3C, FeC, Fe_7C_3, $Fe_{23}C_6$
	Molybdenum Carbide	M_2C, M_6C	Mo_2C, $(Fe, Mo)_6C$
	Vanadium Carbide	MC	V_4C_3, V_2C
	Chromium Iron Boride	M_2B	$(Fe, Cr)_2B$
	Manganese Iron Phosphide	M_3P	$(Fe, Mn)_3P$
HAZ	Chromium Carbide	$M_{23}C_6$, M_7C_3	$Cr_{23}C_6$, $(Cr, Mo)_{23}C_6$, Cr_7C_3
	Iron Carbide	M_3C	Fe_3C
	Molybdenum Carbide	M_2C, M_6C	Mo_2C, $(Fe, Mo)_6C$
	Vanadium Carbide	MC	V_4C_3
Weld metal	Chromium Carbide	$M_{23}C_6$, M_7C_3, M_3C_2	$(Cr, Fe)_{23}C_6$, $(Cr, Mo)_{23}C_6$, Cr_7C_3, Cr_3C_2

The carbide phases were selected based on literature and the level of peak matching, taking into account the FOM ranking (Dobrzanski, et al., 2011; Cullity & Stock, 2014). Carbide phase must be more than 5% in steel to be observable by XRD (Baltusnikas & Levinskas, 2006). However, several chemical and electrochemical etching techniques may also be used to highlight the carbide phases. This can be done by trying different solutions of etchants and varying their concentration or increasing etching time and applying successive polishing and etching techniques.

4.8 General Discussion

4.8.1 Microstructural Changes

Since pre-service data was not available for the service-exposed material, it was not possible to assess changes in the material's microstructure directly. However, correlation to literature data and comparisons to a similar material with no service history could be made. For instance, the optical microscopy evaluations of the service-exposed and virgin material revealed the differences that might have been introduced by long-term operation in creep conditions as shown in Figure 4.111. It was ascertained that 14MoV6-3 materials typically have a microstructure composed of ferrite and pearlite/bainite (with very little carbide precipitation) in its initial conditions. The ferritic and pearlitic/bainitic microstructure becomes degraded with time in service. The ferrite and pearlite/bainite structure changes to a much simpler ferritic structure with carbides of varying size along the grain boundaries and inside the grains. Depending on the service time, creep damage may also be present as it was the case on the examined material where isolated creep voids were found on the grain boundaries. The creep damage was even higher in the HAZ area of the service-exposed weldment. An average void density of 392 voids/mm² was recorded on the ICHAZ compared to the bulk service-exposed parent material where the void density was observed to be less than 50 voids/mm². No creep damage was noted on the virgin parent material.

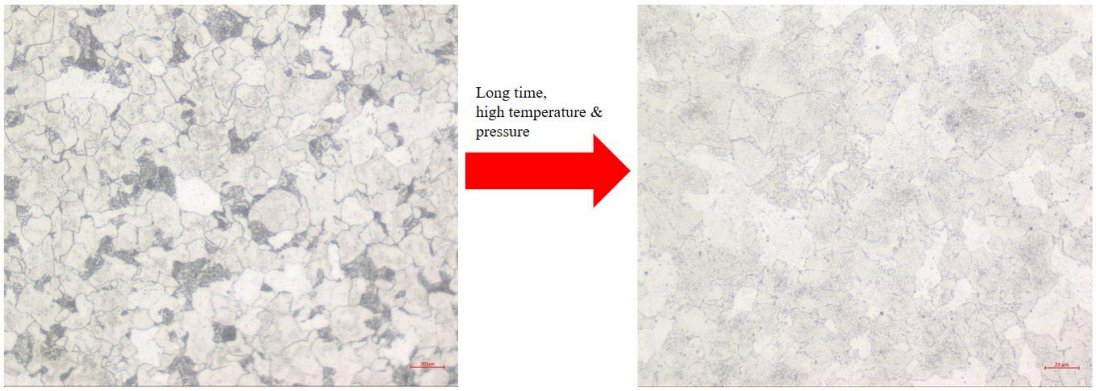

Figure 4.111 Changes in 14MoV6-3 steel microstructure due to long-term service in creep conditions

The change of grain size with time in service could not be ascertained. However, it is not expected that the ferrite grain size would change much in service since the material is operated well below its austenite phase range. The difference in grain size as shown in Table 4.45 could have been due to composition and heat treatment during production and fabrication. This could also be supported by the average grain size of the HAZ, which was

estimated at 5.5 μm. Furthermore, the interplanar spacing, dislocation density and crystallite size calculated from the XRD data was comparable for the service-exposed and virgin material. This could be an indication that there were no changes in grain size during service.

Table 4.45 Average grain size of the service-exposed and virgin material as estimated with the mean lineal intercept method

Material	Grain size (μm)
Service-exposed PM	8.8
Virgin	9.6
Service-exposed HAZ	5.5

4.8.2 Changes in Room Temperature Mechanical Properties

The estimated changes in mechanical properties of 14MoV6-3 steel as measured at room temperature are shown in Table 4.46. The changes are likely due to the long-term operation of the material in creep conditions. The strength, ductility and hardness of the service-exposed material showed considerable reduction. However, the most drastic reduction was observed in the impact properties of the service-exposed material. The impact energy of the service-exposed parent material differed by up to 97% from that of the virgin parent material.

Table 4.46 Effect of long-term high temperature and pressure operation on the properties of 14MoV6-3 steel at room temperature

Condition	Tensile properties			Impact energy (J)	Hardness HV10
	Yield (MPa)	UTS (MPa)	%Elongation		
Virgin	381	553	34	368	164
Service-exposed	326	516	30	12	154
Weldment	371	530	17	98	179
BS EN 10216-2	320 (min.)	460 – 610	20 (min.)	40 (min.)	140 – 190

The service-exposed material showed good tensile properties despite having been in service for over 30 years. The degradation of tensile properties is more pronounced on the yield strength and ductility. The loss in ductility was observed to be even more pronounced in the service-exposed weldment specimens, differing by more than 40% from both virgin and

service-exposed parent material specimens. This may be explained as the effect of high temperature that was experienced by this area during fabrication and subsequent operation in creep conditions. However, the effect of alloying elements could also contribute to the differences in the tensile properties. For instance, an increase in phosphorus content is usually observed to lead to a reduction in ductility and impact toughness of steel. Figure 4.112 shows a comparison of tensile properties and phosphorus content of the research materials.

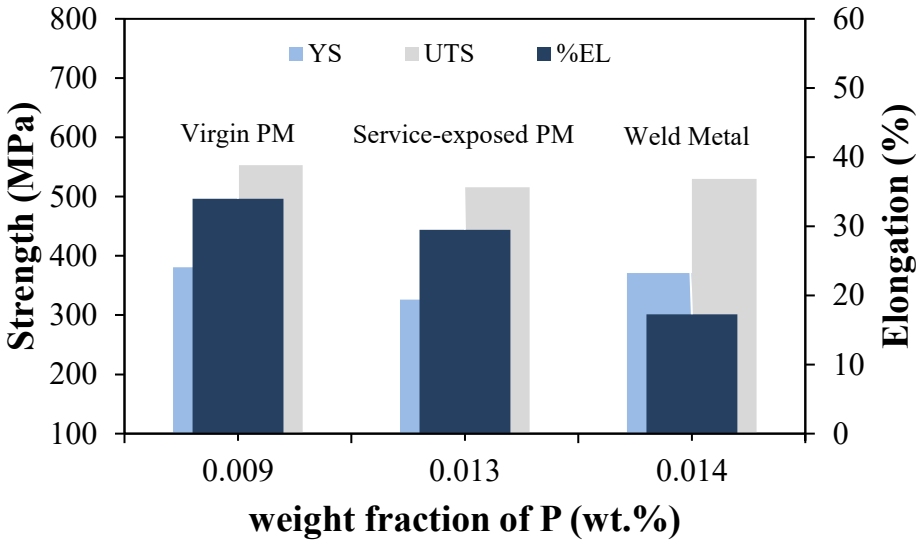

Figure 4.112 Comparison of the 14MoV63 material tensile properties in relation to their Phosphorous content

The evolution of hardness on the service-exposed material correlates to the changes observed in the tensile and impact properties of the material in that it has reduced with time in service. The change in hardness may be quantified by evaluating the ratio H/H_0, which is the ratio of hardness of the material in service (H) to its initial state hardness (H_0) (Endo, et al., 2003). The H/H_0 ratio was estimated at approximately 0.94 for 14MoV6-3 material after ~277 khr of operation at 540°C and 3.75 MPa. Ideally, these measurements should be taken at various stages throughout the service life of the component to establish a trend that can be related to life consumption and used as part of RLE to estimate microstructural changes (softening) and remnant life of the material (Maharaj, et al., 2009). Also, the H/H_0 ratio is valid during the secondary creep stage before full creep exhaustion of the material. The exhaustion degree of service-exposed materials with the same hardness (H) tend to differ during the tertiary creep stage.

4.8.3 Changes in Elevated Temperature Mechanical Properties

The ductile-to-brittle transition behaviour of the virgin and service-exposed parent materials are shown in Figure 4.113. The significant shift of the DBTT, from 0°C in the virgin parent material to 75°C in the service-exposed parent material, is likely due to long-term service in creep conditions. The DBTT of the HAZ features of the service-exposed weldment was estimated at approximately 30°C and that of the weld metal was estimated at 90°C. The shift in the DBTT indicates a higher likelihood of damage that could occur in service-exposed pipework during dynamic loading conditions. The dynamic loading conditions in power plants are typical during boiler start up and pressure testing, which pass through these transition temperatures.

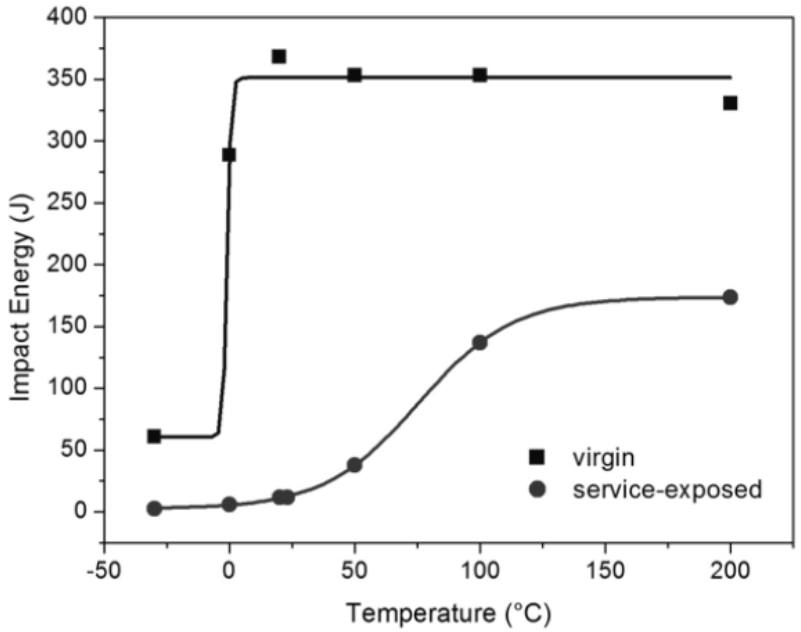

Figure 4.113 Change of ductile-to-brittle transition temperature in the 14MoV6-3 steel due to long-term operation in creep conditions

The effect of long-term service on the yield strength of 14MoV6-3 steel at elevated temperature is shown in Figure 4.114. The yield strength was observed to decrease below the acceptable criteria when tested at temperature higher than 540°C. The decrease in yield strength indicates a higher likelihood of component failure if the service temperature of 540°C is exceeded in operation during further service. Similar observations were made from the results of the Gleeble hot tensile test.

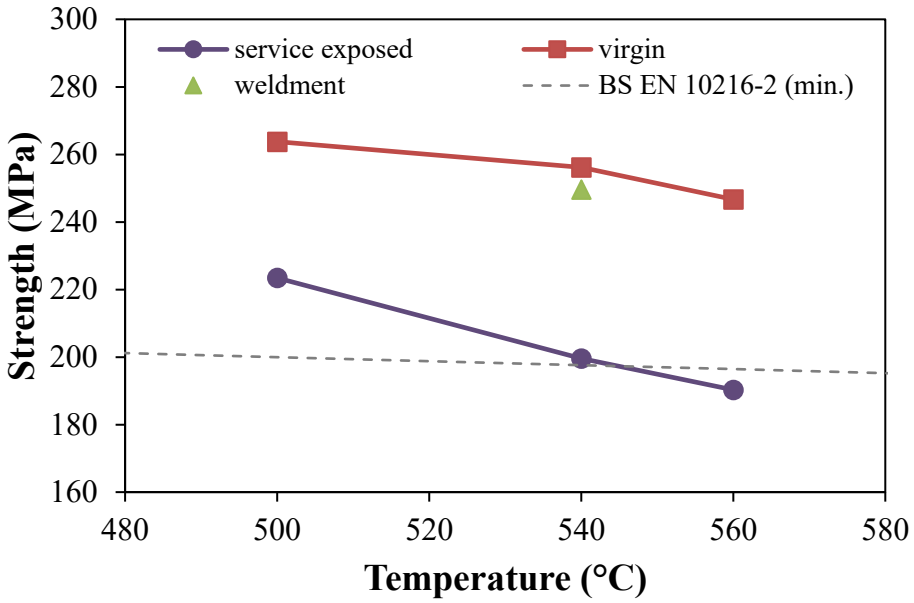

Figure 4.114 Change in proof strength at service temperature in the 14MoV6-3 steel due to long-term operation in creep conditions.

The change of creep properties could not be evaluated since the creep test was only conducted on the service-exposed parent material. Nonetheless, it is evident that the degradation of mechanical properties is due to the microstructural changes that occur during the long-term operation under high temperature and pressure. This was also evident from the creep test as the prior creep damage of the material contributed to the failure of the specimen outside the predicted scatter band of the ECCC master curves.

4.8.4 Effect of Welding and PWHT on the Microstructure, Hardness and Impact properties of 14MoV6-3 Steel

Welding simulations were done on the Gleeble® machine to estimate the metallurgical sub zones that would be obtained on the HAZ when welding is done on the virgin and service exposed 14MoV6-3 parent material. The ICHAZ, FGHAZ and CGHAZ sub zones were simulated and analysed in the as-weld and PWHT conditions that had different cooling rates. Peak temperatures of 860, 1080 and 1280°C were selected to correspond with the ICHAZ, FGHAZ and CGHAZ, respectively. In addition, the as-received parent materials were subjected to the same PWHT and different cooling rates as the simulated HAZ sub regions for comparison. Vickers hardness tests and Charpy V-Notch impact tests were done on the simulated HAZ and parent material specimens to evaluate the effects of welding and PWHT on virgin 14MoV6-3 material and material that had been in long-term service in a creep

regime. The simulated HAZ and parent material specimens were cooled either in a furnace or in ambient air to examine the effects of cooling rate following PWHT.

A variety of ferritic/bainitic microstructures with different characteristics were obtained when welding was simulated on the virgin and service-exposed 14MoV6-3 parent materials. The microstructure of the of the HAZ that was simulated on the virgin and service-exposed parent materials varied with increasing peak temperature and cooling conditions, after PWHT. Nonetheless, the obtained microstructures were typically of ferrite with upper bainite. Upper bainite generally forms at higher temperatures during transformation from austenite in low alloy bainitic steels (Bramfitt & Lawrence, 2004). Specimens that were subjected to peak temperature of 1280°C and cooled in the furnace were characterised by laths of ferrite that contain carbides at the grain boundaries. However, the air-cooled specimens had a coarse bainite/pearlite structure that contained islands of ferrite grains. Significant grain growth was observed on the furnace-cooled and air-cooled virgin material specimens at the peak temperature of 1080°C. A similar observation was made on the air-cooled service-exposed material specimens. However, an acicular ferrite structure was observed on the furnace-cooled service exposed material specimens. Furthermore, the furnace-cooled virgin material simulated HAZ had a duplex grain structure. The specimens that were welded and not subject to any PWHT (as-weld) showed progressive increase of cementite phase with increase in peak temperature, going from a bainite/pearlite structure to a bainite/martensite structure.

The microstructure of the virgin and service-exposed parent materials that were subjected to the heat treatment did not show many differences. Particularly the virgin parent material, which had microstructures that were very similar regardless of cooling rate. Nonetheless, the air-cooled service-exposed parent material specimens seemed to retain a lot more cementite than the furnace-cooled specimens. The effects of the PWHT were further observed on the change of grain size in relation to the cooling rate, as shown in Table 4.47. The virgin parent material specimens experienced some grain refinement, whereas the service-exposed parent material specimens experienced a slight increase or decrease in grain size depending on cooling rate.

Table 4.47 Effect of PWHT and cooling rate on the grain size of the virgin and service-exposed 14MoV6-3 material

	Grain size (μm)		
Specimen condition	**As-received**	**Furnace-cooled**	**Air-cooled**
Virgin	9.6	8.4	8.6
Service-exposed	8.8	8.6	9

The summary of the hardness and impact properties of the simulated HAZ is provided in Table 4.48. The hardness and impact values of both the virgin and service exposed simulated HAZ were averaged from the ICHAZ, FGHAZ and the CGHAZ. The hardness and impact values of the parent materials that were subjected to PWHT are also shown.

Table 4.48 Hardness and impact properties of the simulated HAZ

Material properties	**Virgin material**				**Service-exposed material**			
	Material/cooling conditions							
	FC/AC PM	As-weld	Furnace	Air	FC/AC PM	As-weld	Furnace	Air
Hardness (HV_{10})	122/120	216	135	128	122/121	173	144	141
Impact Energy (J)	–/331	139	373	235	364/68	116	251	199

The hardness of the virgin and service-exposed parent materials is comparable regardless of the material service history and applied cooling rate after PWHT. However, the hardness of these specimens fell below the acceptable specification of 14MoV6-3 steel but met the minimum criteria of the impact properties. The heat-treated parent material specimens represent the tempered region of the HAZ. The as-weld and PHWT HAZ of the virgin and service-exposed materials have hardness that is typical on 14MoV6-3 weldments and relatively good impact toughness despite the softening experienced on the air-cooled FGHAZ region of the virgin material.

The change in hardness of the virgin and service-exposed materials due to the welding simulation heat cycles, PWHT and cooling rate in relation to the impact energy is shown in Figure 4.115. The impact toughness of the as-weld and air-cooled HAZ, which were simulated from the virgin parent material (a), was observed to sharply increase with a slight increase in hardness. The furnace-cooled specimens did not show any significant change in impact toughness with increasing hardness.

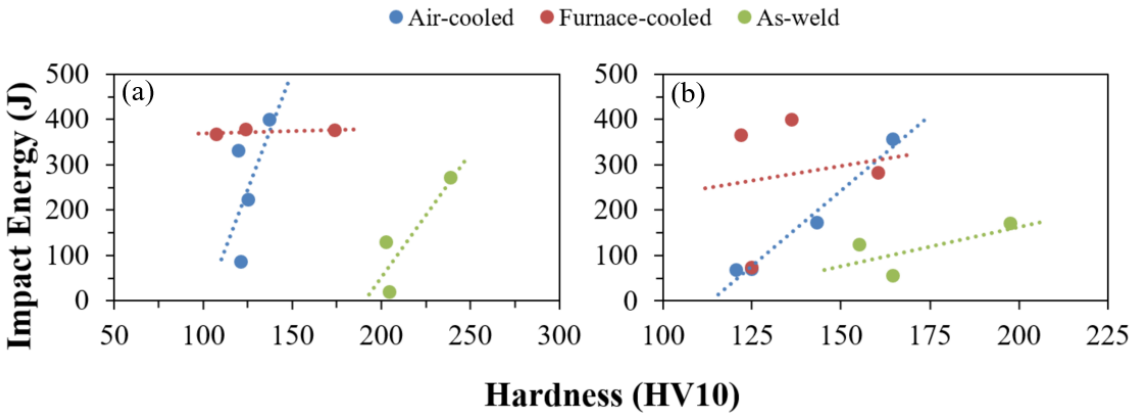

Figure 4.115 Variation of hardness with impact energy and specimen condition for (a) virgin material and (b) service-exposed material

The as-weld and air-cooled HAZ specimens that were simulated from the service-exposed material (b) were observed to have impact energy that increases with increasing hardness. Although it has large scatter, only a slight increase with increasing hardness is observed on the impact energy of the furnace-cooled specimens. The observed behaviour correlates with the difficulties that are usually encountered with impact testing of the HAZ on actual weldments.

4.8.5 Extent of Life Exhaustion and Remaining Life Estimation

The ECCC master equation and creep damage model were used for estimating the remaining life of the service-exposed parent material and service-exposed weldment. A life exhaustion of 15% and 32% was estimated for the service-exposed parent material based on ECCC mean and ECCC mean plus 20% data, respectively. A creep test was done using the service-exposed parent material and the specimen ruptured within the scatter band of the ECCC mean plus 20% data for parent materials. However, the specimen ruptured much earlier than it was predicted with the ECCC master equation. The reason for specimen rupture at an earlier time than predicated may be due to its service history in creep conditions. This was addressed by determining the P_{LM} of the service-exposed parent material from the residual creep strength t_{re} and extrapolating the disposable residual life from the stress and temperature conditions that were assumed to reflect operating conditions. It was estimated that the parent material had a life exhaustion of 58% and the pipe could be safely operated for a further 14 years. However, this does not take into account the additional thermal stress the material would be

further exposed to during the welding process, which will lead to further material degradation and creep life consumption.

The creep damage model estimated a life exhaustion of 59% for the service-exposed parent material and complete exhaustion for the HAZ based on the material creep ductility parameter of γ=3.4. The remaining life was calculated to be 22 years and 36 years for the service-exposed parent material when using maximum and average creep void density, respectively. The HAZ was calculated to have three (3) years remaining life using the average creep void density. However, the HAZ was estimated to have reached the end of life when the remaining life was estimated from the maximum creep void density. The service-exposed parent material was estimated to have a life fraction of ~0.4 to 0.6 based on the exhaustion degree classification method by Dobrzanski et. al. (2011). The HAZ was also estimated to have a life fraction of ~0.4 to 0.6 from this model. The creep damage model of the utility is more conservative compared to the classification method by Dobrzanski et. al. The RLE model by Dobrzanski et. al also relates the estimated life fraction of material to the carbide phases that are likely to be present at that life fraction. The SEM analysis of the service-exposed parent material and the weldment showed presence of $M_{23}C_6$ and M_3C carbides. Furthermore, XRD analysis was done to detect carbides that are present in service-exposed parent material and weldment. Table 4.49 shows the carbides that were detected by XRD analysis to be present in the service-exposed parent material and HAZ as estimated from the RLE. The M_6C carbide was detected in the parent material although the RLE model does not anticipate the M_6C carbide to be present in the material at life fraction of 0.4 to 0.6. M_6C is only expected to precipitate in the final structural change of ferrite, arranged uniformly along with MC precipitates within ferrite grains and large $M_{23}C_6$ carbides along the grain boundaries. Previously, the appearance of M_6C was believed to coincide with the end of the material's useful life, which has since been shown to not be the case. A similar observation was made in the HAZ with regards to the M_6C carbide as it was not anticipated to be present at the life fraction of 0.4 to 0.6 but was identified in the XRD analysis.

Table 4.49 XRD analysis of carbides that are present in relation to life fraction of 0.4 – 0.6

Material	M_3C	MC	$M_{23}C_6$	M_2C	M_7C_3	M_6C
Parent	✓	✓	✓	✓	✓	✓
HAZ	✓	✓	✓	✓	✓	✓

Thermo-Calc was used for thermodynamic modelling of equilibrium phases at service temperature 540°C. The MC and M_6C carbides were predicted to be the dominant stable phases at service temperature, respectively. The $M_{23}C_6$ phase was predicted to be fully dissolved at temperatures that are lower than 540°C. Table 4.50 summarises the dissolution temperatures of $M_{23}C_6$, M_6C and MC precipitates under equilibrium for the different material samples.

Table 4.50 Thermo-Calc predicted $M_{23}C_6$, M_6C and MC precipitates dissolution temperatures (°C)

Material	$M_{23}C_6$	M_6C	MC
Virgin PM	468	416	368
Service-exposed PM	402	555	422
Weld Metal	340	626	1065

The analysis of the carbides using SEM could not yield conclusive results regarding the morphology and type carbides that were observed on the research materials, especially on the virgin material where carbide composition could not be distinguished from the matrix. However, the carbides that were observed on the service-exposed material and weld metal were estimated to be $M_{23}C_6$ and M_3C based on the EDX analysis, Thermo-Calc modelling and literature. Also, some amounts of impurity phases MnS were observed on the materials by SEM but could not be matched during XRD analysis. The M_3P phase was matched on the service-exposed material as predicted by Thermo-Calc but could not be observed by microscopy. The Thermo-Calc calculations showed the presence of M_3P phases at a temperature below 325°C (virgin), 350°C (service-exposed) and 400°C (weld metal). The difficulty in matching or identifying these phases could be attributed to their small quantity and the suitability of analysis techniques.

The next chapter presents concluding remarks and recommendations for future work.

Chapter 5: Conclusions and Recommendations for Further Work

The work that was presented in this report covered the assessment of mechanical properties and microstructure of a virgin 14MoV6-3 pipe material and service-exposed 14MoV6-3 material that was taken from pipework that are used in a coal-fired power plant. The service-exposed pipework contained a weldment (girth weld) that was evaluated as well. The service-exposed pipe had been in service for over 277 khr and was operated under creep conditions. The performance and behaviour of the virgin parent material was compared to that of the service-exposed parent material and the service-exposed weldment under various testing conditions. The analyses were made to estimate changes that may have been induced by the long-term operation in high temperature and pressure compared to the material that has never been put in service. Final remarks and recommendations on the observations that were made are discussed in the following sections.

5.1 Conclusions

- The deterioration of mechanical properties is due to changes that take place in the microstructure during long-term service in the creep regime. The material taken from service after accumulating more than 277 khr had a degraded ferrite microstructure that features relatively large carbides at the grain boundaries and contains smaller ones within the grains. The typical pearlite/bainite islands that feature in the ferrite microstructure of virgin 14MoV6-3 low alloy steel were completely depleted. Scattered creep voids could also be noted on the service-exposed microstructure.
- Perhaps the most notable reduction in mechanical properties was in the yield strength and impact properties of the service-exposed material. This was even more pronounced at elevated temperature where the yield strength was noted to decrease with increasing test temperature. The slight difference in the average grain size of the virgin material compared to the service-exposed material could also be contributing to the lower strength values of the service-exposed material compared to the virgin material. However, the grain size of the service-exposed material is not believed to have evolved during service. On the other hand, the changes in impact energy revealed a shift of the DBTT by approximately $\Delta 75°C$ with the absorbed energy quickly falling below standard specifications at temperatures below 50°C.

- Hardness measurements were made around the circumference of the service-exposed pipework and through the pipe wall thickness. Although the hardness had decreased from an estimated 164 HV10 to 154 HV10 in service, it did not appear to change with depth of the pipe wall thickness or position on the circumference.
- Creep testing of the service-exposed parent material showed the effects of prior creep damage on the creep strength of the tested specimen. However, additional creep testing is still required to be able to confidently quantify the effects of service on creep strength and determine a strength reduction factor that can be applied to account for the welding thermal cycle and prior creep damage of specimens when estimating time to rupture.
- A variety of microstructures were obtained from the simulation of HAZ sub regions on the Gleeble® thermo-mechanical simulator. These microstructures were characteristic of bainite/pearlite to bainite/martensite due to the very short time of transformation from 800 to 500°C, $\Delta t_{5\text{-}8} = 7.5$ seconds. The application of PWHT and different cooling rates (ambient air and furnace at 10°C/min) also resulted in a multitude of microstructures. The lowest hardness and impact energy values were generally measured at the ICHAZ region, which is consistent with the expected behaviour of low alloy steel weldments. Cooling the specimens in furnace resulted in a more homogenous HAZ for the new material but not for the service-exposed material.
- It is not uncommon for power plant engineers to be faced with challenges to meet production demands during repair welding or installations and having to decide between putting the component back in service as-weld or cooled in ambient air to save some time. The simulated HAZ results can provide insight to the effects such decisions may have on the performance of the welded component in service.
- Thermodynamics modelling of equilibrium phases showed the phases that can be expected in the virgin and service-exposed 14MoV6-3 low alloy steel based on material composition. The solvus temperature and range of stability was identified for the phases. The chemical composition and behaviour of elements as a function of temperature was estimated for the predicted phases.
- SEM investigation of carbides noted on the grain boundaries and inside the grains could not reveal conclusive results regarding the type and morphology of these carbides. However, the carbides were estimated to be $M_{23}C_6$ and M_3C based on the EDX analysis, Thermo-Calc modelling and literature description of these carbides. The SEM analyses were supplemented by XRD analyses that could at least reveal a number of thermodynamically stable carbides including $M_{23}C_6$, MC, M_2C, M_3C, M_6C and M_7C_3

carbides. Thermo-Calc modelling of equilibrium phases had estimated the dominant carbides to be $M_{23}C_6$ and M_6C. However, the M_6C carbide was poorly matched in the XRD analysis but its composition could be estimated in Thermo-Calc. Small amounts of MC, M_2B and MnS were predicted to be stable throughout the analysed temperature range. Nevertheless, the type and amount of carbides that may dissolve or nucleate and grow in service evolve due to the prolonged effects of temperature and stress.

5.2 Recommendations for Further Work

- Long-term creep tests can be conducted for the service-exposed weldment (cross-weld), virgin and service-exposed parent materials to evaluate the effects of service on the creep strength. Some of the creep tests may be interrupted to examine the evolution of hardness, creep voids and microstructure during creep conditions.
- Prospects of conducting the more rapid abridged creep testing should be explored to supplement the long-term creep tests.
- The effects of welding and PWHT on service-exposed material can be evaluated by testing at predetermined conditions, e.g. repair welding of creep-damaged pipe and joining of new spool to a creep-damaged pipe. The tests may be done by fabricating actual welded samples (test coupons) with joints of the (1) service-exposed material welded to a service-exposed material, (2) virgin material welded to a service-exposed material and (3) virgin material weld to a virgin material. Actual peak temperatures may be measured during welding at various points away from the weld and can be used for the simulation of HAZ regions on the Gleeble® machine. In addition, the effects of different PWHT temperatures and cooling times ($\Delta t_{5\text{-}8}$) may be studied on the simulated HAZ regions.
- The virgin and service-exposed parent materials may be aged at different times to simulate the effects of high temperature on the material in service and estimate the changes in macrostructure and material properties due to high temperature service.
- Explore practical and reliable methods for determining the shape, form and composition of carbide phases that are present in a material in relation to its life fraction. This may be combined with the replication method already employed in the power generation industry.
- Investigate the evaluation of the hardness ratio H/H_0 and the feasibility of developing a model relating the hardness ratio to life exhaustion.

Chapter 6: References

Abbaschian, R., Abbaschian, L., & Reed-Hill, R. (2009). *Physical Metallurgy Principles.* Connecticut: Cengage Learning.

Abe, F., Kern, T.-U., & Viswanathan, R. (2008). *Creep-resistant steels.* Cambridge, England: Woodhead Publishing Limited.

Abhijit, A., Varghese, J., Chalavadi, P., Sai Karthik, P., Bhanu Sankara Rao, P., & Rajulapati, K. (2019). Negative Strain Rate Sensitivity in Two-Phase Nanocrystalline CoCrFeMnNi High-Entropy Alloy with Broader Grain Size Distribution Studied by Nanoindentation. *Transactions of the Indian Institute of Metals, 72*, 2861–2867. doi:10.1007/s12666-019-01762-5

Akhtar, M. (2017). *Metallurgical Characterisation of Simulated Heat Affected Zone in Boron Modified P91 Steel.* Warangal: National Institute of Technology Warangal.

Ali, B. S. (2014). *Development of Non-Destructive Small Specimen Creep Testing Techniques.* University of Nottingham, Department of Mechanical, Materials and Manufacturing Engineering. Nottingham: University of Nottingham.

Aliya, D., & Lampman, S. (2004). Physical Metallurgy Concepts in Interpretation of Microstructures. In A. International, & G. F. Vander Voort (Ed.), *ASM Handbook Vol 9, Metallography and Microstructures* (pp. 44–70). Cleveland: ASM International.

Anderson, T. (2005). *Fracture Mechanics: Fundamentals and Applications* (Third Edition ed.). Boca Raton: CRC Press.

Arruabarrena, J., Uranga, P., López, B., & Rodriguez-Ibabe, J. (2011). Carbide Spheroidization Kinetics in a Low Alloy Medium Carbon Steel: Relevance of Deformation After Transformation. *Materials Science and Technology Conference. 9*, pp. 698-705. Columbus: Iron and Steel Technology.

ASM International. (1999). *Hardness Testing, 2nd Edition.* (H. Chandle, Ed.) Cleveland: ASM International.

ASM International. (2004). *Metallography and Microstructures* (Vol. 9). (G. F. Vander Voort, Ed.) Cleveland: ASM International.

ASM International. (2012). *Phase Diagrams-Understanding the Basics.* (Campbell, & F.C., Eds.) Cleveland: ASM International.

ASTM International. (2003). *ASTM E139 Standard Test Methods for Conducting Creep, Creep-Rupture, and Stress-Rupture Tests of Metallic Materials.* ASTM International. Pennsylvania: ASTM International.

ASTM International. (2010). *ASTM E112-10 Standard Test Method for Determining Average Grain Size.* West Conshohocken, PA: ASTM International.

ASTM International. (2013). *ASTM E140 Standard Hardness Conversion Tables for Metals Relationship Among Brinell Hardness, Vickers Hardness, Rockwell Hardness, Superficial Hardness, Knoop Hardness, Scleroscope Hardness, and Leeb Hardness.* West Conshohocken, PA: ASTM International.

ASTM International. (2013). *ASTM E23 − 12c - Standard Test Methods for Notched Bar Impact Testing of Metallic Materials.* ASTM. West Conshohocken, PA: ASTM International.

Auerkari, P., Barraclough, D., Buchmayr, B., Coussement, C., Granacher, J., Holdsworth, S., . . . Vanderschae, A. (2001). *Data acceptability criteria and data generation: Generic recommendations for creep, creep rupture, stress rupture and stress relaxation data.* European Creep Collaborative Committee. ECCC.

Auerkari, P., Barraclough, D., Buchmayr, B., Coussement, C., Granacher, J., Holdsworth, S., . . . Vanderschae, A. (2005). *Data acceptability criteria and data generation: creep data for welds.* European Creep Collaborative Committee. ECCC.

Auerkari, P., Buchmayr, B., Bullough, C., Coussement, C., Granacher, J., Holdsworth, S., . . . Sandstrom, R. (2011). *Terms and Terminology for Weld Creep Testing.* European Creep Collaborative Committee. Rotherham: ECCC.

Avner, S. H. (1974). *Introduction to Physical Metallurgy.* Singapore: McGraw-Hill Book Company.

Bailey, N. (1994). *Weldability of ferritic steels.* Cambridge: Abington Publishing.

Baltusnikas, A., & Levinskas, R. (2006). XRD Analysis of Carbide Phase in Heat Resistant Steels. *ISSN 1392-1320 Materials Science (Medziagotyra), 12*(3), 192-198.

Beres, L., Balogh, A., & Irmer, W. (2001). Welding of martensitic creep-resistant steels: The relationship between preheat and MS temperatures was investigated. *Welding Research Supplement*, 191-s-195s.

Bezuidenhout, M., Beukes, D., & van Zyl, F. (1997). Assessment of the Condition and Refurbishment of the Main Steam Pipework at Hendrina Power Station. *Operating Pressure Equipement.* Brisbane: IMMA.

Bezuidenhout, M., Bhimma, D., Doubell, P., Downes, A., Havinga, F., Mkhize, M., . . . Scheepers, R. a. (2010). *Integrity and Lifing of Defect Free Components in Eskom Power Plant.* Johannesburg: Eskom.

Bhadeshia, H. (2015). *Bainite In Steels: Theory and Practice.* Leeds: Maney Publishing.

Blondeau, R. (2008). *Metallurgy and Mechanics of Welding: Processes and Industrial Applications.* (R. Blondeau, Ed.) New Jersey: John Wiley & Sons, Inc.

Bohler Welding. (2009). Welding Guide. *Technical Handbook of Bohler Welding Products, 06/2009*. Austria: Bohler Welding.

Bohme, W. (2002). Results of a DVM Round Robin on Instrumented Charpy Testing. In D. Francois, & A. Pineau (Ed.), *From Charpy to Present Impact Testing. 30*, pp. 189-196. Poitiers: Elsevier Science Ltd. and ESIS.

Bohme, W., & Schindler, H.-J. (2000). Application of Single-Specimen Methods on Instrumented Charpy Tests: Results of DVM Round-Robin Exersices. In T. A. Siewert, M. R. Manahan Sr., T. A. Siewert, & M. R. Manahan Sr. (Eds.), *Pendulum Impact Testing: A Century of Progress, STP 1380* (pp. 327-336). West Conshohocken, PA: ASTM International.

Bramfitt, B. L., & Lawrence, S. J. (2004). Metallography and Microstructures of Carbon and Low-Alloy Steels. In A. International, & G. F. Vander Voort (Ed.), *ASM Handbook Vol 9, Metallography and Microstructures* (pp. 608–626). Cleveland: ASM International.

Brett, S. (2004). Type IIIa Cracking in ½CrMoV Steam Pipework Systems. *Science and Technology of Welding & Joining, 9*(1), 41-45. doi:10.1179/136217104225017134

Brett, S., Buchanan, L., Concari, S., Cosso, G., Fenton, S., Fleming, A., . . . Seliger, P. (2005). *Residual life assessment and microstructure.* European Creep Collaborative Committee. ECCC. Retrieved from http://www.ommi.co.uk/etd/eccc/advancedcreep/open.htm

British Standard Institution. (1990). *BS 3604-1:1990 - Steel pipes and tubes for pressure purposes: ferritic alloy steel with specified elevated temperature properties - Part 1: Specification for seamless and electric resistance welded tubes.* London: BSI Standards Limited.

British Standards Institution. (1996). *BS EN 1043-1:1996 Destructive tests on welds in metallic materials. Hardness testing — Part 1: Hardness test on arc welded joints.* London: BSI Standards Limited.

British Standards Institution. (2007). *BS EN 10216-2:2002 - Seamless steel tubes for pressure purposes - Technical delivery conditions - Part 2: Non-alloy and alloy*

steel tubes with specified elevated temperature properties. The British Standards Institution. London: BSI Standards Limited.
British Standards Institution. (2007). *BS EN 10216-2:2002 - Seamless steel tubes for pressure purposes - Technical delivery conditions - Part 2: Non-alloy and alloy steel tubes with specified elevated temperature properties.* The British Standards Institution. London: BSOL Standards Online.
British Standards Institution. (2012). *BS EN ISO 15614-1:2004+A2:2012 - Specification and qualification of welding procedures for metallic materials — Welding procedure test — Part 1: Arc and gas welding of steels and arc welding of nickel and nickel alloys.* The British Standards Institution. London: BSI Standards Limited.
British Standards Institution. (2015). *BS EN ISO 14556:2015 - Metallic materials - Charpy V-notch pendulum impact test - Instrumented test method.* London: BSI Standards Limited.
British Standards Institution. (2017). *BS EN 13480-3:2017 Metallic industrial piping - Part 3: Design and calculations.* The British Standards Institution. London: BSI Standards Limited.
British Standards Institution. (2020). *BS EN ISO 643:2020 Steels - Micrographic determination of the apparent grain size.* The British Standards Institution. London: BSI Standards Limited.
Broitman, E. (2017). Indentation Hardness Measurements at Macro-, Micro-, and Nanoscale: A Critical Overview. *Tribol Lett, 65*(23), 1-18. doi:10.1007/s11249-016-0805-5
Burke, K. (2009). *Microstructural evolution in service exposed low alloy power plant steels.* Loughborough University, Department of Materials. Loughborough: Kate Burke. Retrieved from https://dspace.lboro.ac.uk/2134/16773
Callister, W. D., & Rethwisch, D. G. (2008). *Fundamentals of Materials Science and Engineering: An Integrated Approach.* Hoboken: John Wiley & Sons, Inc.
Cane, B., & Aplin, P. (1994). Creep life assessment methods. *The Journal of Strain Analysis for Engineering Design, 29*(3), 225-232. doi:10.1243/03093247V293225
Cerjak, H. (2008). The Role of Welding in the Power Generation Industry. *61st IIW Annual Assembly* (pp. 17-27). Graz: Safety and Reliability of Welded Components in Energy and Processing Industry.
Cole, D. G. (2000). *Design of heat-resistant steels for small power plant.* University of Cambridge, Department of Materials Science and Metallrgy. Cambridge: University of Cambridge.
Coleman, K., & Newell Jr, W. (2007). P91 and beyond: Welding the new-generation Cr-Mo alloys for high-temperature service. *Welding Journal*, 29-33.
Craddock Dyson, C., Sun, W., Hyde, C., Brett, S., & Hyde, T. (2016). *Use of Small Specimen Creep Data in Component Life Management: A Review.* University of Nottingham, Department of Mechanical, Materials and Manufacturing Engineering. Nottingham: University of Nottingham.
Cullity, B., & Stock, S. (2014). *Elements of X-Ray Diffraction* (Third Edition ed.). Harlow: Pearson Education Limited.
Cvetkovski, S., Adziev, T., Adziev, G., & Sedmak, A. (2002). Instrumented Testing of Simulated Charpy Specimens Made of Microalloyed Mn-Ni-V Steel. In D. Franqois, A. Pineau, D. Franqois, & A. Pineau (Eds.), *From Charpy to Present Impact Testing* (pp. 95-102). Oxford: Elsevier Science Ltd. and ESIS.
Davis, J. (2004). *Tensile Testing.* Cleveland: ASM International.
Day, A., Mehnert, K., & Neumann, B. (1999). *Channel 4 - Revealing Microstructure.* Hobro: HKL Technology ApS.

Di Gianfrancesco, A. (2017). Technologies for Chemical Analyses, Microstructural and Inspection Investigations. In A. Di Gianfrancesco, & A. Di Gianfrancesco (Ed.), *Materials for Ultra-Supercritical and Advanced Ultra-Supercritical Power Plants* (pp. 197-245). Cambridge: Woodhead Publishing. doi:10.1016/B978-0-08-100552-1.00001-4

Di Gianfrancesco, A. (2017). The Fossil Fuel Power Plants Technology. In A. Di Gianfrancesco, & A. Di Gianfrancesco (Ed.), *Materials for Ultra-Supercritical and Advanced Ultra-Supercritical Power Plants* (pp. 1-29). Cambridge: Woodhead Publishing. doi:10.1016/B978-0-08-100552-1.00001-4

Dieter, G. (1961). *Mechanical Metallurgy.* New York: McGraw-Hill Book Company.

Dlamini, P. (2013). *240-106628253 - Eskom Standard for Welding Requirements on Eskom Plant.* Eskom, Group Technology. Eskom Materials, Welding and NDT Study Committee.

Dobrzanski, J. (2005). The classification method and the technical condition evaluation of the critical elements' material of power boilers in creep service made from the 12Cr–1Mo–V. *Journal of Materials Processing Technology, 164*(165), 785–794. doi:10.1016/j.jmatprotec.2005.02.055

Dobrzanski, J. (2020). The Procedure for Determining the Time of Safe Service beyond the Design Service Time Based on Creep Testing. In Tanski, & A. Tomasz, *Creep Characteristics of Engineering Materials* (pp. 1-20). London: IntechOpen. doi:10.5772/intechopen.86078

Dobrzanski, J. (2020). The Procedure for Determining the Time of Safe Service beyond the Design Service Time Based on Creep Testing. In T. Tanski, M. Sroka, A. Zielinski, & G. Golanski, *Creep Characteristics of Engineering Materials* (pp. 1-20). Gliwice: IntechOpen. doi:10.5772/intechopen.84986

Dobrzanski, J., Hernas, A., & Moskal, G. (2011). Microstructural degradation in boiler steels: materials developments, properties and assessment. In J. E. Oakey, & J. E. Oakey (Ed.), *Power plant life management and performance improvement* (pp. 222-271). Cambridge: Woodhead Publishing Limited.

Dobrzanski, J., Hernas, A., & Moskal, G. (2011). Microstructural degradation in boiler steels: materials developments, properties and assessment. In J. E. Oakey, & J. E. Oakey (Ed.), *Power plant life management and performance improvement* (pp. 222-271). Cambridge: Woodhead Publishing Limited.

Dobrzanski, J., Zielinski, A., & Krzton, H. (2007, July). Mechanical properties and structure of the Cr-Mo-V low-alloyed steel after long-term service in creep condition. *Journal of Achievements in Materials and Manufacturing Engineering, 23*(1), 39-42.

Dong, J., Shin, K., He, Y., Song, G., & Jung, J. (2010). Evolution of morphology and composition of the carbides in Cr-Mo-V steel after service exposure. (Z. Yunfeng, C. W. Su, & P. X. Hui Xia, Eds.) *Advanced Materials and Processing*, 101-104. doi:10.1142/9789814322799_0024

Dorazila, O., Matochaa, K., Zhuc, J., & Chen, Y. (2015, December 10). The effect of long term exposition at 540◦C on the empirical correlations for determination of mechanical properties of low alloy CrMoV steel from the results of Small Punch tests. *Perspectives in Science: Proceedings ofthe 1st Czech-China Scientific Conference 2015, (2016)*(7), 156—160. doi:10.1016/j.pisc.2015.11.025

Dossett, J. L., & Boyer, H. E. (2006). *Practical Heat Treating: Second Edition.* Cleveland: ASM International.

Dowling, N. (2012). *Mechanical Behavior of Materials, Engineering Methods for Deformation, Fracture, and Fatigue* (4th ed.). Harlow: Pearson Education.

Du Toit, M. (2012). Welding Metallurgy NSW700- Study Theme 2.14 Low alloy creep resistant steels. Pretoria: Univerisity of Pretoria.

Dwornicka, R., & Pietraszek, J. (2010). A comparison of allowable heating and cooling rates based on TRD regulations and PN-EN 12952-3 code for T-pipes of 13HMF steel. *Technical Transactions - Mechanics, 107*(8), 39-47.

Dynamic Systems Inc. (2014). *Gleebe Systems - Thermal-Mechanical Simulator Solutions Guide.* New York: Dynamic Systems Inc.

Dziuba-Kałuża, M., Zieliński, A., Dobrzański, J., & Sroka, M. (2014, March). The evaluation of suitability for operation of low-alloy Cr-Mo and Cr-Mo-V steel welded joints beyond the design work time. *Archives of Materials Science and Engineering, 66*(1), 21-30.

Easterling, K. (1992). *Introduction to the Physical Metallurgy of Welding.* Oxford: Butterworths-Heinemann.

Eissa Abd elmaoula, A., Abdelaziz, H., Mosa, E., Morsi, M., & Atlam, A. (2015). Effect of post weld heat treatment and filler metals on microstructures and mechanical properties of GTAW and SMAW weldments between P11 and P91 steels. *International Journal of Scientific & Engineering Research, 6*(4), 620-631.

Endo, T., Masuyama, F., & Park, K.-S. (2003). Change in Vickers Hardness and Substructure during Creep of a Mod.9Cr–1Mo Steel. *Materials Transactions, 44*(2), 239-246.

Ennis, P. (2014). Ferritic and Martensitic Steels for Power Plants. In A. Shirzadi, & J. Susan, *Structural Alloys for Power Plants: Operational Challenges and High-Temperature Materials* (pp. 188-220). Cambridge: Woodhead Publishing. doi:10.1533/9780857097552.2.188

EPRI. (1997). *Review of Type IV Cracking in Piping Welds.* Palo Alto, CA: Electric Power Reseach Institute.

EPRI. (2007). *Fossil Plant High-Energy Piping Damage: Theory and Practice, Volume 1: Piping Fundamentals.* Electric Power Research Institute. Palo Alto, CA: EPRI.

EPRI. (2008). *Metallurgical Guidebook for Fossil Power Plant Boilers.* Electric Power Research Institute. Palo Alto, CA: EPRI.

EPRI. (2009). *Weld Metal Metallurgical Handbook.* Structural Integrity Associates, Inc. Palo Alto: Electric Power Research Institute.

Eskom. (1985). *Data Sheet: Hot Reheat System.* Witbank: Matla Power Station.

Eskom. (2011, May 17). Matla Power Station Unit 1 Hot Reheat System Weld Details. *TDRW000066*. Johannesburg, Gauteng, South Africa: Steinmuller Africa.

Eskom. (2017). *Fact Sheet - Generation plant mix.* Eskom Generation Division, Corporate Affairs Division. Johannesburg: Eskom. Retrieved from http://www.eskom.co.za/AboutElectricity/FactsFigures/Pages/Facts_Figures.aspx

Eskom. (2017). *Fact Sheet - How electricity is produced at a coal fired power plant.* Eskom, Generation Communication. Johannesburg: Eskom.

Eskom. (2018). *Integrated report.* eskom, Corporate Affairs. Johannesburg: Eskom.

Fakic, B., Buric, A., & Horoz, E. (2020). Microstructure Assessment of Steel for Elevated Temperatures by the Replica. In I. Karabegovic, & I. Karabegovic (Ed.), *New Technologies, Development and Application III* (Vol. 128, pp. 292-298). Cham: Springer. doi:https://doi.org/10.1007/978-3-030-46817-0_33

Fang, J., & Ding, F. (2009, September 09). Force based analysis on the instrumented Charpy impact and its industrial application. *DYMAT*, 779–783. doi:DOI: 10.1051/dymat/2009109

Furtado, H. C., & Le May, I. (2004, March). High Temperature Degradation in Power Plants and Refineries. *Materials Research, 7*(1), 103-110. doi:10.1590/S1516-14392004000100015

Heuser, H., & Jochum, C. (n.d.). *Alloy design for similar and dissimilar welding and thier behaviours.* Retrieved August 15, 2017, from International Atomic Energy Agency: https://www.phase-trans.msm.cam.ac.uk/2005/LINK/182.pdf

Hibbeler, R. C. (2011). *Mechanics of Materials.* Upper Saddle River, NJ: Pearson Prentice Hall.

Hinton, R., & Wiswesser, R. (2008). Estimating welding preheat requirements for unknown grades of carbon and low-alloy steels. *Welding Journal, 87*, 273-s-278-s.

Hodzic, D., & Hajro, I. (2007). Assessment of Microstructure Degradation of Creep Exposed Boiler Steels. *Trends in the Development of Machinery and Associated Technology* (pp. 275-278). Hammamet: TMT.

Hodzic, D., & Hajro, I. (2010). Impact Toughness of Steamline Material 14MoV6-3 Aftre Long-Term Exploitation. *14th International Research/Expert Conference "Trends in the Development of Machinery and Associated Technology"* (pp. 129-132). Meditarranean cruise: TMT.

Hodzic, D., & Hajro, I. (2011). Hardness as Indicator of Material Degradation After Long-Term Exploitation of Steamline in Thermal Power Plant. *15th International Research/Expert Conference "Trends in the Development of Machinery and Associated Technology"* (pp. 177-180). Prague: TMT.

Hodzic, D., & Hajro, I. (2012). Microstructure degradation after prolonged exploitation of heat resistant steel 14MoV6-3. *16th International Research/Expert Conference - "Trends in the Development of Machinery and Associated Technology"*, (pp. 155-158). Dubai.

Holdsworth, S. (2004). 0.5Cr-0.5Mo-0.25V steel. In K. Yagi, G. Merckling, T. Kern, H. Irie, & H. Warlimont (Eds.), *Creep Properties of Heat Resistant Steels and Superalloys* (pp. 54-56). Berlin, Heidelberg: Springer-Verlag.

Hu, Z.-F. (2011). Heat-resistant steels, microstructure evolution and life assessment in power plants. In M. Rasul (Ed.), *Thermal Power Plants* (pp. 195-226). Rijeka: InTech .

Hyde, T., & Sun, W. (1998). Creep of welded pipes. *The Proceedings of the Institution of Mechanical Engineers, 212*(Part E), 171-182.

Ibrahim, O. (2011). Comparison of Impact Properties for Carbon and Low Alloy Steels. *Science Direct, 27*(10), 931-936.

Igwemezie, V., Ugwuegbu, C., & Mark, U. (2016). Physical Metallurgy of Modern Creep-Resistant Steel for Steam Power Plants: Microstructure and Phase Transformations. *Journal of Metallurgy, 2016*, 1-19. doi:10.1155/2016/5468292

International Organisation for Standardization . (2016). *ISO 148-1:2016 - Metallic materials - Charpy pendulum impact test - Part 1: Test method.* ISO.

International Organisation for Standardization. (2009). *ISO 204:2009 - Metallic materials - Uniaxial creep testing in tension - Method of test.* ISO.

International Organisation for Standardization. (2011). *ISO 6892-2:2011 - Metallic materials -Tensile testing - Part 2: Method of test at elevated temperature.* International Standards Organisation. ISO.

International Organisation for Standardization. (2016). *ISO 6892-1:2016 - Metallic materials - Tensile testing - Part 1: Method of test at room temperature.* International Standards Organisation. ISO.

International Organisation for Standardization. (2018). *ISO 6507-1:2005 - Metallic materials - Vickers hardness test Part 1: Test method.* International Standards Organisation. Geneva: ISO.

Jankowski, A., Chames, J., Gardea, A., Nishimoto, R., & Brannigan, E. (2019). The softening factor cb of commercial titanium alloy wires. *International Journal of Materials Research, 110*(11), 990-999. doi:10.3139/146.111834

Janovec, J., Polachova, D., & Junek, M. (2012). Lifetime Assessment of a Steam Pipeline. *Acta Polytechnica, 52*(4/2012).

Jelwan, J., Chowdhry, M., & Pearce, G. (2011). Creep Life Forecasting of Weldment. *Journal of Solid Mechanics, 3*(1), 42-63.

Junek, M., & Janovec, J. (2015). Life Assessment of High Pressure Steam Piping Bend Working Under Conditions of Creep Damage. *Metal 2015*, (pp. 1-6). Brno.

Kang, S., Jin, H., Jang, J., Choi, Y., Oh, K., Foley, D., & Zhang, X. (2013). A Quantitative Evaluation of Microstructure by Electron Back-Scattered Diffraction Pattern Quality Variations. *Microscopy and Microanalysis, 19*(S5), 83–88. doi:10.1017/S1431927613012397

Khan, A., Farrokh, B., & Takacs, L. (2008). Compressive properties of Cu with different grain sizes: sub-micron to nanometer realm. *Journal of Materials Science, 43*, 3305–3313. doi:10.1007/s10853-008-2508-2

Knutsen, R., & George, S. (2015). Introduction to Materials Science and Materials Under Stress - Part D: Materials under stress. Cape Town: University of Cape Town.

Korzhavyi, P., Gorbatov, O., & Selleby, M. (2018). *Precipitation of Late Blooming Phases in Iron-Based Alloys - Theoretical Modelling.* KTH Royal Institute of Technology, Department of Materials Science and Engineering. Stockholm: Svensk Karnbranslehantering AB.

Kou, S. (2003). *Welding Metallurgy.* New Jersey: John Wiley & Sons, Inc.

Langford, J., & Wilson, A. (1978). Scherrer after Sixty Years: A Survey and Some New Results in the Determination of Crystallite Size. *Journal of Applied Crystallography, 11*(2), 102-113. doi:10.1107/s0021889878012844

Li, L. (2012). *Effect of post-weld heat treatment on creep rupture properties of grade 91 steel heavy section welds.* Reactor Concepts RD&D.

Li, X., Cabrillat, M., & Lejeail, Y. (2006). *Study of modified 9Cr-1Mo welds.* Retrieved August 18, 2017, from International Atomic Energy Agency.

Liu, Z., Liu, C., Miao, L., Guo, X., Ding, J., & Zhang, H. (2019, May 27). The Evolution of Complex Carbide Precipitates in a Low Alloy Cr–Mo–V Steel after Long-Term Aging Treatment. *Materials, 12*(1724), 1-16. doi:10.3390/ma12101724

Lomozik, M. (2013). Structure and plastic properties of HAZ area in 13HMF steel after over 130 000 hours of operation while subjected to simulation welding thermal cycles. *BIULETYN INSTYTUTU SPAWALNICTWA, 4*, 22-30.

Loots, R. (2003). *Susceptibility of service exposed creep resistant materials to reheat cracking during repair welding.* University of Pretoria, Metallurgical Engineering. Pretoria: University of Pretoria.

Maharaj, C., Dear, J., & Morris, A. (2009). A Review of Methods to Estimate Creep Damage in Low Alloy Steel Power Station Steam Pipes. *Strain, 45*(4), 316–331. doi:10.1111/j.1475-1305.2008.00465.x

Maile, K. (2003, July 23). Creep Loading of Pressurized Components - Phenomena and Evaluation. Stuttgart: MPA University of Stuttgart.

Majola, W. (2016). *Generation Fleet Renewal Strategy.* Eskom.

Marder, A. (1989). Replication microscopy techniques for NDE. *ASM Handbook, 17*, 52-56.

Marx, G. (2016). *Quantitative microstructural evaluation of 12Cr creep aged steels after welding.* Nelson Mandela Metropolitan University. Port Elizabeth: Nelson Mandela Metropolitan University.

Masuyama, F. (2001). History of Power Plants and Progress in Heat Resistant Steels. *ISIJ International, 41*(6), 612–625.

Mathers, G. (2019). *Hardness Testing Part 1*. Retrieved from TWI Ltd Web site.

Mayr, P. (2007). *Evolution of microstructure and mechanical properties of the heat affected zone in B-containing 9% chromium steels.* Graz: Graz University of Technology.

Middleton, P. (Ed.). (2017, September 4). Creep, cracks and fitness for service. *African Fusion(August 2017)*, 28-29. Berdfordview: Crown Publications. Retrieved from https://user-54716422671.cld.bz/African-Fusion-August-2017

Milicka, K., & Dobe, F. (2004). The High-Temperature Characterisation of Welded Joints Using Small-Punch Testing. *MATERIALI IN TEHNOLOGIJE, 38(1–2)*(9(2004)), 9-12.

Mohyla, P., & Koukal, J. (2000). Changes of mechanical properties in 0.5Cr-0.5Mo-0.3V steel welds after long term exposition at high temperatures. *Acta Metallurgica Slovaca, 2000*(4), 396-404.

Molokwane, T. (2013). *Microstructural and property assessment of creep aged 12Cr steel after welding.* University of Cape Town, Cape Town.

Monshi, A., Foroughi, M. R., & Monshi, M. R. (2012, August 28). Modified Scherrer Equation to Estimate More Accurately Nano-Crystallite Size Using XRD. *World Journal of Nano Science and Engineering*, 154-160. doi:10.4236/wjnse.2012.23020

Morige, E. (2015). *Field metallography.* Illinois Tool Works. Illinois: Buehler.

Mphaphathi, T. (2016). *Characterisation of Suitable Fillers for a Butt Weld of Creep Aged X20 and Virgin P91 Pipes.* University of the Witwatersrand, School of Chemical and Metallurgical Engineering. Johannesburg: University of the Witwatersrand.

Ngoasheng, T. (2016). *Standard for Evaluation of Surface Microstructures Using the Metallographic Replication Technique.* Johannesburg: Eskom.

Ngoasheng, T. (2017). *Standard for Metallographic Replication Standard Applicable to High Temperature High Pressure Components in Eskom Plant.* Group Technology. Johannesburg: Eskom.

Oxford Instruments HKL. (2007). *Oxford Instruments HKL Technology Channel 5.* Hobro: Oxford Instruments HKL.

Ozaki, M., Tokiyoshi, T., Nishimura, N., Koba, K., & Kanaya, A. (2005). Effect of repair welding on the creep rupture strength of an aged weldment. *Welding in the World, 49*(7/8), 67-72.

Patterson, A. (1939, November 15). The Scherrer Formula for X-Ray Particle Size Determination. *Physical Review, 56*(10), 978–982. doi:10.1103/physrev.56.978

Rantala, J., Auerkari, P., Holmstrom, S., Salonen, J., & Laukkanen, A. (2009, April). Creep Strain, Damage and Life Predition for Welded 0.5CrMoV Steel. *OMMI, 6*(1), 1-12. Retrieved from www.ommi.co.uk

Rasiawan, T. (2017). *The influence of prior creep damage on the fracture localisation in X20CrMoV12-1 cross-weld creep tests.* Univeristy of Cape Town. Cape Town: Univeristy of Cape Town.

Ryner, G. (2004). *Creep of welded branched pipes.* Nottingham: University of Nottingham.

Schuller, H., Hagn, L., & Woitscheck, A. (1974). Cracking in the weld region of shaped components in hot steam lines – materials investigations. *Der Maschinenschaden, 47*(1), 1-13.

Sekido, K., Ohmura, T., Hara, T., & Tsuzaki, K. (2012, March 28). Effect of Dislocation Density on the Initiation of Plastic Deformation on FeC. *Materials Transactions, 53*(5), 907-912.

Server, W. L. (1978, April). General Yielding of Charpy V-Notch and Precracked Charpy Specimens. *Journal of Engineering Materials and Technology*, 183-188.

Server, W. L. (2002). Instrumented Charpy Test Review and Application to Structural Integrity. *From Charpy to Present Impact Testing. 30*, pp. 205-212. Poitiers: Elsevier Science Ltd. and ESIS.

Shibli, A. (2014). *Coal Power Plant Materials and Life Assessment - Developments and Applications.* (A. Shibli, Ed.) Cambridge, England: Woodhead Publishing Limited.

Shrestha, T., Alsagabi, S., Charit, I., Potirniche, G., & Glazoff, M. (2015). Effect of Heat Treatment on Microstructure and Hardness of Grade 91 Steel. *Metals, 5*(1), 131-149.

Smit, W. (2015). *240-88300199 - Creep Remaining Life Monitoring Standard.* Materials, NDE and Welding Study Committee. Eskom Materials, NDE and Welding Study Committee.

Smith, D., Walke, N., & Kimmins, S. (2003). Type IV creep cavity accumulation and failure in steel welds. *International Journal of Pressure Vessels and Piping, 80*, 617–627. doi:10.1016/S0308-0161(03)00134-0

Smith, R., & Sandland, G. (1922). An Accurate Method of Determining the Hardness of Metals, with Particular Reference to Those of a High Degree of Hardness. *Proceedings of the Institution of Mechanical Engineers*, 623–641.

Spindler, M. (2017). *ECCC Data Sheets.* The European Creep Collaborative Committee (ECCC). Gloucester: ECCC.

Spindler, S., Allen, D., Baker, A., & Spindler, M. (2010). Analysis of cross-weld creep rupture data on the ½Cr½Mo¼V typeIV zone. *International Journal of Pressure Vessels and Piping, 87*, 296-303.

Sroka, M., Zielinski, A., & Mikuła, J. (2014). The Service Life of the Repiar Welded Joints of Cr-Mo/Cr-Mo-V. *Archives of Metallurgy and Materials, 61 (2016)*(3), 1315–1320. doi:10.1515/amm-2016-0217

Sroka, M., Zielinski, A., Dziuba-Kałuza, M., Kremzer, M., Macek, M., & Jasinski, A. (2017). Assessment of the Residual Life of Steam Pipeline Material beyond the Computational Working Time. *Metals, 7*(82), 1-12. doi:10.3390/met7030082

Steel Data. (2019, May 23). *14MoV6-3 Steel.* Retrieved May 23, 2019, from Database of Steel Transformation Diagrams v.4.0 - Demo Version: http://www.steeldata.info/std/demo/help/legend.html

Stemmer, S. (2014, June 30). Quantitative Scanning Transmission Electron Microscopy. Santa Barbara: University of California.

Stracey, M. G. (2016). *Continuum Damage Mechanics (CDM) modelling of dislocation creep in 9-12% Cr creep resistant steels.* University of Cape Town, Cape Town.

Suman, P., & Pal, S. (2004, June). Microstructure Degradation after Prolonged Exploitation of Heatresistant Steel 14MoV6-3. *Internation Journal of Modern Engineering Research, 4*(6), 42-46.

Sun, W. (1996). *Creep of service-aged welds.* University of Nottingham. Nottingham: University of Nottingham. Retrieved from http://eprints.nottingham.ac.uk/11727/1/339681.pdf

Swinburne University of Technology. (n.d.). *Swinburne Harvard style guide*. (Swinburne University of Technology) Retrieved August 11, 2017, from http://www.swinburne.edu.au/library/referencing/harvard-style-guide/

Taban, E., Kaluc, E., Atici, T., & Kaplan, E. (2012). 9-12% Cr steels: properties and weldability aspects, the situation in Turkish industry. *2nd International Conference on Welding technologies and Exhibiton*.

Taler, J., & Duda, P. (2006). *Solving Direct and Inverse Heat Conduction Problems.* Berlin: Springer-Verlag Berlin Heidelberg.

Tejedor, A. (2011). Gas turbine materials selection, life management and performance improvement. In J. E. Oakey (Ed.), *Power plant life management and performance improvement* (pp. 330-419). Cambridge: Woodhead Publishing Limited.

The Welding Institute. (2014). *Defects/imperfections in welds - reheat cracking.* TWI Ltd. Retrieved from www.twi-global.com

Thermo-Calc. (2006). *Data Base Guide (For Uses in TCC/TCW/DICTRA).* Stockholm: Thermo-Calc Software AB.

Thermo-Calc. (2020). *TCS Steel and Fe-alloys Database (TCFE).* Stockholm: Thermo-Calc Software AB.

Totten, G. E. (2007). *Steel Heat Treatment: Metallurgy and Technologies.* Boca Raton: CRC Press.

Tshamano, L. O. (2017). *Development of the Small Punch Test Platform to Evaluate the Embrittlement of Power Plant Materials.* University of Cape Town. Cape Town: University of Cape Town.

Tu, S.-T., Segle, P., & Gong, J.-M. (1996). Strength Design and Life Assessment of Welded Structures Subjected to High Temperature Creep. *International Journal of Pressure Vessels and Piping*, 171-186.

van Zyl, E. (2013). *High Pressure Pipework for Fossil Fired Power Stations Standard.* Group Technology. Johannesburg: Eskom.

van Zyl, E. (2019). *HP Pipework - Group Technology Strategic Report 2019.* Johannesburg: Eskom.

van Zyl, F. (1997). Life Assessment of High Temperature and Pressure Components in South Africa – An Overview of Philosophy, Methodology and Techniques in Use. *Operating Pressure Equipment* (pp. 141-153). Brisbane: IMMA.

van Zyl, F. H., Bezuidenhout, M. E., Doubell, P., Havinga, F. C., Pegler, D. A., Newby, M., & Smit, W. (2005). Life Assessment and Creep Damage Monitoring of High Temperature Pressure Components in South Africa's Power Plant. *ECCC 2005 - Creep and Fracture in High Temperatur Components - Design and Life Assessment Issues* (pp. 932-943). London: ECCC.

Varma, R. K., & Loveday, M. S. (2002). The Validation of the Draft Standard for Instrumented Impact Testing (IIT) of Metallic Materials Version 10:1994. In D. Francois, & A. Pineau (Ed.), *From Charpy to Present Impact Testing. 30*, pp. 181-188. Poitiers: Elsevier Science Ltd. and ESIS.

Viswanathan, R. (1989). *Damage Mechanisms and Life Assessment of High-Temperature Components.* Ohio: ASM International.

Vyrostkova, A., Kepic, J., Macko, R., & Homolova, V. (2011). Degradation of 0.5Cr-0.5Mo-0.25V steel microstructure during exploitation. *Materials Engineering - Materiálové inžinierstvo, 18 (2011)*, 73-78.

Wits MMU. (2019). *Bruker D2 Phaser XRD User Manual.* Johannesburg: University of the Witwatersrand.

Wyman-Gordon Forgings. (2011). *Certificate of test.* PCC, Wyman-Gordon Forgings. Houston: Wyman-Gordon Forgings.

Yang, T., Li, Z., Wang, J., & Jin, P. (2021, September 17). Hot Tensile Deformation Behavior of Mg-4Li-1Al-0.5Y Alloy. *Frontiers in Materials, 8*(714455), 1-12. doi:10.3389/fmats.2021.714455

Yang, T., Li, Z., Wang, J., & Jin, P. (2021, September 17). Hot Tensile Deformation Behavior of Mg-4Li-1Al-0.5Y Alloy. *Frontiers in Materials, 8*(714455), 1-12. doi:10.3389/fmats.2021.714455

Zeman, M. (2003). Weldability of 13HMF steel after a period of prolonged. *Welding international, 17*(9), 677-683. doi:10.1533/wint.2003.3167

Zhang, J.-S. (2010). Evolution of Dislocation Substructures During Creep. In J.-S. Zhang, *High Temperature Deformation and Fracture of Materials* (pp. 14-27). Cambridge: Woodhead Publishing Limited.

Zielinski, A., Dobrzanski, J., & Dziuba-Kałuza, M. (2013). Structure of welded joints of 14MoV6-3 and 13CrMo4-5 steel elements after design work time under creep conditions. *Archives of Materials Science and Engineering, 61*(2 (2013)), 69-76.

Zielinski, A., Dobrzanski, J., & Jozwik, T. (2012). Assessment of loss in life time of the primary steam pipeline material after long-term service under creep conditions. *Journal of Achievements in Materials and Manufacturing Engineering, 54*(1), 67-74.

Zrilic, M., & Aleksic, R. (2003). The effect of long term exposure to elevated temperature on steam line steel properties. *Thermal Science, 7*(1), 33-46.

Zuidema, W. (2015). *Investigation of the coarse grained heat-affected zone microstructure and hardness of multipass welded X65 linepipe steel.* Delft: Delft University of Technology. Retrieved from http://repository.tudelft.nl/

Chapter 7: Appendix

7.1 Manufacturer's Certificate of Test

Material	according to	Edition
EN 10216-2: 14MoV6-3	1.7715	2007 Annex B Rev 1

State of delivery

Normalised and Tempered

Melting process

E, fully killed

Marking designation		Heat No.
Seamless pipe ID 540 mm t 25 mm	SN 134975 L	Q68441

Heat treatment

Heat treatment	Temperature [°C]	Time at Temperature [hours]	Cooling media
Normalise	946.1	One (1)	Air
Temper	715.6	Two (2)	Air

Tensile test

Temperature [°C]	UTS [MPa]	YS 0.2% [MPa]	%EL	%RA	Bar size [mm]	Test direction
20	526.1	351.6	25.5	76.1	10	Transverse
550	359.9	244.0	32	80	5	Transverse

Brinell hardness

Test location	BHN
Outer Diameter	156
Mid-wall	163
Inner Diameter	156

Charpy – Room temperature (20°C)

Sample	Absorbed energy [J]	Mils Lat. Expansion	%Shear	Direction
1	324.0	89	100	C-L
2	242.7	86	70	C-L
3	248.1	92	75	C-L
Average	271.6	89	82	-

Chemistry (wt. %)

C	Mn	P	S	Si	Cr	Ni	Mo	V	Al	Cu
014	0.51	0.01	0.001	0.26	0.52	0.20	0.59	0.24	0.023	0.12

Micro-Lab-Steel

Microstructure	Photomic	Photomic	Micro etch
Ferrite + Bainite	100×	500×	Nital

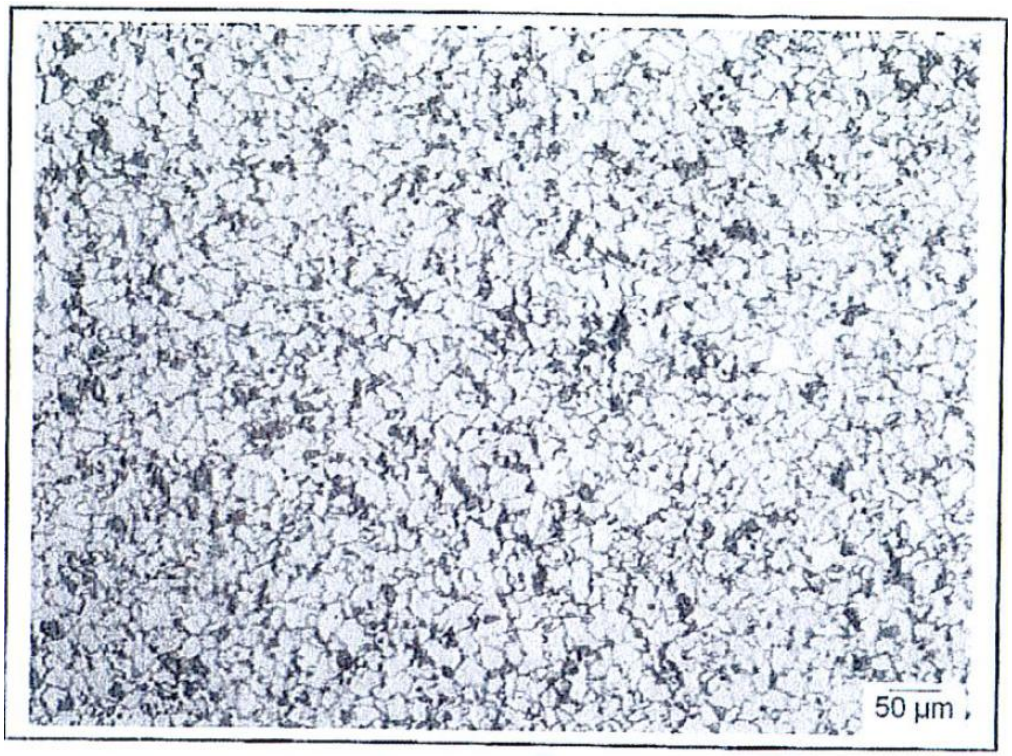

100×

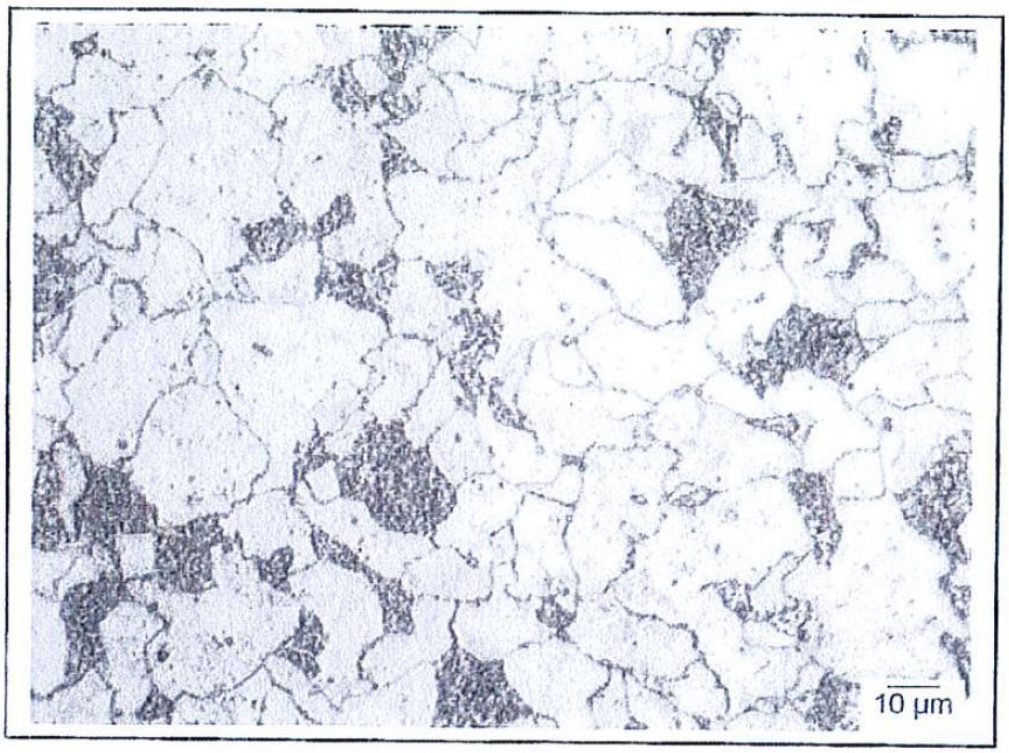

500×